Western Australia School of Mines: Minerals, Energy and Chemical Engineering

Synthesis and Properties of Layered g-C_3N_4 and Their Applications

Xiao Zhang

This thesis is presented for the Degree of
Doctor of Philosophy
of
Curtin University

May 2021

Declaration

To the best of my knowledge and belief this thesis contains no material previously published by any other person except where due acknowledgement has been made.

This thesis contains no material which has been accepted for the award of any other degree or diploma in any university.

Signature:……..

Date:……..11/03/2021……..

Abstract

Investigation of graphitic carbon nitride (g-C_3N_4, a conventional metal-free photocatalysts) with a bandgap of around 2.7 eV that is suitable for visible-light-driven photocatalysis has become a hot topic recent years. The photocatalytic performances of g-C_3N_4 are related to the composition, morphology, microstructures of the material. Thus, morphology control, homojunction and heterostructure construction, as well as property evolution of g-C_3N_4 are keys to improve its performances. The objective of the project is to synthesize g-C_3N_4 with different crystallinities and morphologies, as well as to construct g-C_3N_4-based homojunctions and heterostructures that can be used in various photo- and electro-catalytic applications. During the project, superior thin g-C_3N_4 nanosheets with controlled composition, crystallinity, and high photo-/electro-catalytic properties are prepared via two-step thermal polymerization procedure. g-C_3N_4 crystalline/amorphous lateral-like homostructures are prepared using crystalline g-C_3N_4 nanosheets as seeds via sequential edge-epitaxial growth. The homojunction effectively separates photogenerated charge carriers, resulting in high photo- and electro-catalytic activities. A molten-salt-assisted route is used to prepare red-coloured superior thin carbon nitride (g-C_3N_4) nanosheets which revealed redshifted absorption spectrum and a narrowed bandgap of 1.9 eV. Appealingly, a transparent colloidal solution of red-coloured g-C_3N_4 sheet assembly containing Na^+ ions with increased structural defects is created. The fluorescent g-C_3N_4 sheet assembly solution is stable and reveals concentration-dependent photoluminescence (PL) in the blue to yellow region. At relatively lower concentration, a blue-emitting band is observed, while a green-emitting band is observed at higher concentration. Lateral-like homostructures consisted of both red and light-yellow g-C_3N_4 are prepared using superior thin red g-C_3N_4 nanosheets as seeds via sequential edge-epitaxial growth.

To adjust the morphology of g-C_3N_4, spine-like g-C_3N_4 cages are created for the first time via a novel three-step synthesis method. Especially, the self-assembly of layered precursors (with the assistance of H^+ ions) via acid treatment process plays an important role for the cage shape formation of g-C_3N_4.The H_2 evolution efficiency of hollow spine-like g-C_3N_4 cages is 4000 $\mu molg^{-1}h^{-1}$, which is 7.3 times higher than that of the bulk g-C_3N_4 sample. The g-C_3N_4 cages reveal high CH_4 generation rate (CO_2 reduction) that is 8.7 times as high as that of the

bulk g-C_3N_4 sample. After Pt loading, a rate of 1.93 $\mu molg^{-1}h^{-1}$ is obtained for CH_4 generation without using any co-catalyst or sacrificial agent.

Construction of g-C_3N_4 layered heterostructure is crucial for enhancing charge carrier separation and for expanding photo-adsorption in visible light region. In situ grown of WO_x nanobelts can be achieved on ultrathin g-C_3N_4 nanosheets to create a WO_x/g-C_3N_4 layered heterostructure. Amorphous and crystalline thin g-C_3N_4 nanosheets are produced by adjusting the thermal polycondensation process of precursors. Amorphous $W_{18}O_{49}$/g-C_3N_4 layered heterostructures reveal enhanced photocatalytic degradation performance under visible light irradiation (4 times higher than that of g-C_3N_4), while crystalline $W_{18}O_{49}$/g-C_3N_4 layered heterostructure exhibits excellent hydrogen generation efficiency (nearly 7 times higher than that of g-C_3N_4). WS_2/WO_x composites are grown on crystalline g-C_3N_4 nanosheets to form heterostructures using hydrothermal treatment method. Under full solar spectrum irradiation, the average H_2 evolution rate of the sample is increased by 5.7 times comparing with that of the sample tested under visible light condition.

Layered double hydroxides (LDHs) are popular choices of anionic pollutants adsorbents in wastewater or air treatment fields due to its excellent anion exchange capacity. Horizontally grown and homogeneously distributed NiCoLDH nanoparticles deposited graphitic carbon nitride (g-C_3N_4) nanosheets with different crystallinities (amorphous to crystalline) are created. Congo red (CR) and hexavalent chromium ion (Cr(VI)) adsorption performances of g-C_3N_4/NiCoLDH composites are tested under visible light condition. The presence of NiCoLDH promotes adsorption of the anionic pollutants while g-C_3N_4 in the composite system results in quick photodegradation of CR and photoreduction of Cr(VI). The g-C_3N_4/NiCoLDH composite prepared using amorphous-crystalline g-C_3N_4 homojunctions showed the best adsorption capacity. The kinetics data exhibit improved correlation coefficient for pseudo-second-order (R_2>0.99) and Freundlich isotherm model. The g-C_3N_4/NiCoLDH composites are able to achieve efficient separation of photogenerated electron and hole pairs to improve Cr(VI) adsorption and photo-reduction performances. The maximum monolayer adsorption capacity of CR and Cr(VI) ions of sample LDH-700 are 1100 and 46 mgg^{-1} at 30 °C, respectively.

In addition to the main objective of the project on synthesis, characterization and application of various nanostructured g-C_3N_4, work has also been done in carbon nanotubes

(CNTs) based electrocatalysts for energy conversion and storage. Due to the limited space, the details of the work are not included in the thesis and only the highlights are given here. Palladium nanoparticles (NPs) (with the diameter of Pd NPs to be less than 5 nm on average) deposited Ni-doped CNTs are synthesized. The average Ni metal NPs size is around single atom to 1-2 nm scale. Mono-dispersed Pd NPs are homogeneously immobilized on Ni- and N-doped CNTs and on N-doped commercial made CNTs using poly(diallyldimethyl ammonium) chloride (PDDA) as the key binding component. Such bimetallic doped CNTs show an enhanced electrocatalytic activity as compared with that of the commercial Pd/C (40 wt%) electrocatalysts. In addition, Ni nanoparticles with a Ni_3C shell structure are embedded on N-doped CNTs by thermal condensation of melamine while using Ni salts as the metal source followed by MoS_2 nanosheets deposition. Surprisingly, secondary diffusion of these embedded Ni nanoparticles occurred during the stage of MoS_2 deposition on the CNTs with the help of excess of S precursors. The diffusion results in homogeneous distribution of Ni metal nanoparticles (with an average particle size of less than 3 nm), clusters, and single atoms in both CNTs and MoS_2 nanosheets. The as-prepared MoNiCNTs electrocatalysts exhibit outstanding HER activity with low onset potential and small Tafel slope value in both acidic and alkaline conditions.

Acknowledgements

I would like to first give my sincere gratitude to my supervisor Professor Sanping Jiang, co-supervisor Prof. Zongping Shao, and Prof. Shaomin Liu for giving me inspiration of new ideas, consistent support, and invaluable guidance. It is such an honor for me to be their student, this thesis would not have been completed without their patient guidance. I would like to thank our group members for the friendship and help during my PhD study, especially Dr. Shiyong Zhao, Ms. Xiaoran Zhang, Dr. Yu Liu, Dr. Jianyun Zheng, and Dr. Shuai He for their help on XANES and TEM analysis. I would like to thank Ms. Angelina Rossiter, Mr. Nathan Tarom and Ms. Lana McQueen for their support on lab safety and administrative issues.

I would also like to express my heartfelt gratitude to members of John De Laeter Research Center Dr. Jean-Pierre Veder, Dr. Zakaria Quadir and Dr. Ellaine Miller, as well as Associate Prof. Martin Saunders and Dr. Alexandra Suvorova from University of Western Australia for their help on XPS, SEM and TEM analysis and for providing me with invaluable advices. Special thanks shall go to Prof. Ping Yang and her group for the constant encouragement and support on the project.

List of Publications

1. **Xiao Zhang**, Ping Yang, and San Ping Jiang, Ni diffusion in vertical growth of MoS_2 nanosheets on carbon nanotubes towards highly efficient hydrogen evolution, Carbon, **2021**, 175, 176-186.
2. **Xiao Zhang**, Shuai He and San Ping Jiang, WOx/g-C_3N_4 layered heterostructures with controlled crystallinity towards superior photocatalytic degradation and H_2 generation, Carbon, **2020**, 156, 488-498.
3. **Xiao Zhang**, Jean-Pierre Veder, Shuai He, and San Ping Jiang, Construction of 2D g-C_3N_4 lateral-like homostructures and their photo- and electro-catalytic activities, Chem. Commun., **2019**, 55, 1233-1236.
4. **Xiao Zhang**, Ping Yang, and San Ping Jiang, The edge-epitaxial growth of yellow g-C_3N_4 on red g-C_3N_4 nanosheets with superior photocatalytic activities, Chem. Commun., **2021**, 57, 3119 - 3122.
5. **Xiao Zhang**, PingYang, and San Ping Jiang, Pd nanoparticles assembled on Ni- and N-doped carbon nanotubes towards superior electrochemical activity, Int. J. Hydrog. Energy, **2021**, 46, 2065-2074.
6. **Xiao Zhang**, Peng Wang, Ping Yang, and San Ping Jiang, Photo-chemical property evolution of superior thin g-C_3N_4 nanosheets with their crystallinity and Pt deposition**,** Int. J. Hydrog. Energy, **2020**, 45, 21523-21531.
7. **Xiao Zhang**, Ping Yang, and San Ping Jiang, Horizontally-growth of WS_2/WO_x heterostructures on crystalline g-C_3N_4 nanosheets towards enhanced photo/electro-chemical performance, J. Nanostructure Chem., **2021**, https://doi.org/10.1007/s40097-020-00373-7.
8. **Xiao Zhang,** Ping Yang, and San Ping Jiang, Pt nanoparticles embedded spine-like g-C_3N_4 cages with superior photocatalytic activity for H_2 generation and CO_2 reduction, Nanotechnology, **2021**, 32, 175401.
9. **Xiao Zhang**, Ping Yang, and San Ping Jiang, Horizontally-grown NiCo-LDHs on g-C_3N_4 nanosheets with enhanced adsorption capacity and photoreduction efficiency of Congo red and Cr(VI), Appl. Sur. Sci., **2021**, https://doi.org/10.1016/j.apsusc.2021.149772.

10. **Xiao Zhang**, San Ping Jiang, and Ping Yang, Bright and tunable photoluminescence from the assembly of red g-C_3N_4 nanosheets, J. Lumin., **2021**, 235, 118055.

Table of Contents

Chapter 1: Introduction

1.1 Background

Ever increasing in global energy demand, excess use of fossil fuels and associated environment issues such as emission of greenhouse gases and wastewater pollutions are serious challenges facing the society today. Development of novel technologies in materials science and engineering helps sorting out effective ways for solving energy crisis and supporting environmental protection, e.g., developing advanced materials that are able to convert and store renewable energy from a variety of intermittent energy sources for continuous power supply related applications [1-6]. Heretofore various semiconducting photocatalysts have been created for achieving efficient energy conversion [7, 8]. To solve environmental and energy crisis in an environmental-friendly and sustainable way, conversion of solar energy to energy fuels such as hydrogen has become a hot topic [9-11]. Moreover, appropriate semiconducting photocatalysts with increased absorbance in the whole solar spectrum region are required to carry out various catalytic reactions [12-14]. These semiconducting photocatalysts have been developed and used for CO_2 reduction; water splitting to generate H_2 and O_2; as well as degradation and reduction of pollutants [15-18].

Various semiconducting photocatalysts (e.g. Bi_2WO_6, $BiVO_4$, ZnO, Fe_2O_3, carbon nitride) have been developed to date [19-22]. Among them, TiO_2 is a typical semiconducting photocatalyst discovered by Fujishima and Honda in 1972 [23]. However, one of the limitations of TiO_2 as a photocatalyst is its ultraviolet (UV) light driven activation nature. To expand the absorbance of the photocatalysts, visible-light and near-infrared-light active photocatalysts are of great significance due to the fact that only ~ 4 % of the sunlight energy that reaches the Earth ground is within UV spectrum. In order to achieve efficient utilization of solar energy, development of high quality semiconducting photocatalysts that is active in visible-light region has been receiving growing attention for dealing with environmental threats and addressing energy shortage related issues.

Carbon nitride as a semiconducting photocatalyst has seven phases involving g-o-triazine, β-C_3N_4, cubic C_3N_4, pseudocubic C_3N_4 g-h-triazine, α-C_3N_4, and g-h-heptazine that possess

band gap values in the 0.93~5.49 eV range [24]. Graphitic carbon nitride (as a stable polymeric semiconducting material) consisted of earth-abundant carbon and nitrogen elements is the most stable allotrope of carbon nitrides with diverse properties under ambient conditions [2, 25]. An ideal graphitic carbon nitride nanosheet is composed of melem building blocks involving tri-s-triazine (C_6N_7) and triazine (C_3N_3) rings [26]. Moreover, crystallinity of graphitic carbon nitride can be affected by the distribution of these building blocks. Crystallinity is one of the key factors for determining photoreactivity of g-C_3N_4. Namely, high crystallinity results in decrease in recombination of charge pairs, thus promoting electrochemical performances [27]. In addition, g-C_3N_4, as an organic semiconductor, can be prepared via thermal polymerization reactions which is hard to control over the polymerization process. Hence it is still a challenge adjusting composite, crystallinity and microstructure of the g-C_3N_4 and g-C_3N_4-based material in order to achieve enhanced photo-/electro-chemical activities.

1.2 Objectives and outline of the thesis

The major objective of this thesis is the synthesis and optimization of two-dimensional (2D) to three-dimensional (3D) layered g-C_3N_4 and their homo- and hetero-structures as well as their applications in various fields including photocatalytic water splitting, photo-degradation and photo-reduction in wastewater treatment etc. Various nano-structured thin g-C_3N_4 nanosheets/nanorods were synthesized and their microstructures and properties were comprehensively investigated. These nanostructured g-C_3N_4 with homo- and hetero-structures was shown to have enhanced photo- and electro-chemical activities.

This thesis is composed of 8 chapters. The first chapter is introductory and summarizes the background and the outline of this thesis. Chapter 2 presents a literature review on g-C_3N_4 nanosheets and related topics. The experiment results and discussions are dealt with in chapter 3-9 in detail. Conclusions and future work are present in Chapter 10.

Chapter 1: Introduction

This chapter briefly introduces the background and objectives of the development of g-C_3N_4 based photocatalysts for energy conversion and environment applications.

Chapter 2: Literature Review

A comprehensive review on synthesis methods, microstructure and performances of 2D to

3D layered g-C_3N_4 is presented in this chapter. Detailed analysis and discussion of synthesis, characterization of g-C_3N_4 nanosheets and g-C_3N_4 -based material as well as their applications in various areas are included.

Chapter 3: Superior thin g-C_3N_4 nanosheets: composition, crystallinity, photodegradation properties and their homojunctions

Superior thin g-C_3N_4 nanosheets were prepared using a two-step thermal polymerization procedure to control their composition, crystallinity, and properties. A g-C_3N_4 crystalline/amorphous lateral-like homostructure was prepared using crystalline g-C_3N_4 nanosheets as the seeds material via sequential edge-epitaxial growth. The homojunction effectively promotes the separation of photogenerated charge carriers, leading to high photo- and electro-catalytic activities.

Chapter 4: Superior thin red g-C_3N_4 nanosheets: synthesis, photoluminescence, and their homojuntion

Superior thin red g-C_3N_4 nanosheets were prepared via a moltens salt assisted thermal polymerization method to control the composition, crystallinity, and properties of the material. The photoluminescence (PL) properties of the red coloured g-C_3N_4 nanosheets were systimatically studied for the first time. The red g-C_3N_4 nanosheets were then used as seeds for synthesis of red-yellow g-C_3N_4 lateral-like homojunctiom. The homojunction effectively separates photogenerated charge carriers, resulting in improved photo- and electro-catalytic performances.

Chapter 5: Spine-like g-C_3N_4 cages with superior photocatalytic performance.

This chapter deals with the first synthesis and characterization of spine-like g-C_3N_4 cages using a three-step synthesis method. The self-assembly of small layered precursors (using H^+ ions) via acid treatment forming the caged shape is discussed and the formed composite was used as catalyst for photocatalytic H_2 evolution and CO_2 reduction.

Chapter 6: Growth control of WO_x and WS_2/WO_x on g-C_3N_4 forming heterostructures towards enhanced photo/electro-chemical performances

Two sorts of heterostructures were constructed to study the growth mechanism of the heterostructures. The preparation conditions and properties of WO_x/g-C_3N_4 and

$WS_2/WO_x/g\text{-}C_3N_4$ layered heterostructures are discussed including their photo- and electro-chemical performances. Both $WO_x/g\text{-}C_3N_4$ and $WS_2/WO_x/g\text{-}C_3N_4$ are promising materials for photocatalytic H_2 generation and can be used for photodegradation of organic dyes.

Chapter 7: NiCo-layered double hydroxide/g-C_3N_4 heterostructures with enhanced adsorption capacity and photoreduction of Cr(VI)

Horizontal growth of completely homogeneous NiCo-layered double hydroxides (LDHs) nanoparticles on $g\text{-}C_3N_4$ nanosheets with different degrees of crystallinity (amorphous or crystalline) are reported in this chapter. The adsorption performance of $g\text{-}C_3N_4$/NiCoLDH composites were tested under visible light condition for photodegradation of Congo red (CR) and photoreduction of hexavalent chromium ion (Cr(VI)).

Chapter 8: Conclusions and recommendations for future work

The main results in the thesis are summarized and the recommendations for future work are also addressed in this chapter.

1.3 References

[1] Y. Luo, Y. Yan, S.a Zheng, H. Xue, H. Pang, J. Mater. Chem. A, 2019, 7, 901–924.

[2] W. J. Ong, L. L. Tan, Y. H. Ng, S. T. Yong, S. P. Chai, Chem. Rev. 2016, 116, 7159−7329.

[3] L. Dai, D. W. Chang, J.-B. Baek, W. Lu, Small, 2012, 8, 1130−1166.

[4] K. Liao, P. Mao, N. Li, M. Han, J. Yi, P. He, Y. Sun, H. Zhou, J. Mater. Chem. A, 2016, 4, 5406–5409.

[5] Y. Gong, J. Wang, Z. Wei, P. Zhang, H. Li, Y. Wang, ChemSusChem, 2014, 7, 2303−2309.

[6] C. George, M. Ammann, MB; D'Anna, D. J. Donaldson, S. A. Nizkorodov, Chem. Rev., 2015, 115, 4218−4258.

[7] M. Kapilashrami, Y. Zhang, Y.-S. Liu, A. Hagfeldt, J. Guo, Chem. Rev., 2014, 114, 9662−9707.

[8] L. Wondraczek, E. Tyystjarvi, J. Mëndez-Ramos, F. A. Müller, Q. Zhang, Adv. Sci., 2015, 2, 1500218.

[9] D. Kim, K. K. Sakimoto, D. Hong, P. Yang, Angew. Chem. Int. Ed., 2015, 54, 4−3266.

[10] Z. Li, J. Feng, S. Yan, Z. Zou, Nano Today, 2015, 10, 468−486.

[11] D. Kang, T. W. Kim, S. R. Kubota, A. C. Cardiel, H. G. Cha, K.-S. Choi, Chem. Rev., 2015, 115, 12839−12887.

[12] M. G. Kibria, Z. Mi, J. Mater. Chem. A, 2016, 4, 2801−2820.

[13] R. Long, Y. Li, L. Song, Y. Xiong, Small, 2015, 11, 3873−3889.

[14] K. Meyer, M. Ranocchiari, J. A. van Bokhoven, Energy Environ. Sci., 2015, 8, 1923−1937.

[15] S. Liu, Z. R. Tang, Y. Sun, J. C. Colmenares, Y. J. Xu, Chem. Soc. Rev., 2015, 44, 5053−5075.

[16] X. Chen, S. Shen, L. Guo, S. S. Mao, Chem. Rev., 2010, 110, 6503−6570.

[17] S. J. A. Moniz, S. A. Shevlin, D. J. Martin, Z. X. Guo, J. Tang, Energy Environ. Sci., 2015, 8, 731−759.

[18] J. Ran, J. Zhang, J. Yu, M. Jaroniec, S. Z. Qiao, Chem. Soc. Rev., 2014, 43, 7787−7812. C 2015, 119, 3068−3078.

[19] S. Sun, W. Wang, D. Jiang, L. Zhang, X. Li, Y. Zheng, Q. An, Nano Res., 2014, 7, 1497−1506.

[20] H. Li, H. Yu, X. Quan, S. Chen, H. Zhao, Adv. Funct. Mater., 2015, 25, 3074−3080.

[21] X. Zhou, Q. Xu, W. Lei, T. Zhang, X. Qi, G. Liu, K. Deng, J. Yu, Small, 2014, 10, 674−679.

[22] X. Bai, L. Wang, R. Zong, Y.; Lv, Y. Sun, Y. Zhu, Langmuir, 2013, 29, 3097−3105.

[23] A. Fujishima, K. Honda, Nature, 1972, 238, 37−38.

[24] D. M. Teter, R. J. Hemley, Science, 1996, 271, 53−55.

[25] J. Fu, J. Yu, C. Jiang, B. Cheng, Adv. Energy Mater., 2017, 8, 3, 1701503.

[26] X. Wang, K. Maeda, A. Thomas, K. Takanabe, G. Xin, J. Carlsson, K. Domen, M. Antonietti, Nat. Mater., 2009, 8, 76-80.

[27] X. Zhang, J-P. Veder, S. He, S. P. Jiang, Chem. Commun., 2019, 55, 1233-1236.

Chapter 2: Literature Review

2.1 Introduction

Environmental threats caused by the excess use and combustion of fossil fuels (e.g., oil, natural gas, etc) are examples of some of the biggest challenges facing the mankind in the 21st century [1-3]. It is urgently required to seek clean, renewable, and carbon-neutral alternatives to fossil fuel energy resources. Solar energy as an economical, abundant, and clean energy resource has been widely accepted and could meet the current and future needs of the society [4, 5]. Harvesting and conversion of solar energy into an utilizable energy form became a global priority target over the past decade [6, 7]. The solar light-induced photocatalytic reactions offer efficient approaches for the conversion of solar energy to chemical energy, among which H_2O splitting and CO_2 reduction have mostly been studied. Photocatalysts are able to store the energy of solar photons in chemical bonds [8-11]. Solar spectrum is composed of infrared (IR), ultraviolet (UV), and visible (Vis) wavelength components, whereas visible and IR radiation make up of majority of the solar spectrum (about 43 and 52 %, respectively) [12-14]. Although significant progress has been made in developing semiconducting photocatalysts, the application for maximizing efficient use of solar energy is not fully realized yet [15-20]. For instance, titanium dioxide (TiO_2) as a stable, nontoxic and economical photocatalyst has limited absorption in UV light region [21-26]. Synthesis of photocatalysts to achieve full solar light spectrum absorption therefore is a meaningful but challenging topic.

In general, the three steps involved in photocatalytic water splitting reaction are generation of charge pairs under solar light condition; migration and separation of charge carriers; and the stage of electron/hole reacting with H_2O to generate H_2 or O_2 [27, 28]. The conversion efficiency of solar energy can be affected by the photocatalytic properties of the catalysts. Photocatalyst with narrow band gap promotes the adsorption of light. A relatively negative conduction band enhances the reduction potential of water aiming for H_2 generation and relatively positive valence band improves the oxidation potential of water for O_2 generation [29-32]. Therefore, the development of photocatalysts with suitable band gap; efficient photogenerated carrier separation and high surface area to increase the number of active cites;

and that can absorb greater proportions of solar spectrum is of great significance [24, 33-36]. Efficient photocatalysts possess outstanding Vis and near IR light absorption performance, and are stable under harsh chemical and thermal conditions [37]. The application of traditional inorganic semiconductors (e.g. TiO_2 and CdS) is limited due to their UV excitation responsive nature [38-40]. It is of significant importance to construct highly efficient photocatalysts that are abundant, stable, facile to fabricate.

g-C_3N_4 as a stable semiconducting material that is composed of earth-abundant N and C atoms, has been considered to be the most chemically and thermally stable carbon nitride allotropes with various unique properties [41-43]. Ideal graphitic carbon nitride nanosheets are composed of triazine (C_3N_3) and heptazine (C_6N_7, also called tri-s-triazine) building blocks [44]. The crystallinity of g-C_3N_4 generally can be affected by the distribution of triazine and heptazine unis. Crystallinity is one of the key factors that determines the photoreactivity of g-C_3N_4 material. In fact, high crystallinity can reduce the number of recombination centers for charge carriers and thus enhance electrochemical activity of the material [45]. Triazine or tri-s-triazine rings can be cross-linked for achieving construction of the g-C_3N_4 system (Fig. 1-1) [46, 47].

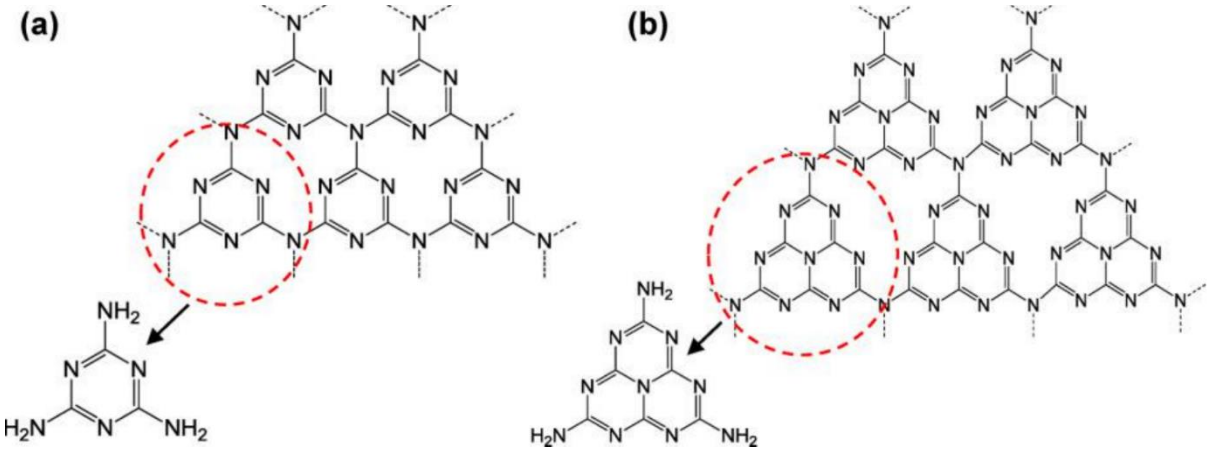

Figure 1-1. (a) Triazine building blocks of g-C_3N_4. (b) Tri-s-triazine building blocks of g-C_3N_4. Reprinted with permission from ref [8]. Copyright 2018 American Chemical Society

Owing to the existence of N and sp^2-hybridized C which results in formation of the π-conjugated system, g-C_3N_4 has relatively lower band gap value among the carbon nitrides allotrope family [41-47]. Compared with typical TiO_2-based photocatalysts, conventional g-C_3N_4 exhibits band gap at around 2.7~2.8 eV which is able to absorb visible light at ~460 nm

(blue). g-C_3N_4 (as a precedent metal-free organic semiconducting catalyst) plays a significant role in photocatalytic applications owing to the aromatic C−N heterocycles in the g-C_3N_4 network as well as thermally and chemically stable nature of the material [48]. However, factors that inhibits practical application of g-C_3N_4 include relatively high photogenerated charge carrier recombination efficiency; limited absorption in the wavelength range of greater than 460 nm and extremely low conductivity [49, 50]. For enhancing the charge carrier separation efficiency and for optimizing photocatalytic activities, different methodologies have been developed to modify bulk g-C_3N_4, including band gap and electronic structure modulation; heterostructure formation; as well as 0-3 dimensional (0-3D) shape control of g-C_3N_4 [51]. Typical examples include introducing metal (e.g. transition metal Ni and Co) and nonmetal (e.g. B, C, P, and N) doping ions during the copolymerization process, that resulting in adjustment of electronic structure and energy band configuration of the g-C_3N_4 matrix thus leads to changes in adsorption region [52, 53]. The control of layers and geometrical shapes of g-C_3N_4 can be achieved utilizing various synthesis methods, such as, mechanical and chemical exfoliation method, hard and soft templating method and supramolecular preorganization methods [54-56]. Development of g-C_3N_4 based heterostructures and hybrid nanocomposites provides ideal approaches for improving physiochemical properties and enhancing photocatalytic performances of the catalysts [57]. Because of the fact that enhanced charge separation efficiency is crucial for enhancing photocatalytic performances, g-C_3N_4-based heterojunctions possessing appropriate band structures in the heterojunction interface have been widely studied.

2.2 Synthesis of g-C_3N_4

Bulk g-C_3N_4 (as an organic semiconductor) normally can be synthesized via thermal polymerization of N- and C-rich organic precursors at relatively high temperature. Fig. 1-2 shows the schematic diagram for the synthesis of carbon nitride via polycondensation of N-rich precursors including urea, dicyandiamide, and melamine. Even though bulk g-C_3N_4 (with semiconductor-like absorption in Vis blue wavelength region) possesses a bandgap at around 2.7 eV, bulk g-C_3N_4 cannot be considered as an ideal photocatalyst, because of its relatively low specific surface area (that is less than 20 m^2g^{-1}) and blocked active sites that impedes

incorporation of g-C_3N_4 into the photocatalytic reactions due to the existence of closed-packed lattice of bulk g-C_3N_4 layers [58]. Efforts have been done on improving the photocatalytic performance of g-C_3N_4 based and g-C_3N_4 materials, such as, structural design and adjustment [59, 60]. Facile strategies that are able to improve the morphology and property of g-C_3N_4 based and g-C_3N_4 are greatly sought after.

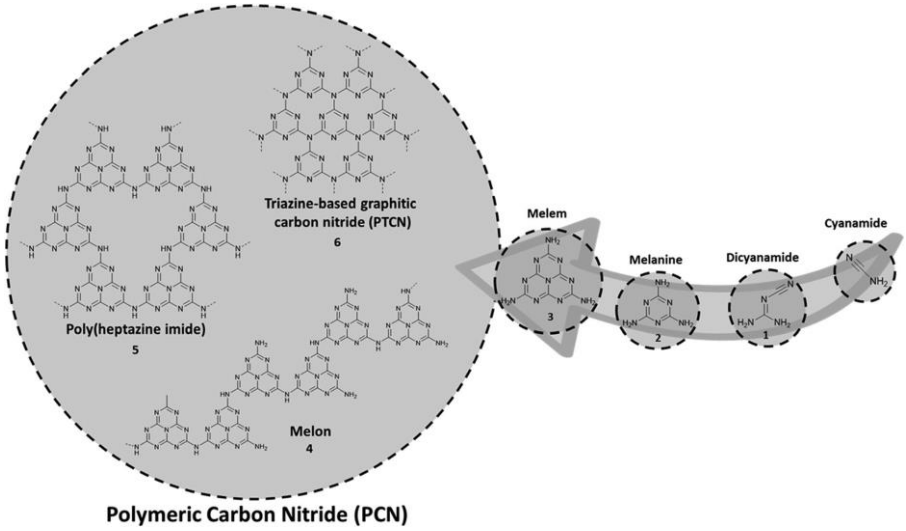

Figure 1-2. Formation diagram of polymeric carbon nitride via N-rich precursors polycondensation. Reprinted with permission from ref [8]. Copyright 2018 American Chemical Society

2.2.1 Synthesis of thin g-C_3N_4 nanosheets

Among the various strategies hitherto developed (e.g. heteroatom doping, heterojunctions, and nanostructure design), exfoliation of bulk g-C_3N_4 crystals for forming their nanosheets counterparts has attracted considerable attention [7]. In general, ultrathin g-C_3N_4 possesses increased number of exposed active sites, relatively larger surface area, shorter diffusion paths as well as relatively higher conductivity in comparison with its bulk counterparts [61, 62]. Moreover, the electronic band gap of g-C_3N_4 materials can be increased by shifting of the band edges to the opposite directions thus having enhanced redox capability for various reactions due to the quantum confinement effect of the material. On the other hand, photophysical behavior of g-C_3N_4 can also be altered to extend the lifetime of photogenerated electron-hole pairs. Top-down process of the exfoliation method can be used to create single graphene oxide layer from high-quality bulk crystalline graphite. However, unlike graphite the planar atomic structure of bulk g-C_3N_4 may be seriously damaged during the exfoliation process because of

the fact that hydrogen bondings between the strands of melem building blocks are quite weak. Bottom-up strategies in contrast are a quite promising method for production of high quality 2D g-C_3N_4 nanosheets. For example, Xiao and co-workers developed a low-cost bottom-up method using molecular self-assembly to construct porous few-layered C_3N_4 with improved photocatalytic hydrogen generation efficiency [63]. Fig. 1-3 shows the formation process of the porous few-layered C_3N_4. According to Xiao et. al., self-assembly of cyanuric acid and melamine can be utilized to construct a layered rod nanocomposite with abundant -NH_2 and -OH functional groups in between heptazine layers as well as a large interlamellar distance of 0.315 nm [63]. Due to the unique features of cyanuric acid, small polar molecules can be easily intercalated into the layered rod precursors for achieving production of porous few-layered g-C_3N_4.

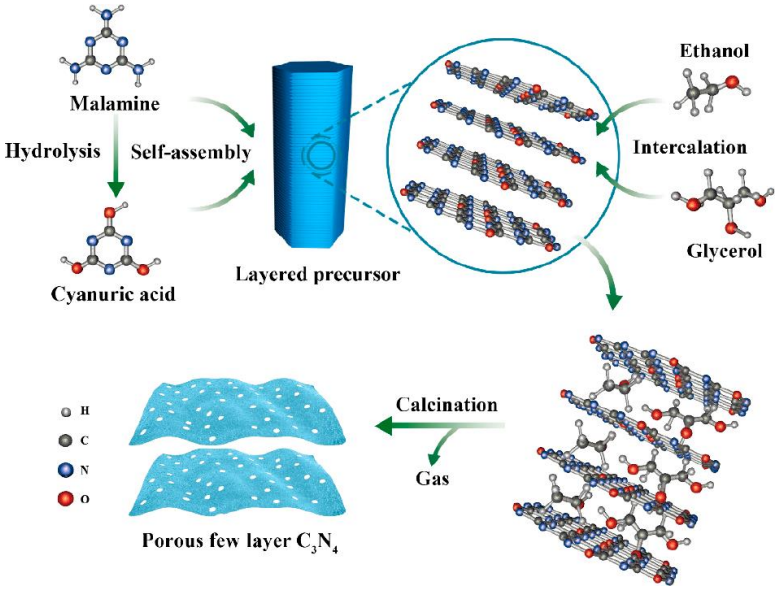

Figure 1-3. Schematic representation of the few-layered C_3N_4. Reprinted with permission from ref [63]. Copyright 2019 American Chemical Society.

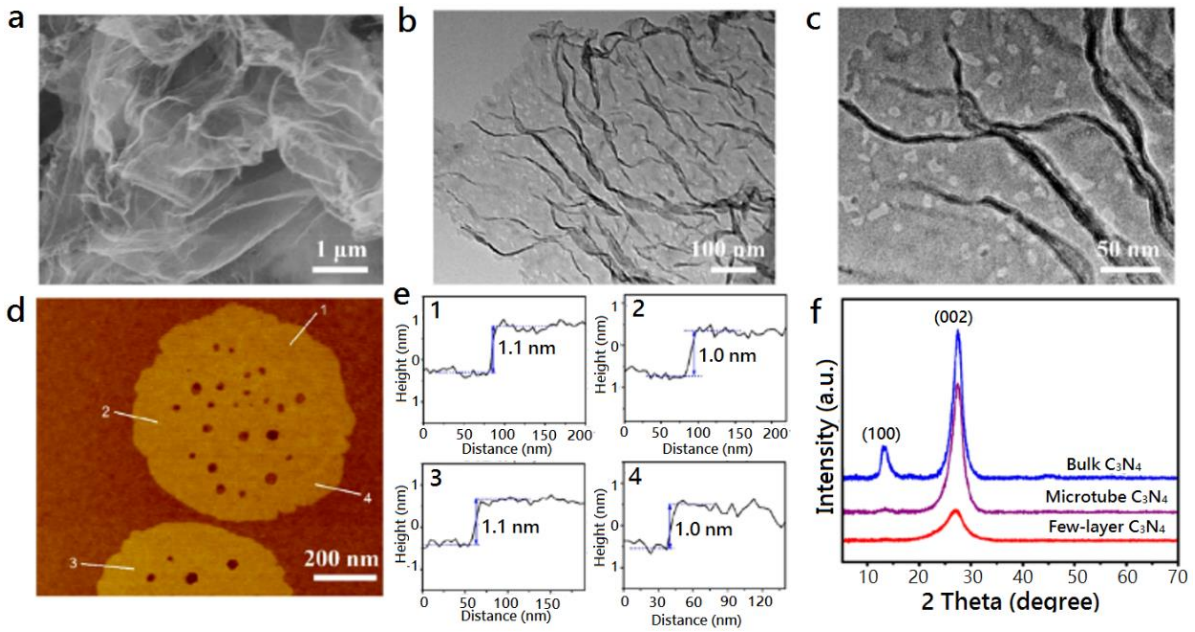

Figure 1-4. SEM and TEM images of the few-layered g-C_3N_4: (a) SEM image; (b & c) TEM images with different magnifications; (d) magnified AFM image with (e) showing the corresponding height profiles (along the four white lines in d). (f) XRD patterns of the few-layered g-C_3N_4. Reprinted with permission from ref [63]. Copyright 2019 American Chemical Society.

SEM, TEM, and AFM images in Fig. 1-4 show an example of a the few-layered g-C_3N_4 with the ordinary sheet-like morphology and tens of micrometers nanosheets size [63]. Nanopores ranging from ~2 to 15 nm can be observed (as shown in Fig. 1-4b to 4d). The tendency of these nanosheets for forming bent or curved shape at relatively high temperature settings can be explained by the lowering of the material's surface energy.

Another typical method to prepare ultra thin g-C_3N_4 nanosheets is the harsh Lewis acid treatment method [64]. Pristine g-C_3N_4 can be dispersed into concentrated H_2SO_4 solution with vigorous stirring. An example of the product obtained after centrifugation and washing process in literature are shown in the TEM images in Fig. 1-5a and 5b. As presented in Figure 1-5c and 5d, the thickness of randomly selected g-C_3N_4 nanosheets is in the range of 0.46 to 0.93 nm, suggesting the exfoliated g-C_3N_4 nanosheets to have one to two stacked layers [65]. The XRD patterns in Fig. 1-5e demonstrates that the acid treated g-C_3N_4 (g-C_3N_4-H_2SO_4) and pure g-C_3N_4 have similar crystal structure.

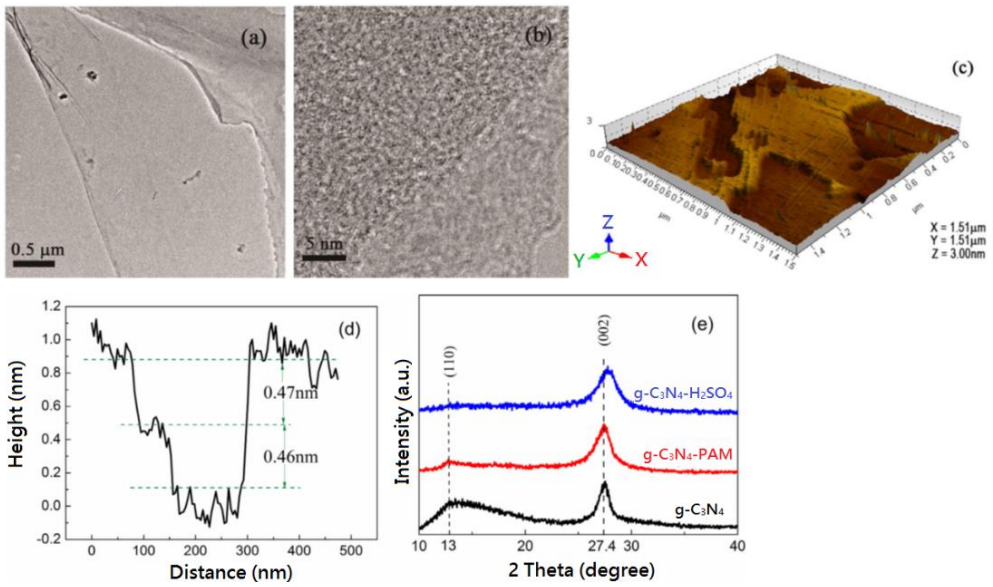

Figure 1-5. TEM and AFM images obtained for g-C_3N_4 nanosheets: (a & b) TEM images; (c) AFM image of selected g-C_3N_4 nanosheets; (d) height graph of the selected g-C_3N_4 nanosheets. (e) XRD patterns obtained for g-C_3N_4-H_2SO_4, pristine g-C_3N_4, g-C_3N_4-PAM. Reprinted with permission from ref [64]. Copyright 2017 Elsevier.

2.2.2 Synthesis of mesoporous g-C_3N_4

Construction of porous structures with increased number of active sites and higher surface area (compared with conventional nanosheets structure) has been considered as a precedent approach for enhancing photocatalytic performances of materials. Mesoporous g-C_3N_4 nanostructures have been attracting considerable attention. Among a variety of methodologies, hard and soft templating approach has been widely studied to construct porous g-C_3N_4. However, since toxic agents and organic solvents are normally utilized for removing the templates, salt template has been considered as the precedent candidate recently to replace the traditional templating methods to achieve facile synthesis, easy movability, and scalable production. For example, a straightforward NaCl-assisted ball-milling strategy was developed by Qian and co-workers to construct 3D porous g-C_3N_4 networks since 3D porous networks can be tailored by using cubic NaCl particles as the easy-to-move template, which at the same time is able to prevent the aggregation of g-C_3N_4 during calcination [65]. Fig. 1-6 shows the preparation process of the porous g-C_3N_4 networks. In this method, NaCl crystals was attached to melamine after ball-milling followed by thermal condensation of melamine and NaCl melting with increasing temperature. Moreover, during the annealing process, the in-situ grown g-C_3N_4 nanosheets can be pierced by the NaCl crystals in the composites system. The porous

3D g-C_3N_4 nanosheets as the final product can be obtained after NaCl removal.

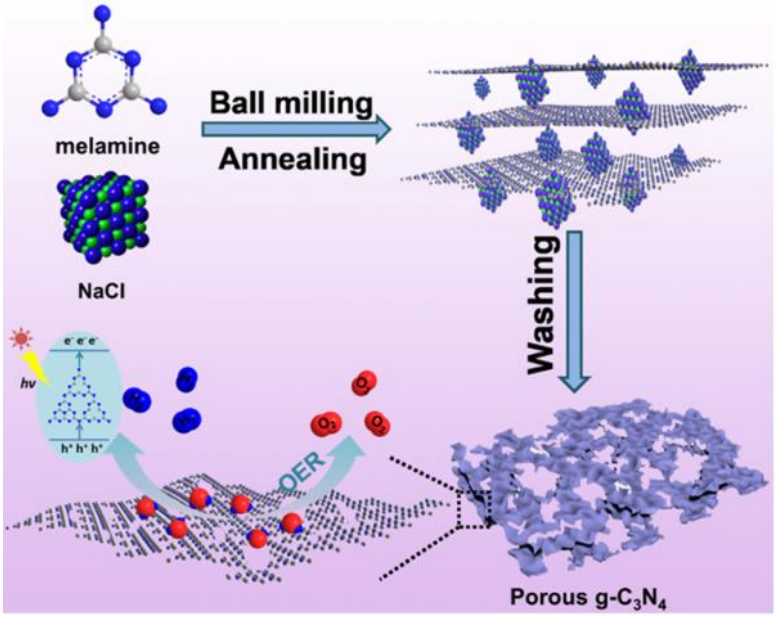

Figure 1-6. Schematic representation for the NaCl-template assisted synthesis of porous g-C_3N_4. Reprinted with permission from ref [65]. Copyright 2019 American Chemical Society.

Morphologies of the g-C_3N_4 samples with different amount of NaCl added are shown in Fig. 1-7 [65]. According to Qian et.al., comparing with the conventional bulk g-C_3N_4 nanosheets (with no NaCl addition shown in Fig. 1-7a) exhibiting thick nanosheets structure, the NaCl incorporated g-C_3N_4 samples reveal a completely different 3D porous structure (Fig. 1-7b~e) with adjustable NaCl amount. The melting-salt method developed by Wang's group to construct water-soluble and porous g-C_3N_4 nanosheets is shown in Fig. 1-8 [66].

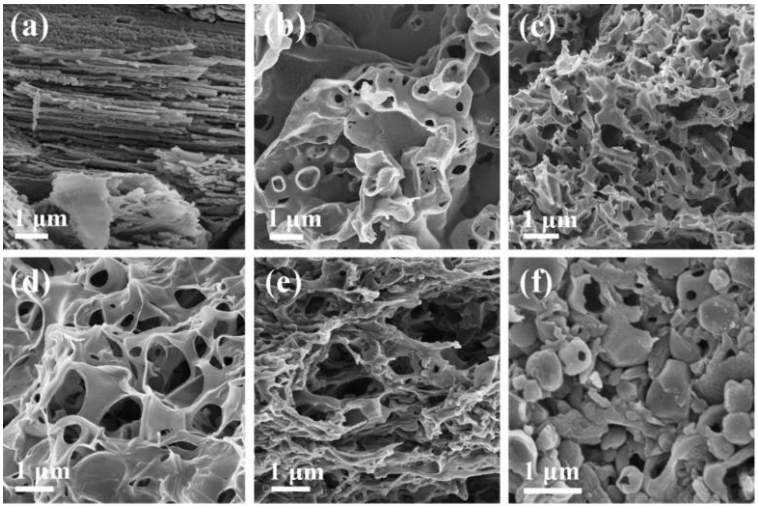

Figure 1-7. SEM images of NaCl incorporated g-C_3N_4 using varying concentrations of NaCl: (a) with no NaCl addition; (b to f) various amounts of NaCl incorporated. Reprinted with permission from ref [65]. Copyright 2019 American Chemical Society.

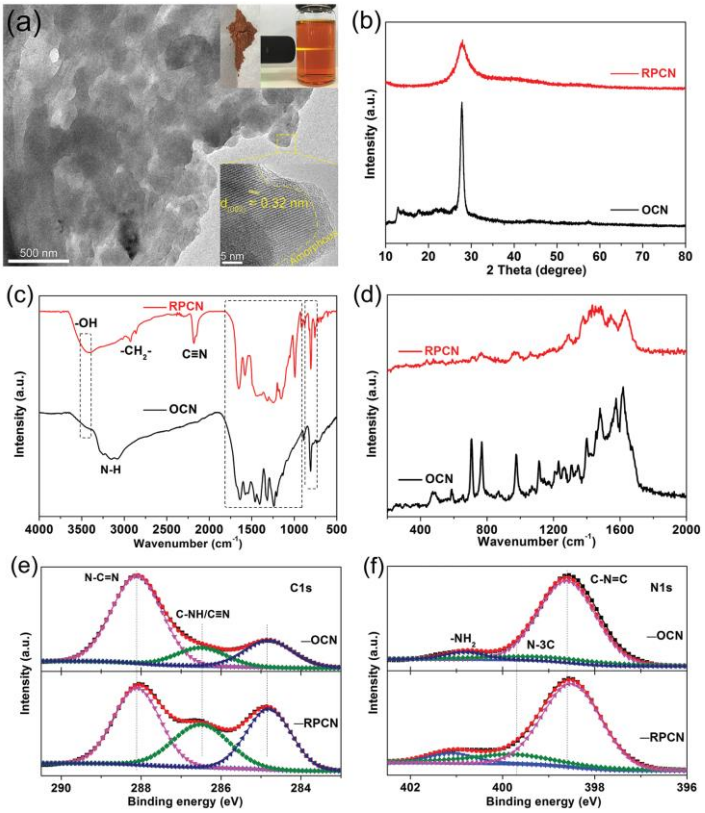

Figure 1-8. (a) TEM images of the g-C_3N_4 nanosheets (sample RPCN), with the insets showing the HRTEM image of RPCN (lower-right) and the digital image of RPCN in powder and in aqueous solution form (upper-right). Spectra and patterns of bulk g-C_3N_4 (OCN) and RPCN: (b) XRD patterns; (c) FTIR spectra; (d) Raman spectra; (e) XPS C 1s spectra; (f) XPS N 1s spectra. Reprinted with permission from ref [66]. Copyright 2018 John Wiley & Sons, Inc.

2.2.3 Doping of g-C_3N_4

Photocatalytic activities can be affected by the amount of exposed active sites in the material. The structural modification of photocatalyst, as a promising methodology, is able to tune the electronic and physicochemical properties to achieve enhancement in photocatalytic activities of the catalyst. Elemental doping, morphology control, defect engineering, crystallinity manipulation, and heterojunction construction are methodologies that are able to improve photocatalytic performances of g-C_3N_4 materials. Among these, doping is able to cause reduction in energy band gap and to introduce impurity intermediate energy levels in forbidden energy band [53]. Examples of elemental doping on g-C_3N_4 include metal and non-metal doping. These doping elements enter the g-C_3N_4 network to adjust the band gap of the material. In comparison with those metal elements, the non-metal elements normally are able to enter the g-C_3N_4 network more easily.

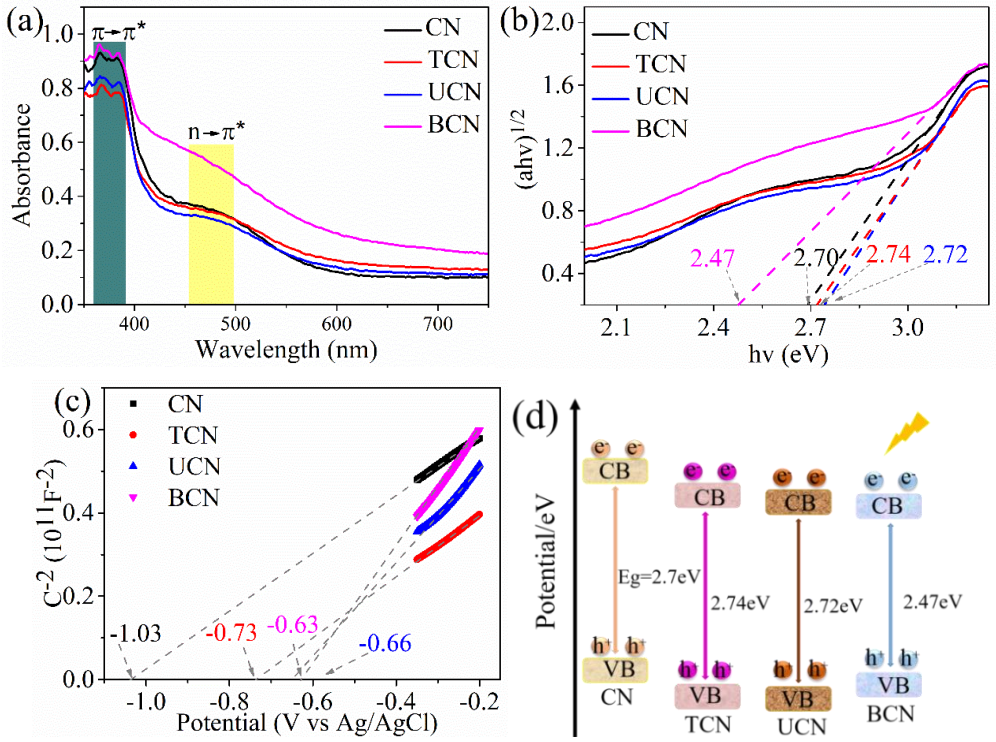

Figure 1-9. (a) UV-Vis diffuse reflectance spectra obtained for the non-metal doped C_3N_4 composites. (b) $[F(R\infty)h\nu]^{1/2}$ *vs.* hν plots of the non-metal doped C_3N_4 composites. (c) Flat band potentials calculated for the non-metal doped C_3N_4 composites based on Mott-Schottky plots (x-intercept). (d), Band structures of the non-metal doped C_3N_4 composites. Reprinted with permission from ref [53]. Copyright 2020 Elsevier.

Among the various doping strategies developed, the introduction of heteroatoms causes changes of band structure of g-C_3N_4, significantly expanding visible-light response range in order to enhance the photocatalytic performances of the material. For instance, elements such as F, O, S, C, and I can be incorporated into g-C_3N_4 network to achieve modification on electronic and optical properties of the materials [67]. Huang and co-workers discovered that drastic decrease in bandgaps of g-C_3N_4 can be observed upon O doping [68]. Dong and co-workers found that C atoms in the g-C_3N_4 system can be replaced by N atoms, resulting in a band gap change of 2.72 to 2.65 eV [69]. Recently, Yang's group reported the construction of S, C, and N atoms doped ultra-thin g-C_3N_4 nanosheets (denoted as TCN, BCN, and UCN) via two-step high-temperature calcination treatment by using thiourea, barbituric acid, urea and melamine as the precursors [53]. Enhancement in photo-catalytic hydrogen evolution activity of the g-C_3N_4 materials can be observed after barbituric acid doping. According to Wang et.al., the highest hydrogen generation rate was able to reach 2.35 $mmolg^{-1}h^{-1}$ (BCN) which is 8.1 times of that of the pure g-C_3N_4 (Fig. 1-9) [53]. This can be ascribed to the tendency of g-C_3N_4

becoming planarized due to C doping so that visible light absorption range of the materials can be extended. Moreover, photocatalytic organic dyes degradation efficiency of the g-C_3N_4 samples were enhanced after doping using urea. Changes in band gaps (shown in Fig. 1-9c and 9d) can be observed after doping due to the structure and layer number changes of the composites. The C-doped g-C_3N_4 shows a reduced band gap value, while S and N-doped g-C_3N_4 exhibits increased bandgap values.

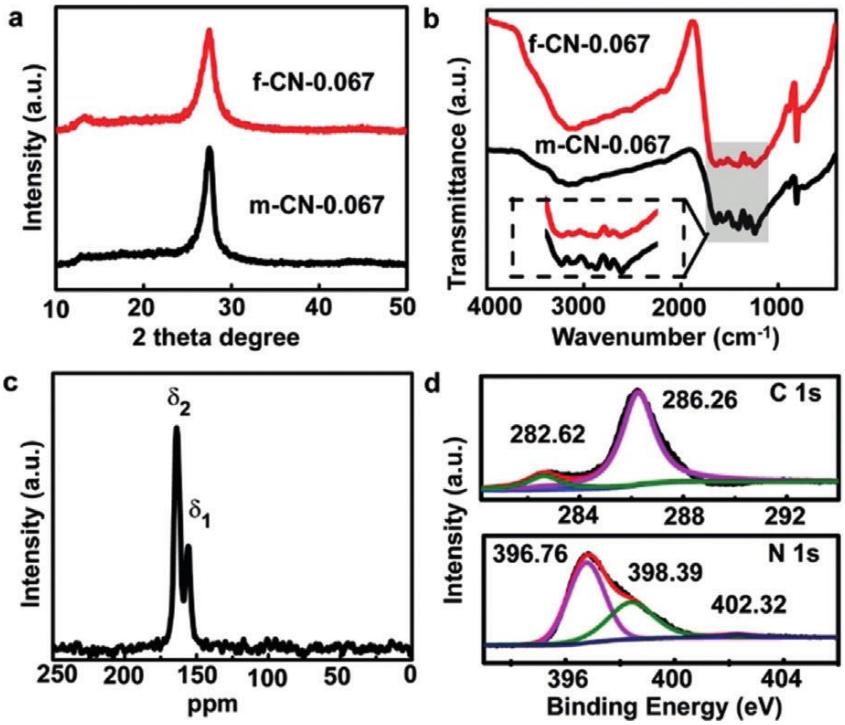

Figure 1-10. Data collected for m-CN-0.067 and f-CN-0.067: (a) XRD patterns, (b) FTIR spectra. Inset in (b) shows the fingerprint bands of the two samples in the range of 1200 to 1640 cm^{-1}. (c) ^{13}C MAS NMR spectra obtained for m-CN-0.067. (d) XPS spectra data collected for m-CN-0.067. Reprinted with permission from ref [70]. Copyright 2019 John Wiley & Sons, Inc.

To deal with the energetic barrier of replacement of N with C in g-C_3N_4, efforts have been made on copolymerization of melamine with π-electron rich aromatic monomers. Li and co-workers developed a simple route for incorporation of C in g-C_3N_4 to produce an efficient photocatalysts via microwave-assisted calcination of monomers for H_2 generation as shown in Fig. 1-10 [70]. According to Li et.al., the π- rich aromatic barbituric acid and melamine can be used to be copolymerized to form the composite samples among which sample f-CN-0.067 (the reference sample) was synthesized via calcination in a furnace at 520 ºC using the 2,4,6-trihydroxy-1,3-diazine (THD) to melamine ratio to be 0.067, and sample m-CN-0.067 was

prepared using microwave-assisted heat treatment at 520 ºC for 4 hours in air. Both these two composite samples show very similar XRD and FTIR spectra Fig (1-10).

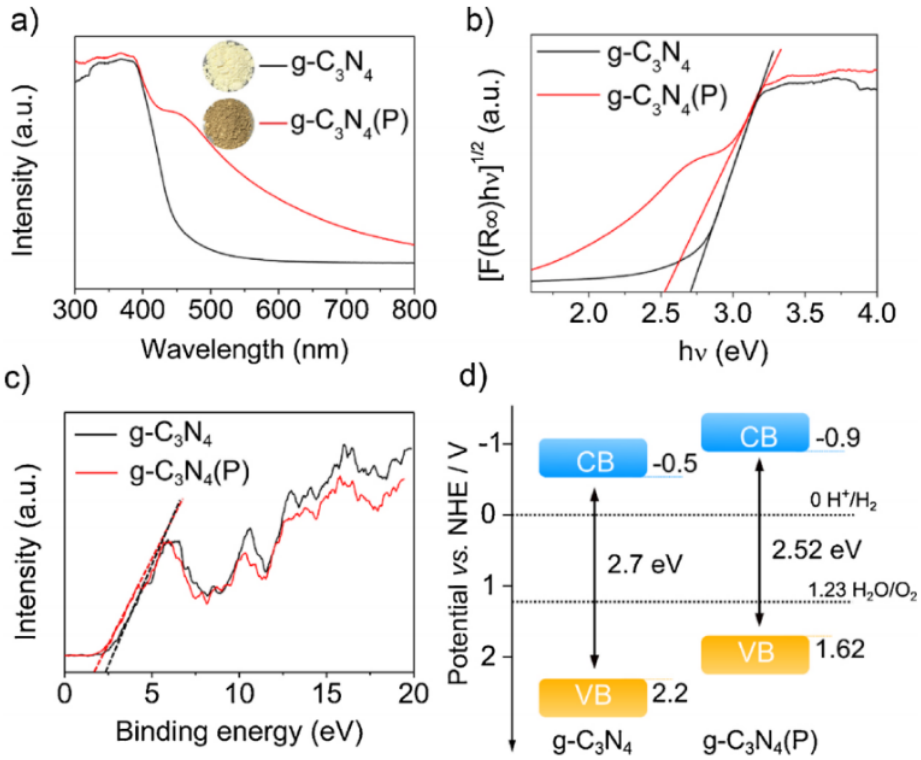

Figure 1-11. (a) UV–Vis absorption spectra obtained for sample g-C_3N_4(P) and pristine g-C_3N_4, with insets showing the pictures of actual g-C_3N_4 samples. (b) The $[F(R\infty)h\nu]^{1/2}$ *vs.* hν plots of sample g-C_3N_4(P) and pristine g-C_3N_4. (c) XPS valence band spectra of g-C_3N_4(P) and g-C_3N_4. (d) Illustration of band structures of g-C_3N_4(P) and pristine g-C_3N_4. Reprinted with permission from ref [71]. Copyright 2020 Elsevier.

One commonly utilized strategy for adjusting bandgap of g-C_3N_4 nanosheets is the post-treatment method using different gases (e.g., H_2, NH_3, H_2S) to introduce non-metal elements into g-C_3N_4 framework. Wang and coworkers were able to modify the microstructure of g-C_3N_4 nanosheets via partial substitution of corner site carbon atoms with phosphorous heteroatoms through thermal phosphorization process [71]. Fig. 1-11 shows the changes occurred in g-C_3N_4 nanosheets after P doping. In comparison with the pristine g-C_3N_4, phosphorized g-C_3N_4 revealed enhanced photocatalytic hydrogen generation activity [71]. This can be explained by factors including enhanced photogenerated charge carrier transfer rate, narrowed bandgap, and the presence of hydrophilic surface absorbing molecule of the phosphorized g-C_3N_4 nanosheets. Mechanical grinding treatment of the mixture of NaH_2PO_2 and bulk g-C_3N_4 nanosheets plays a key role in triggering reaction between PH_3 and g-C_3N_4

forming homogenous composite material.

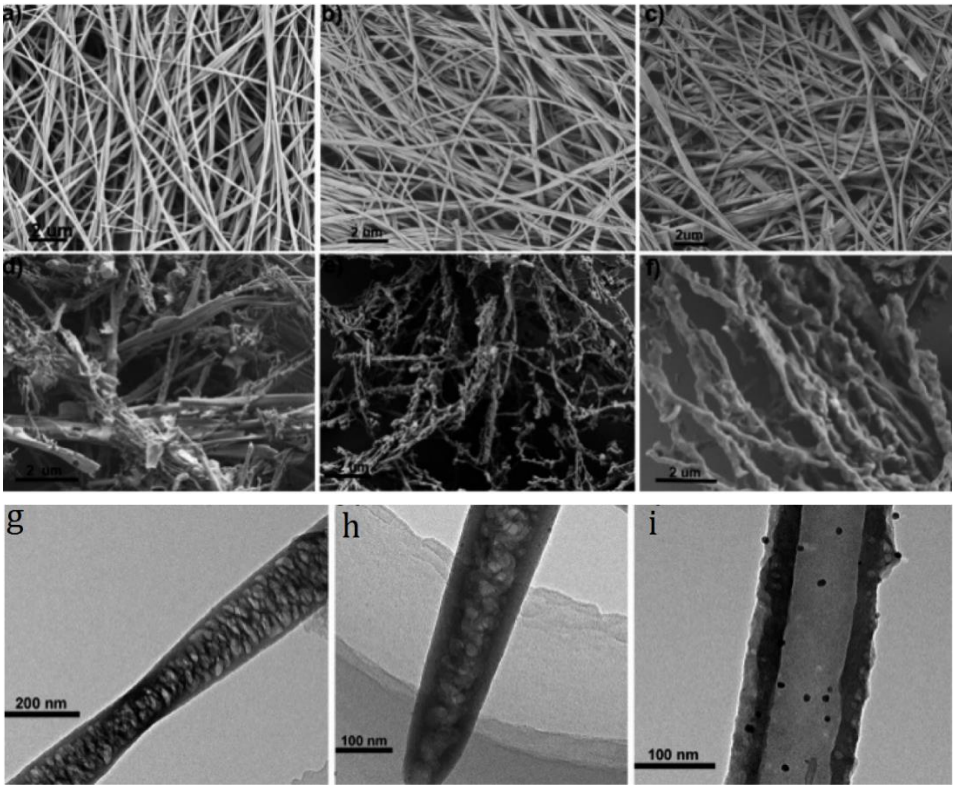

Figure 1-12. SEM images of Ag decorated g-C_3N_4 precursors: (a) AgMA3; (b) AgMA2; (c) AgMA1. SEM images of Ag/g-C_3N_4 nanocomposites after calcination: (d) Ag-g-C_3N_4-3; (e) Ag-g-C_3N_4-2; (f) Ag-g-C_3N_4-1.TEM images of Ag/g-C_3N_4 nanocomposites after calcination: (g) Ag-g-C_3N_4-1; (h) Ag-g-C_3N_4-2; (i) Ag-g-C_3N_4-3. Reprinted with permission from ref [74]. Copyright 2017 American Chemical Society.

Loading of metal co-catalyst is another commonly used approach for enhancing photo- and electro-catalytic activities of g-C_3N_4 based materials. Introduction of cocatalysts is crucial for enhancing hydrogen evolution reaction (HER) activity of g-C_3N_4 [72]. Transition metals are typical examples of low-cost cocatalysts. Cobalt nanocomposites including $CoSe_2$, $Co(OH)_2$, CoP, and Co_2P are popular cocatalysts for achieving enhanced electrochemical performances with high durability [73].

In general, Ag as a low-cost noble metal can be used in synthesis of various composite materials. For instance, an organic metal supramolecular hydrogel method was developed by Wang et. al. for the construction of porous Ag/g-C_3N_4 composite nanofiber with improved photocatalytic H_2 evolution activity [74]. According to the authors, the organic metal supramolecular networks can be created via self-assembly of organic ligands and metallic nodes, in which bondings including π−π interaction, metal coordination, and hydrogen bonding

are formed. The Ag deposited g-C_3N_4 precursors (AgMA-1, AgMA-2, and AgMA-3) were synthesized by calcination of the Ag-melamine hydrogel mixture (in which the Ag to melamine molar ratio of 1:12, 1:6, and 1:2 were used, respectively), and the Ag deposited g-C_3N_4 composites possessing varying concentrations of Ag nanoparticles (Ag-g-C_3N_4 samples) were formed via calcination of AgMA-n precursors at 550 °C in Ar. Fig. 1-12 illustrates that the TEM and SEM images of samples (prepared at different synthetic stages) show homogeneous distribution of Ag nanoparticles on g-C_3N_4 porous fibers due to the utilization of self-assembly processes.

2.2.4 Surface and structural engineering

The construction of built-in electric field (BIEF) is useful for achieving efficient carrier separation, in which surface and structural engineering help to form BIEF in g-C_3N_4. BIEF developed within organic semiconductor facilitates faster migration of charge carriers leading to enhanced electroconductivity. Yu et. al. found out that, compared with semiconducting heterojunctions using suitably aligned energy levels, gradient doping is able to establish BIEF within the same phase for eliminating the effects resulted from the presence of interface impurity to achieve better separation efficiency [75]. Surface and structural engineering has been commonly utilized to enhance the photocatalytic performances of g-C_3N_4 and g-C_3N_4 composite materials. Decrease in layer numbers of g-C_3N_4 using thermal etching and exfoliation method leads to increasing in number of active sites on g-C_3N_4 as well as to shorten the carrier diffusion path [75]. Both nanoscale pore casting and 2D conjugate layer breaking can enhance photocatalytic efficiency of the material.

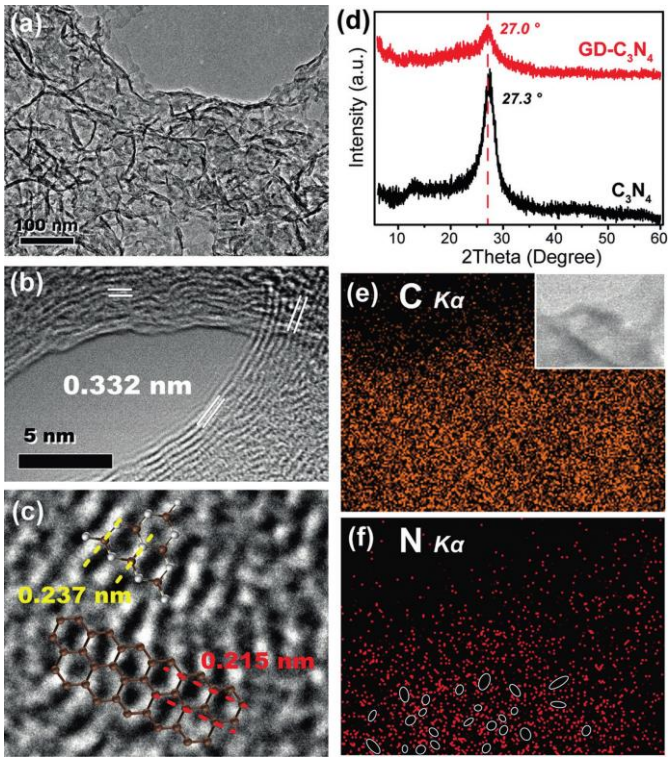

Figure 1-13. (a) TEM image of GD-C_3N_4 composites. (b & c) HRTEM images of GD-C_3N_4 composites. (d) XRD patterns of GD-C_3N_4 composites and C_3N_4. (e & f) Elemental mapping of GD-C_3N_4 composites with the inset in (e) showing the corresponding part of the sample photograph. Reprinted from ref [75]. Copyright 2018 John Wiley & Sons, Inc.

Yu and co-workers reported a surface engineering strategy on g-C_3N_4, in which various coplanar graphitic carbon rings were incorporated in g-C_3N_4's conjugated system along surface [75]. Fig. 1-13 shows the TEM images, XRD patterns, and elemental mapping of the synthesized g-C_3N_4 composites. The sample was referred by the authors as GD-C_3N_4 with GD to be the abbreviation of gradual doping. The result confirms that gradual rearrangement of components (which related to the band levels and establishment of BIEF) facilitates charge-pair separation and transfer, and thus enhancing the photocatalytic hydrogen evolution efficiency and stability of the composite material [75]. In Fig. 1-13b, the lattice fringes of 0.332 nm spacing emerged on the edges of the base material. The interplanar distance is greater than the commonly encountered value of 0.325 nm because of the periodic stacking of layers of the composites, and the interplanar distance is similar to the interlayer spacing of graphite (0.335 nm). X-ray diffraction (XRD) patterns in Fig. 1-13d also confirms gradual doping on g-C_3N_4.

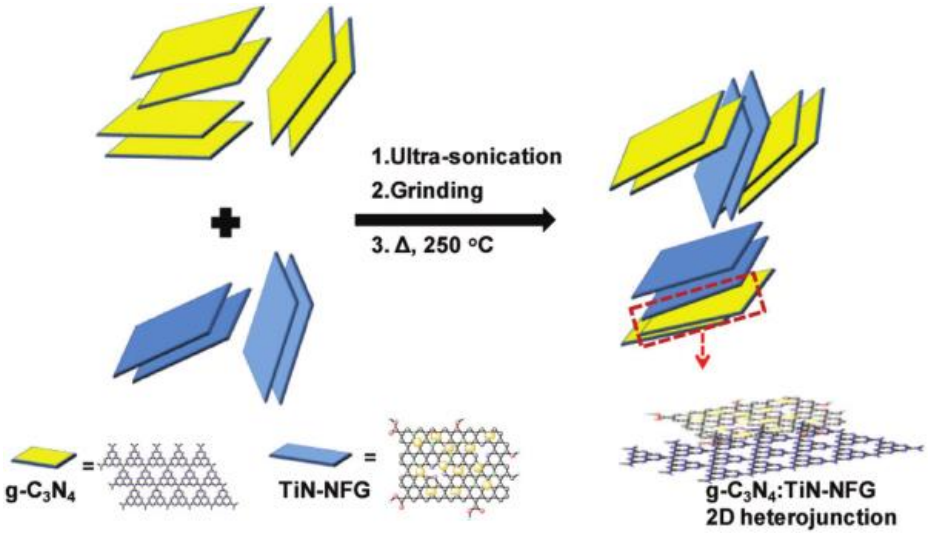

Figure 1-14. Formation diagram of 2D g-C_3N_4/TiN-NFG composite. Reprinted from ref [76], Copyright 2018 John Wiley & Sons, Inc.

Layered g-C_3N_4 photocatalyst can be used as base material to form 2D heterostructure via structural engineering. Shanker and coworkers reported a titanium nitride (TiN) nanocrystal decorated N-doped few-layered graphene (NFG) referred as TiN-NFG. This co-catalyst possesses significantly enhanced water reduction efficiency compared with that on pristine g-C_3N_4 (about 16 times higher in water reduction) [76]. Fig. 1-14 shows the detailed preparation process of g-C_3N_4/TiN-NFG 2D nanocomposite. According to the authors, the TEM images of the composites in Fig. 1-15 confirms the composites consisting of TiN nanoparticles tightly bonded to the ultrathin 2D layered g-C_3N_4 having a porous structure. Clear lattice fringe of 0.24 nm for the TiN component of the g-C_3N_4/TiN-NFG 2D nanocomposites can be observed (Fig. 15d).

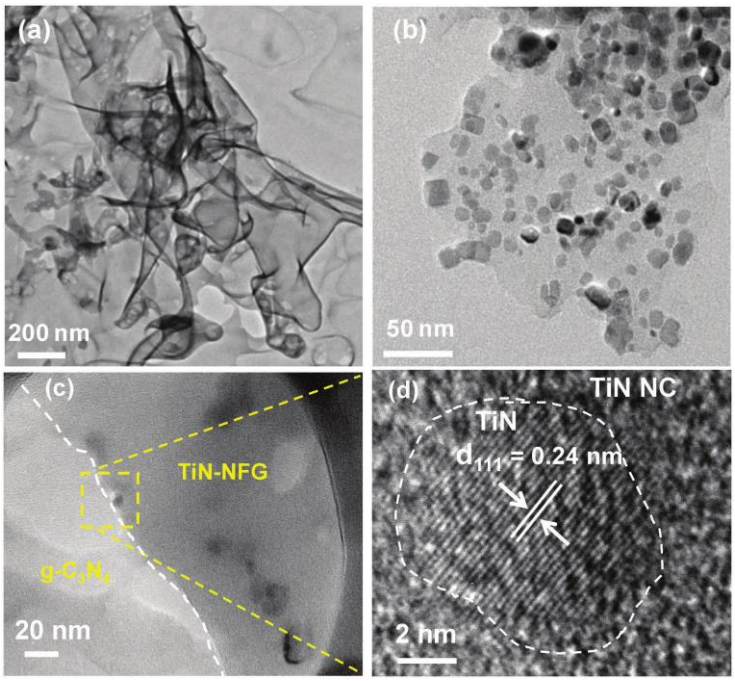

Figure 1-15. TEM images of the g-C_3N_4 composites: (a) pristine g-C_3N_4; (b) TiN-NFG; (c) g-C_3N_4/TiN-NFG nanocomposite; and (d) g-C_3N_4/TiN-NFG and an enlarged portion of the image (yellow dots line area in c). Reprinted from ref [76], Copyright 2018 John Wiley & Sons, Inc.

2.2.5 Homojunctions

Since polymeric C_3N_4 (PCN) is composed of triazine or heptazine building blocks, the homojunctions of g-C_3N_4 can be formed by control of the polymerization processes. Unlike surface engineering with gradual doping, the g-C_3N_4 homojunctions with porous structure consist of a phase with different degrees of crystallinity. For example, Zhang and co-workers introduced a triazine-heptazine copolymer that can be constructed via post-calcination treatment on polymeric g-C_3N_4 using eutectic salts to adjust condensation process and to achieve optimized microstructure. These heterojunctions are supposed to be able to enhance the interface charge transfer efficiency thus enhancing the photocatalytic performance of the material [77]. The crystallinity degree of g-C_3N_4 can be related to the condensation conditions (e. g. temperature) used for synthesis. Yang's group discovered a crystalline g-C_3N_4 (CGCN) and an amorphous g-C_3N_4 (AGCN) synthesized using varying temperature settings [78]. The tendency of CGCN and AGCN forming close-coupled copolymers is due to their different band gap structures. Fig. 1-16 shows the synthetic procedure for A-CGCN composites via a two-step calcination method. The authors use CGCN as the seeds material to prepare amorphous/crystalline g-C_3N_4 homojunction (A-CGCN) composite via polymerization of

melamine [78].

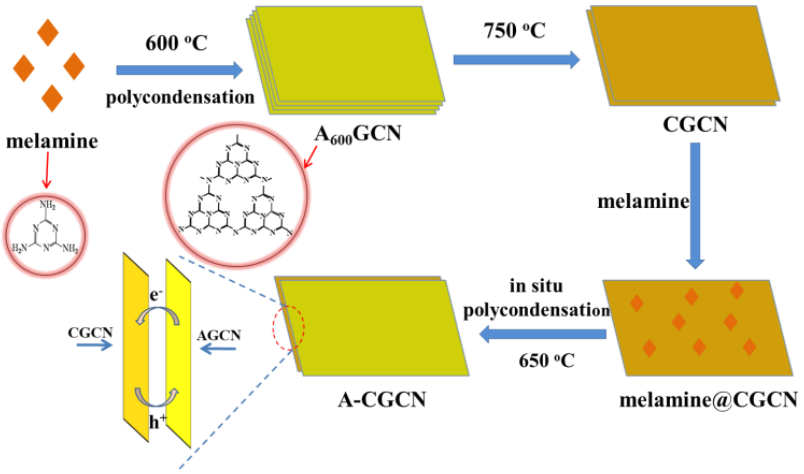

Figure 1-16. Detailed preparation process of A-CGCN composites. Reprinted with permission from ref [78]. Copyright 2014 Royal Society of Chemistry.

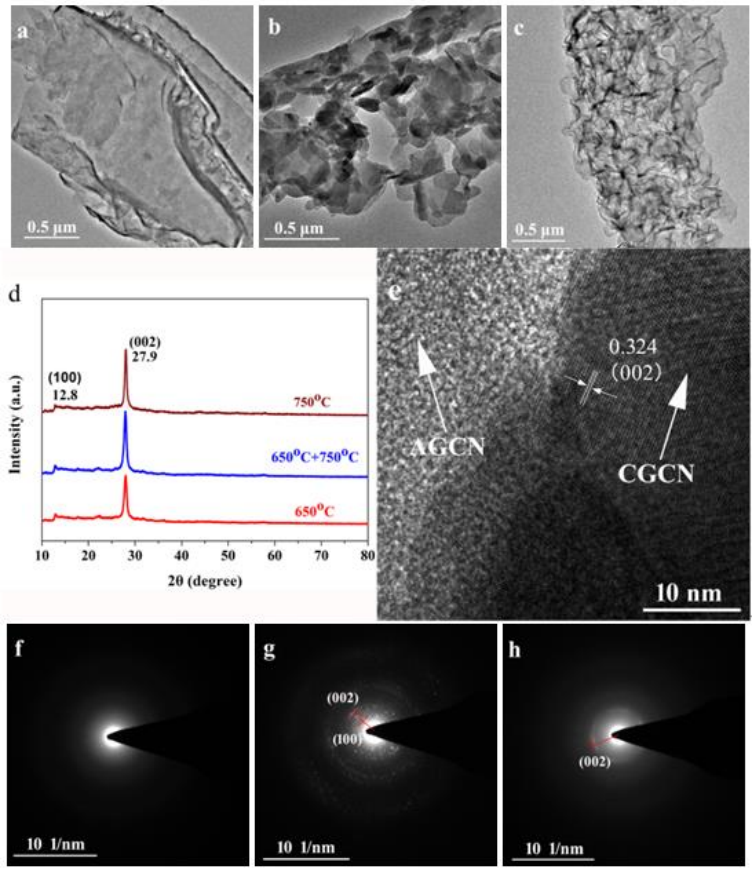

Figure 1-17. TEM images of the g-C_3N_4 composites: (a) AGCN, (b) CGCN and (c) A-CGCN. XRD patterns of the g-C_3N_4 composites (d). High resolution TEM image of A-CGCN (e). SAED patterns of the composites: (f) AGCN, (g) CGCN and (h) A-CGCN. Reprinted with permission from ref [78]. Copyright 2014 Royal Society of Chemistry.

Fig. 1-17 shows the TEM images and XRD patterns of AGCN, CGCN and A-CGCN, with the interface present in between amorphous (AGCN) and crystalline (CGCN) phases (Fig. 1-17e). According to Liu et.al., specific surface area of the crystalline g-C_3N_4 (CGCN) was examined to be the highest among the g-C_3N_4 composites (119.1 m^2g^{-1}) due to relatively high temperature calcination treatment procedure (750 °C). Moreover, drastic increase in specific surface area was observed for g-C_3N_4 homojunction (A-CGCN, 87.6 m^2g^{-1}) compared with that of amorphous g-C_3N_4 (57.7 m^2g^{-1}) [78].

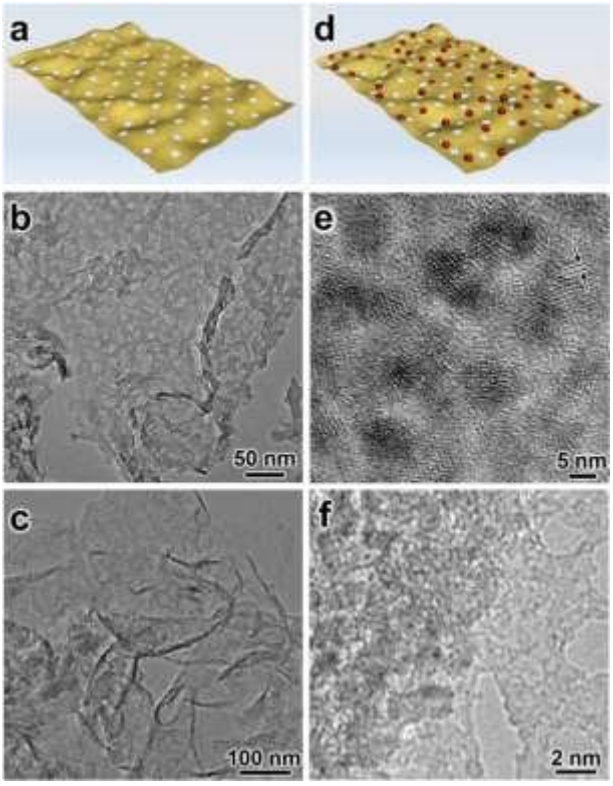

Figure 1-18. (a) g-C_3N_4 model; (b & c) TEM images collected for g-C_3N_4; (d) p-CNCS model; (e & f) HRTEM images obtained for p-CNCS composite. The lattice fringe spacing (0.352 nm) in (e) corresponds to (111) facet of the CdSe QDs in the composite material. Reprinted from ref [79], Copyright 2019 John Wiley & Sons, Inc.

2.2.6 Heterostructures

Construction of heterostructures has been considered one feasible approach for improving catalytic activities of layered g-C_3N_4-based materials. Due to the flexibility and opened-up 2D morphology of g-C_3N_4 nanosheets, g-C_3N_4 nanosheets are considered as an ideal matrix for construction of heterostructures with different components. Examples of different categories of g-C_3N_4-based heterostructures include metal/g-C_3N_4, inorganic semiconductor/g-C_3N_4, and

polymer/g-C_3N_4 etc [51]. Li et. al. reported the design and fabrication of a polymeric-C_3N_4/CdSe QDs (p-CNCS) composite for CO_2 photoreduction with varying CdSe QDs particle sizes [79]. Fig. 1-18 shows the schematic models and TEM images of the polymeric-C_3N_4 composites. For photoreduction using g-C_3N_4-based QDs heterostructures, the energy of electrons on the conduction band can be adjusted to enhance the generation of CH_3OH and to limit H_2 evolution owing to the quantum confinement effect of the QDs [79].

The bandgap of g-C_3N_4 can be reduced by bandgap engineering to extend the visible-light-response range of the material through adjustment of conduction band (CB) and valance band edge positions. Plasmonic metal decorated g-C_3N_4 photocatalysts are able to keep the redox ability of the g-C_3N_4 while extending the light absorption range of the heterostructural material because of the localized surface plasmon resonance effects of the noble metals, which is able to improve the catalytic performances of g-C_3N_4 heterostructure. Zhang and co-workers reported Au nanorods (NRs) deposited g-C_3N_4 nanotubes (Au NRs/CNNTs) using impregnation–annealing approach [80]. According to Zhang et.al., the light absorption ability of the Au NRs/CNNTs was prolonged to the near-infrared region.

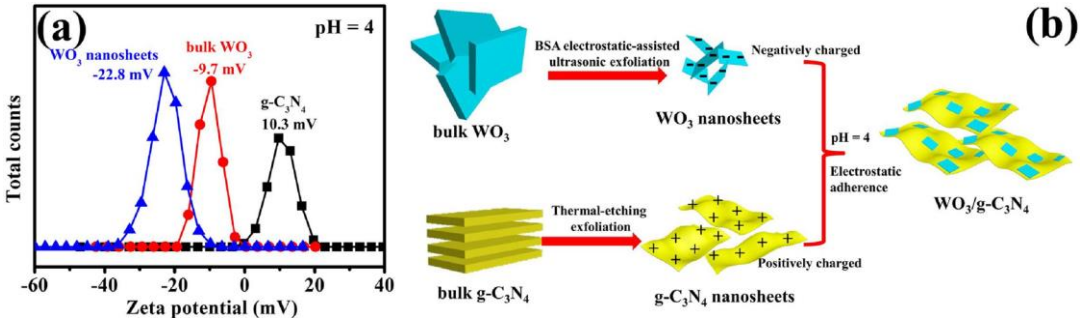

Figure 1-19. (a) Plots of zeta potential data obtained on WO_3 nanosheets, g-C_3N_4 and bulk WO_3 at pH 4. (b) Schematic diagram for synthetic process of 2D-2D WO_3/g-C_3N_4 heterojunctions. Reprinted with permission from ref [81]. Copyright 2019 Elsevier.

Appropriate interfacial contact of heterostructures is critical for separation and transport of the interfacial electron and hole pairs in the material. In general, 2D/2D surface-to-surface heterostructures possess enhanced photocatalytic activities owing to the drastically increased contact area of the heterostructural material that improves interfacial charge transport efficiency. Fu and co-workers created a 2D/2D WO_3/g-C_3N_4 composite heterostructure with step-like charge transport characteristics via electrostatic self-assembly of ultrathin WO_3 nanosheets and the g-C_3N_4 base [81]. The surface photocatalytic reaction efficiency of the

heterostructure was improved due to the fact that the photogenerated charge carriers at the heterogeneous interface can be easily transferred to the surface of the material. The Zeta potential data of the samples at pH=4 (Fig. 1-19) shows that in comparison with the positive zeta potential of g-C_3N_4, the WO_3 deposited g-C_3N_4 revealed a negative zeta potential value, indicating successful construction of WO_3/g-C_3N_4 composites.

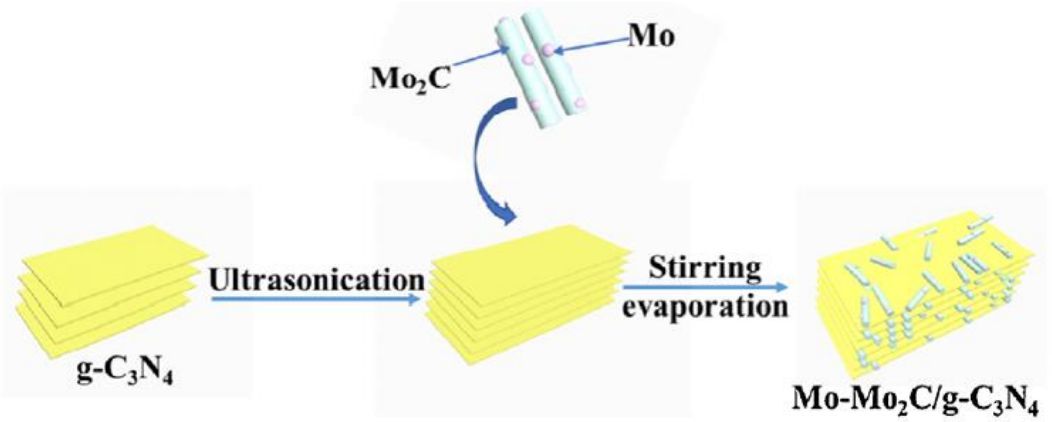

Figure 1-20. Schematic illustration of synthetic procedure of Mo-Mo_2C/g-C_3N_4 photocatalyst. Reprinted with permission from ref [82]. Copyright 2019 Elsevier.

Stable and highly efficient cocatalysts are keys in enhancing photocatalytic performances of g-C_3N_4 and g-C_3N_4-based composite materials. Recently, a metal-semiconducting composite cocatalyst was developed by Dong et. al. for improving light adsorption range and to enhance proton reduction capacity of the g-C_3N_4-based material [82]. Mo-Mo_2C cocatalyst loaded g-C_3N_4 was formed for achieving high photocatalytic H_2 generation from water. Fig. 1-20 shows the synthetic method for constructing g-C_3N_4-based Mo-Mo_2C catalyst, in which $(NH_4)_6Mo_7O_{24}\cdot 4H_2O$ was used as the non-metal source and the composites were prepared using temperature-programmed reaction. According to Dong et. al., the Mo-Mo_2C decorated g-C_3N_4-based composites exhibited decent photocatalytic performances due to optimized preparation parameters. The H_2 evolution efficiency estimated for this Mo-Mo_2C/g-C_3N_4 composite is extremely high (219.7 $\mu molh^{-1}g^{-1}$, 440 times of that of conventional pristine g-C_3N_4 nanosheets).

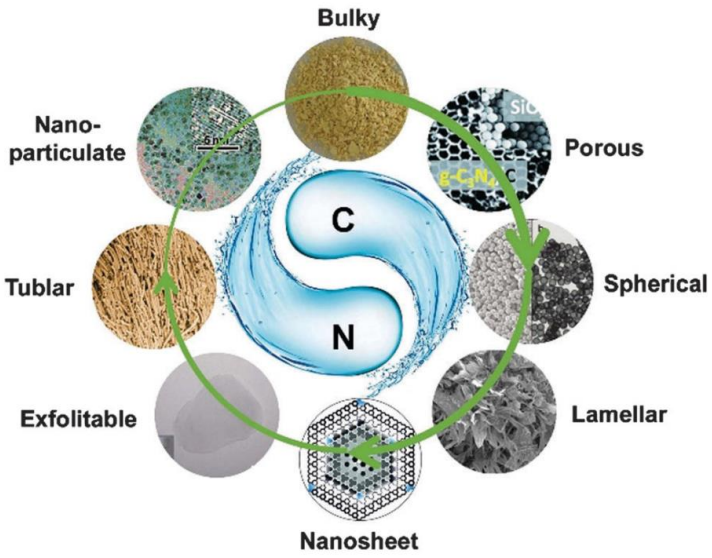

Figure 1-21. Morphologies of the g-C_3N_4 family with dimensions ranging from bulk to nanoparticulate scale. Reprinted with permission from ref [47], Copyright 2016 Royal Society of Chemistry.

2.2.7 Morphology controlled synthesis of g-C_3N_4

g-C_3N_4 materials can have a variety of morphologies (as shown in Fig. 1-21) [47]. Since morphologies of g-C_3N_4 can be affected by factors such as, surface area, band gap, and active sites; morphology control of layered g-C_3N_4 has become a hot topic. Lower dimensional g-C_3N_4 nanomaterials, especially zero-dimensional (0D) g-C_3N_4 nanoparticles, generally possess abundant exposed active sites and shorter charge transport distance. Examples of researchs done for addressing these issues include, reducing the dimensionality of the material to enhance hydrophilic property as well as to increase the surface area of g-C_3N_4. However, morphology control of layered g-C_3N_4 is not easy, especially in case of template-free synthesis. Free-templating method thus has become a hot issue in regulating the morphology of g-C_3N_4. The supramolecular assembly theory proposed by Ranganathan and co-workers in 1999 has become one of the most popular methodologies for achieving morphology control of layered g-C_3N_4 [90]. Organic channel structure adducts can be created by reactions between melamine and cyanuric acid with a ratio of 1:1 [90]. g-C_3N_4 with a variety of morphologies can be constructed by utilization of these adduct precursors at high temperature via thermal polycondensation, e.g., sea urchin like structure, hexagonal nanotubes, and porous yolk-shell nanotubes [91, 92].

According to Jiang et. al., hexagonal g-C_3N_4 nanotubes can be synthesized using hexagonal precursors as the starting material via thermal polycondensation process. Fig. 1-22 shows the schematic synthetic procedure of the hexagonal g-C_3N_4 nanotubes. According to the authors, the resulting hexagonal g-C_3N_4 nanotubes revealed improved photocatalytic hydrogen generation efficiency (14 times as high as that of conventional pure g-C_3N_4 nanosheets) [54]. The precursors utilized for preparation of g-C_3N_4 are able to affect the morphology of the final product. g-C_3N_4-based composites synthesized using melamine, O-doped g-C_3N_4, and g-C_3N_4 as precursors correspond to the MH-g-C_3N_4, UH-g-C_3N_4, and GH-g-C_3N_4 composites in Fig. 1-22 and 1-23, respectively. Fig. 1-23 shows the TEM images of the MH-g-C_3N_4, UH-g-C_3N_4 and GH-g-C_3N_4 composites with different hexagonal g-C_3N_4 nanotubes morphologies.

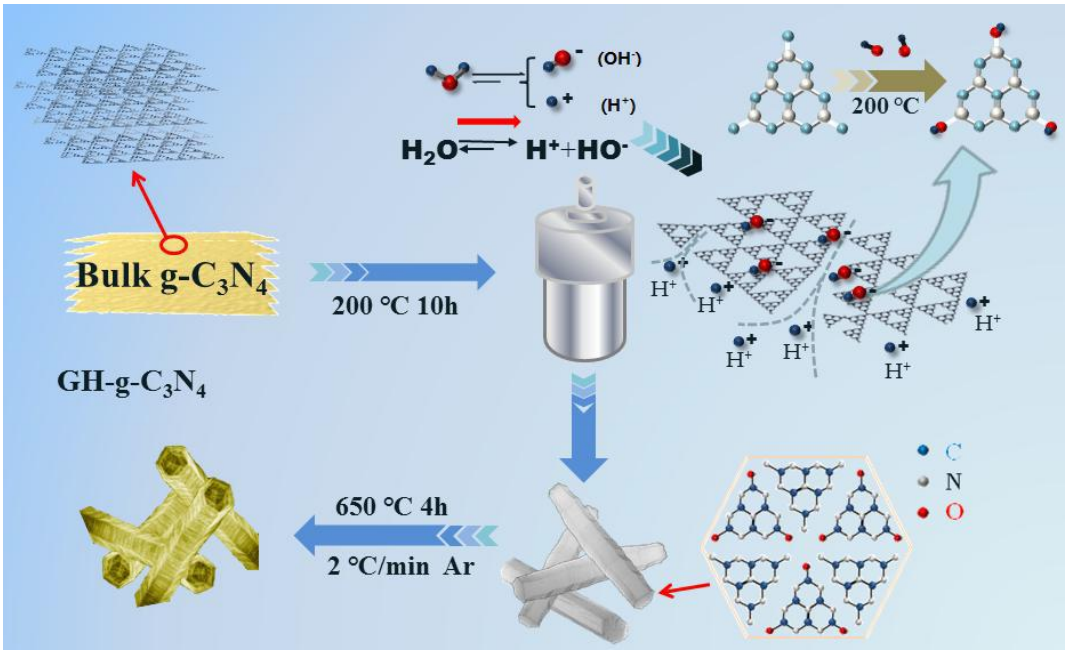

Figure 1-22. Schematic synthetic diagram of hexagonal g-C_3N_4 nanotubes. Reprinted with permission from ref [54]. Copyright 2020 Elsevier.

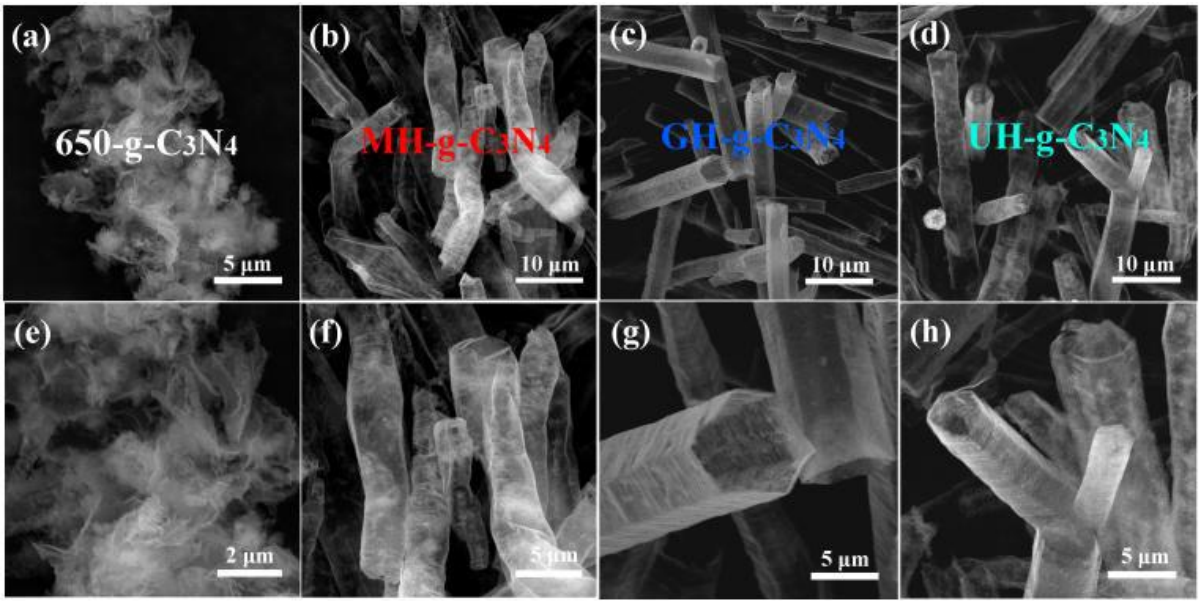

Figure 1-23. SEM images of g-C_3N_4 nanosheets and nanotube composites: (a & e) 650-g-C_3N_4 nanosheets, (b & f) MH-g-C_3N_4 nanotubes, (c & g) GH-g-C_3N_4 nanotubes, and (d, h) UH-g-C_3N_4 nanotubes. Reprinted with permission from ref [54]. Copyright 2020 Elsevier.

Compared with 1D to 3D layered g-C_3N_4, 0D g-C_3N_4 nanoparticles has advantages over other g-C_3N_4 materials because of their extended visible adsorption and abundant active sites nature. However, easy aggregation and fast photogenerated charge carrier recombination rate impair the photocatalytic performances of the material. Wang and co-workers reported a hydroxyl (-OH) modified g-C_3N_4 nanoparticles by using hydrothermal synthesis method without adding any etching agents [93]. Fig. 1-24 shows the preparation process and characterization graph of g-C_3N_4 dots. Despite of high hydrophilicity and small size nature of the material, -OH modified zero-dimensional g-C_3N_4 nanoparticles exhibited relatively high reduction potential and a relatively narrower bandgap.

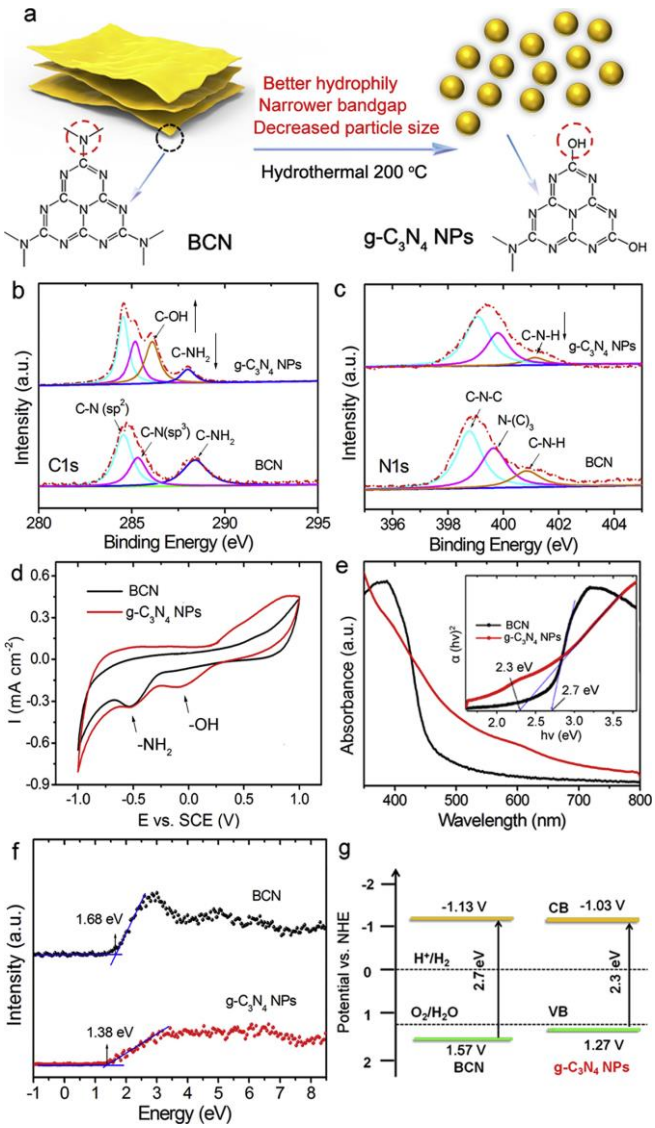

Figure 1-24. (a) Schematic diagram of formation of g-C_3N_4 nanoparticles via hydrothermal treatment of bulk g-C_3N_4. XPS spectra of g-C_3N_4 nanoparticles and bulk g-C_3N_4: (b) C1 s, (c) N1 s. (d) CV plots of the g-C_3N_4 nanoparticles containing -NH_2 and -OH groups and bulk g-C_3N_4. (e) Bandgap structure and UV–Vis absorption graph of g-C_3N_4 nanoparticles and bulk g-C_3N_4. (f) XPS valence band spectra of g-C_3N_4 nanoparticles and bulk g-C_3N_4. (g) Band structure alignments of bulk g-C_3N_4 and g-C_3N_4 nanoparticles. Reprinted with permission from ref [93]. Copyright 2019 Elsevier.

To achieve higher dispersity and improved charge carrier separation efficiency, 0D and 3D g-C_3N_4 nanoparticle/ZnS heterostructures were developed by Wang and co-workers to extend sunlight absorption capacity and passivates surface defects of the material [93]. According to Wang et. al., high photocatalytic activity was achieved under visible light condition. The H_2 generation performance of the g-C_3N_4 nanoparticle/ZnS heterostructures was estimated to be about 140 times higher than that observed on pristine 0D g-C_3N_4 nanoparticles and pristine

ZnS nanocomposites.

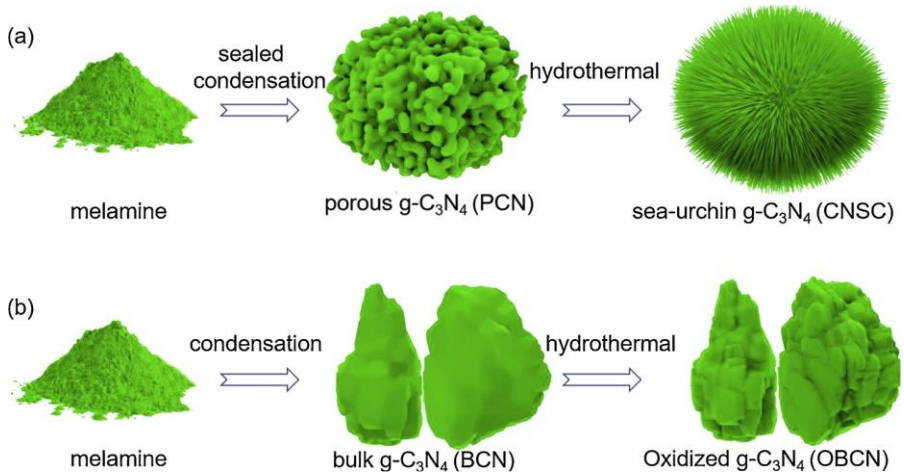

Figure 1-25. Diagram of formation mechanism of sea-urchin shaped g-C_3N_4: (a) hierarchical sea-urchin g-C_3N_4 formed via sealed condensation method; (b) oxidized bulk g-C_3N_4 synthesized via traditional condensation method. Reprinted with permission from ref [94]. Copyright 2019 Elsevier.

g-C_3N_4 possessing band gap values at around 2.0 eV can be considered a popular choice for water splitting in full solar spectrum condition. Such g-C_3N_4 can be synthesized via chemical etching in H_2, sodium borohydride etching of bulk g-C_3N_4, or calcination of bulk g-C_3N_4 at high temperature settings in Ar. Multi-step calcination process in reducing gases environment and the incorporation of alkali ions are the commonly used methods for constructing g-C_3N_4 with narrowed bandgap, larger specific surface area, and rational band structure, thus boosting the catalytic performances of the material. Zeng and co-workers discovered a sea-urchin nanostructured g-C_3N_4 nanocomposites with a narrowed bandgap of 2.07 eV synthesized by using a facile hydrothermal approach as shown in Fig. 1-25 [94].

2.3 Photocatalysis development and electrochemical catalysis trends

As a typical visible-light-responsive photocatalyst, conventional g-C_3N_4 shows band gap energy in void region covering in between the filled VB and the vacant CB. The generated charge carriers in the excited states can be transported onto the surface of g-C_3N_4 in order to initiate various catalytic oxidation and reduction reactions (Fig. 1-26) [46].

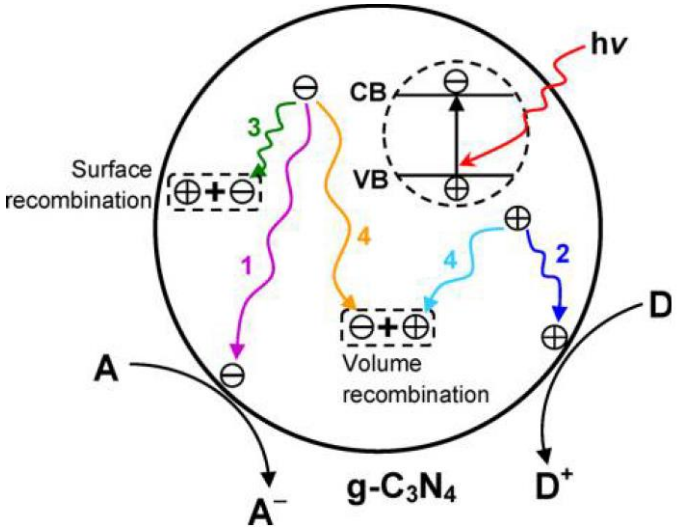

Figure 1-26. Schematic representation of photoexcited charge pairs in g-C_3N_4 shown with the decay pathways, in which A denotes the electron acceptor while D referred to the donor. Reprinted with permission from ref [46]. Copyright 2016 American Chemical Society.

It is noteworthy that the efficient separation of photogenerated carriers is the key to enhance the photocatalytic performances of the material. Once recombination process takes place, electrons in the excited states are able to be reverted back to the VB, leading to release of heat and fluorescence emission. In this case, these excited electrons are able to react with the adsorbed species on g-C_3N_4 surface [46]. A variety of strategies have been developed to suppress the photogenerated charge carrier recombination rate of the g-C_3N_4 materials for achieving improved photocatalytic activities. Typically, g-C_3N_4-based heterostructure photocatalysts can be engineered using combinations of g-C_3N_4 and other semiconducting material (or co-catalyst). In case of g-C_3N_4-based semiconducting nanocomposites heterojunction material, the conduction band and valence band of the semiconducting materials can be lowered or increased utilizing different combinations of material and preparation conditions. Fig. 1-27 illustrates the typical bandgap structures of various semiconducting photocatalysts and the relevant redox potential values estimated for various molecules in CO_2 reduction, water splitting, and pollutant photodegradation related reactions [46].

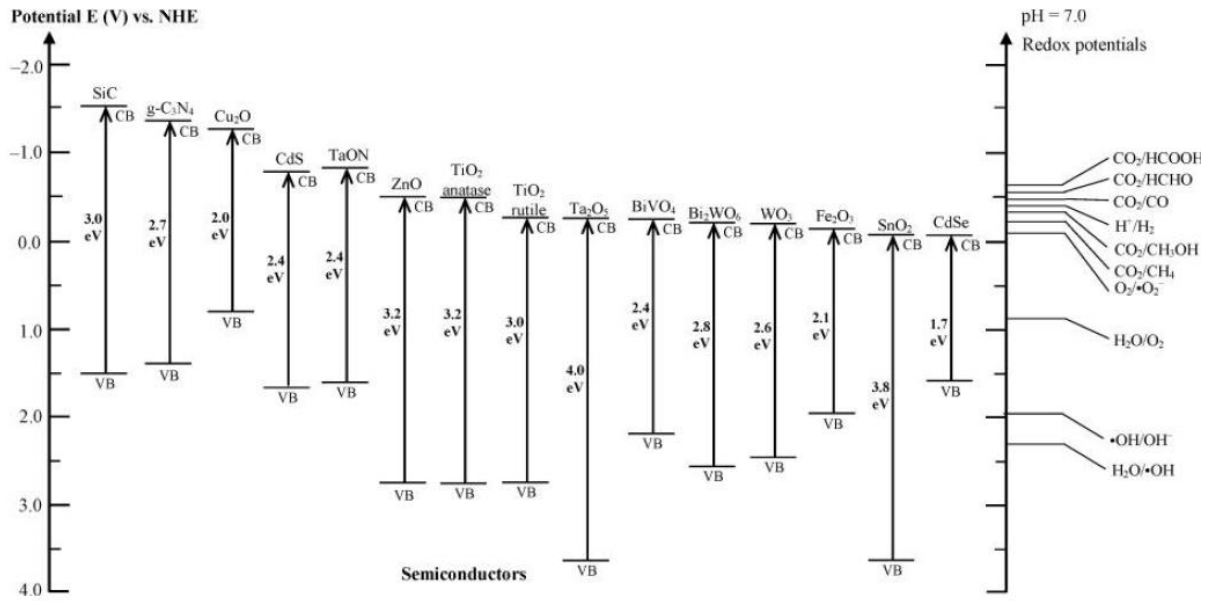

Figure 1-27. The band gap energy level of different semiconducting photocatalysts, as well as the redox potentials for various species in reactions including CO_2 reduction, H_2O splitting, and photodegradation of pollutants at pH 7. Reprinted with permission from ref [46]. Copyright 2016 American Chemical Society.

Electrochemical CO_2 reduction has become a hot topic in production of renewable fuels with the assistance of solar and wind energy [95]. Due to the stability of CO_2 molecule, the sluggish kinetics of CO_2 reduction reaction is the main cause for the requirement of efficient electrocatalysts that can facilitate CO_2 conversion. Zhi et.al. performed electrochemical CO_2 reduction on a series of g-C_3N_4/doped graphene hybrid sample either with or with no heteroatom doping [95]. It is determined that the free energies of the intermediate including *COOH, *CO, *CHO can be linearly correlated with coordination number, and that a volcano-type CO_2 reduction reaction activity trend can be observed (Fig. 1-28).

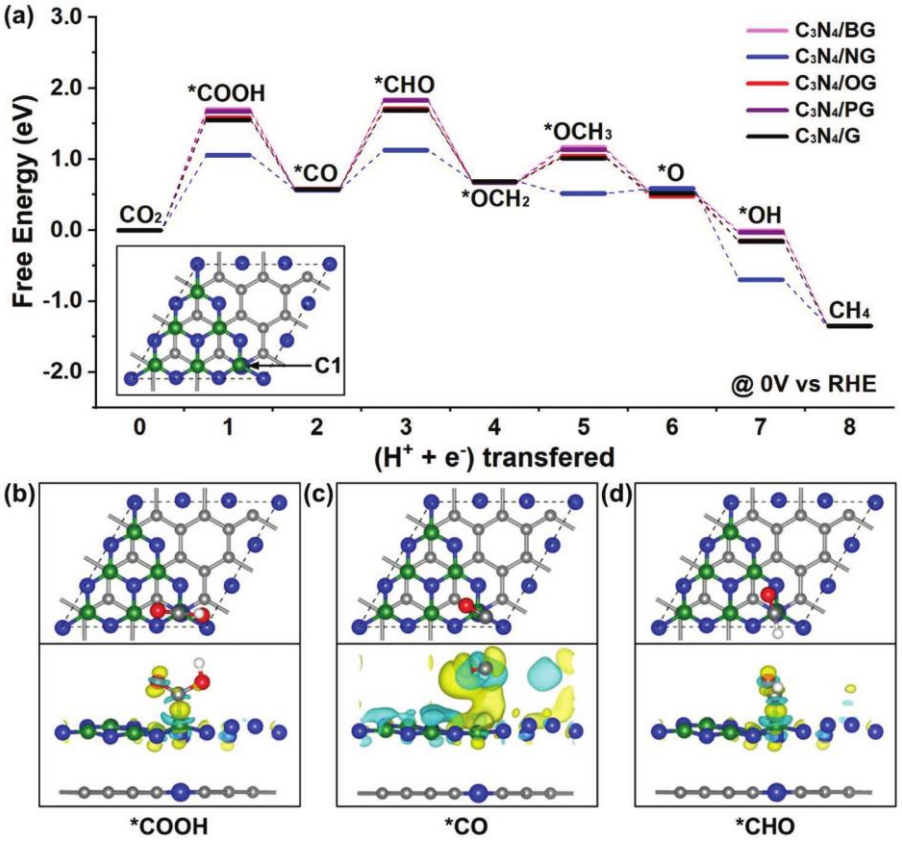

Figure 1-28. (a) Free energy diagrams of reduction of CO_2 to CH_4 on C1 site of C_3N_4/XG composites (where XG corresponds to G, OG, NG, PG, and BG), while the inset in (a) exhibits C1 site of the material. (b) Optimized electron transport of *COOH intermediates adsorbed on C1 site and geometries of C_3N_4/NG; (c) diagram in case of *CO intermediates; and (d) diagram in case of *CHO intermediates. The gray, green, blue, red, and white atoms represent carbon in graphene layer and adsorbates, carbon in g-C_3N_4 layer, nitrogen, oxygen, and hydrogen atoms, respectively. The yellow and cyan isosurface represent electron accumulation and electron depletion, respectively. Reprinted from ref [95], Copyright 2018 John Wiley & Sons, Inc.

According to the thermal, electric and photo-properties of g-C_3N_4, it is challenging improving the electrocatalytic hydrogen evolution activity of g-C_3N_4 materials [96]. Due to the fact that g-C_3N_4 has mostly been used as a conventional photocatalyst rather than as an electrocatalyst, development of electrocatalytic applications of highly stable low-cost g-C_3N_4 is still at an early stage.

2.4 Summary and Perspective

g-C_3N_4 (a conventional metal-free photocatalyst) possessing a band gap of around 2.7 eV that is suitable for visible-light-driven photocatalytic reactions has provided important

platforms for exploiting novel photo- and electro-chemical phenomenon. Layered g-C_3N_4 as an organic semiconductor has advantages for photocatalytic applications in case of adjusting morphology and constructing heterostructurs. However, it is extremely difficult to synthesize regularly shaped fine g-C_3N_4 microstructure due to the surface and structural nature of g-C_3N_4. Table 1 lists a summary of the examples of g-C_3N_4-based and g-C_3N_4 materials (with various morphologies and using different synthetic processes) that have been reported in the literature so far.

Table 1. Properties and morphologies of g-C_3N_4 reported in literature.

Morphology	Synthesis method	Band gap (eV)	Photocatalystic H_2 evolution (μmol/h/g)	Ref./year
Porous few layered nanosheet	Self-Assembly	2.66	40.2	63/2019
Defected amorphous nanosheet	Thermal polymerization	1.78	37480	97/2018
Bulk	Thermal polymerization	2.61	4365	97/2018
Homojunction	Thermal polymerization	2.7	1179	78/2018
Homojunction	Thermal polymerization	2.7	1150	45/2018
Sea-urchin	Thermal polymerization	2.0	21.5	94/2019
N-doped nanosheet	Thermal polymerization	2.56	5.7	98/2020
N/O co-doped nanosheet	Thermal polymerization	2.72	3.5	98/2020
Seaweed	Freeze-drying-assembled	2.61	9900	99/2015

The photocatalytic performances of g-C_3N_4 depend on its composition, morphology, microstructures. Efforts still need to be made on morphology control, construction of homojunction and heterostructure, as well as property enhancement of g-C_3N_4 towards various applications. Topics that are going to be explored are shown as follows.

(a) To discover the ways to control the degree of crystallinity of g-C_3N_4 during polymerization and formation of homojunctions. Adjustment of preparation conditions and discovering novel procedures considering factors such as, composition, crystallinity, and properties of

superior thin g-C_3N_4 nanosheets will be investigated. Edge-epitaxial growth method will be used for preparing lateral-like homostructures.

(b) To explore applications of red porous g-C_3N_4 nanosheets with narrow band gap for creating heterostructures. Red porous g-C_3N_4 nanosheets are water-soluble and porous. Applications in photoluminescence and lateral-like homostructures related fields will be studied.

(c) To explore methods for achieving morphology change of g-C_3N_4 in order to enhance photocatalytic performances. Special 3D morphology will be created via self-assembly of layered precursors (with the help of H^+ ions) in acidic condition.

(d) To adjust the growth direction of WO_x and WS_2/WO_x on g-C_3N_4 for the formation of g-C_3N_4-based heterostructures, mainly focuses on controlling the facet growth due to the fact that different facets have different active sites and surface energy.

(e) To explore the preparation methods for synthesis of g-C_3N_4 based heterostructures that can be used in pollutants treatment related environmental applications. The growth of completely homogeneous NiCoLDH nanoparticles can be achieved on g-C_3N_4 nanosheets with different degrees of crystallinity (amorphous to crystalline). The Congo red (CR) and hexavalent chromium ion (Cr(VI)) adsorption kinetics of g-C_3N_4/NiCoLDH composites will be tested under visible light irradiation.

2.5 References

[1] P. W. Du, R. Eisenberg, Energy Environ. Sci., 2012, 5, 6012.

[2] N. S. Lewis, D. G. Nocera, Proc. Natl. Acad. Sci. U. S. A., 2006, 103, 15729–15735.

[3] A. J. Ragauskas, C. K. Williams, B. H. Davison, G. Britovsek, J. Cairney, C. A. Eckert, W. J. Frederick Jr., J. P. Hallett, D. J. Leak, C. L. Liotta, J. R. Mielenz, R. Murphy, R. Templer, T. Tschaplinski, Science, 2006, 311, 484–489.

[4] J. C. Colmenares, R. Luque, J. M. Campelo, F. Colmenares, Z. Karpin´ski, A. A. Romero, Materials, 2009, 2, 2228.

[5] C. Chen, W. Ma, J. Zhao, Chem. Soc. Rev., 2010, 39, 4206–4219.

[6] Y. Q. Qu, X. F. Duan, Chem. Soc. Rev., 2013, 42, 2568.

[7] J. Ran, J. Zhang, J. Yu, M. Jaroniecc, S. Z. Qiao, Chem. Soc. Rev., 2014, 43, 7787-7812.

[8] I. Teixeira, E. Barbosa, S. Tsang, P. Camargo, Chem. Soc. Rev. 2018, 47, 7783−7817.

[9] T. Wang, X. Zhang, P. Yang, S. P. Jiang, Inorganic Chemistry Frontiers, 2020, 7, 3578 – 3587.

[10] P. Huang, J. Huang, S. Pantovich, A. Carl, T. Fenton, C. Caputo, R. Grimm, A. Frenkel, G. Li, J. Am. Chem. Soc., 2018, 140, 16042−16047.

[11] Y. Liu, X. Zhang, K. Matras-Postolek, P. Yang, J. Alloys Compounds, 2021, 854, 157111.

[12] C. Jia, X. Zhang, K. Matras-Postolek, B. Huang, P. Yang, Carbon, 2018, 139, 415-426.

[13] N. Wei, H. Cui, Q. Song, L. Zhang, X. Song, K. Wang, et al. Appl. Catal. B, 2016, 198, 83-90.

[14] T. Liu, B. Liu, L. Yang, X. Ma, H. Li, S. Yin, T. Sato, T. Sekino, Y. Hua, Appl. Catal. B, 2017, 204, 593-601.

[15] Y. Tang, W. Di, X. Zhai, R. Yang, W. Qin, ACS Catal., 2013, 3, 3, 405–412.

[16] Y. Song, Y. Wang, P. Yang, J. Li, Mater. Charact., 2020, 169, 110655.

[17] J. Di, J. Xia, X. Chen, M. Ji, S. Yin, Q. Zhang, Z. Chen, H. Li, Carbon, 2017,114, 601-607.

[18] Y. Zhao, X. Zhang, T. Wang, T. Song, P. Yang, Inter. J. Hydrogen Energy, 2020, 45, 21409-21421.

[19] J. Tian, Y. Leng, Z. Zhao, Y. Xia, Y. Sang, P. Hao, J. Zhan, M. Li, H. Liu, Nano Energy, 2015, 11, 419-427.

[20] Y. Wei, X. Zhang, Y. Liu, C. Jia, P. Yang, Electrochimica Acta, 2020, 349, 136366.

[21] Y. Kim, S. Sharker, I. In, S. Park, Carbon, 2016, 103, 412-420.

[22] J. Tian, Y. Sang, G. Yu, H. Jiang, X. Mu X, Liu H. Adv. Mater. 2013, 25, 36, 5075-5080.

[23] C. Jia, T. Dong, M. Li, P. Wang, P. Yang, J. Alloys Compounds, 2018, 769, 521-531.

[24] W. Wang, Q. Shang, W. Zheng, H. Yu, X. Feng, Z. Wang, Y. Zhang, G. Li, J. Phys. Chem. C, 2010, 114, 32, 13663-13669.

[25] Y. Zheng, X. Hu, P. Yang, CrystEngComm, 2018, 20, 4485-4491.

[26] Y. Sang, Z. Zhao, M. Zhao, P. Hao, Y. Leng, H. Liu. Adv. Mater., 2015, 27, 2, 363-369.

[27] S. Cao, J. Yu, J. Phys. Chem. Lett. 2014, 5, 2101−2107.

[28] Y. Tachibana, L. Vayssieres, J. R. Durrant, Nat. Photonics, 2012, 6, 511−518.

[29] P. D. Tran, L. Wong, J. Barber, J. S. C. Loo, Energy Environ. Sci., 2012, 5, 5902−5918.

[30] Q. Xiang, J. Yu, J. Phys. Chem. Lett., 2013, 4, 753−759.

[31] A. Kudo, Y. Miseki, Chem. Soc. Rev., 2009, 38, 253−278.

[32] T. Dong, M.Li, P. Wang, P. Yang, Inter. J. Hydrogen Energy, 43, 2018, 14569-14577.

[33] X. Zhang, P. Wang, P. Yang, S. P. Jiang, Inter. J. Hydrogen Energy, 2020, 45, 21523-21531.

[34] Y. Kim, S. Sharker, I. In, S. Park, Carbon, 2016, 103, 412-420.

[35] T. Dong, P. Wang, P. Yang, Inter. J. Hydrogen Energy, 2018, 43, 20607-20615.

[36] Z. Liu, G. Wang, P. Yang, J. Indust. Eng. Chem., 2018, 66, 262–268.

[37] C. Jia, T. Dong, M. Li, P. Wang, P. Yang, J. Alloys Compounds, 2018, 769, 521-531.

[38] J. Tian, Y. Leng, Z. Zhao, Y. Xia, Y. Sang, P. Hao et al. Nano Energy 2015, 11, 419-27.

[39] O. Elbanna, S. Kim, M. Fujitsuka, T. Majima. Nano Energy, 2017, 35, 1-8.

[40] A. Sousa-Castillo, M. Comesaña-Hermo, B. Rodríguez-González, M. Perez-Lorenzo, Z. Wang, X. Kong, A. O. Govorov, M. A. Correa-Duarte, J. Phys. Chem. C, 2016, 120, 21, 11690-11699.

[41] Y. Wang, X. Wang and M. Antonietti, Angew. Chem. Int. Ed., 2012, 51, 68–89.

[42] A. Thomas, A. Fischer, F. Goettmann, M. Antonietti, J.-O. Müller, R. Schlögl and J. M. Carlsson, J. Mater. Chem., 2008, 18, 4893–4908.

[43] E. Kroke, M. Schwarz, E. Horath-Bordon, P. Kroll, B. Noll and A. D. Norman, New J. Chem., 2002, 26, 508–512.

[44] X. Wang, K. Maeda, A. Thomas, K. Takanabe, G. Xin, J. Carlsson, K. Domen, M. Antonietti, Nat. Mater., 2009, 8, 76-80.

[45] X. Zhang, J-P. Veder, S. He, S. P. Jiang, Chem. Commun., 2019, 55, 1233-1236.

[46] W. J. Ong, L. L. Tan, Y. H. Ng, S. T. Yong, S. P. Chai, Chem. Rev., 2016, 116, 7159−7329.

[47] J. Liu, H. Wang, M. Antonietti, Chem. Soc. Rev., 2016, 45, 2308-2326.

[48] X. Wang, S. Blechert, M. Antonietti, ACS Catal., 2012, 2, 1596−1606.

[49] D. J. Martin, P. J. T. Reardon, S. J. A. Moniz, J. Tang, J. Am. Chem. Soc., 2014, 136, 12568−12571.

[50] C. Ye, J. X. Li, Z. J. Li, X. B. Li, X. B. Fan, L. P. Zhang, B. Chen, C. H. Tung, L. H. Wu, ACS Catal., 2015, 5, 6973−6979.

[51] D. Zheng, C. Pang, Y. Liu, X. Wang, Chem. Commun., 2015, 51, 9706−9709.

[52] C. Wang, P. Yang, B. Wang, J. Electroanal. Chem., 2021, 880, 114943.

[53] Y. Wang, Y. Cao, Y. Liu, P. Yang, Int. J. Hydrog. Energy, 2020, 45, 16519-16527.

[54] Z. Jiang, C. Jia, B. Wang, P. Yang, G. Gao, J. Alloys. Compd., 2020, 826,154145.

[55] Y. Wang, X. Zhang, B. Wang, Y. Liu, C. Xie, Y. Song, P. Yang, Int. J. Hydrog. Energy, 2019, 44, 30151-30159.

[56] Z. Jiang, X. Zhang, H. S. Chen, X. Hu, P. Yang, ChemCatChem, 2019, 11, 4558–4567.

[57] Z. Liu, X. Zhang, Z. Jiang, H-S. Chen, P. Yang, Inter. J. Hydrogen Energy, 2019, 44, 20042.

[58] B. X. Zhou, S. S. Ding, B. J. Zhang, L. Xu, R. S. Chen, L. Luo, W. Q. Huang, Z. Xie, A. Pan, G. F. Huang, Appl. Catal. B, 2019, 254, 321−328.

[59] R. L. Huang, W. Q. Huang, D. F. Li, L. L. Ma, A. Pan, W. Hu, X. Fan, G. F. Huang, J. Phys. D: Appl. Phys., 2018, 51, 135501.

[60] Y. Zheng, Y. Jiao, J. Chen, J. Liu, J. Liang, A. Du, W. Zhang, Z. Zhu, S. C. Smith, M. Jaroniec, J. Am. Chem. Soc., 2011, 133, 20116−20119.

[61] J. Jia, E. R. White, A. J. Clancy, N. Rubio, T. Suter, T. S. Miller, K. McColl, P. F. McMillan, V. Brazdova, F. Cora, C. A. Howard, R. V. Law, C. Mattevi, S. P. Shaffer, Angew. Chem., Int. Ed., 2018, 57, 12656−12660.

[62] K. Schwinghammer, M. B. Mesch, V. Duppel, C. Ziegler, J. Senker, B. V. Lotsch, J. Am. Chem. Soc., 2014, 136, 1730−1733.

[63] Y. Xiao, G. Tian, W. Li, Y. Xie, B. Jiang, C. Tian, D. Zhao, H. Fu, J. Am. Chem. Soc., 2019 141, 2508−2515

[64] A. Shi, H. Li, S. Yin, B. Liu, J. Zhang, Y. Wang, Appl. Cata. B: Environ., 2017, 218, 137–146.

[65] X. Qian, X. Meng, J. Sun, L. Jiang, Y. Wang, J. Zhang, X. Hu, M. Shalom, J. Zhu, ACS Appl. Mater. Interfaces, 2019, 11, 27226−27232.

[66] Y. Yang, S. Wang, Y. Jiao, Z. Wang, M. Xiao, A. Du, Y. Li, J. Wang, and L. Wang, Adv. Funct. Mater., 2018, 1805698.

[67] W. Zhang, J. Barrio, C. Gervais, A. Kocjan, A. Yu, X. Wang, M. Shalom, Angew. Chem. Int. Ed., 2018, 57, 9764–9769.

[68] Z. F. Huang, J. Song, L. Pan, Z. Wang, X. Zhang, J. J. Zou, W. Mi, X. Zhang, L. Wang, Nano Energy., 2015, 12, 646–656.

[69] G. Dong, K. Zhao, L. Zhang, Chem. Commun., 2012, 48, 6178–6180.

[70] J. Li, D. Wu, J. Iocozzia, H. Du, X. Liu, Y. Yuan, W. Zhou, Z. Li, Z. Xue, Z. Lin, Angew. Chem. Int. Ed., 2019, 58, 1985-1989.

[71] B. Wang, H. Cai, D. Zhao, M. Song, P. Guo, S. Shen, D. Li, S. Yang, Applied Catalysis B: Environ., 2019, 244, 486–493.

[72] D. Zeng, W. Xu, W. J. Ong, J. Xu, H. Ren, Y. Chen, H. Zheng, D. L. Peng, Appl. Catal. B, 2018, 221, 47−55.

[73] N. Zhao, L. Kong, Y. Dong, G. Wang, X. Wu, P. Jiang, ACS Appl. Mater. Interfaces, 2018, 10, 9522−9531.

[74] J. Wang, J. Cong, H. Xu, J. Wang, H. Liu, M. Liang, J. Gao, Q. Ni, J. Yao, ACS Sustain. Chem. Eng., 2017, 5, 10633.

[75] Y. Yu, W. Yan, X. Wang, P. Li, W. Gao, H. Zou, S. Wu, K. Ding, Adv. Mater., 2018, 1705060.

[76] G. S. Shanker, R. Bhosale, S. Ogale, A. Nag, Adv. Mater. Interfaces, 2018, 1801488.

[77] G. Zhang, L. Lin, G. Li, Y. Zhang, A. Savateev, S. Zafeiratos, X. Wang, M. Antonietti, Angew. Chem., 2018, 130, 9516-9520.

[78] Z. Liu, G. Wang, H. S. Chen, P. Yang, Chem Commun., 2018, 54, 4720–4723.

[79] A. Li, T. Wang, C. Li, Z. Huang, Z. Luo, J. Gong, Angew. Chem. Inter. Edi., 58, 2019, 3804-3808.

[80] L. Zhang, N. Ding, L. Lou, K. Iwasaki, H. Wu, Y. Luo, D. Li, K. Nakata, A. Fujishima, and Q. Meng, Adv. Funct. Mater., 2018, 29, 1806774.

[81] J. Fu, Q. Xu, J. Low, C. Jiang, J. Yu, Appl. Cata. B: Environmental, 2019, 243, 556–565.

[82] J. Dong, Y. Shi, C. Huang, Q. Wu, T. Zeng, W. Yao, Appl. Cata. B: Environ., 2019, 243, 27–35.

[83] J. Sun, J. Zhang, M. Zhang, M. Antonietti, X. Fu, X. Wang, Nat. Commun., 2012, 1139.

[84] J. Liang, Y. Zheng, J. Chen, J. Liu, D. Hulicova-Jurcakova, M. Jaroniec, S. Z. Qiao, Angew. Chem., Int. Ed., 2012, 51, 3892–3896.

[85] X. Zhang, X. Xie, H. Wang, J. Zhang, B. Pan, Y. Xie, J. Am. Chem. Soc., 2012, 135, 18–21.

[86] G. Algara-Siller, N. Severin, S. Y. Chong, T. Bjo¨rkman, R. G. Palgrave, A. Laybourn, M. Antonietti, Y. Z. Khimyak, A. V. Krasheninnikov, J. P. Rabe, Angew. Chem., Int. Ed., 2014,

53, 7450–7455.

[87] X. H. Li, J. Zhang, X. Chen, A. Fischer, A. Thomas, M. Antonietti, X. Wang, Chem. Mater., 2011, 23, 4344–4348.

[88] J. Zhou, Y. Yang, C. Zhang, Chem. Commun., 2013, 49, 8605–8607.

[89] J. Liu, J. Huang, D. Dontsova, M. Antonietti, RSC Adv. 2013, 3, 22988–22993.

[90] A. Ranganathan, V. R. Pedireddi, C. N. R. Rao, J. Am. Chem. Soc., 1999, 121, 1752.

[91] S. E. Guo, Z. P. Deng, M. X. Li, B. J. Jiang, C. G. Tian, Q. J. Pan, H. G. Fu, Angew. Chem. Int. Ed., 2016, 55, 1830.

[92] N. Tian, K. Xiao, Y. H. Zhang, X. X. Lu, L. Q. Ye, P. X. Gao, T. Y. Ma, H. W. Huang, Appl. Catal. B: Environ., 2019, 253, 196.

[93] L. Wang, G. Zhou, Y. Tian, L. Yan, M. Deng, B. Yang, Z. Kang, H. Sun, Appl. Catal. B: Environ., 2019, 244, 262–271.

[94] Y. Zeng, H. Li, J. Luo, J. Yuan, L. Wang, C. Liu, Y. Xia, M. Liu, S. Luo, T. Cai, S. Liu, J. C. Crittenden, Appl. Catal. B: Environ., 2019, 249, 275–281.

[95] X. Zhi, Y. Jiao, Y. Zheng, S. Z. Qiao, Small, 2019, 1804224.

[96] J. Zhang, F, Guo, X. Wang, Adv. Funct. Mater, 2013, 23, 3008.

[97] Q. Han, Z. Cheng, B. Wang, H. Zhang, L. Qu, ACS Nano, 2018, 12, 5221−5227.

[98] B. Yan, C. Du, G. Yang, Small, 2020, 16, 1905700.

[99] Q. Han, B. Wang, Y. Zhao, C. Hu, L. Qu, Angew. Chem. Int. Ed., 2015, 54, 11433 – 11437

Every reasonable effort has been made to acknowledge the owners of copyright material. I would be pleased to hear from any copyright owner who has been omitted or incorrectly acknowledged.

Chapter 3: Superior thin yellow g-C_3N_4 nanosheets: composition, crystallinity, homojunctions and their photo-/electrocatalytic performance*

Abstract

Superior thin g-C_3N_4 nanosheets are prepared using a two-step thermal polymerization method to control the composition, crystallinity, and properties. The crystallinity and composition of g-C_3N_4 can be controlled by varying synthetic temperature settings. g-C_3N_4 prepared at 600 °C reveals high N/C ratio and amorphous structure. With increased temperature setting, the N/C ratio decreases, the crystallinity degree increases. g-C_3N_4 with amorphous/crystalline structure is obtained at 700 °C and a crystalline g-C_3N_4 with C/N ratio of nearly 0.75 is obtained at 750 °C. The band gap and photodegradation kinetics of samples vary with the types of g-C_3N_4. Photocatalytic degradation plots of RhB using amorphous g-C_3N_4 nanosheets can be fitted with the pseudo-first-order model, while the bulk g-C_3N_4 prepared at 550 °C reveals zero-order kinetics reaction. This phenomenon is attributed to the surface states of g-C_3N_4 nanosheets. In addition, g-C_3N_4 nanosheets prepared at 700 °C show the best photocatalytic performance. Considering the samples with both amorphous and crystalline features, the as-synthesized g-C_3N_4 nanosheets are composed of amorphous/crystalline homojunctions, which possesses unique properties for photocatalytic applications. Furthermore, g-C_3N_4 crystalline/amorphous lateral-like homostructures are prepared using crystalline g-C_3N_4 nanosheets as seeds via sequential edge-epitaxial growth. The homojunction has excellent photogenerated charge carrier separation efficiency, resulting in high photo- and electro-catalytic activities. Au and Pt particles are decorated onto the g-C_3N_4 to enhance the photocatalytic and electrocatalytic performances of the material.

Reprinted (adapted) with permission from Xiao Zhang, Jean-Pierre Veder, Shuai He, and San Ping Jiang, Construction of 2D g-C_3N_4 lateral-like homostructures and their photo- and electro-catalytic activities, Chem. Commun., 2019, 55, 1233--1236. Copyright 2019 Royal Society of Chemistry; and from Xiao Zhang, Peng Wang, Ping Yang, and San Ping Jiang,

Photo-chemical property evolution of superior thin g-C_3N_4 nanosheets with their crystallinity and Pt deposition, International Journal of Hydrogen Energy, 2020, 45, 21523-21531. Copyright 2020 Elsevier.

3.1 Introduction

Carbon nitride, with seven different phases e.g., α-C_3N_4, β-C_3N_4, cubic C_3N_4, pseudocubic C_3N_4 g-h-triazine, g-o-triazine, and g-h-heptazine, have band gaps of around 5.49, 4.85, 4.30, 4.13, 2.97, 0.93, and 2.88 eV, respectively [1]. As a stable polymeric semiconductor, graphitic carbon nitrate (g-C_3N_4) made up of earth-abundant carbon and nitrogen elements is one of the most stable carbon nitride allotropes under ambient conditions with diverse properties [2, 3]. An ideal g-C_3N_4 sheet is constructed from melem units including triazine (C_3N_3) and tri-s-triazine (so-called heptazine, C_6N_7) rings [4]. In general, crystallinity of g-C_3N_4 is related to the distribution of these triazine and heptazine units. Crystallinity plays an important role in improving photocatalytic performances of g-C_3N_4. Higher crystallinity leads to reduction in charge carrier recombination rate and improves electrochemical performances [5]. Since it is hard to control the thermal polymerization process of preparation of g-C_3N_4, to adjust the microstructure of g-C_3N_4 with different crystallinities and to improve photo- and electro-chemical performances of g-C_3N_4 is challenging.

Bulk g-C_3N_4 prepared via thermal polymerization of carbon- and nitrogen-containing precursors (e.g., dicyandiamide melamine and urea) has an estimated bandgap of 2.7 eV. The material shows intrinsic semiconductor-like absorption in visible blue light region. However, g-C_3N_4 in bulk form is not an ideal photocatalyst due to its low specific surface area nature (typically below 20 m^2g^{-1}). Close packing between layers can block reactive sites and hinder the participation of g-C_3N_4 in various reactions [6]. To improve photocatalytic performance of g-C_3N_4, it is necessary to achieve narrowed bandgaps and to enhance the light harvesting efficiency of g-C_3N_4, as well as to increase charge migration rate (conductivity) from the extended π-conjugated system and the delocalized π-electron. Structural defects engineering is an effective approach for improving photocatalytic efficiency. For instance, elemental doping (e.g. S, P, and metal ion doping) has been used to modify the electronic structure of g-C_3N_4 to achieve high photocatalytic performances [7, 8]. The delamination of bulk g-C_3N_4 into

monolayer or superior thin layer is another effective strategy for achieving larger specific surface area due to the fact that the theoretical specific surface area value of an ideal g-C_3N_4 monolayer is as high as 2500 m^2g^{-1} [9-11]. However, fabrication of these monolayers is not easy.

g-C_3N_4 nanosheets have been attracting extensive attention due to their high surface area, short transfer distance, and the ability of facilitating diffusion of reactants [12, 13]. Various strategies have been developed to fabricate g-C_3N_4 nanosheets, e.g., thermal oxidation etching exfoliation [14, 15]. Substantial efforts have been devoted to synthesize few-layered and single-layer g-C_3N_4. The most commonly applied method for preparing g-C_3N_4 nanosheets with melon-based structure is thermal polymerization of N containing precursors [16]. Since amorphous and semi-crystalline g-C_3N_4 synthesized via polymerization method often exhibits moderate photocatalytic activities, various strategies have been developed to enhance the photocatalytic activities of g-C_3N_4 [17, 18]. To increase the crystallinity of g-C_3N_4 nanosheets is an efficient way to enhance and adjust photocatalytic activity of the material. Highly crystalline g-C_3N_4 can be obtained under high temperature and high pressure conditions but with limitations, due to the fact that the precursors used are normally unfavorable for further polycondensation during preparation processes at high pressure condition [19-21]. Novel approaches for synthesis of highly crystalline g-C_3N_4 are expected. Moreover, while the composition of g-C_3N_4 varies with synthetic conditions, the effect of composition on band gap and structure of N-rich g-C_3N_4 may affect its photocatalytic performances. Thus, it is of significant importance to study the effect of C/N ratios on photocatalytic performances of g-C_3N_4 for thermal-induced polymerization.

Construction of two-dimensional (2D) in-plane heterojunctions have been considered a hot topic due to the superior properties of the material which are related to electrons that are free to move but restricted in the third direction [22]. Such 2D heterostructures consisting of one to several atomic layers do not exist in nature and can be fabricated through epitaxial growth strategy. Currently, the study of 2D in-plane heterojunctions mainly focuses on transition metal dichalcogenides (TMD) due to the heterostructure nature of the material. As an example, Chiu and co-workers reported on TMD artificial heterostructures prepared using a multistep chemical vapor deposition (CVD) synthesis

method [22-25]. Duan's group fabricated a 2D WS_2-WSe_2 heterostructure with precisely controlled spatial modulation [24]. For other layered materials with covalent bondings (e.g. carbon-based materials), the construction of few-layered 2D lateral heterostructures has become a challenge due to their structural feature [26]. As a metal-free polymeric photocatalyst, graphitic carbon nitride (g-C_3N_4) with a suitable bandgap of 2.7 eV for visible light photocatalysis has been attracting considerable attention in comparison with other 2D nanomaterials (e.g. graphene, MoS_2) due to the organic features of the material [27, 28]. g-C_3N_4 can be synthesized using a variety of methods, such as simultaneous exfoliation of bulk C_3N_4 into layers of C_3N_4 via mechanical grinding, as well as other chemical and physical routes. The molecular structure and electronic properties of g-C_3N_4 could be easily modulated by formation of heterostructures via semiconductor phase growth, doping, and noble metal modification [29-33]. However, construction of lateral heterostructures of g-C_3N_4 are rarely reported due to the difficulties confronted in synthesis. The heterostructure of g-C_3N_4 can be created via π-π stacking interactions, in which, vertical growth of heterojunctions are achieved [26]. In comparison, unique in-plane 2D heterojunctions can be obtained using direct chemical vapor deposition (CVD) via edge epitaxial growth. Since it is facile to prepare TMD lateral heterostructures via CVD growth, a novel method with precise control is required for constructing g-C_3N_4 lateral-like heterostructures with highly efficient photo- and electro-catalytic properties.

3.2 Experimental

3.2.1 Preparation of g-C_3N_4

Melamine and triethanolamine (TEOA, ≥ 78 %) were purchased from Sigma Aldrich. Deionized water was obtained from a Millipore system ultrapure water instrument. All chemicals were used without further purification. Bulk g-C_3N_4 sample was prepared using a one-step thermal-induced polymerization method. 4 g of melamine was added into a porcelain boat, followed by thermal-polycondensation in a temperature range of 500 to 600 °C for 4 hours at a 10 °C/min ramp rate in nitrogen. g-C_3N_4 nanosheet samples were obtained by a two-step thermal-polycondensed procedure [34]. Typically, 3 g of g-C_3N_4 sample prepared using a

one-step slow thermal-induced polymerization at 600 °C was further thermal-polycondensed at a temperature range of 650 to 750 °C for 1 hour with a 2 °C/min ramp rate in nitrogen atmosphere. The sample was then sonicated followed by selection using controlled centrifugation speed. Precipitation of suspension containing thin specimen sample was selected and washed with water and ethanol. The preparation conditions and samples properties are illustrated in Table 3-1.

Table 3-1. Preparation conditions and properties of g-C_3N_4 samples.

Sample	Procedure	Temperature	Morphology	Crystallinity degree
1	One-step	500	Bulk	Amorphous
2	One-step	550	Bulk	Amorphous
3	One-step	600	Thick sheet	Amorphous
4	Two-step	650	Thin sheet	Amorphous
5	Two-step	680	Thin sheet	Amorphous/crystalline
6	Two-step	700	Thin sheet	Amorphous/crystalline
7	Two-step	710	Thin sheet	Amorphous/crystalline
8	Two-step	750	Thin sheet	Crystalline

3.2.2 Preparation of g-C_3N_4 homostructures

For the preparation of crystalline/amorphous g-C_3N_4 homostructures (sample CN-750@650), 1 g of selected CN-750 was ground with 2 g of melamine for 2 hours. The sample was then added to a quartz boat and calcined at 650 ºC in Ar for 2 hours with a heat-treat rate of 5 ºC/min. finally, sample was dispersed in water with sonication and selective separation. To deposit Au or Pt nanoparticles, 10 mg of as-prepared samples was uniformly dispersed into 5 ml of deionized water. 10 µl of 50 M $HAuCl_4$ or $HPtCl_4$ aqueous solution was added and stirred for 5 min. The solution was sonicated for a certain reaction time. To control the size of nanoparticles, the reaction time can be altered. The as-prepared precipitate was washed for three times with water and ethanol followed by drying in the oven. For comparison, Au and Pt nanoparticles were deposited via a reflux system using $NaBHO_4$ as the reductant. A $NaBHO_4$ solution was added to the solution with g-C_3N_4 sample and Au or Pt ion solution. After reflux for 10 to 30 min, the as-prepared samples were precipitated and washed.

3.2.3 Material characterization

The TEM and high resolution TEM (HRTEM) images were recorded using a transmission

electron microscope (FEI Titan G2 80-200 TEM/STEM with Chemi STEM Technology, FEI company, US). The X-ray diffraction (XRD) patterns of g-C_3N_4 samples were obtained on an X-ray diffractometer (Bruker D8, Germany) with Cu Kα radiation source. The X-ray photoelectron spectroscopy (XPS) was used to collect the spectra of g-C_3N_4 samples on Kratos Axis Ultra DLD spectrometer with a monochromatic AlKα (1486.6eV) X-rays operating at 150 W. The UV-Vis diffuse reflectance and absorption spectra of samples were obtained using a UV-Vis spectrophotometer (U-4100, Hitachi).

3.2.4 Photocatalytic and electrochemical measurement

Photocatalytic H_2 generation performance was measured using a connected system of Pyrex top-irradiation reaction vessel and a glass-closed gas circulation. 10 mg of g-C_3N_4 sample and 100 ml of TEOA (20 vol%): water = 1:9 aqueous solution were mixed followed by sonication (25 min) before light exposure. The system was evacuated to remove air before testing. 50 ml of chloroplatinic acid solution (H_2PtCl_6, 3 wt%) was added into the reaction system and sonicated for 30 min. With constant stirring of the sample solutions, the measurements were then done using a 300 W Xe lamp with a cutoff filter allowing $\lambda > 420$ nm. Shimadzu GC-7920 gas chromatography (Argon as carrier gas) was used to measure the amount of H_2 evolved.

The hydrogen evolution activity of samples was estimated by comparing the amount of produced hydrogen in 4 hours as a cycle. Apparent quantum efficiency (AQE) is calculated using eq. 3-1 below:

$$AQE = Ne/Np = 2MN_Ahc/SPt\lambda \quad (3\text{-}1)$$

where, Ne and Np are the amount of reaction electrons and the incident photons, respectively. N_A is the Avogadro constant. M is the amount of H_2. c is light speed. S is the irradiation area. P is the intensity of the irradiation. t is the photoreaction time. λ is the wavelength of the monochromatic light.

Rhodamine B (RhB) photocatalytic degradation was carried out under visible light irradiation. RhB solutions (50 ml, 10 mgL^{-1}) were used to mix with 30 mg of samples followed by stirring in dark for 1 hour in order to achieve equilibrium absorption state. The absorbance of RhB was then measured on a UV-Vis spectrophotometer with 300 W Xe arc lamp and a UV-cut off filter allowing $\lambda \geq 420$ nm.

The electrochemical performance of samples was measured using CHI 660E electrochemical

analyzer (Chen Hua Instruments, Shanghai, China) with a three-electrode system and 300 W Xe lamp with wavelength selection filters as the light source. Na_2SO_4 aqueous solution (0.1 M) was used as electrolyte. For reference electrode, Ag/AgCl was used, while Pt plate was used as counter electrode, and catalyst sample solution casted on indium tin oxide (ITO) glass was used as working electrode. The 2 $mgmL^{-1}$ catalyst ink solution of samples was prepared by mixing the sample with a Nafion (5 wt %) mixture solution (V_{Nafion}:V_{water}:$V_{alcohol}$ = 0.025:4:1), followed by pipetting 6 μL of the prepared ink onto the working electrode to achieve a sample loading of 0.17 $mgcm^{-2}$. Linear sweep voltammetry (LSV) curve was then measured in a 0.5 M H_2SO_4 solution with a scan rate of 5 mVs^{-1}. EIS measurements were done at open circuit potential, using 10 mV alternating current amplitude with a 10 mHz to 100 kHz frequency range.

3.3 Results and discussion

3.3.1 The fabrication of g-C_3N_4 nanosheets with temperature

The conventional method used for fabrication of g-C_3N_4 is thermal polycondensation of organic monomers with various architectures [35, 36]. The thermal polymerization of N-rich process leads to the formation of a melon-based structure named melon-based C_3N_4 (also known as bulk C_3N_4) which is composed of one-dimensional heptazine units connected by bridging imide forming zigzag-type chains [4]. Due to incomplete polymerization of the precursors, the bulk C_3N_4 synthesized generally has amorphous or semi-crystalline phases [37，38]. It is thus important to have a controlled thermal-induced polycondensation route that enables adjustment of C_3N_4 microstructures to improve electronic and optical properties. Herein, a two-step thermal-induced polycondensation strategy was developed to prepare thin g-C_3N_4 nanosheets. Bulk g-C_3N_4 was obtained via a one-step polycondensation process at a relatively lower temperature. The re-polymerization of the bulk g-C_3N_4 helps constructing thin g-C_3N_4 nanosheets. Fig. 3-1 shows the TEM and SEM images of g-C_3N_4 samples. The results indicate sample 1 to be in the bulk form as shown in Fig. 3-1a. By increasing calcination temperature up to 600 °C, decreasing in thickness of bulk g-C_3N_4 (sample 2) was observed. In case of using two-step polymerization process, the thickness of samples can be significantly reduced as observed for sample 4 and 8. Fig. 3-1c and 3-1d shows the SEM images of sample

4 and 8 prepared at 650 and 750 °C, respectively. g-C_3N_4 samples with thin nanosheet structural feature was confirmed by the TEM images in Fig. 3-1e and 3-1f, with the insets showing sample 4 to be amorphous and sample 8 to be crystalline due to the regular lattice fringes observed. The result confirms that temperature settings during polymerization process is the key factor for formation of crystalline structural feature of g-C_3N_4. In this chapter, thin g-C_3N_4 nanosheets samples are prepared in a temperature range of 650 to 750 °C as indicated in Table 3-1.

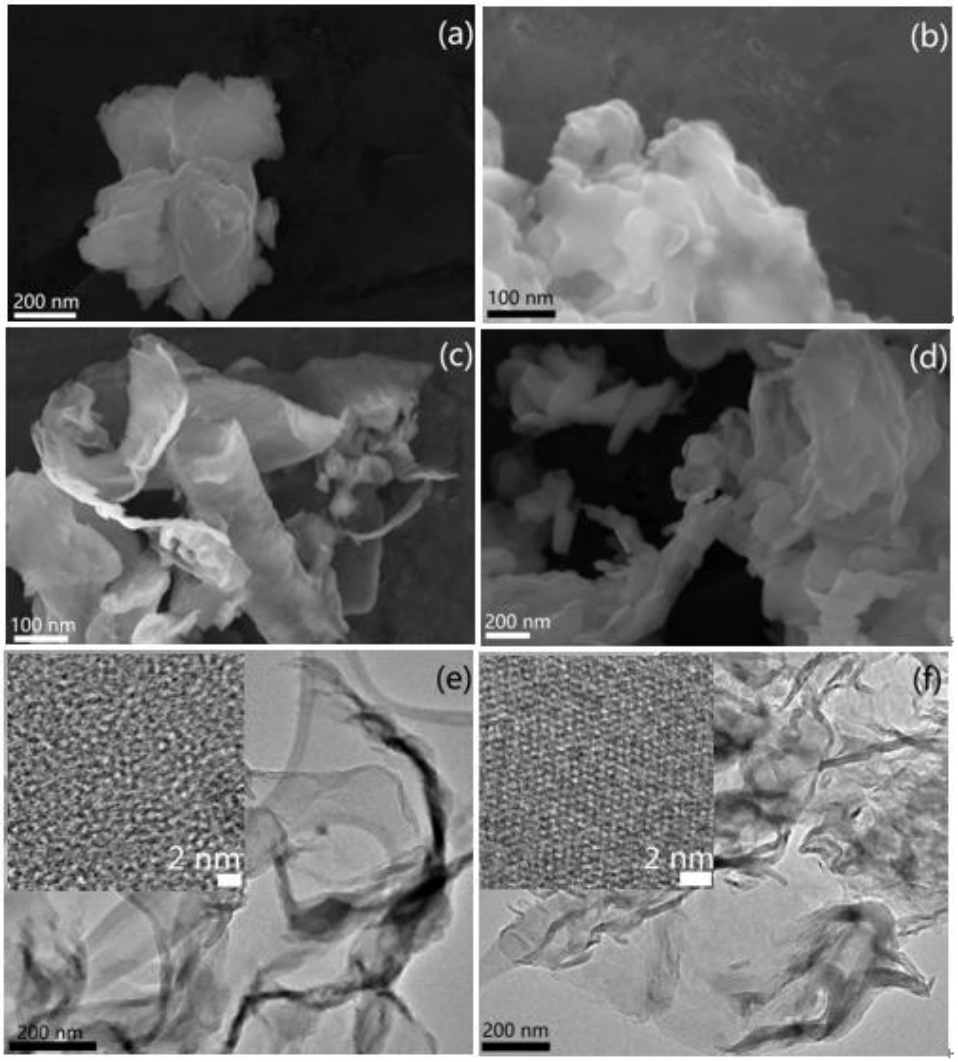

Figure 3-1. SEM (a to d) and TEM (e and f) images of g-C_3N_4 samples prepared under different conditions. (a) Sample 1 prepared at 500 °C. (b) Sample 3 prepared at 600 °C. (c) Sample 4 prepared at 650 °C. (d) Sample 8 prepared at 750 °C. (e) TEM image of sample 4. (f) TEM image of sample 8. Insets in (e) and (f) show the HRTEM images of samples 4 and 8, respectively.

Because of the possibility of breaking of bonds between carbon and nitrogen at high temperature and the existence of structural defects on carbon nitride structures, g-C_3N_4

cannot achieve ideal crystallinity compared with other semiconducting materials. Incorporation of nitrogen atoms and hydrogen/oxygen atoms (generated from decomposition of the melon precursor process) leads to formation of ammonia and nitrogen oxide. This can also be confirmed by XPS analysis shown later in the chapter. Moreover, high temperature and slow polymerization process promote the construction of crystalline g-C_3N_4.

Two peaks around 12.8° and 27.9° for samples 4 and 7 corresponding to (100) and (002) planes are shown in the XRD patterns of sample 4, 7 and 8 in Fig. 3-2. The (100) facet at 12.8° is related to the periodic arrangement of triazine in g-C_3N_4 while the (002) facet is related to the stacking of the conjugated aromatic system of g-C_3N_4. For sample 8, the narrowed peak around 28° assigned to the (002) plane of layered g-C_3N_4 revealed a small shift to a larger angle. This can be attributed to the gradual decrease in crystal lattice structural features, which is caused by the overlapping of conjugated aromatic system [34]. Namely, high temperature setting caused the reduction of irregular bulge and depression between crystallographic laterals.

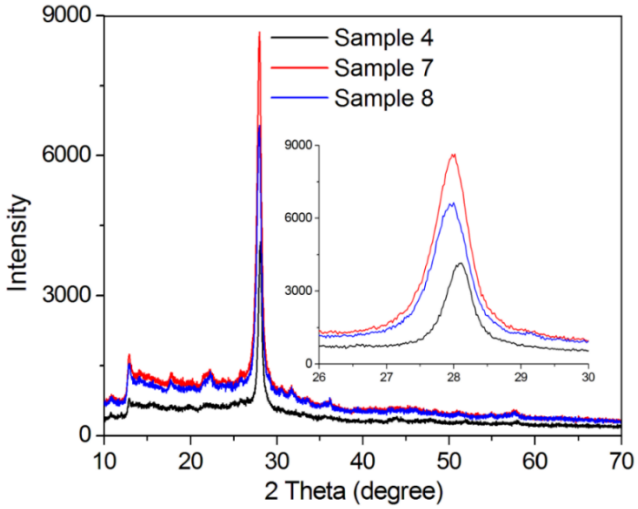

Figure 3-2. XRD patterns of samples 4, 7, and 8. The inset shows an enlarged area in the 26-30 degree range.

To examine the composition of the samples, XPS analysis was carried out. Differences in C/N ratios of the samples are due to the distillation of N element occurred at higher temperature [39]. The C/N molar ratio of sample 8 is around 0.75. The C/N ratio of samples obtained from XPS analysis are listed in Table 3-2. A trend in increasing C/N molar ratio with rising temperature can be observed. At lower temperature, samples can be considered to be relatively

N-rich. When temperature reaches 750 ºC, C/N molar ratio reaches 0.75 as the N components in the sample become less abundant.

Table 3-2. Properties of g-C_3N_4 samples.

Sample	C/N molar ratio	Band gap (eV)	Degradation kinetics	Degradation rate *k* (*10^{-2}/min)
1	0.589	2.83	Zero order	0.58
2	0.598	2.79	Zero order	0.62
3	0.615	2.58	Pseudo first order	4.60
4	0.660	2.54	Pseudo first order	12.8
5	0.661	2.73	Pseudo first order	16.38
6	0.665	2.76	Pseudo first order	22.31
7	0.691	2.79	Pseudo first order	19.75
8	0.745	2.85	Pseudo first order	12.01

Superior thin g-C_3N_4 nanosheets were obtained by using a two-step thermal polycondensation strategy. The bulk g-C_3N_4 was first prepared via polymerization of precursors to work as a seeds material for constructing thin g-C_3N_4 nanosheets. When temperature reaches > 650 ºC, the precursors decompose to generate a large quantity of gaseous products which causes sharp increase in internal gas pressure between layers of bulk g-C_3N_4. This leads to the breaking of π-π interaction cohered layer strands. Moreover, the released gas assists the expansion of stacked layers. Small volume shrinkage of bulk g-C_3N_4 precursor during thermal polycondensation process also promotes the construction of crystalline g-C_3N_4 nanosheets.

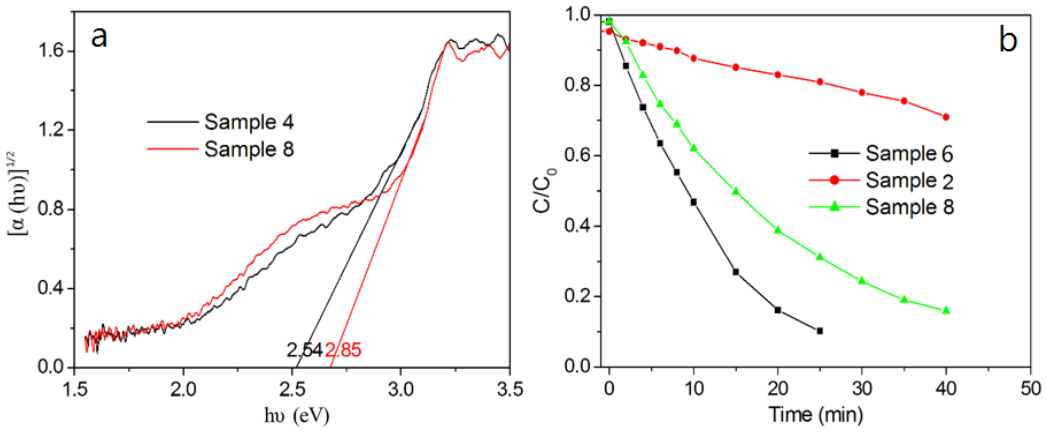

Figure 3-3. (a) UV-Vis diffuse reflectance spectra of g-C_3N_4 samples. (b) RhB photocatalytic degradation plots for samples under visible light irradiation (> 420 nm).

Fig. 3-3a shows the $(\alpha_{hv})^{1/2}$ vs photon energy plots of two typical samples obtained from UV-

Vis diffuse reflectance spectra. The band gap of the samples was estimated using the transformed Kubelka–Munk function ($A(h\nu-Eg)r = \alpha h\nu$) [39-41]. The band gaps of samples 4 and 8 were estimated to be 2.54 and 2.85 eV, respectively (with the band gap of all samples illustrated in Table 3-2). At lower temperature, the band gap values of bulk samples are close to each other. Trend of decreasing band gap was observed for sample 1-4 with rising temperatures (up to 650 °C). However, when preparation temperature increased further, the band gap started to increase (for sample 5-8). This is due to the increasing in crystallinity of sample 5-8, among which sample 8 was shown (from TEM images in Fig. 3-1) to be crystalline, sample 4 to be amorphous and sample 5 to 7 contain both amorphous and crystalline features. To further examine the effects of crystallinity towards photocatalytic performances of samples, photo-degradation kinetics of samples was studied.

3.3.2 Photocatalytic degradation performance

Photocatalytic degradation of organic pollutants (RhB) was performed to study the effects of composition, morphology, and crystallinity towards photocatalytic performance of g-C_3N_4 samples. Fig. 3-3b shows the typical plots of photo degradation of RhB solutions using samples 2, 6, and 8. For bulk g-C_3N_4, RhB was degraded to 70 % after 40 min while crystalline g-C_3N_4 nanosheets (sample 8) was able to degrade RhB to 16 %. Surprisingly, sample 6 prepared at 700 ºC was able to degrade RhB to 30 % within 10 min exhibiting the best photocatalytic activity. The photodegradation plot of sample 1 and 2 was fitted using a zero-order degradation kinetics (Table 3-2). Other plots were fitted with the pseudo-first-order degradation model below,

$$\ln(C_0/C) = kt \qquad (3\text{-}2)$$

where k is the apparent first-order rate constant, C_0 and C are the initial concentration of RhB solution, C is the concentration at time t, and k is degraded kinetic constant [3, 5]. The corresponding kinetic constants (k) were estimated and illustrated in Table 3-2. The degradation rate of bulk g-C_3N_4 is remarkably low, whereas the degradation rate of sample prepared using the two-step synthetic method (sample 4) is drastically high compared with that of bulk g-C_3N_4 prepared using the one-step calcination method (sample 3). This is due to the fact that thin g-C_3N_4 nanosheets possesses more active sites and larger surface area. For samples prepared using the two-step synthetic method, degradation rate increases with rising

temperature in the beginning, with sample 6 revealed the highest activity. The degradation rate decreased for sample 7 and 8 with sample 8 being the lowest. This phenomenon may be ascribed to the varying of crystallinity of g-C_3N_4 nanosheets. The photocatalytic performances are related to the number of active sites on the surface of samples. Sample 6 with the highest degradation efficiency has structural features of both amorphous and crystalline, with some areas to be amorphous and other areas to be crystalline. Homojunctions thus are formed in this case. Similar amorphous/crystalline heterostructures were reported in literature [5, 42]. Moreover, the cyclic stability of sample 6 was tested, and the result demonstrates that a similar level of reactivity after four cycles of measurement was retained and the slight decrease in reactivity has to be derived from the inevitable loss of catalyst sample during cyclic stability test.

H_2 evolution for water splitting under visible light irradiation ($\lambda \geq 420$ nm) was carried out for the of g-C_3N_4 samples. Fig. 3-4a and 4b show the H_2 evolution plots and apparent rate constants plots for samples 4 to 8 under visible light ($\lambda > 420$ nm) irradiation. The result suggests a significant performance difference between amorphous and crystalline g-C_3N_4. The average H_2 evolution efficiency of sample 8 is 1300 $\mu molh^{-1}g^{-1}$ which is almost 6 times higher than that of the amorphous g-C_3N_4 (sample 4, 230 $\mu molh^{-1}g^{-1}$). Sample 6 shows the highest efficiency of 2312 $\mu molh^{-1}g^{-1}$. The enhanced photocatalytic performance of sample 6 can be attributed to the formation of homojunctions in the sample. Similarly, the efficiency of samples 5 and 7 measured are also higher than that of sample 8. According to eq. 3-1 in experimental session, the AQE of sample 6 is 1.80 % at 420 nm. The H_2 evolution rate of sample 6 is still very high after four cycles of stability test.

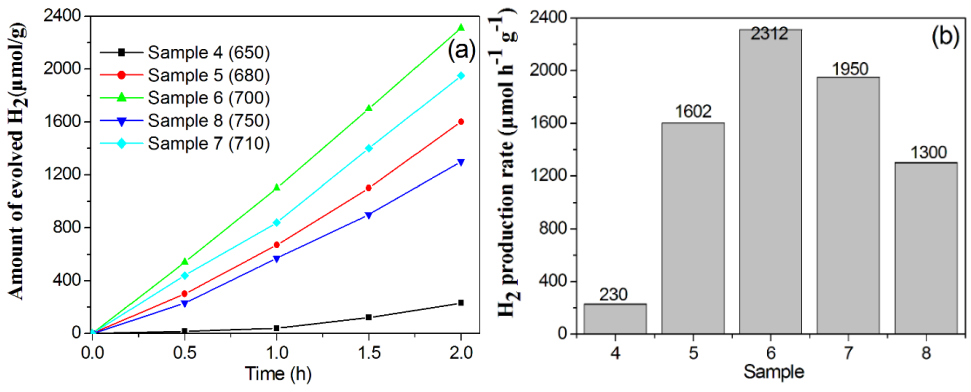

Figure 3-4. (a) H_2 evolution plots and (b) apparent rate constants for H_2 evolution of samples

4 to 8 under visible light (λ > 420 nm) irradiation.

Separation efficiency of photo-generated charge carries is another key factor for improving photocatalytic performance of materials. g-C_3N_4 as a photocatalyst in visible light condition, generally has a quick re-combination rate of the charge carriers that limits their performances. Under visible light irradiation, the electrons in valence band are excited and transported to conduction band while holes are retained in valence band [42]. For sample 6, since the band gap of amorphous and crystalline g-C_3N_4 nanosheets are about 1.54 and 2.85 eV, respectively, a type II homojunctions were formed. Due to the fact that the difference between conduction band and valence band of amorphous phase and crystalline phase is relatively small, the electron excited by visible light was transported from the conduction band of the crystalline phase to the conduction band of amorphous phase. Fig. 3-5 shows the schematic illustration of separated electrons and holes. Separation and transport of the charge carriers occurs at the interface of amorphous and crystalline areas. The charge transfer leads to the accumulation of separated electrons on crystalline area, whereas the holes are accumulated on the amorphous area. Such spatial separation would be beneficial to reduce the recombination rate of charge carriers, thus, enhancing photocatalytic performance of the homojunction (sample 6).

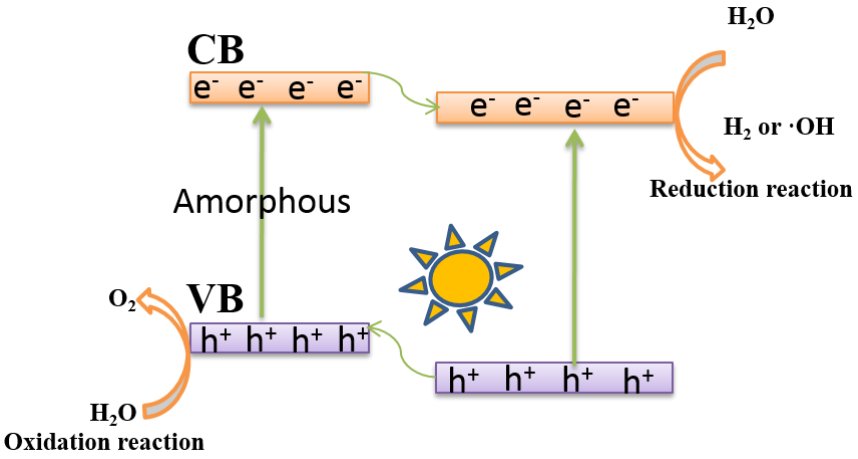

Figure 3-5. Schematic illustration of electron-hole separation and transport in the interface of amorphous and crystalline areas.

3.3.3 Construction of 2D g-C_3N_4 lateral-like homostructures and their photo- and electro-catalytic activities

Fig. 3-6 shows the TEM and high-resolution TEM images of g-C_3N_4 samples. The results

indicate that sample prepared at 650 °C (CN-650) is amorphous (Fig. 3-6a) while sample prepared at 750 °C (CN-750) is crystalline (Fig. 3-6b). The crystallinity of CN-750 is related to the slow multistep treatment procedure, multistep control, and high temperature setting. g-C_3N_4 crystalline/amorphous lateral-like homostructures were created using CN-750 as seed and were calcined at 650 ºC (CN-750@650). The nanosheets morphology of CN-750@650 was still retained as shown in Fig. 3-6c. Fig. 3-6d shows a typical interface of crystalline and amorphous g-C_3N_4. The lattice fringe measured is 0.324 nm corresponding to the (002) facet. Due to the crystallinity of CN-750, the edge-epitaxial growth of amorphous phase occurred. The interface of g-C_3N_4 crystalline/amorphous lateral-like homostructures is different from that of TMD in-plane heterostructures, but still can be clearly observed. Moreover, g-C_3N_4 crystalline/amorphous lateral-like homostructures are composed of few layers of g-C_3N_4.

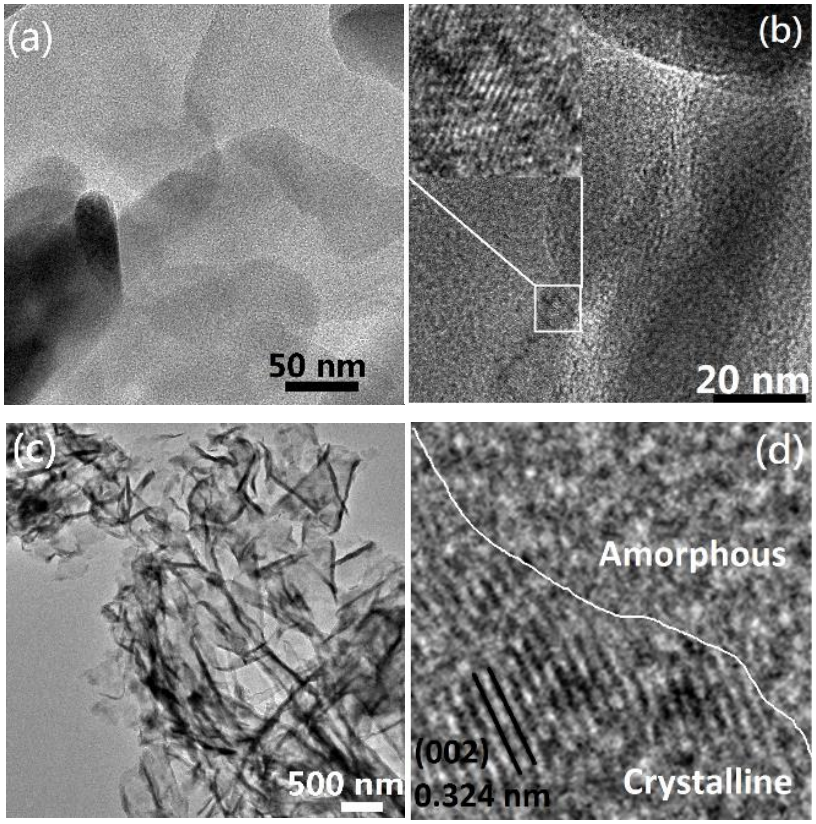

Figure 3-6. TEM images of samples: (a) CN-650; (b) CN-750; (c) and (d) CN-750@650. The inset in (b) shows the lattice fringes of crystalline g-C_3N_4.

The X-ray diffraction (XRD) patterns of samples (Fig. 3-7) indicate that two XRD peaks at 12.8 and 27.9° were observed for all three samples corresponding to the (100) and (002) facets, respectively. The weak peak is caused by the periodic arrangement of

the triazine units in g-C_3N_4 and the higher intensity peak is related to the stacking of the conjugated aromatic system of carbon nitride [43, 44]. All samples possess g-C_3N_4 phase and XRD peaks at the same location. Namely, the XRD peak intensity of CN-750 is the highest, suggesting calcination at high temperature being able to improve the crystallinity of the g-C_3N_4. The XRD peak intensity of CN-750@650 was also enhanced compared with that of CN-650 due to the presence of crystalline g-C_3N_4 in the sample (Fig.3-6d).

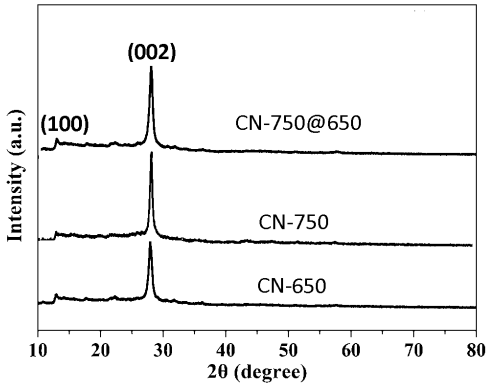

Figure 3-7. XRD patterns of g-C_3N_4 samples.

Fig. 3-8a to 8f shows the X-ray photoelectron spectroscopy (XPS) spectra (e.g., C1s and N1s spectra) of CN-650 (a, b), CN-750 (c, d), and CN-750@650 (e, f). The C1s spectra of samples in Fig. 3-8a, 8c, and 8e shows peaks corresponding to the C-C, C-O-C/C-OH, C=N, C-N, and satellite C1s peak. The peak position was labeled in Fig. 3-8a to 3-8f. The peak intensity ratios are listed in Table 3-3 and 3-4.

Table 3-3. Peak intensity ratios of samples in C1s spectra.

Sample	C-C	C-O-C& C-OH	C=N	C-N	Sat
CN-650	2.0	1.0	5.6	11.6	0.87
CN-750	1.8	1.0	2.0	5.1	0.2
CN-750@650	2.9	1.0	4.9	22.3	1.8

The N1s spectra of samples in Fig. 3-8b, 8d, and 8f have three main peaks corresponding to C-N=C (Pyridinic-N), N-$(C)_3$ (Pyrrolic-N), N-H (graphitic N). Due to the fact that C 1s and N 1s spectra of the samples are very similar, their microstructure can be considered to be almost the same. Sample CN-650 shows high C-C and N-$(C)_3$ ratios compared with that of sample CN-750, indicating that distillation of N elements occurred at higher temperature. For the homostructure sample, the ratio of C-N peak is the highest, which confirms that the homojunction forms through C-N binding.

Table 3-4. Peak intensity of samples in N1s spectra.

Sample	C-N=C (Pyridinic)	N-$(C)_3$ (Pyrrolic)
CN-650	44.84	25.45
CN-750	52.44	22.15
CN-750@650	46.81	29.22

The N/C ratio of CN-650, CN-750, and CN-750@650 are 1.16, 0.90, and 1.17, respectively, and this also confirms that the amount of N element decreased with increasing temperature. According to the UV-Vis diffuse reflectance spectra, the band gap of the samples was estimated by using the transformed Kubelka–Munk function (A(hν-Eg)r = αhν) [45, 46]. The band gaps of CN-650, CN-750, and CN-750@650 were estimated to be 2.55, 2.75, and 2.70 eV, respectively (Fig, 3-9). The band gap of CN-750@650 is in between the band gap value of CN-650 and CN-750.

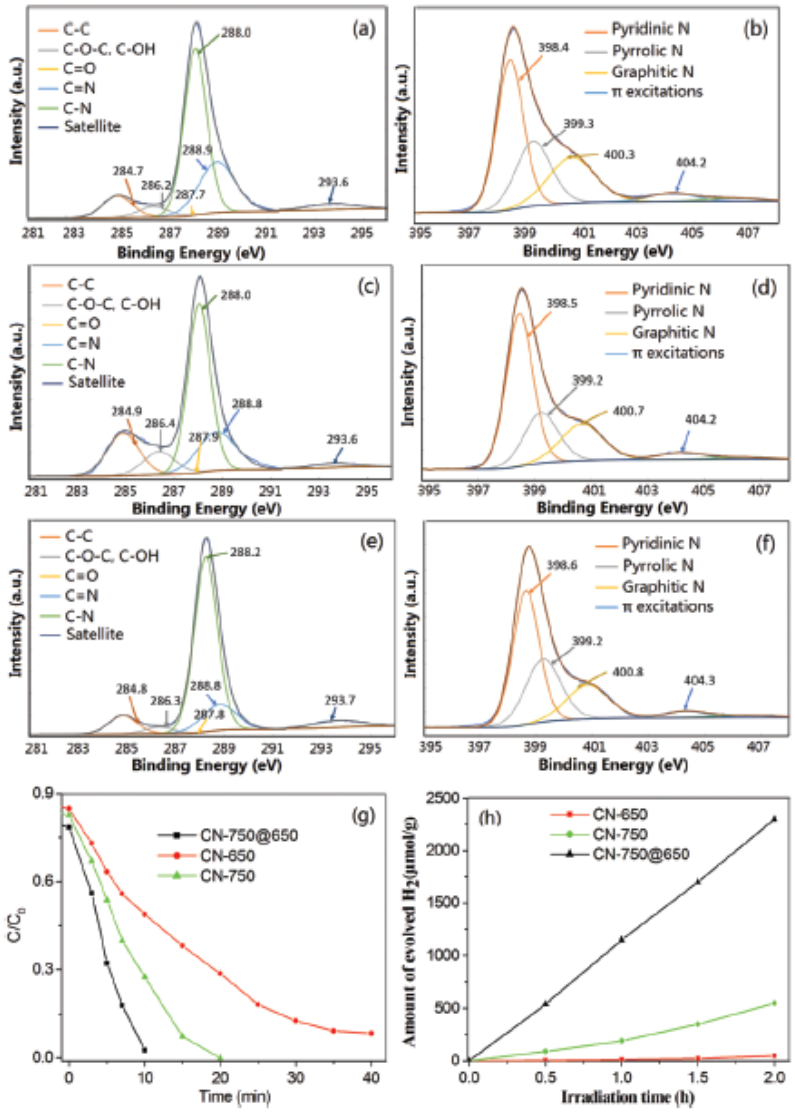

Figure 3-8. XPS spectra (a to f) and photocatalytic performance (g & h) of g-C_3N_4 samples. (a,

b) CN-650. (c, d) CN-750. (e, f) CN-750@650C. (g) PhB photocatalytic degradation plots with time and (h) H_2 production curves for H_2 evolution of samples under visible light irradiation ($\lambda > 420$ nm).

g-C_3N_4 has been utilized as a typical visible-light-driven photocatalyst material. The microstructure adjustment results in the change in photocatalytic activities of the material. Fig. 3-8g shows the plots of rhodamine B (RhB) degradation under visible light irradiation. CN-750@650 revealed the highest degradation rate, in which RhB in the solution was degraded completely within 10 min. In case of CN-750, the degradation rate was half of that of the CN-750@650 sample. Moreover, only less than 50 % of RhB was degraded after 10 min in case of utilizing CN-650 sample. The enhanced photocatalytic performance of CN-750@650 homostructures is associated with the contribution of the defects in the interface between crystalline and amorphous phase which increased the number of active sites and promotes the formation of lateral-like crystalline/amorphous homojunctions. These result in efficient separation of photogenerated charge carriers. This lateral-like homo-structure revealed higher RhB degradation efficiency compared with that of the layer-like g-C_3N_4 homo-structure [47, 48]. In addition, crystalline g-C_3N_4 revealed better photocatalytic activities compared with the amorphous one, which can be ascribed to the changes in composition and structure that leads to increased number of active sites. For comparison, crystalline and amorphous g-C_3N_4 were mixed to examine the photocatalytic performance of the mixture. It was found that the photocatalytic performances of the mixed sample were only slightly better than that of the amorphous CN-650 sample. This confirms that g-C_3N_4 crystalline/amorphous homojunctions (CN-750@650) shows obvious improvement in photocatalytic activities.

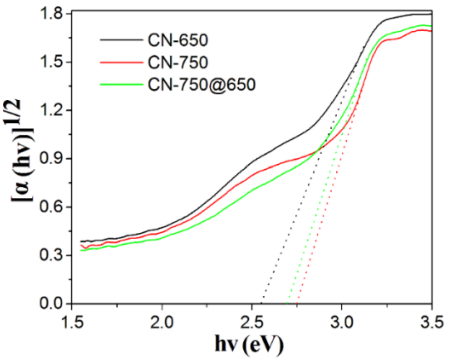

Figure 3-9. $(\alpha h\nu)^{1/2}$ versus photon energy plots of sample CN-650, CN-750, and CN-750@650.

Fig. 3-8h shows the H_2 evolution plots for water splitting as a function of irradiation time. The amount of H_2 generated increased linearly with irradiation time. The efficiency of CN-750@650 is 46 times and 5-6 times higher than that of the CN-650 and CN-750 samples, respectively. The causes for enhanced photocatalytic performance observed for CN-750@650 can be discussed as follows. Both crystalline and amorphous g-C_3N_4 are formed through polymerization reactions [49, 50]. One characteristic of g-C_3N_4 photocatalyst is the quick recombination rate of photogenerated electrons and holes that results in low photocatalytic efficiency [51-55]. Amorphous g-C_3N_4 was sequential edge-epitaxially grown on crystalline g-C_3N_4 to form the homostructure. Although the composition of the two phases is similar, the change in crystallinity and N/C ratio (1.16 and 0.90 for sample CN-650 and CN-750, respectively) lead to changes in band gap of the samples. Thus, it is obvious that the homojunctions promote spatial separation of electrons and holes and reduce the charge carrier recombination rate. Stability test shows that the hydrogen generation and RhB degradation efficiencies of the homojunction sample remained almost unchanged after 5 cycles.

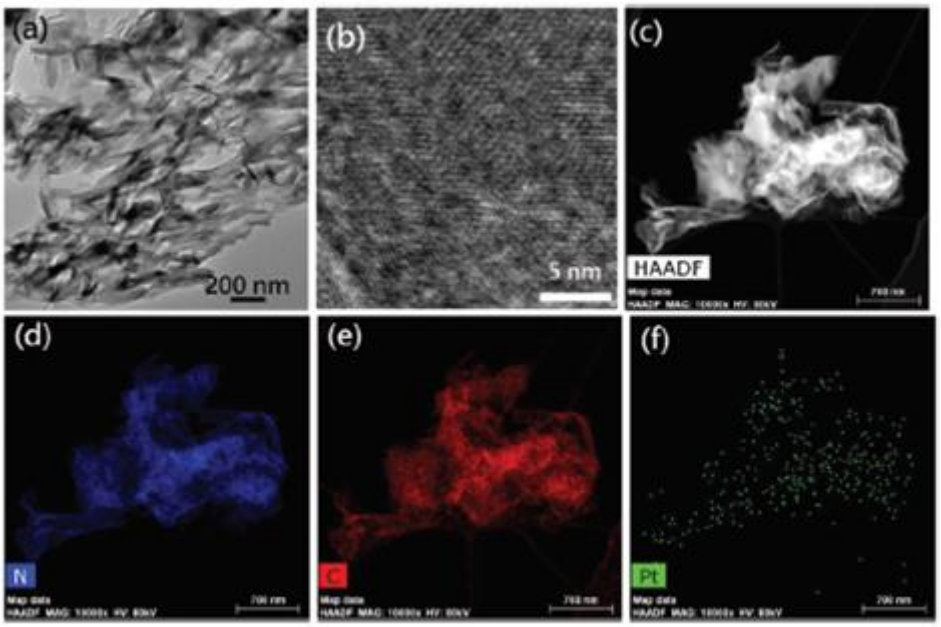

Figure 3-10. (a) TEM, (b) HRTEM, (c) HAADF-STEM images; N (d), C (e), and Pt (f) mapping of Pt-deposited CN-750@650-0.5.

To improve electrochemical properties and to test charge transfer system of the material, Pt was deposited onto g-C_3N_4 via ultrasonic treatment and reduction by reflux

processes. Fig. 3-10 shows the TEM, HRTEM, high-angle annular dark-field scanning TEM (HAADF-STEM) images and the corresponding elemental mapping of Pt-deposited CN-750@650-0.5 (with 0.5 denotes the reaction time to be 0.5 hour of sonication). The image in Fig. 3-10a shows that the morphology of Pt-deposited g-C_3N_4 is much curled on the edges after Pt deposition. The HRTEM image in Fig. 3-10b shows the sample with clear lattice fringes, but they do not match with that of the crystalline g-C_3N_4 or Pt. This can be attributed to the overlap of different crystal phases. The successful deposition of Pt can be associated with the generation of reductant species (e.g. H atoms) during sonication, wherein, H atoms are generated from sonolysis of water [51-55]. It is found that N, C, and Pt were homogeneously distributed in the whole specimen area (Fig. 3-10c to 10f). However, the amount of Pt incorporated is limited.

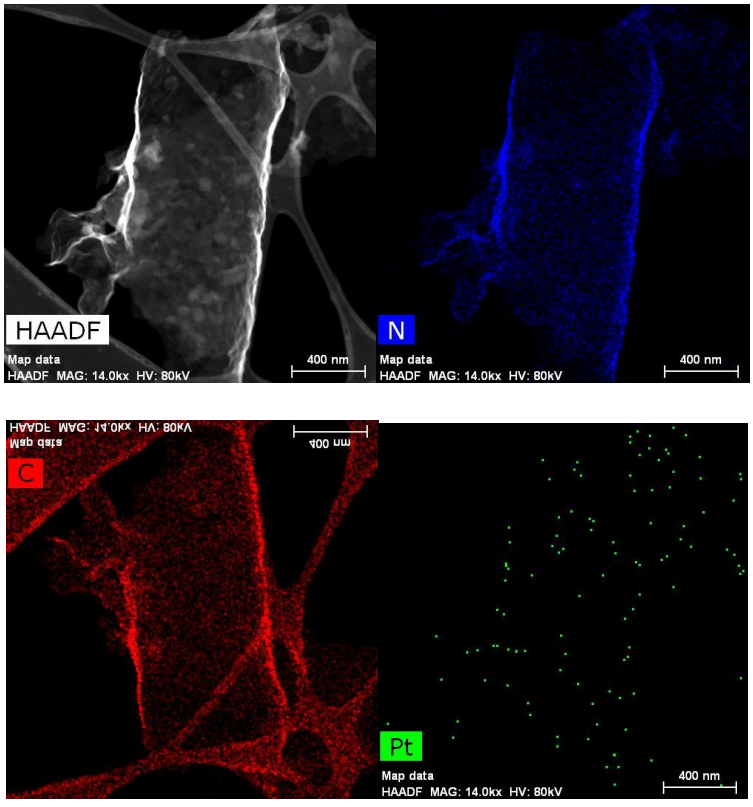

Figure 3-11. (a) HAADF-STEM images and N (b), C (c), Pt (d) mapping of Pt-deposited CN-750@650-1.

To increase the amount of Pt decoration, reaction time was increased to 2 hours (Fig. 3-11 and 3-12). The distribution of Pt particles is homogeneous for all samples. In the case of 2 hours of reaction time, an obvious increase in the amount of Pt incorporated

was observed. This confirms electron generation during the sonication process with no reductants added, leading to homogeneous Pt attachment on g-C_3N_4. The photodegradation activity of Pt decorated samples was tested (Fig. 3-13). Pt decorated sample with shortest deposition time of 0.5 hour revealed the best performance.

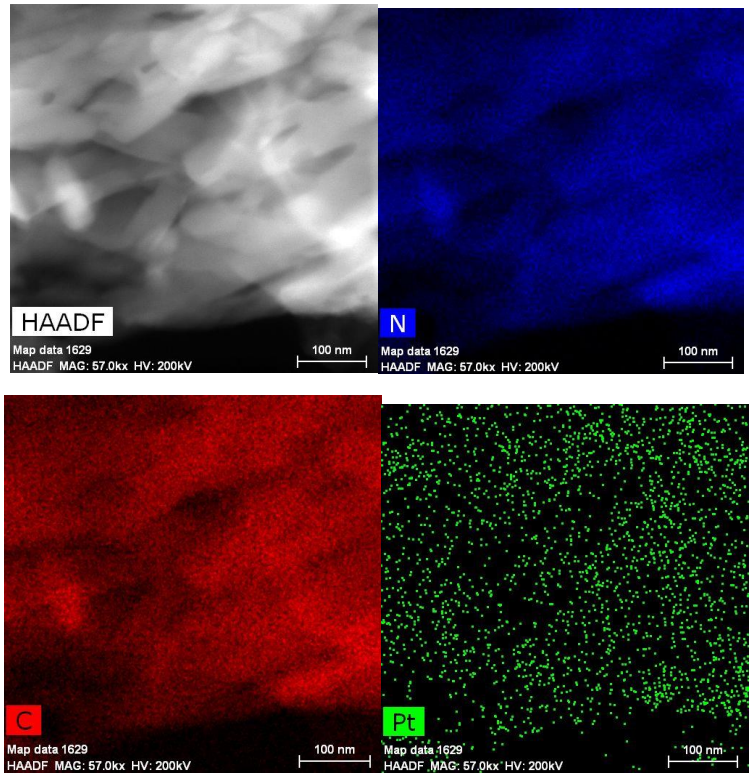

Figure. 3-12. (a) HAADF-STEM images and N (b), C (c), Pt (d) mapping of Pt-deposited CN-750@650-2.

After Pt modification, the catalytic performances of CN-650 and CN-750 were enhanced while that of the CN-750@650 sample diminished. And this is owing to the fact that charge transfer in the homojunction was inhibited due to the electron transfer to Pt, confirming successful formation of homostructures. The XPS analysis for Pt-modified sample CN-750 indicates that the amount of Pt incorporated increases with time. In addition, it is still challenging developing g-C_3N_4 with improved electrocatalytic hydrogen evolution activity[56].

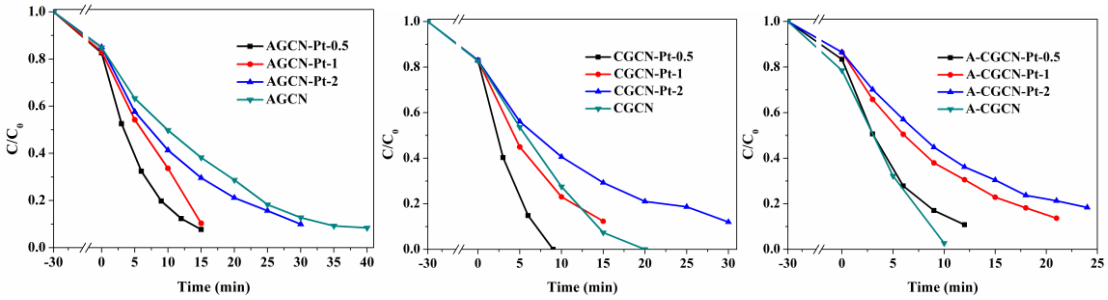

Figure 3-13. RhB photocatalytic degradation plots for g-C_3N_4 samples: (left) CN-650, (middle) CN-750, (right) CN=750@650. Pt-deposited sample with 0.5 hour of reaction time revealed the highest performance.

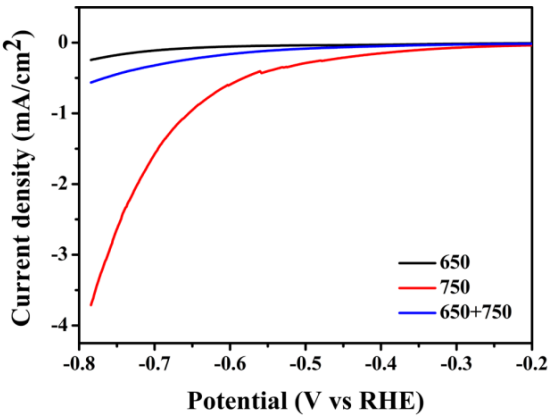

Figure 3-14. HER polarization curves of g-C_3N_4 samples under visible light irradiation with a scan rate of 5 mVs^{-1}.

Since g-C_3N_4 is commonly used as a photocatayst rather than an electrocatalyst, to exploit the electrocatalytic applications of highly stable g-C_3N_4 under visible light irradiation is of great significance. The HER polarization curves of g-C_3N_4 samples under visible light irradiation condition with a scan rate of 5 mVs^{-1} are shown in Fig. 3-14. As expected, crystalline CN-750 revealed the highest performance eventhough the onset overpotential of the sample is not high. In order to achieve high electrocatalytic activity, Au particles were decorated onto CN-750. The HER polarization curves of CN-750 before and after Au or Pt deposition are shown in Fig. 3-15a. It is clear that the Pt decorated samples possess higher HER activity than that of Au-modified samples due to the higher intrinsic activity of Pt nanoparticles, which causes reduction of hydrogen adsorption free energy. Pt deposited sample with 3 hours of reaction time reveals the best activity. As the ultrasonic treatment duration increases, improvement in HER activity was observed, which is due to the increased amount of small and uniformly

distributed Pt nanoparticles incorporated on g-C_3N_4. The Tafel slopes were further used to characterize the reaction kinetics. The reaction pathway obeys the Volmer-Heyrovsky mechanism, with the hydrogen adsorption reaction to be the rate-determining step.

$$M + H+ + e- \leftrightarrows M\text{-Hads} \quad (3\text{-}3)$$

$$M\text{-Hads} + H+ + e- \leftrightarrows M + H_2 \quad (3\text{-}4)$$

$$2M\text{-Hads} \leftrightarrows 2M + H_2 \quad (3\text{-}5)$$

The HER activities of samples are assessed by Tafel slopes (Fig. 3-15b) which were calculated from the polarization curves based on the Tafel equation [57, 58].

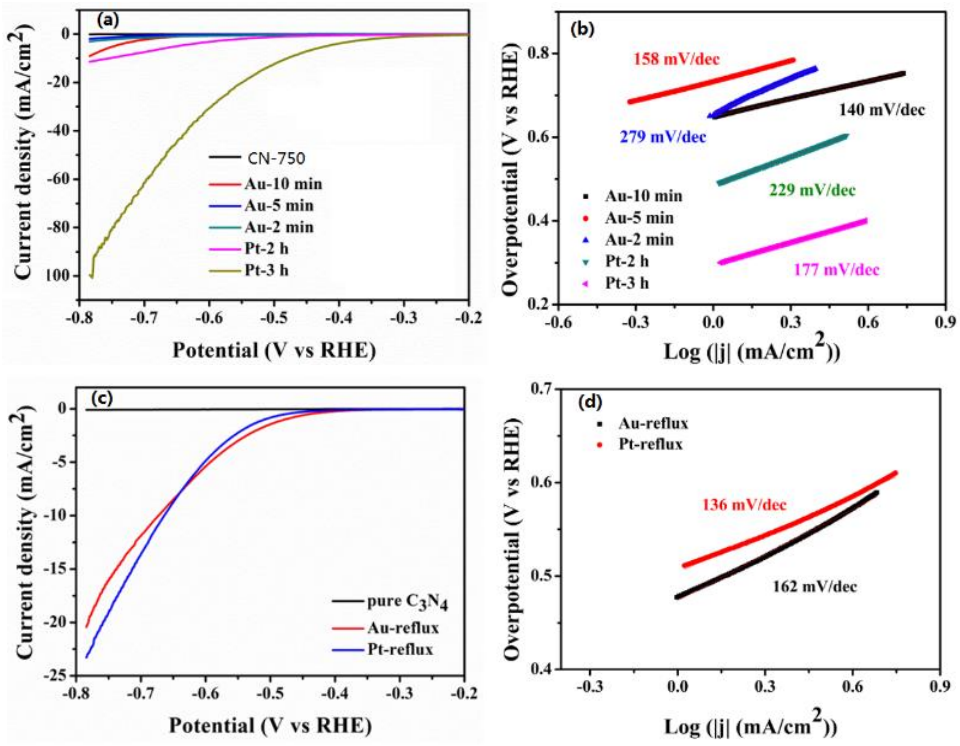

Figure 3-15. (a) HER polarization curves of CN-750 before and after Au, Pt modification with different sonication time. (b) Tafel plots of the samples derived from HER polarization curves in (a). (c) HER polarization curves of CN-750 modification with Au and Pt via reflux. (d) Tafel plots of the samples derived from HER polarization curves in (c).

As shown in Fig. 3-15a, the H_2 evolution performance of 3-hour Pt deposited CN-750 sample was significantly enhanced compared with that of other samples. This is due to the increasing amount of small and uniformly distributed Pt nanoparticles on g-C_3N_4. The reaction was determined by Volmer step (eq.3-3), and the decrease in value of Tafel slopes reveals the accelerated reaction kinetic. This result does not coincide with what was observed for the photocatalytic tests. Sample with 0.5 hour of Pt deposition time

revealed the highest photocatalytic activity. This phenomenon is derived from the differences in reaction mechanisms for photocatalysis and electrocatalysis. For comparison, Au and Pt nanoparticles were deposited using $NaHBO_4$ via reflux process. The HER performances of the Au-reflux and Pt-reflux samples (Fig. 3-15c and 15d) show that the HER activities of these samples are not as good as that obtained on the Pt deposited sample using sonication (3-hour) method. This is due to the fact that the sizes of Au and Pt nanoparticles decorated via relux are relatively larger and are not homogeneous. Sonication thus can be considered as one sufficient approach for construction of composite materials with fine microstructure and superior electrochemical activities.

3.4 Conclusions

A two-step heat-treatment process was developed for creating superior thin g-C_3N_4 nanosheets with different composition, crystallinity, and properties. At lower temperature (less than 550 ºC), bulk g-C_3N_4 can be obtained via one-step thermal polymerization process. g-C_3N_4 sample prepared at 600 °C reveals lower C/N ratio and amorphous structural feature. Using g-C_3N_4 prepared at 600 °C as seed precursors, ultrathin g-C_3N_4 nanosheets were fabricated. C/N ratio and degree of crystallinity increased with rising temperature. g-C_3N_4 sample with both amorphous and crystalline feature were obtained at 700 °C. Crystalline g-C_3N_4 nanosheets with a C/N ratio of about 0.75 were obtained at 750 °C. The effects of composition and crystallinity of samples on the photodegradation kinetics of RhB were tested. Bulk g-C_3N_4 prepared at 550 °C reveals zero-order kinetics while superior-thin g-C_3N_4 nanosheets samples fit for pseudo-first-order model. Crystalline g-C_3N_4 shows higher photocatalytic activity comparing with that of the amorphous g-C_3N_4. The g-C_3N_4 nanosheets prepared at 700 °C revealed the highest photodegradation efficiency and enhanced H_2 evolution efficiency (1.80 % at 420 nm). Namely, using crystalline g-C_3N_4 as seeds, the amorphous/crystalline homostructures were edge-epitaxially grown at 650 °C via control of the synthetic procedure. The homostructures reveal high photodegradation activity (twice as that of amorphous g-C_3N_4) and H_2 generation efficiency (about 46 times and 5-6 times higher than that of the amorphous and crystalline g-C_3N_4, respectively). The

performances of g-C_3N_4 are significantly enhanced after Au and Pt deposition. However, g-C_3N_4 with different Pt loading shows different effects on photocatalytic and electrocatalytic performances. Owing to the unique microstructure and enhanced properties of the material, these amorphous/crystalline homostructures and Pt modified composites would be of significant importance for electrocatalytic and photocatalytic applications.

3.5 References

[1] D. M. Teter, R. J. Hemley, Science 1996, 271, 53−55.

[2] W. J. Ong, L. L. Tan, Y.H. Ng, S.T. Yong, S-P. Chai, Chem. Rev., 2016, 116, 7159−7329.

[3] J. Fu, J. Yu, C. Jiang, B. Cheng, Adv. Energy Mater. 2018, 8, 3, 1701503.

[4] X. Wang, K. Maeda, A. Thomas, K. Takanabe, G. Xin, J. Carlsson, K. Domen, M. Antonietti, Nat. Mater., 2009, 8, 76-80.

[5] X. Zhang, J-P. Veder, S. He, S. P. Jiang, Chem. Commun., 2019, 55, 1233—1236.

[6] G. Dong, H. Fan, K. Fu, L. Ma, S. Zhang, M. Zhang, J. Ma, W. Wang, Compos. B. Eng., 2019, 162, 369-377.

[7] S. Lu, C. Li, H. H. Li, Y. F. Zhao, Y. Y. Gong, L. Y. Niu, X. J. Liu, T. Wang, Appl. Surf. Sci., 2017, 392, 966.

[8] J. Ran, T. Y. Ma, G. Gao, X. W. Du, S. Z. Qiao, Energy Environ. Sci. 2015, 8, 3708.

[9] Y. Li, R. Jin, Y. Xing, J. Li, S. Song, X. Liu, M. Li, R. Jin, Adv. Energy Mater. 2016, 6, 1601273.

[10] X. Dong, F. Cheng, J. Mater. Chem. A, 2015, 3, 23642.

[11] J. Jia, E. R. White, A. J. Clancy, N. Rubio, T. Suter, T. S. Miller, K. McColl, P. F. McMillan, V. Brazdova, F. Cora, C.A. Howard, R.V. Law, C. Mattevi, S. P. Shaffer, Angew. Chem. Int. Ed., 2018, 57, 12656−12660.

[12] M.Z. Rahman, C.W. Kwong, K. Davey, S. Z. Qiao, Energy Environ. Sci., 2016, 9, 709−728.

[13] C. Tan, X. Cao, X. J. Wu, Q. He, J. Yang, X. Zhang, J. Chen, W. Zhao, S. Han, G. H. Nam, M. Sindoro, H. Zhang, Chem. Rev., 2017, 117, 6225−6331.

[14] P. Niu, L. Zhang, G. Liu, H. M. Cheng, Adv. Funct. Mater., 2012, 22, 4763.

[15] K. Schwinghammer, M. B. Mesch, V. Duppel, C. Ziegler, J. Senker, B. V. Lotsch, J. Am. Chem. Soc., 2014, 136, 1730−1733.

[16] D. J. Martin, K. Qiu, S. A. Shevlin, A. D. Handoko, X. Chen, Z. Guo, J. Tang, Angew. Chem. Int. Ed., 2014, 53, 9240-9245.

[17] Z. Lin, X. Wang, Angew. Chem. Int. Ed., 2013, 52, 1735-1738.

[18] G. Liu, P. Niu, C. Sun, S. C. Smith, Z. Chen, G. Q. Lu, H. M. Cheng, J. Am. Chem. Soc., 2010, 132, 11642-11648.

[19] A. J. Stevens, T. Koga, C. B. Agee, M. J. Aziz, C. M. Lieber, J. Am. Chem. Soc., 1996, 118, 10900-10901.

[20] I. Alves, G. Demazeau, B. Tanguy, F. Weill, Solid State Commun., 1999, 109, 697-701.

[21] Z. Zhang, K. Leinenweber, M. Bauer, L. A. J. Garvie, P. F. McMillan, G. H. Wolf, J. Am. Chem. Soc., 2001, 123, 7788-7796.

[22] K. C. Chiu, K. H. Huang, C. A. Chen, Y. Y. Lai, X. Q Zhang, E. C. Lin, M. H. Chuang, J. M. Wu, Y. H. Lee, Adv. Mater., 2017, 1704796.

[23] P. K. Sahoo, S. Memaran, Y. Xin, L. Balicas, H. R. Gutiérrez, Nature, 2018, 553, 64.

[24] Z. Zhang, P. Chen, X. Duan, K. Zang, J. Luo, X. Duan, Science, 2017, 357, 788.

[25] C. Jia, X. Zhang, K. Matras-Postolek, B. Huang, P. Yang, Carbon, 2018, 139, 415.

[26] J. Ji, J. Wen, Y. Shen, Y. Lv, Y. Chen, S. Liu, H. Ma, Y. Zhang, J. Am. Chem. Soc., 2017, 139, 11698.

[27] J. T. Yin, Z. Li, Y. Cai, Q. F. Zhang, W. Chen, Chem. Commun., 2017, 53, 9430.

[28] Y. Liu, X. Zhang, J. Wang, P. Yang, Phys. Chem. Chem. Phys., 2016. 18. 31513.

[29] L. Huang, Z. Liu, W. Chen, D. Cao, A. Zheng, J. Mater. Chem. A, 2018, 6, 7168.

[30] Y. Wei, Z. Zhao, P. Yang, ChemElectroChem, 2018, 5, 778.

[31] F. Zhang, Q. Wen, M. Hong, Z. Zhuang, Y. Yu, Chem. Eng. J., 2017, 307, 593.

[32] M. Li, X. Zhang, K. Matras-Postolek, H. S. Chen, and P. Yang, J. Mater Chem C, 2018, 6, 5506.

[33] L. Shi, Z. Li, K. Marcus, G. Wang, K. Liang, W. Niua, Y. Yang, Chem. Commun., 2018, 54, 3747.

[34] C. Wang, H. Fan, X. Ren, J. Fang, J. Ma, N. Zhao, Mater. Charact., 2018, 139, 89–99.

[35] F. Goettmann, A. Fischer, M. Antonietti, A. Thomas, Angew. Chem. Int. Ed.,2006, 45, 4467-4471.

[36] M. Groenewolt, M. Antonietti, Adv. Mater., 2005, 17, 1789-1792.

[37] B. V. Lotsch, M. Döblinger, J. Sehnert, L. Seyfarth, J. Senker, O. Oeckler, W. Schnick, Chem. Eur. J., 2007, 13, 4969-4980.

[38] M. Zhou, Z. Hou, L. Zhang, Y. Liu, Q. Gao, X. Chen, Sustain. Energy Fuels, 2017, 1, 317-323.

[39] X. Zhang, C. Jia, Y. Xue, P. Yang, RSC Adv., 2017, 7, 43888-43893.

[28] Z. Jiang, X. Zhang, J. Wang, L. Chen, H.-S. Chen, P. Yang, Chem. Commun., 2018, 54, 13519-13522.

[40] C. Wang, H. Fan, X. Ren, J. Ma, J. Fang, W. Wang, ChemSusChem, 2018, 11, 700-708.

[41] Z. Liu, G. Wang, H. S. Chen, P. Yang, Chem. Commun., 2018, 54, 4720–4723.

[42] G. Zhang, A. Savateev, Y. Zhao, L. Li, M. Antonietti, J. Mater. Chem. A, 2017, 5, 12723-12728.

[43] F. He, G. Chen, Y. Yu, Chem. Commun., 2015, 51, 6824.

[44] Y. Hou, A. Laursen, J. Zhang, G. Zhang, Y. Zhu, X. Wang，S. Dahl, I. Chorkendorff, Angew. Chem. Int. Ed., 2013, 52, 3621.

[45] R. Ye, H. Fang, Y. Zheng, N. Li, Y. Wang, and X. Tao, ACS Appl. Mater. Interfaces, 2016, 8, 13879.

[46] Q. Han, C. Hu, F. Zhao, Z. Zhang, N. Chen, L. Qu, J. Mater. Chem. A, 2015, 3, 4612.

[47] X. Chen, W. Lu, T. Xu, Chem. Eng. J., 2017, 328, 853.

[48] Y. Li, J. Zhang, Q. Wang, Y. Jin, D. Huang, Q. Cui, G. Zou, J. Phys. Chem. B, 2010, 114, 9429.

[49] X. Chen, Y. Jun, K. Takanabe, K. Maeda, K. Domen, X. Z. Fu，M. Antonietti, X. Wang, Chem. Mater., 2009, 21, 4093.

[50] X. Li, J. Zhang, X. Chen, A. Fischer, A. Thomas, M. Antonietti, X. Wang, Chem. Mater., 2011, 23, 4344.

[51] G. Jiang, C. Zhou, X. Xia, F. Yang, D. Tong, W. Yu, S. Liu, Mater. Lett., 2010, 64, 2718.

[52] H. Shi, G. Chen, C. Zhang, ACS Catal., 2014, 4, 3637.

[53] X. Song, X. Zhang, and P. Yang, RSC Adv. 2016, 6, 107433.

[54] X. Song, Y. Liu, Y. Zheng, K. Ding, S. Nie, P. Yang, Phys. Chem. Chem. Phys. 2016, 18, 4577.

[55] P. Yang, X. Song, C. Jia, H. S. Chen, J. Indust. Eng. Chem., 2018, 62, 250.

[56] J. Zhang, F, Guo, X. Wang, Adv. Funct. Mater. 2013, 23, 3008.

[57] P. Liu, J. Y. Zhu, J. Y. Zhang, P. X. Xi, K. Tao, D. Q. Gao, D. S. Xue, ACS Energy Lett., 2017, 2, 745.

[58] J. Luxa, V. Mazanek, D. Bousa, Z. D. Sedmidubsky, M. Pumera, Z. Sofer, ChemElectroChem., 2016, 3, 565.

Chapter 4: Superior thin red g-C_3N_4 nanosheets: composition, heterostructures and their photoluminescence performance*

Abstract

It is challenging to construct g-C_3N_4 (a conventional photocatalyst) with tunable and stable photoluminescence (PL) in solution or in powder form. In this chapter, a molten-salt-assisted route is developed to prepare red-coloured superior thin carbon nitride (g-C_3N_4) nanosheets with redshifted absorption range and narrowed bandgap of 1.91 eV. Interestingly, these g-C_3N_4 nanosheets exhibit excellent water-soluble nature. The colloidal solution of the nanosheets reveal bright, stable, and tunable PL from blue to yellow light region. The PL of samples depends on the concentration of g-C_3N_4 nanosheets. At lower concentration, a blue-emitting band is observed, while a green to yellow emitting band is recorded at higher concentration. Furthermore, the powder sample shows a broad green to yellow emitting band. A reversible PL phenomenon can be observed by precipitation of g-C_3N_4 colloidal solution. The PL efficiency of red-coloured g-C_3N_4 nanosheets powder is ~ 75 %. g-C_3N_4 samples reveal excellent PL stability both in colloidal solution and in powder form. The PL intensity and efficiency of the powder samples remain almost unchanged after six months. In addition, red g-C_3N_4 nanosheets with narrowed bandgap (E_g ~ 1.89 eV) prepared via a molten-salt-assisted route are used as seeds to edge-epitaxially grow yellow g-C_3N_4 (E_g ~ 2.59 eV), in which type II heterostructure is successfully formed. The formed heterostructure effectively separates photogenerated charge carriers, resulting in superior photocatalytic activity for H_2 generation and CO_2 reduction.

**Reprinted (adapted) with permission from Xiao Zhang, Ping Yang, and San Ping Jiang, The edge-epitaxial growth of yellow g-C_3N_4 on red g-C_3N_4 nanosheets with superior photocatalytic activities, Chem. Commun. 2021, 57, 3119 – 3122; and Bright and tunable photoluminescence from the assembly of red g-C_3N_4 nanosheets, J. Lumin. 2021, 235, 118055.*

4. 1 Introduction

Although graphitic carbon nitride (g-C_3N_4) as a layered material has emerged as one of the most promising metal-free photocatalysts, it is still a challenge developing g-C_3N_4 as an efficient luminescent material due to the fact that the photoluminescence (PL) efficiency of g-C_3N_4 is usually quite low and that its PL emission peak is not tuneable [1, 2]. g-C_3N_4 prepared by thermal condensation of C and N precursors possesses a melon-based structure which is consisted of one-dimensional heptazine (tri-s-triazine) building blocks connected by bridging imide [3-5]. Due to the presence of defects on the layered g-C_3N_4 as active sites, g-C_3N_4 reveals excellent photochemical performances under visible light irradiation. Since the presence of active sites promotes separation of photogenerated charge carriers, the PL of g-C_3N_4 (coming from the recombination of charge carriers on defects) has weak broad PL peaks located at blue region. The advantages of layered g-C_3N_4 as a PL material include its metal-free nature with excellent photostability and low toxicity [6, 7]. Control of defects thus plays the key role in developing materials with extremely stable PL and high efficiency. Though studies on PL of layered g-C_3N_4 in blue and green region have been reported in literature, the PL study of layered g-C_3N_4 is still at a very early stage.

The metal-free, outstanding biocompatibility, straightforward preparation method and low-cost characteristics of g-C_3N_4 meets most of the demands for environmental protection. Studies on PL properties of g-C_3N_4-based materials have been reported in literature. Zheng and co-workers developed a metal-free blue-emitting melem with a PL efficiency of ~ 57 % that is about 1.6 times higher than that of the ordinary melem [7]. Moreover, layered g-C_3N_4 synthesized by thermal polymerization of melem has been found to have excellent luminescence properties [8-11]. Zhang and co-workers reported on g-C_3N_4 single-layered quantum dots as a fluorescent probe for two-photon fluorescence imaging of the cellular nucleus [12]. A composite material as a white-emitting diode possessing a color rendering index of 94 was synthesized by Guo et. al. [13]. In general, g-C_3N_4 luminescent materials are prepared using physical and chemical methods. For physical stripping route (e.g., H_2SO_4 assisted ultra-sonication), bulk g-C_3N_4 can be stripped to ultrathin nanosheets with defect blue-emitting [14]. Chemical methods focus on bandgap and structural defect adjustment by control

of preparation conditions. Chemical methods are much more favourable for preparation of g-C_3N_4 luminescent materials since it provides the possibility of creating materials with tunable luminescence and high PL efficiency. Development of g-C_3N_4 luminescent material with tunable and stable PL as well as high PL efficiency thus is desirable.

To develop highly fluorescent layered g-C_3N_4 materials, the PL activity of the material has been studied. Layered g-C_3N_4 can be synthesized by calcination of melamine, urea, dicyandiamide or cyandiamide in ambient or inert atmosphere at temperatures ranging from 400 to 750 °C. The precursors are condensed into melem composed of carbon, nitrogen and hydrogen first. The melem can then be further condensed into g-C_3N_4 [15]. The PL peaks of melem at 432 and 454 nm are due to the δ* and π* states related transition [7, 16]. The cathodic electrogenerated chemiluminescence (ECL) behaviour of layered g-C_3N_4 while using $K_2S_2O_8$ as a co-reactant was reported by Cheng and co-workers, in which the excited state formation of g-C_3N_4 in ECL is different from the direct bandgap excitation in PL [17]. Since redox potential of Cu^{2+}/Cu^{+} is located in between the CB and the VB of g-C_3N_4, the PL of g-C_3N_4 nanosheets can be quenched by Cu^{2+} through photoinduced electron transfer [18]. PL evolution of superior thin g-C_3N_4 nanosheets in alkaline solution has been reported in literatures [6]. Reversible PL phenomenon was observed for those assembled nanosheets, e.g., a PL efficiency of 78 % was observed for green-emitting assemblies in solid printed patterns.

In this chapter, a molten-salt-assisted route was developed to prepare porous red-coloured g-C_3N_4 nanosheets via a two-step synthetic method at 700 °C using melamine, NaCl, and KCl. These red-coloured g-C_3N_4 nanosheets with relatively narrower bandgap (~ 1.91 eV) revealed excellent water solubility. The powder sample showed a couple of emission bands (from blue to yellow) depending on the excitation wavelengths used. Moreover, the powder sample exhibited high PL efficiency of ~ 75 % and high stability in air. The colloidal solution of these g-C_3N_4 nanosheets revealed tunable PL and absorption spectra. To further exploit the potential applications of red g-C_3N_4, it is highly desirable developing layered g-C_3N_4 nanosheets with various homojunction structures to improve photogenerated charge separation efficiency for overcoming the above-mentioned drawbacks. Thus, a type II red/yellow g-C_3N_4 lateral heterostructures and water-soluble red g-C_3N_4 nanosheets were prepared, with the heterostructures formed by using red g-C_3N_4 nanosheets as seeds to achieve edge-epitaxial

growth via CVD growth and thermal condensation. These heterostructures exhibit enhanced photocatalytic H_2 generation and CO_2 reduction activity as well as outstanding stability.

4.2 Experimental

4.2.1 Synthesis of red g-C_3N_4

Superior thin and porous g-C_3N_4 nanosheets were prepared via a two-step thermal polymerization process. Melamine was first calcined at 500 ºC for 2 hours in tube furnace under argon atmosphere with a ramp rate of 2 ºC/min to obtain the layered bulk g-C_3N_4. 4 g of bulk g-C_3N_4 was then mixed with 4 g of NaCl and KCl followed by grinding. The pale-yellow powders obtained were calcined at 700 °C for 1 hour with a ramp rate of 2 °C/min. The resulting powder sample was washed with water for several times to remove NaCl and KCl crystals to obtain the red g-C_3N_4 powder. For the preparation of g-C_3N_4 colloidal solutions, red g-C_3N_4 powder was ground and re-dispersed in water using different g-C_3N_4 concentrations. The solution was centrifuged at 6000 rpm for 10 min to remove unwanted large particles. A clear yellow solution of g-C_3N_4 assemblies was obtained. Table 4-1 illustrates the preparation conditions and properties of samples. For comparison, yellow g-C_3N_4 nanosheets were prepared via a two-step polymerization process [5, 6]. Bulk g-C_3N_4 was obtained by thermal polymerization of melamine at 500 °C. The bulk g-C_3N_4 was then further thermally polymerized at 700 °C to obtain a yellow g-C_3N_4 powder (sample YCN).

Table 4-1. Preparation conditions and properties of samples

Sample	g-C_3N_4 (mg/mL)	PLQYs (%)	Sample condition
RCN-1	N/A	75	Powder
RCN-2	0.05	85	Colloidal solution
RCN-3	0.10	82	Colloidal solution
RCN-4	0.25	78	Colloidal solution
RCN-5	0.50	78	Colloidal solution
RCN-6	1.00	76	Colloidal solution

4.2.2 Preparation of red/yellow g-C_3N_4 heterostructures

Bulk g-C_3N_4 (named as BCN) was prepared at 500 ºC. 10 g of melamine was added into a quartz boat and calcined at 500 ºC in Ar for 2 hours with a ramp rate of 5 ºC/min. The obtained sample was then washed with deionized water and ethanol for several times. Yellow g-C_3N_4 nanosheets (referred as YCN) were prepared through polymerization of BCN. 10 g of BCN was added to a quartz boat and calcined at 650 ºC in argon for 2 hours with a heat-treat rate of 5 ºC/min. Red g-C_3N_4 nanosheets were prepared using a molten salt assisted method. 10 g of melamine was mixed with 8 g of mixtures of NaCl and KCl (mole ratio = 1:1). The mixture was ground evenly by adding ethanol and water to obtain a powder sample. The obtained sample was then calcined at 700 °C for 1 hour using a ramp rate of 5 °C/min in a muffle furnace. The product was purified using ethanol and H_2O and was dried to obtain sample RCN. The yellow/red g-C_3N_4 heterostructures (named as HCN-1 to HCN-4) were prepared by using red g-C_3N_4 as seeds. 0.4 g of selected sample RCN was ground with 10 g of bulk g-C_3N_4 for 2 hours. The sample was then added to a quartz boat and calcined at 650 ºC in Ar for 2 hours with a ramp rate of 5 ºC/min. Finally, the sample was dispersed in water with sonication and selective separation. The amount of sample RCN was adjusted to 4, 8, 12, and 15 wt%, respectively.

4.2.3 Characterization

The morphology observation of the RCN and YCN samples was performed using transmission electron microscope (TEM) (Titan G2 80-200 TEM/STEM, FEI, US). The X-ray diffraction (XRD) patterns of the samples were collected using an X-ray diffractometer (Ultima IV, Japan) with a Cu Kα radiation source using a 2θ range of 10-80°. X-ray photoelectron spectroscopy (XPS) data for the samples were collected using the X-ray photoelectron spectroscopy analyzer (Kratos Axis Ultra DLD spectrometer). UV-Visible spectrophotometer (U-4100, Hitachi) was used to collect the UV-Vis diffuse reflectance (DRS) and adsorption spectra of the g-C_3N_4 powder and solution samples. The photoluminescence (PL) spectra of water-soluble sample were obtained using Hitachi F-4600 fluorescence spectrometer at room temperature in a wavelength range of 380-700 nm at different excitation wavelengths. Data including FTIR spectra

(Nicolet 380, Thermo, America), Brunauer-Emmett-Teller (BET) specific surface area and pore diameter distribution of samples (MFA-140, Beijing Builder Company) were also collected. PL lifetime of the RCN samples was collected using the single-photon counting time-resolved spectral fluorescence lifetime instrument (Jobin Yvon IBH, Horiba, Japan, at λex=374 nm). Secondary fitting double-exponential decay function was used for fitting. The fluorescence decay curve was fitted using the double exponential model as shown by the equations below.

$$F(t)=A+B_1\exp(-t/\tau_1)+ B_2\exp(-t/\tau_2) \quad (4\text{-}1)$$

The fluorescence lifetime was calculated by using the following equation.

$$\tau = (B_1 \times \tau_1^2 + B_2 \times \tau_2^2) / (B_1 \times \tau_1 + B_2 \times \tau_2) \quad (4\text{-}2)$$

The fluorescence observation of the particles of g-C_3N_4 samples were obtained using a fluorescence microscope (Olympus IX71, Olympus Corporation, Japan) at room temperature, and the sample was excited by a 473 nm picosecond diode laser. The PL quantum yields (PLQYs) was recorded using the Edinburgh FLS920 fluorescence spectrophotometer.

4.2.4 Photocatalytic performance measurement

A system consisting of a Pyrex top-irradiation reaction vessel and a glass-closed gas circulation system was used for photocatalytic H_2 production measurement. 10 mg of each of the g-C_3N_4 samples was dispersed in a 100 ml (triethanolamine: deionized water = 1:9) aqueous solution. The g-C_3N_4 sample solution was sonicated for 20 min and evacuated before light exposure and testing. The sample solution with constant stirring was then irradiated under a 300 W Xe lamp with a cutoff filter (λ > 420 nm). The amount of H_2 evolved was detected using Shimadzu GC-7920 gas chromatography with Ar as carrier gas. The hydrogen evolution activity data of the samples were collected in a 4-hour cycle. The hydrogen evolution stability test was performed for 4 cycles.

The apparent quantum efficiency (AQE) of samples was calculated using the equation shown below.

$$\mathrm{AQE} = \frac{N_e}{N_p} = \frac{2\times M\times N_A\times h\times c}{S\times P\times t\times \lambda} * 100\% \quad (4\text{-}3)$$

where Ne and Np are the amount of reaction electrons and the incident photons, respectively.

M is the amount of H_2 molecule, N_A the Avogadro constant, c is the speed of light, S is irradiation area, P is irradiation intensity, t is the time, and λ the wavelength of monochromatic light.

Photocatalytic CO_2 reduction measurement of samples was performed, and the data were analyzed by using gas chromatography (Shimadzu GC-7920). 20 mg of sample was added to 15 mL of water to obtain a homogeneous suspension. CO_2 bubbling of the sample solutions was done with vigorous stirring for 20 min to remove air. A 300 W Xe lamp with a cut off filter of 420 nm was used as light source during CO_2 reduction.

4.3 Results and discussion

4.3.1 Red g-C_3N_4 nanosheets with bright concentration-dependent photoluminescence and stability

Layered bulk g-C_3N_4 was synthesized via thermal polymerization of melamine or other N-rich precursors at high temperature. In this section, molten-salt-assisted route was used to introduce K and Na ions into the interlayers of g-C_3N_4 to prepare porous and water-soluble red g-C_3N_4 nanosheets. During preparation, melamine was ground with NaCl and KCl evenly by adding ethanol and deionized water. Thus, the in-situ introduction of these alkali heteroions (Na and K) can be achieved. The obtained mixture was then heat-treated at 700 ºC for thermal polymerization. Na and K ions are embedded into the space in between the adjacent heptazine unit of the g-C_3N_4 nanosheets. Fig. 4-1 shows the TEM images and XRD pattern of sample RCN-3 and YCN. Sample RCN exhibited a large-scale layered feature with porous structure as shown in Fig. 4-1a and 1b. In contrast, sample YCN did not show porous structure (Fig. 4-1c). The specific surface area measured for sample RCN-3 and YCN were 201.3 and 112.5 m^2g^{-1}, respectively.

Fig. 4-1d shows the XRD patterns of the g-C_3N_4 samples. The intensity of the (002) facet peak for YCN has increased compared with that of bulk g-C_3N_4, suggesting improved crystallinity of YCN. The XRD pattern of RCN is different from that of the conventional g-C_3N_4 (YCN and bulk g-C_3N_4). A broad diffraction peak at 28.5°on the XRD pattern of sample RCN-3 can be assigned to the (002) facet, representing the

interlayer stacking of nanosheets in the sample [19]. Other sharp peaks for sample RCN-3 are related to the NaCl phase. The peak at ~13.0° was not observed for RCN-3, suggesting the breaking of long-range order in the intralayer arrangement during the molten salt assisted reaction at high temperature. In addition, the diffraction intensity of sample RCN at 28.5° is relatively weak compared with that of bulk g-C_3N_4 [20], suggesting the breaking of the interlayer structure of melamine due to the reaction between alkali species and melamine during the thermal polymerization process [21]. Such structure significantly narrows the bandgap and drastically reduces the energy barrier for charge carrier transport within both interlayers and intralayers [12].

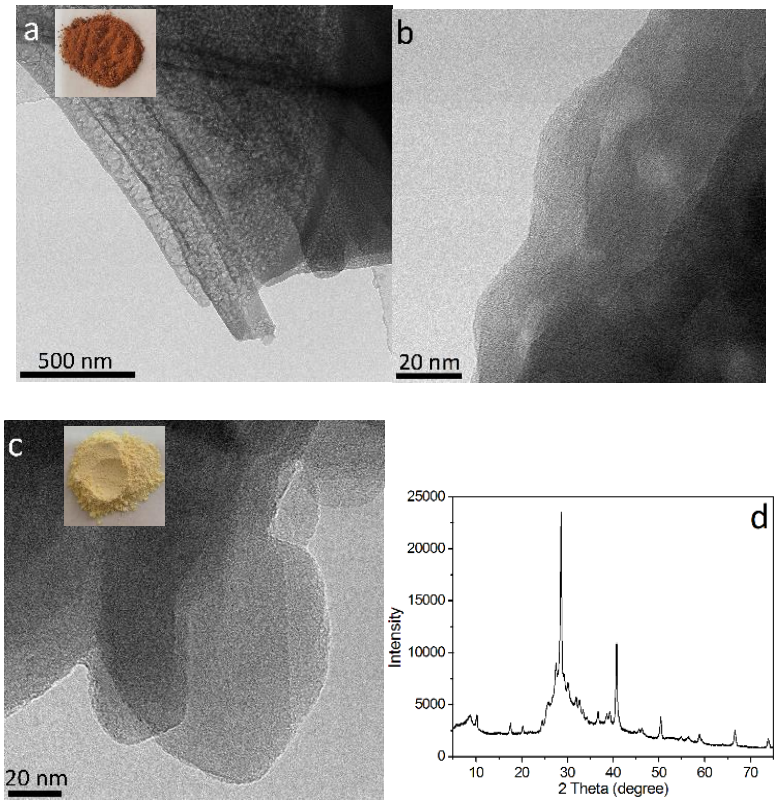

Figure 4-1. TEM images and XRD pattern of samples. (a, b) TEM images of sample RCN-3. (c) TEM image of sample YCN. (d) XRD pattern of sample RCN-3. Insets in (a) and (c) show the pictures of sample RCN and YCN.

The Tauc plots in Fig. 4-2a are obtained from their UV-Vis DRS using the following formula: $\alpha h\upsilon = A(h\upsilon - E_g)^n$. Where α, h, υ, and E_g, are absorption coefficient, Planck constant, light frequency, and band gap, respectively. The n value equals to 1/2 and 2 in case of indirect and direct band gap semiconductor, respectively. The Tauc plot of sample RCN-1 has redshifted in visible region due to the incorporation of alkali ions in g-C_3N_4. The Tauc plots in Fig. 4-2a

show a drastically reduced bandgap from 2.55 eV (sample RCN-1) to 1.91 eV (sample YCN). The redshift of the absorption edge and reduced bandgap is to some extent related to the incorporation of Na and K ions.

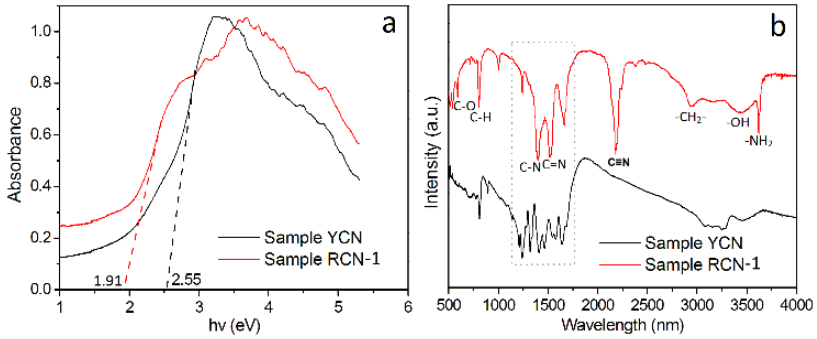

Figure 4-2. (a) Tauc plots and (b) FTIR spectra of sample YCN and RCN-1.

Fig. 4-2b shows the FTIR spectra of sample RCN-1 and YCN. Both samples exhibit the feature peak at 810 cm^{-1} and peaks in 900–1800 cm^{-1} region corresponding to the typical stretching vibration peaks for bending mode of heptazine rings and N-C=N/N–C_3 of the melon unit in g-C_3N_4 [21]. The result indicates that the molten-salt-assisted route breaks the ordered unit arrangement and interlayer structure of g-C_3N_4 but the basic structure of g-C_3N_4 can be maintained [12].

The band signal originating from -OH stretching vibration located between 3385 and 3520 cm^{-1} is much stronger for sample RCN due to the water-soluble nature of red g-C_3N_4. The peaks emerged at 2175 cm^{-1} and 2865–2920 cm^{-1} in the spectra of sample RCN can be ascribed to the presence of asymmetric stretching vibration of cyano groups and asymmetric stretching vibration of methylene groups (-CH_2), respectively. The stretching vibration of -NH_2 was observed for sample RCN-1.

Fig. 4-3 shows the XPS spectra of sample RCN-1 including survey spectrum, C 1s, N 1s, Na 1s, and O 1s spectra. The peaks at 401.0, 399.5, and 398.7 eV of the N 1s spectra (Fig. 4-3a) correspond to graphitic N, pyrrolic N, and pyridinic N, respectively. Typical peaks at 289.3, 288.1, 286.2, and 284.5 eV are assigned to the C-N/C-O, O-C=O, C-OH, and C-C groups, respectively (Fig. 4-3b). The spectra in Fig. 4-3c and 4-3d examined that Na and K components still remained in sample RCN-1 after washing. The FTIR spectra support the idea that amide groups were partially removed, and that hydroxyl groups were generated during the thermal treatment [4]. The amount of K and

Na left in sample RCN-1 are about 1.1 and 0.8 wt%, respectively. This confirms that introduction of Na and K ions in red g-C_3N_4 has a negligible effect on the intralayer and interlayer structure of C_3N_4. The molar ratio of K and Na estimated are 0.2 and 1 %, respectively. The O1s spectrum has peaks assigned to oxide, -OH group, and H_2O, confirming the adsorption of H_2O and -OH groups in RCN-3.

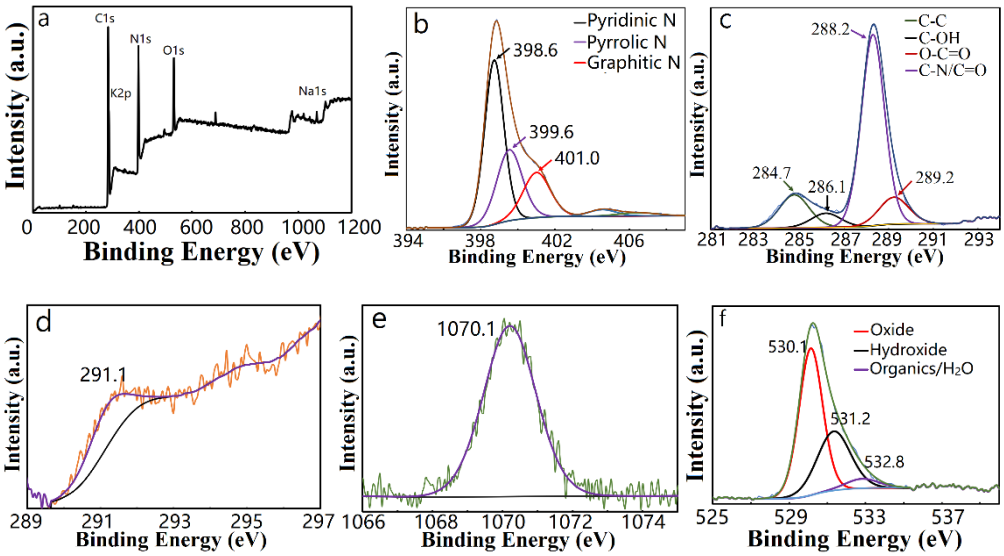

Figure 4-3. XPS spectra of water-soluble red g-C_3N_4 (RCN-3): (a) survey spectrum, (b) N 1s, (c) C 1s, (d) K 2p, (e) Na 1s, (f) O 1s.

Table 4-2. Preparation conditions and properties of samples

Sample	g-C_3N_4 (mg/mL)	PLQYs (%)	Sample situation
RCN-1	N/A	75	Powder
RCN-2	0.05	85	Colloidal solution
RCN-3	0.10	82	Colloidal solution
RCN-4	0.25	78	Colloidal solution
RCN-5	0.50	78	Colloidal solution
RCN-6	1.00	76	Colloidal solution

The conventional yellow-coloured g-C_3N_4 is a photocatalyst normally used for visible light related applications. However, the red g-C_3N_4 nanosheets did not show any photocatalytic activity (e. g. dye photodegradation and photo-catalytic H_2 generation). This phenomenon might be related to the quick recombination of photogenerated charge carriers. Fig. 4-4 shows the excitation and PL spectra of g-C_3N_4 samples in powder and colloidal solution form. The PL spectra of red-coloured g-C_3N_4 are excitation wavelength-dependent. Fig. 4-4a shows the PL spectra of sample RCN-1 (powder) and

sample RCN-2 (colloidal solution). The PLQYs of sample RCN-1 and RCN-2 are 75 and 76 %, respectively, as illustrated in Table 4-2. Sample RCN-1 revealed a bright broad blue to yellow emitting band with a maximum PL peak wavelength at 480 nm. Sample RCN-2 to RCN-6 were prepared by dispersing different amount of sample RCN-1 in deionized water to form a colloidal solution. Due to high water solubility of the sample, sample RCN-2 to RCN-6 were completely transparent. Compared with sample RCN-1, the PL peak of sample RCN-2 was blue-shifted. This phenomenon is attributed to the fact that PL of g-C_3N_4 nanosheets is dependent on its microstructure. The layered g-C_3N_4 is constructed from melem units consisted of triazine (C_3N_3) and tri-s-triazine (C_6N_7) rings [7]. The PL properties of g-C_3N_4 nanosheets is different from that of semiconductor quantum dots. The distribution of melem units and surface states can affect the PL properties of the materials. For instance, PL of melem units in blue region can be related to the π^* and δ^* state related transitions [22, 23]. Gu and co-workers reported on the PL of g-C_3N_4 quantum dots that changed from 450 to 512 nm after O and N doping [24].

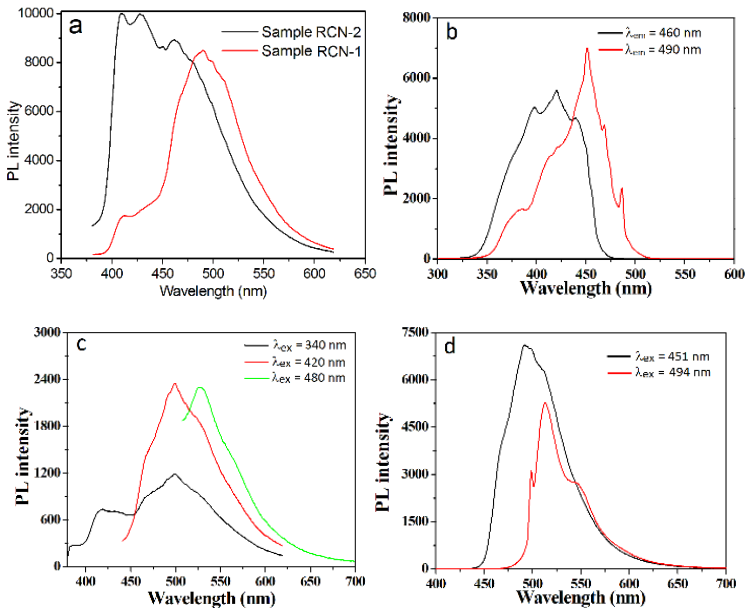

Figure 4-4. Excitation and PL spectra of samples (λ_{ex} = 365 nm). (a) PL spectra of sample RCN-1 (powder) and sample RCN-2 (colloidal solution). (b) Excitation spectra of sample RCN-2 with different emission wavelengths. (c) PL spectra of sample RCN-1 in powder form with different excitation wavelengths. (d) PL spectra of sample RCN-2 at different excitation wavelengths.

Fig. 4-4b shows the excitation spectra of sample RCN-2. Two different broad excitation spectra were observed by choosing 460 and 490 nm as the emission wavelength. The excitation spectra consisted of several excitation peaks can be related to the presence of different luminescent components in g-C_3N_4 nanosheets. The shape and intensity of the excitation spectra collected were completely different. Fig. 4-4c shows the PL spectra of sample RCN-1 with different excitation wavelengths (340, 420, and 480 nm). The PL spectra were redshifted, and the PL intensity increased with increasing excitation wavelength. A broad green to yellow emitting band was observed. Fig. 4-4d shows the PL spectra of sample RCN-2 with different excitation wavelengths (451 and 494 nm). The PL spectra were also redshifted and decreasing of PL intensity was observed with increasing excitation wavelength. Both sample RCN-1 and RCN-2 revealed tunable PL property with excitation wavelength dependency. To further explore the PL mechanism of the sample, PL and absorption spectra of colloidal samples were collected.

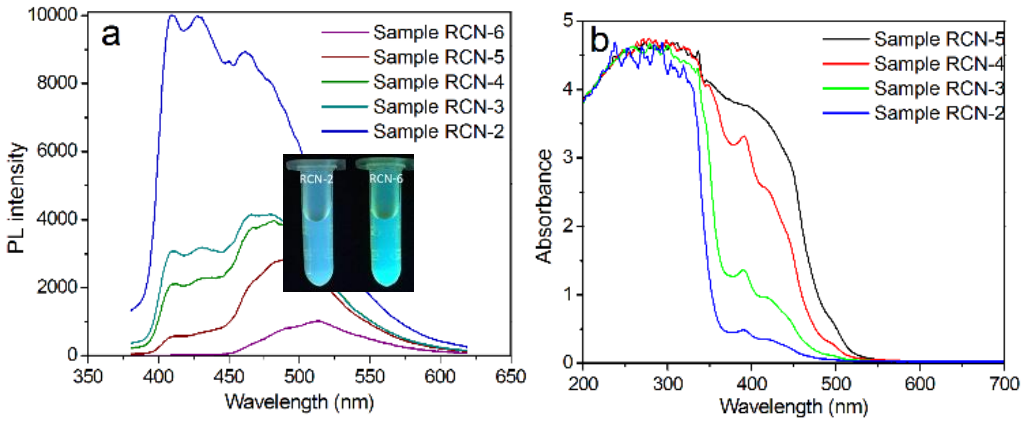

Figure 4-5. Absorbance and PL spectra of samples. (a) Absorbance spectra of samples. (b) PL spectra of samples. Inset in (b) shows the pictures of sample RCN-2 (left) and RCN-6 (right) irradiated by using 365 nm UV light.

Fig. 4-5 shows the PL (λ_{ex} = 365 nm) and adsorption spectra of samples RCN-2 to RCN-6. The inset in Figure 4b shows the pictures of sample RCN-2 and RCN-6 irradiated under 365 nm UV light. With increasing concentration of red g-C_3N_4, the PL intensity of samples decreased, and the PL peaks were redshifted. The PLQYs of samples RCN-2 to RCN-6 are 85, 82, 78, 78, 76 %, respectively, as illustrated in Table 4-1. The PLQYs of samples increases with decreasing concentration of red coloured g-C_3N_4. Fig. 4-5b shows the absorption spectra of samples RCN-2 to RCN-6. The absorption band edge

and the shapes of the absorption peaks observed for these samples are similar. However, the absorption in the 370-500 nm region increased with increasing g-C_3N_4 concentration. This phenomenon can be attributed to the varying of sizes and surface conditions of samples in colloidal solution. The absorption band around 400 nm is related to the surface molecular center and to the fact that absorption edge is assigned to the n→π* transitions of the nonbonding electrons of adatoms [25, 26]. Aggregation of layered g-C_3N_4 nanosheets was observed for the pristine powder sample. Homogeneous dispersion of the aggregated nanosheets in water can be achieved. The lower the concentration of the g-C_3N_4, the lower the degree of aggregation. Moreover, the edge of the absorption band becomes clearer with increasing concentration of g-C_3N_4. To further explore the concentration dependency of PL of the red-coloured g-C_3N_4, sample RCN-2 was further precipitated and washed to obtain the powder sample. The PL spectrum of this powder sample is similar to that of sample RCN-1. This suggests that concentration dependent PL of the samples are reversible. At different concentrations, the samples have different surface adsorbates and different surface conditions, leading to change in PL spectra observed. Fig. 4-6 shows the PL spectra plots of sample RCN-1 and RCN-6. The latter part of PL spectra of the two samples is almost identical, and this result supports the discussions above.

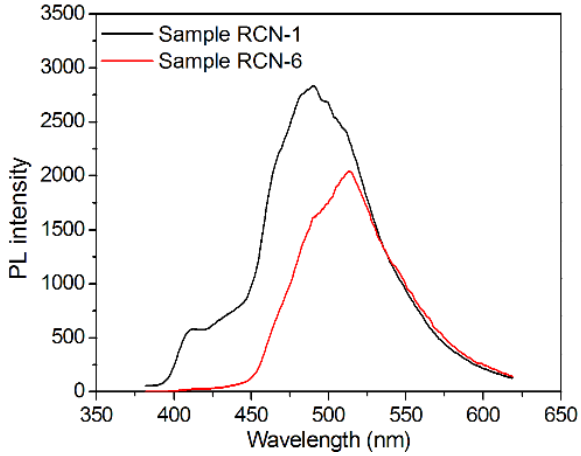

Figure 4-6. Comparison of PL spectra of samples RCN-1 and RCN-6.

The PL spectra of red-coloured g-C_3N_4 samples exhibited blue, green, and yellow emission bands. The PL intensity and peak position can be adjusted with varying sample conditions. The tunable PL of layered g-C_3N_4 nanosheets with a single band gap structure is due to the (π*–π) transitions [24]. Electrons in π* states are excited from the valence band to the conduction band

and transferred to the valence band to emit visible light. Electrons in δ* states can be relaxed to the π* state and transfer to the valence band to generate the secondary emission band [27]. In addition, due to the presence of the functional groups (e.g. -OH, -NH_2) as well as adsorption of adatoms and molecules on the surface of g-C_3N_4, the tunable PL of red-coloured g-C_3N_4 samples can be related to the band-to-band and interstate transitions. Functional groups and adsorbed adatoms or molecules work as the radiative recombination centers, which are the keys in electron transition [28]. The presence of Na and K doping ions as well as amino groups causes changes in bonding and anti-bonding orbitals, leading to electron transition [29]. The PL of sample RCN-1 revealed excellent stability. The PL intensity and PL spectra remained almost unchanged after the sample been stored in air for 6 months.

To study the electron transition process, the fluorescence decay plots of samples were recorded. Fig. 4-7 shows the PL decay curve of sample RCN-5 (measured at maximum emission, λex = 374 nm) in a colloidal solution. The PL decay curve was fitted to the double exponential model. The average lifetime of sample RCN-1 to RCN-6 are 9.6, 9.4, 9.8, 9.7, 10.1, and 9.9 ns, respectively. No blinking phenomenon was observed for g-C_3N_4 samples in powder or in colloidal solution form. This indicates that the PL of red-coloured g-C_3N_4 nanosheets is completely different from the intrinsic band gap PL of semiconducting quantum dots [30, 31]. The average lifetime of red-coloured g-C_3N_4 nanosheets is much longer than those reported in literature (3.2 ns) [6]. Rong and co-workers reported a highly fluorescent doped g-C_3N_4 nanodots for label-free detection of Cu^{2+} ions [32]. According to Rong et. al., pristine g-C_3N_4 sample revealed a fluorescence lifetime of 18 ns while the average lifetimes of S and B-doped samples are 15.5 and 12.5 ns, respectively. The inset in Fig. 4-7 shows the dark yield image of sample RCN-5 excited by 480 nm laser, in which bright white emission was observed. The composites as a novel luminescent material can be used for various applications due to the environmental-friendly, economical, and high stability nature of the material.

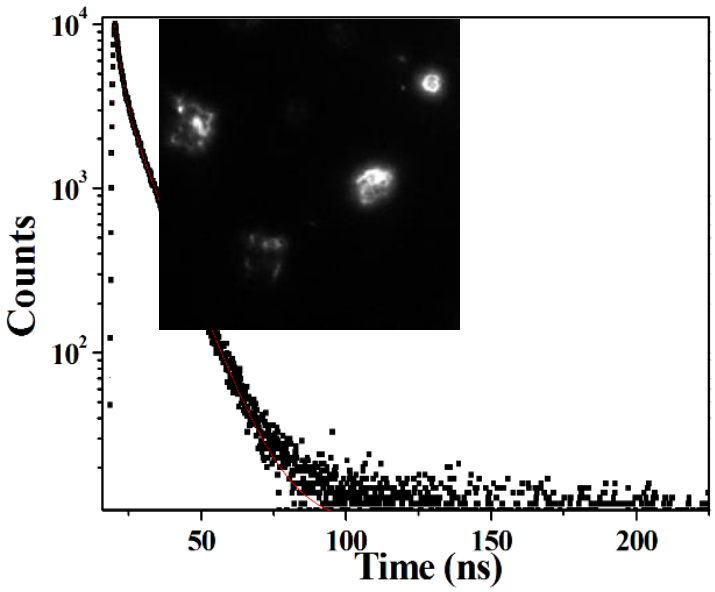

Figure 4-7. PL decay curve of sample RCN-5 (measured at maximum emission peak, λex = 374 nm) in colloidal solution. Reproduced curves for data are plotted as thin red line to calculate the average lifetime. Inset in figure shows the dark yield image of a single particle of sample excited by 473 nm laser.

Layered g-C_3N_4 nanosheets possess abundant surface and structural defects. Increased defects lead to decrease in fluorescence lifetime since these defects are able to trap electrons before releasing photons. For example, the improvement in crystallinity of samples causes reducing in structural defects, which prolongs luminescence lifetime [33]. For g-C_3N_4 nanosheets, structural defects are able to capture electrons in the δ* and π* states located in conduction band, resulting in PL quenching [7]. Although abundant defects exist in the system, the crystallinity of the red g-C_3N_4 sample is much higher than that of the bulk g-C_3N_4 [12]. The fluorescence lifetime of red-coloured g-C_3N_4 nanosheets is in between that of the bulk and doped g-C_3N_4 samples.

*4.3.2 Edge-epitaxial growth of layered yellow g-C_3N_4 on red g-C_3N_4 nanosheets and their superior photocatalytic activities**

Scheme 4-1 shows the formation process of red/yellow g-C_3N_4 nanosheet heterostructures. The preparation conditions of samples are illustrated in Table 4-3. The weight ratios of red and bulk g-C_3N_4 were adjusted to control the components ratios of red and yellow g-C_3N_4 heterostructures. Bulk g-C_3N_4 (BCN) was obtained by thermal polymerization of melamine at 500 ºC. For comparison, yellow g-C_3N_4 (YCN)

nanosheets were obtained by thermal polymerization of BCN at 650 ºC. Fig. 4-8 shows the SEM and TEM images of samples. BCN revealed a thick bulk structure whereas YCN exhibited a layered nanosheets structure owing to the secondary thermal polymerization process shown in Fig. 4-8a and 4-8b [2, 6, 34]. Compared with sample YCN, the red g-C_3N_4 (RCN) sample exhibited large-scale 2D features with porous structures (Fig. 4-8c and 4-8d).

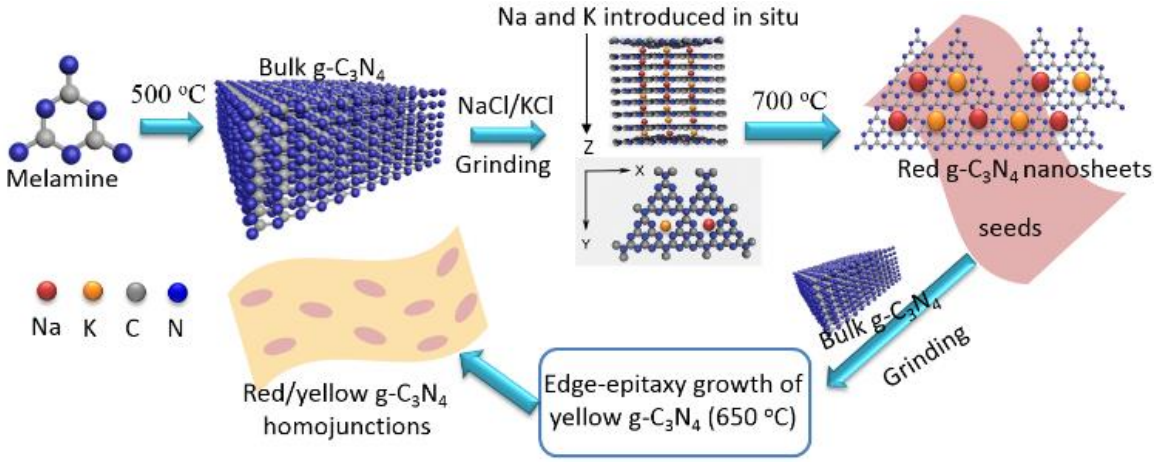

Scheme 4-1. Formation illustration of red/yellow g-C_3N_4 nanosheet heterostructures.

For the edge-epitaxial grown samples, sample HCN-3 still showed nanosheets structure (Fig. 4-8e and 8f). No distinguishable interface between red and yellow g-C_3N_4 was observed. This could be ascribed to the fact that both red and yellow g-C_3N_4 nanosheets have amorphous structures in case of using current experimental conditions. These red and yellow g-C_3N_4 heterostructures consist of a few layers of C_3N_4. The insets in Fig. 4-8 show the pictures of the g-C_3N_4 powder samples. The specific surface areas of samples are illustrated in Table 4-4. All sample have type IV mesoporous structure. The specific surface areas of sample RCN, YCN, and HCN-3 are 198.1, 82.1, and 119.3 m^2g^{-1}, respectively.

Table 4-3. Preparation conditions and properties of g-C_3N_4 samples*

Sample	Composition	Morphology	Temperature (ºC)
BCN	Bulk g-C_3N_4	Bulk	500
RCN	Red g-C_3N_4	Nanosheet	700
YCN	Yellow g-C_3N_4	Nanosheet	650
HCN-1	Red/yellow g-C_3N_4	Nanosheet	650
HCN-2	Red/yellow g-C_3N_4	Nanosheet	650
HCN-3	Red/yellow g-C_3N_4	Nanosheet	650
HCN-4	Red/yellow g-C_3N_4	Nanosheet	650

*RCN/BCN weight ratios of samples HCN-1 to HCN-4 used during preparation are 4, 8, 12, and 15 %, respectively.

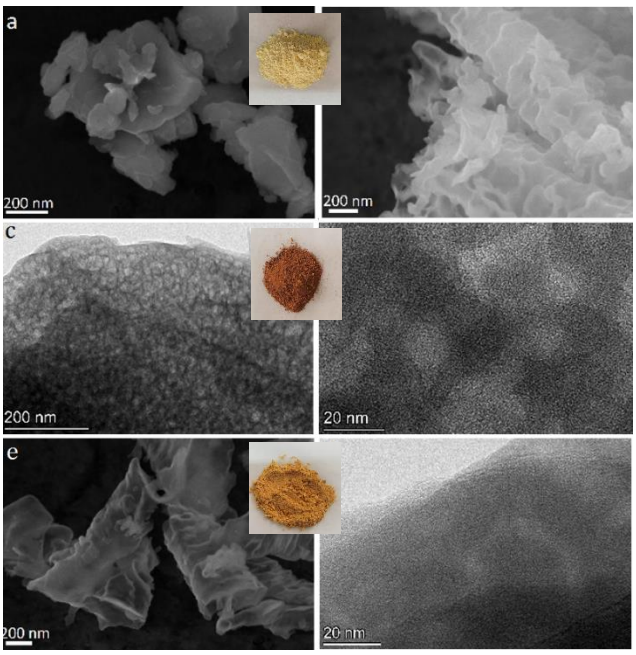

Figure 4-8. SEM and TEM images of g-C_3N_4 samples. (a) SEM image of BCN. (b) SEM image of YCN. (c, d) TEM images of RCN. (e) SEM image of HCN-3. (f) TEM image of HCN-3. The insets in (b), (d), and (f) show the actual pictures of g-C_3N_4 powder samples.

Table 4-4. Specific surface area and pore size of the g-C_3N_4 samples.

Sample	Composition	S (m^2/g)	Pore size (nm)
BCN	Bulk g-C_3N_4	57.7	6.2
RCN	Red g-C_3N_4	198.1	12.0
YCN	Yellow g-C_3N_4	82.1	6.4
HCN-1	Red/yellow g-C_3N_4	94.8	6.6
HCN-2	Red/yellow g-C_3N_4	1.3.5	7.1
HCN-3	Red/yellow g-C_3N_4	119.3	7.4
HCN-4	Red/yellow g-C_3N_4	135.1	7.8

Fig. 4-9 shows the X-ray diffraction (XRD) patterns, Fourier transform infrared (FTIR) spectra, absorbance spectra, and X-ray photoelectron spectroscopy (XPS) analysis data of g-C_3N_4 samples. As shown in Figure 4-9a, a weak diffraction peak at 13.0° and strong diffraction peak at 28.5° were observed for the heterostructure sample (HCN-3) corresponding to the (100) and (002) facets, indicating the intralayer long-range ordered packing and interlayer stacking of nanosheets in the sample, respectively [5, 31, 35]. In contrast, the peak at ~13.0° was not observed in the XRD pattern of sample RCN, suggesting the breaking of long-range order in the intralayer arrangement occurred during the molten-salt-assisted reaction at high temperatures. In addition, the XRD peak of sample RCN at 28.5° is relatively weak compared with that of sample HCN-3, indicating the breaking of stacked interlayer structure occurred due to the reactions between alkali species and bulk g-C_3N_4 during thermal polymerization process.

Fig. 4-9b shows the FTIR spectra of sample RCN and HCN-3. The FTIR spectrum of sample HCN-3 is different from that of sample RCH, but similar to that of the other g-C_3N_4 homojunctions. The featured peaks at around 810 cm^{-1} and around 900–1800 cm^{-1} region correspond to the typical bands of bending mode of heptazine rings and the melon unit in the g-C_3N_4 framework, suggesting that the molten-salt-assisted route only breaks the ordered units arrangement and interlayer structure but the primary structure of g-C_3N_4 is maintained [36]. The band signal of -OH stretching vibration located in between

3385 and 3520 cm^{-1} for sample RCN is stronger than that of the heterostructure sample. This is due to the water-soluble nature of red g-C_3N_4. Two peaks emerged at 2175 cm^{-1} and 2865–2920 cm^{-1} in the spectrum of sample RCN are due to the asymmetric stretching vibration of cyano groups and asymmetric stretching vibration of methylene groups, respectively. The difference of FTIR spectra observed for sample RCN and HCN-3 demonstrates that the intralayer structure of heptazine unit-based g-C_3N_4 was partially damaged during thermal-polymerization with NaCl and KCl at high temperatures. Due to incorporation of alkali elements in g-C_3N_4, the UV–Vis diffuse reflectance spectra (DRS) spectrum of sample RCN has redshifted in visible light region. The transformed Kubelka–Munk function versus energy plots (Fig. 4-9b) show the sample to have a drastically decreased bandgap from 2.45 eV (RCN) to 1.89 eV (HCN-3). The redshift of the absorption edge and reduced bandgap are mainly due to the introduction of Na and K ions.

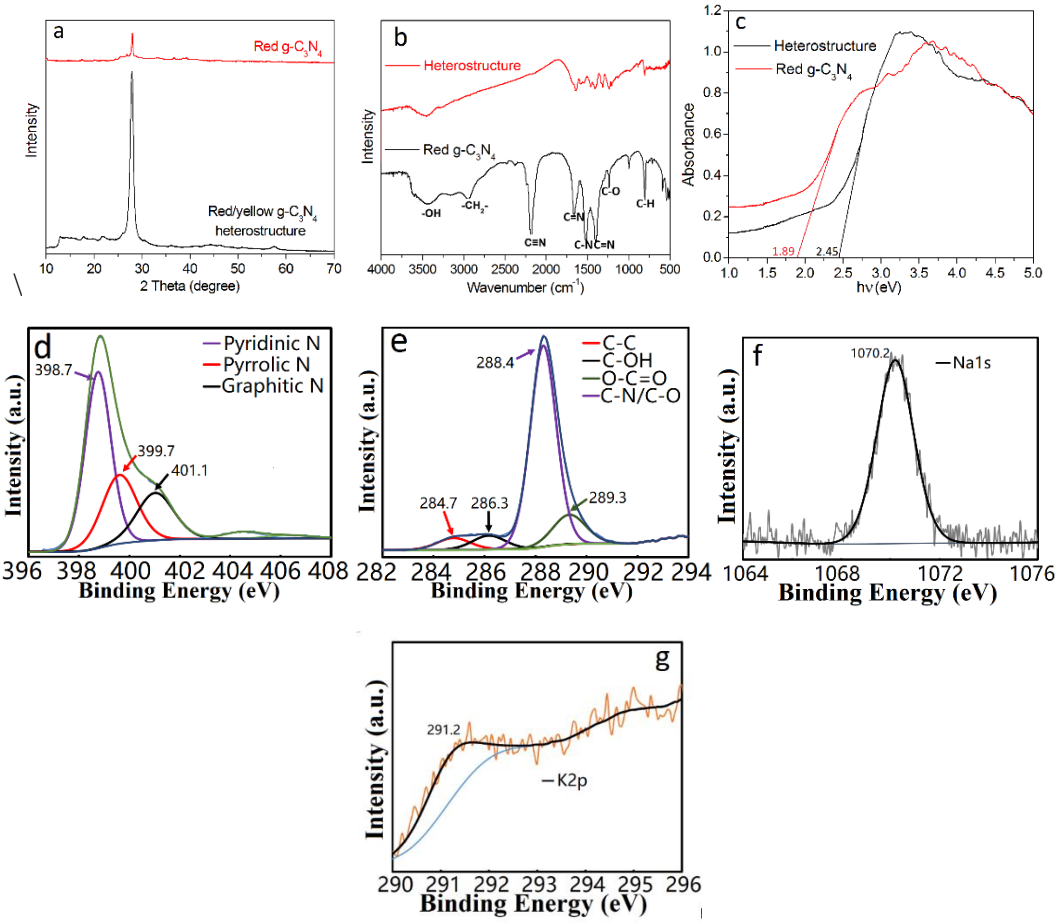

Figure 4-9. XRD patterns (a) FTIR spectra (b) and absorbance spectra (c) of red g-C_3N_4 nanosheets (sample RCN) and red/yellow g-C_3N_4 heterostructures (sample HCN-3).

XPS spectra of sample HCN-3: (d) N 1s spectrum, (e) C 1s spectrum, (f) Na 1s spectrum, and (g) K 2p spectrum.

Fig. 4-9d to 9f shows the XPS spectra of sample HCN-3 including the C 1s, N 1s, K 2p and Na 1s spectra. The peaks at 401.1, 399.7, and 398.7 eV in the N 1s spectrum (Fig. 4-9d) are due to the presence of graphitic N, pyrrolic N, and pyridinic N, respectively. Typical peaks centered at 289.3, 288.4, 286.3, and 284.7 eV correspond to the C-N/C-O, O-C=O, C-OH, and C-C groups in the sample, respectively (Fig. 4-9e). Scarce amount of Na and K components still can be detected in sample HCN-3 as shown in Fig. 4-9f and 9g. Moreover, the FTIR spectra demonstrate that amide groups were partially removed and that hydroxyl groups were formed during the thermal treatment process [36]. The amounts of K and Na in sample RCN are obviously higher than that of sample HCN-3. This confirms the introduction of Na and K ions in red g-C_3N_4 results in negligible effects on change of intralayer and interlayer structure of g-C_3N_4.

The performances of g-C_3N_4 samples are related to the composition and microstructure of the samples. The H_2 generation rate of heterostructure sample HCN-1 to HCN-4 estimated were 2875, 3618, 3996, 3511 $\mu molg^{-1}h^{-1}$, respectively. The optimized ratio of red and yellow g-C_3N_4 estimited was 12 wt%. Fig. 4-10 shows the H_2 evolution plots of samples HCN-3 and YCN for water splitting on a 3-hour-base. The amount of H_2 generated increases linearly with time. The H_2 generation of sample HCN-3 is 8 times higher compared with that of sample YCN. This phenomenon is due to the change of band gaps and increased light absorption of samples. In addition, sample HCN-3 exhibited excellent stability after 4 cycles of H_2 generation test as shown in Fig. 4-10b. In contrast, red g-C_3N_4 (sample RCN) did not show any H_2 generation activity.

CO_2 photocatalytic reduction test for the g-C_3N_4 samples was also performed. Fig. 4-10c shows the CO and CH_4 evolution rate of sample YCN and HCN-3. The photocatalytic reduction of CO (at 420 nm) requires four electrons to be participated into the reaction. Without using any sacrificial agent and co-catalyst, sample HCN-3 revealed enhanced CO (3.8 $\mu molg^{-1}h^{-1}$) and CH_4 (1.6 $\mu molg^{-1}h^{-1}$) evolution compared with that of sample YCH (1.0 $\mu molg^{-1}h^{-1}$ for CO and 0.2 $\mu molg^{-1}h^{-1}$ for CH_4 generation). Since sample RCN showed no CO and CH_4 generation activity, Pt was used as the co-

catalyst. The amount of CO and CH_4 generated with Pt addition for sample RCN is nevertheless still very low. The bad photocatalytic performance of sample RCN might be attributed to their quick recombination rate of photogenerated charge carriers owing to the fact that the sample shows bright blue-green emission with a photoluminescence efficiency of 80 % (Fig. 4-11). To further study the change of band structure of various samples, the valence band position of samples was measured by using XPS valence band spectra. Fig. 4-10d shows that the band gap of samples RCN, YCN, and HCN-3 are 2.59, 2.45, and 1.89 eV, respectively.

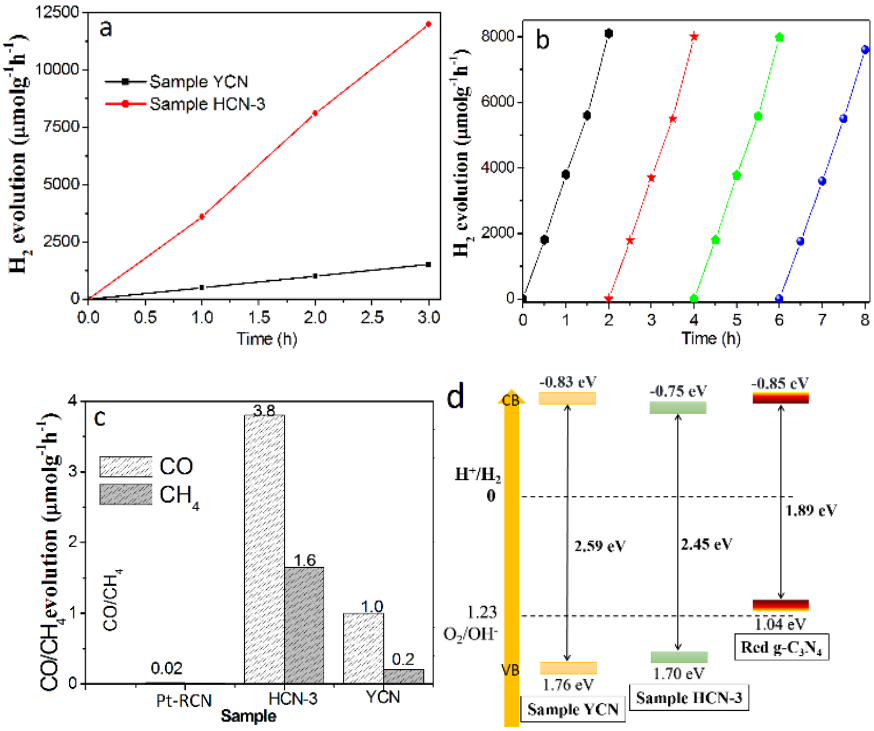

Figure 4-10. (a) Photocatalytic H_2 evolution performance of different samples under visible light irradiation ($\geq$ 420 nm). (b) Stability test of sample HCN-3 for four cycles of H_2 generation. (c) Average CO and CH_4 evolution rate (per hour) of samples. (d) Schematic illustration of band gap of yellow and red g-C_3N_4 and their heterostructures (samples YCN, RCN, and HCN-3).

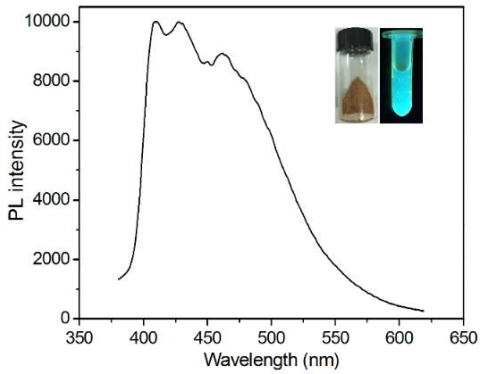

Figure 4-11. PL spectrum of red g-C_3N_4 (sample RCN). Insets in figure show photographs of powder sample (left) and a colloidal solution of sample RCN irradiated under 365 nm UV light.

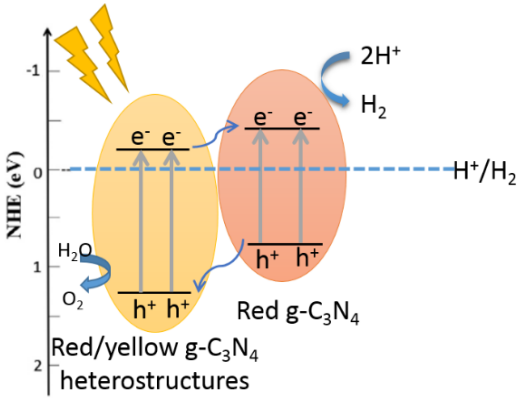

Figure 4-12. Illustration of electron-hole separation and transport in the interface of red and yellow g-C_3N_4.

Fig. 4-12 shows the illustration of electron-hole separation and transport in the interface of red and yellow g-C_3N_4 of the heterostructure sample. The apparent quantum efficiency (AQE) of sample HCN-3 is ~ 4.5 % up to 500 nm. Such high AQE value is due to the activation of n-π* electron transition in the heterostructure [37]. Red g-C_3N_4 has a narrower band gap and broad absorption range in visible light region. The photogenerated charge carriers of red g-C_3N_4 nanosheets was efficiently separated after heterostructure formation to improve the H_2 generation and CO_2 reduction efficiency of the material.

4.4 Conclusions

A molten-salt-assisted route was used to prepare red-coloured superior thin carbon nitride (g-C_3N_4) nanosheets with redshifted absorption spectra and narrowed bandgap

of 1.91 eV. Interestingly, a transparent colloidal solution of g-C_3N_4 nanosheet assemblies was obtained due to the presence of Na^+ ions and the reduction in number of structural defects. The assembly revealed bright and stable PL from blue to yellow region. The PL of the assembly depended on the concentration of g-C_3N_4 nanosheets. At relatively lower concentrations, a blue-emitting band was observed, while a green-emitting band was obtained at higher concentrations. Moreover, the powder sample revealed yellow light emission, which is related to the concentration of the sample. A reversible PL phenomenon was observed by adjusting the concentration of the g-C_3N_4 nanosheets. The PL efficiency of the assembly was ~ 90 %. The PL of the assembly is extremely stable in the NaCl solution or in powder form. In addition, the edge-epitaxial growth of layered yellow g-C_3N_4 with a bandgap of 2.59 eV was done along the edges of red g-C_3N_4 nanosheet to form type II heterostructures. According to the redshifted absorption spectrum of red g-C_3N_4 nanosheets, the heterostructures exhibit enhanced photocatalytic H_2 generation and CO_2 reduction activity as well as excellent stability. The enhanced performances can be ascribed to the efficient separation of photogenerated charge carriers, broadened visible light absorption, and increased surface area.

4.5 References

[1] J. Liu, H. Wang, M. Antoniettia, Chem. Soc. Rev., 2016, 45, 2308-2326.

[2] X. Zhang, J.-P. Veder, S. He, S. P. Jiang, Chem. Comm., 2019, 55, 1233-1236.

[3] X. C. Wang, K. Maeda, A. Thomas, K. Takanabe, G. Xin, J. M. Carlsson, K. Domen, M. Antonietti, Nat. Mater. 2009, 8, 76.

[4] X. Zhang, X. Xie, H. Wang, J. Zhang, B. Pan, Y. Xie, J. Am. Chem. Soc., 2013, 135, 18.

[5] Z. G. Liu, G. Wang, H. S, Chen, P. Yang, Chem. Commun. 2018, 54, 4720.

[6] Z. Jiang, X. Zhang, J. P. Wang, L. Chen, H. S. Chen, P. Yang, Chem. Commun., 2018, 54, 13519.

[7] H. B. Zheng, W. Chen, H. Gao, Y. Y. Wang, H. Y. Guo, S. Q. Guo, Z. L. Tang, J. Y. Zhang, J. Mater. Chem. C, 2017, 5, 10746-10753.

[8] P. Niu, L. Zhang, G. Liu, H. M. Cheng, Adv. Funct. Mater., 2012, 22, 4763–4770.

[9] S. Yang, Y. Gong, J. Zhang, L. Zhan, L. Ma, Z. Fang, R. Vajtai, X. Wang, P. M. Ajayan, Adv. Mater., 2013, 25, 2452–2456.

[10] Y. Zhang, A. Thomas, M. Antonietti, X. Wang, J. Am. Chem. Soc., 2008, 131, 50–51.

[11] L. Mu, L. Shi, Y. Wang, Q. Zhou, J. Ye, X. Feng, J. Mater. Chem. C, 2018, 6, 12660-12667.

[12] X. Zhang, H. Wang, H. Wang, Q. Zhang, J. Xie, Y. Tian, J. Wang, Y. Xie, Adv. Mater., 2014, 26, 4438.

[13] H. Guo, J. Zhang, L. Ma, J. L. Chavez, L. Yin, H. Gao, Z. Tang, W. Chen, Adv. Funct. Mater., 2015, 25, 6833.

[14] W. Wang, J. Yu, Z. Shen, D. Chan, T. Gu, Chem. Commun., 2014, 50, 10148.

[15] B. Jürgens, E. Irran, J. Senker, P. Kroll, H. Müller, W. Schnick, J. Am. Chem. Soc., 2003, 125, 10288.

[16] D. Das, S. L. Shinde, K. K. Nanda, ACS Appl. Mater. Interfaces, 2016, 8, 2181.

[17] C. Cheng, Y. Huang, X. Tian, B. Zheng, Y. Li, H. Yuan, D. Xiao, S. Xie, M. M. Choi, Anal. Chem., 2012, 84, 4754-4759.

[18] J. Tian, Q. Liu, A. M. Asiri, A. H. Qusti, A. O. Al-Youbi, X. Sun, Nanoscale, 2013, 5, 11604-11609.

[19] X. Zhang, P. Yang, S. P. Jiang, Inter. J. Hydrog. Energy, 2021, 46, 2065-2074.

[20] Z. Jiang, X. Zhang, H. S. Chen, P. Yang, S. P. Jiang, Small, 2021, DOI: 10.1002/smll.202003910.

[21] Z. Jiang, C. Jia, B. Wang, P. Yang, G. Gao, J. Alloys Compd., 2020, 826, 154145.

[22] Y. Iwano, T. Kittaka, H. Tabuchi, M. Soukawa, S. Kunitsugu, K. Takarabe and K. Itoh, Jpn. J. Appl. Phys., 2008, 47, 7842.

[23] D. Das, S. L. Shinde, K. K. Nanda, ACS Appl. Mater. Interfaces, 2016, 8, 2181.

[24] S. Gu, C. T. Hsieh, Y. A. Gandomi, J. K. Chang, J. Li, J. Li, H. Zhang, Q. Guo, K. C. Lau, R. Pandey, J. Mater. Chem. C, 2019, 7, 5468-5476.

[25] M. Xu, G. He, Z. Li, F. He, F. Gao, Y. Su, L. Zhang, Z. Yang, Y. Zhang, Nanoscale, 2014, 6, 10307.

[26] T. Yeh, W. Huang, C. Chung, I. Chiang, L. Chen, H. Chang, W. Su, C. Cheng, S. Chen, H. Teng, J. Phys. Chem. Lett., 2016, 7, 2087.

[27] C. Hsieh, C. Lin, Y. Chen, J. Lin, H. Teng, Carbon, 2013, 62, 109.

[28] S. Zhu, J. Zhang, S. Tang, C. Qiao, L. Wang, H. Wang, X. Liu, B. Li, Y. Li, W. Yu, X. Wang, H. Sun, B. Yang, Adv. Funct. Mater., 2012, 22, 4732.

[29] K. Sandeep, G. R. Roy, D. Sen, U. K. Ghorai, R. Thapa, N. Mazumder, S. Saha, K. K. Chattopadhyay, Nanoscale, 2014, 6, 3384.

[30] M. Li, X. Zhang, K. Matras-Postolek, H. Chen, P. Yang, J. Mater. Chem. C, 2018, 6, 5506.

[31] Y. Zhao, C. Xie, Y. Song, P. Yang, J. Nanopart. Res. 2020, 22, 147.

[32] M. Rong, X. Song, T. Zhao, Q. Yao, Y. Wang, X. Chen, J. Mater. Chem. C, 2015, 3, 10916.

[33] Y. P. Sun, B. Zhou, Y. Lin, W. Wang, K. A. Fernando, P. Pathak, M. J. Meziani, B. A. Harruff, X. Wang, JH. F. Wang, P. G. Luo, H. Yang, M. E. Kose, B. Chen, L. M. Veca, S. Y. Xie, J. Am. Chem. Soc., 2006, 128, 7756.

[34] X. Zhang, P. Wang, P. Yang, S. P. Jiang, Inter. J. Hydrog. Energy, 2020, 45, 21523-21531.

[35] L. Shi, Z. Li, K. Marcus, G. Wang, K. Liang, W. Niu, Y. Yang, Chem. Commun., 2018, 54, 3747.

[36] Y. Yang, S. Wang, Y. Jiao, Z. Wang, M. Xiao, A. Du, Y. Li, J. Wang, L. Wang, Adv. Funct. Mater., 2018, 1805698.

[37] H. Wang, L. Zhang, Z. Chen, J. Hu, S. Li, Z. Wang, J. Liu, X. Wang, Chem. Soc. Rev., 2014, 43, 5234.

Chapter 5: Spine-like g-C_3N_4 cages with superior photocatalytic performance*

Abstract

Layered graphitic carbon nitride (g-C_3N_4) material with its regularly assembled structure enables efficient transport of photogenerated charge carriers and effectively improves photo-catalytic properties. In this chapter, spine-like g-C_3N_4 cages are created for the first time via a new three-step synthesis method. Especially, the self-assembly of small layered precursors (using H^+ ions) via acid treatment process plays an important role for the caged shape formation of g-C_3N_4. Under acidic condition, formation of bondings between positively charged H^+ ions and negatively charged thin g-C_3N_4 precursors leads to decrease in surface energy. The precursors are subsequently assembled in the solution. The control of polymerization kinetics of the precursor assembly further results in the formation of spine-like g-C_3N_4 cages. The morphologies of the samples depend on the pH level of the solution, the concentration of precursor, and the condition used for thermal polymerization process (e.g. temperature). The caged nanostructure and relatively high specific surface area of the spine-like g-C_3N_4 enhance light scattering effect and carrier utilization efficiency, because relatively low conduction and valence band values affect the light response efficiency of the hollow g-C_3N_4 cages in visible light region and enhance the photocatalytic performances. The estimated H_2 evolution efficiency of hollow spine-like g-C_3N_4 cages is 4500 $\mu molg^{-1}h^{-1}$, which is 8.2 times higher than that of the bulk g-C_3N_4. In addition, the spine-like 3D g-C_3N_4 nanostructures show enhanced photocatalytic activity toward CO_2 reduction to CH_4 (0.71 $\mu molg^{-1}h^{-1}$) in contrast to the negligible photocatalytic CO_2 reduction performance of conventional 2D g-C_3N_4. Incorporation of Pt clusters as co-catalysts enhances the CH_4 generation rate of the 3D g-C_3N_4 nanostructures by 4 times (2.7 $\mu molg^{-1}h^{-1}$). Spine-like 3D g-C_3N_4 caged nanostructure possesses drastically increased number of active sites and negatively shifted conduction band in comparison with that of conventional 2D g-C_3N_4, which is favorable for photocatalytic reduction reactions. This study aims to develop novel strategies for synthesizing efficient 3D nanostructured g-C_3N_4 photocatalysts for H_2 generation and conversion of CO_2 to useful fuels

such as CH_4.

Reprinted (adapted) with permission from Xiao Zhang, Ping Yang, San Ping Jiang, Pt nanoparticles embedded spine-like g-C_3N_4 cages with superior photocatalytic activity for H_2 generation and CO_2 reduction, Nanotechnology, 2021, 32, 175401.

5.1 Introduction

Graphitic carbon nitride materials are commonly used as visible-light-driven photocatalysts for driving advanced oxidation/reduction processes, storage and harvest of renewable energy, and wastewater treatment [1-6]. To improve the photocatalytic performance of g-C_3N_4, morphology control has become a hot topic. However, it is extremely difficult to have a regular morphology for g-C_3N_4 because of its layered structural nature. Greenhouse gas CO_2 primarily produced by the combustion of fossil fuels is one of the key reasons that causes global climate change. The splitting of water to generate H_2 and the photocatalytic reduction of CO_2 into CH_3OH, CH_4 and CO are two of the most promising strategies for the generation of clean fuels [7]. To solve this issue, electrocatalysis is normally used with the addition of co-catalysts and sacrificial agent. Electrocatalysts such as, noble metal, semiconducting materials, and various hybrid composites have been developed [8]. In contrast, photocatalysis provides sufficient approaches for H_2 generation and CO_2 reduction due to the direct use of solar energy, especially for visible-light-driven applications. It is still challenging developing stable, highly efficient, and low cost visible-light-driven photocatalyst, and to bring the techniques to the market is of significant importance. Typical photocatalysts (e.g., TiO_2, MoS_2, WOx, and BiOX) have been studied widely. Among theses, carbon nitride (C_3N_4) and other carbon allotropes (as earth-abundant carbon-based materials) have been drawn considerable attention as popular substrate materials for photo- and photoelectro-catalysis in renewable energy conversion and production fields due to their unique physiochemical, optical, electric, and thermal properties.

Comparing with other metal-free semiconducting substrate materials (e.g. $BiVO_4$, TiO_2), 2D graphitic carbon nitride (g-C_3N_4) material (with decent visible-light response ability and high stability in acidic/basic environment) has an appropriate bandgap of around 2.7 eV and most negative conduction band value of -0.86 eV that is narrower than those of other metal-free

semiconducting materials [12, 13]. It is a promising material that can be used for organic dyes photocatalytic degradation and visible-light-driven photoelectro-chemical hydrogen generation [14-16]. However, the conventional 2D g-C_3N_4 with layered structures possesses certain disadvantages that can affect its photocatalytic performances. The flat 2D surface with its limitations in scattering and reflection effects is unfavorable for light harvesting processes [9]. Bulk semiconducting layered structure of g-C_3N_4 also affects the recombination rate of photo-generated charge carriers, which is unfavorable for improving photocatalytic quantum efficiency of the material. To overcome these limitations, efforts have been made on improving photocatalytic performances of g-C_3N_4-based materials by construction of g-C_3N_4-based heterostructures with interfacial electric fields and shortened diffusion pathway of photogenerated charge carriers [10, 11]. The microstructure of g-C_3N_4–based heterostructures is crucial for enhancing photocatalytic activities of the material by creating more defects and active sites and to achieve narrower bandgaps [11, 17].

Another effective strategy for enhancing photocatalytic activity of the g-C_3N_4 is the construction of three-dimensional (3D) g-C_3N_4 with high specific surface area or g-C_3N_4-based composites with various shapes and forms. 3D nanostructured g-C_3N_4 materials possess enhanced photocatalytic activity comparing with their conventional 2D g-C_3N_4 counterparts due to the presence of more active sites and defects in the system. Especially high specific surface area and less-bulky 3D g-C_3N_4 with novel shapes and forms possesses improved photocatalytic performances due to the enhanced light scattering effect and narrowed bandgaps. However, to synthesize 3D g-C_3N_4-based composite materials with specific shapes and forms is not easy due to the fact that 2D g-C_3N_4 tends to form layered or randomly stacked structures. Various hard and soft templating methods have been explored to synthesize flexible 3D porous nanostructured g-C_3N_4 with high surface area and shortened diffusion pathways [18-22]. For instance, Qian et. al. developed a NaCl assisted ball-milling method to fabricate 3D porous g-C_3N_4 in which NaCl particles were served as the template [18].

Template-free synthesis is another option to construct metal-free pristine g-C_3N_4 material with noval nanostrucutres. However, one of the obstacles that has to be surpassed is the tendency of C_3N_4 to form flat layered structure by stacking due to the fact that g-C_3N_4 itself is a 2D materials in nature. Substantial efforts have been made to synthesize randomly shaped

layered g-C_3N_4 nanostructures [23-29]. Xia et. al. synthesized a sheet-like carbon nitride crystal with randomly shaped sheet-like layered structures [23]. Xu and co-workers reported an edelweiss-like g-C_3N_4 assembled by macroscopic bunches of layered g-C_3N_4 [24]. Porous g-C_3N_4 with unsual shapes and irregular nanostructures has also been reported. Zeng et. al. synthesized a relatively bulky sea-urchin-structured g-C_3N_4 using porous g-C_3N_4 as precursor [26]. Han et. al. found a porous seaweed-like g-C_3N_4 with enhanced hydrogen generation efficiency [27]. Only very few of the examples of 3D carbon nitride with highly ordered less-bulky nanostructures were reported, especially with non-metal doping. Guo and co-workers revealed a hexagonal tubular carbon nitride with enhanced photocatalytic H_2 evolution activity in case of phosphorus doping [28]. Zheng et. al. reported a helical rod-like g-C_3N_4 (with unequal amount of right-handed and left-handed twisted nanorods) to have improved photocatalytic performances of the material [29]. It is obvious that controlled template-free formation of 3D g-C_3N_4 with less-bulky and highly ordered nanostructures is feasible but extremely difficult.

In this chapter, a new three-step synthesis method using combinations of hydrothermal, self-assembly and thermal condensation processes has been developed to construct new spine-like 3D g-C_3N_4 cages with enhanced photocatalytic activities comparing with its conventional 2D g-C_3N_4 counterparts. Such hollow spine-like g-C_3N_4 cages revealed significantly enhanced H_2 generation efficiency (4500 $\mu molg^{-1}h^{-1}$), which is 8.2 times higher than that of the bulk g-C_3N_4 catalysts. In particular, the newly developed hollow spine-like g-C_3N_4 cages with Pt clusters showed an unusually high photocatlaytic activity for CO_2 reduction to CH_4 and CO, achieving a high CH_4 production rate of 2.7 $\mu molg^{-1}h^{-1}$.

5.2 Experimental Section

5.2.1 Sample preparation

All chemicals including melamine, cyanuric acid, sulfuric acid (H_2SO_4), and chloroplatinic acid (H_2PtCl_6) were purchased from Sigma Aldrich and were used without further purification. Diluted H_2SO_4 solution (0.5 M) was used during sample preparation. A solution of 1 g of melamine, 0.1 g of cyanuric acid, and 50 mL deionized water was sonicated and placed in a hydrothermal autoclave to undergo a hydrothermal treatment process at 200 °C for 10 hours.

The obtained sample was precipitated and washed with water and ethanol for several times. The precipitation was ground with addition of diluted H_2SO_4 solution. The powder sample was then dispersed into deionized water to obtain a homogeneous suspension. The pH level of the obtained suspension was adjusted using diluted H_2SO_4 solution followed by stirring for 2 hours. The white precipitate was collected after centrifugation and drying. The obtained precipitate was then heated in a tube furnace for 3 hours at 650 °C with a ramp rate of 5 °C /min. To test the effect of varying preparation conditions, the calcination temperature has been adjusted from 600 to 700 °C. For comparison, bulk g-C_3N_4 was prepared by adding 4 g of melamine into a porcelain boat and heated up to 650 °C for 4 hours.

The deposition of Pt clusters in spine-like g-C_3N_4 cages was carried out via sonochemical synthetic method using an ultrasound oscillator (KQ-50E, 50 W). The as-prepared sample (10 mg) was dispersed into a mixture solution of ethanol and deionized H_2O with a volume ratio of 1:1. An ice bath was used during sonication treatment. After 10 min of sonication, 1 mL of 50 mM H_2PtCl_6 solution was added to the sample, and the mixture was treated under ultrasonic-wave irradiation for 1 hour. The obtained sample was then washed with deionized H_2O and ethanol followed by centrifugation.

5.2.2 Characterization

TEM images of the carbon nitride samples were collected using FEI Titan G2 80-200 TEM/STEM (FEI company, US). The SEM images of the samples were recorded using a scanning electron microscope (QUANTA 250 FEG). X-ray photoelectron spectroscopy spectra of the carbon nitride and composite samples were obtained on Kratos Axis Ultra DLD spectrometer with monochromatic AlKα X-rays operating at 150 W and by using a pass energy of 40 eV for high-resolution spectra collection and a pass energy of 160 eV for survey spectra. XRD measurements were performed on an X-ray diffractometer (Bruker D8, Germany) using Cu Kα radiation source. The UV-Vis diffuse reflectance and absorption measurements of the carbon nitride samples were performed on Hitachi U-4100 UV-Vis spectrophotometer. Hitachi F-4600 fluorometer (Japan) and Nicolet 380 FTIR spectrometer (Thermo, America) were used to obtain the fluorescence spectra and FTIR spectra. The specific surface area of the samples was examined by N_2 adsorption-desorption test using multi-functional adsorption instrument (MFA-140, Builder Company, China) to get pore size

distribution of samples using BET equation. Mott-Schottky measurement of samples was performed using a constant frequency of 10 Hz at 10 mV amplitude. Sample ink solution was casted on ITO glass followed by testing using potentials from -0.9 to 0.8 V without light irradiation.

Photocatalytic H_2 generation measurement was performed on a connected system of Pyrex top-irradiation reaction vessel with a glass-closed gas circulation. 10 mg of the sample was added to a 100 mL of triethanolamine aqueous solution (with triethanolamine to deionized water volume ratio to be 1:9) followed by sonication before light exposure. Evacuation was done on the testing system to remove air. A 300 W Xe lamp (with cutoff filter of $\lambda > 420$ nm) and gas chromatography (Shimadzu GC-7920，using nitrogen as carrier gas) were used to measure the H_2 evolved on hourly basis. Constant stirring of sample solution was maintained during testing. The stability of samples for hydrogen production was obtained by recording the amount of hydrogen generated for 10 cycles. The AQE of samples can be calculated using the equation shown below.

$$AQE = \frac{N_e}{N_p} = \frac{2 * M * N_A * h * c}{S * P * t * \lambda} * 100\% \quad (5\text{-}1)$$

Where, Ne and Np are the amount of reaction electrons and the incident photons, respectively. M and N_A are the amount of H_2 molecule and Avogadro constant, respectively. c is the speed of light, S is irradiation area, P is irradiation intensity, t is time, and λ is the wavelength of monochromatic light.

Photocatalytic CO_2 reduction measurement of samples was performed, and the data were analyzed using gas chromatography (Shimadzu GC-7920). 20 mg of sample was added into 15 mL of deionized water to obtain a homogeneous suspension. The CO_2 bubbling of sample solution was done with vigorous stirring for 20 min to remove air. A 300 W Xe lamp with a cut off filter of 420 nm was used as light source during CO_2 reduction.

Table 5-1. Preparation conditions and properties of g-C_3N_4 samples.

Sample	Precursor (mg)*[a]	H^+ treatment*[b]	Morphology
1	10	pH~1	Bended belt
2	20	pH~1	Spine-like
3	40	pH~1	Irregular spine-like
4	20	pH~2	Broad belt
5	20	pH~7	Belt network

*[a] Amount of precursors added in the self-assembly process in acidic solutions.
*[b] The pH level of acidic solutions used in self-assembly process.

5.3 Results and Discussion

5.3.1 Microstructure

Nanostructured spine-like g-C_3N_4 cages were synthesized via a novel three-step synthetic method. Layered 2D g-C_3N_4 precursor can be obtained via hydrothermal treatment of a mixture of melamine, cyanuric acid and deionized water at 200 °C [22]. After grinding, the layered precursors were precipitated and re-dispersed in a H_2SO_4 solution to finalize the self-assembly process. With the presence of positively charged H^+ ions, H^+ intercalation into the layered structure of g-C_3H_4 takes place. The as-treated precursors with different concentrations of precursor and pH levels used were then heat-treated in a furnace to undergo thermal condensation at different temperatures (ranging from 600 to 700 °C). The results show that the best thermal condensation temperature for the formation of spine-like 3D g-C_3N_4 was 650 °C and with a ramp rate of 5 °C/min. The preparation conditions of samples are illustrated in Table 5-1. Scheme 5-1 shows the three-step synthetic processes for the construction of g-C_3N_4 samples with different morphologies.

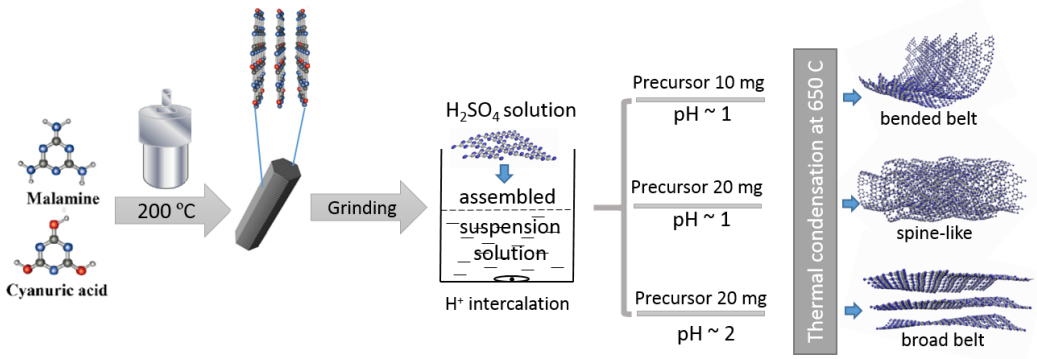

Scheme 5-1. Formation mechanism of g-C_3N_4 samples with different morphologies.

Fig. 5-1 shows the SEM images of the precursor and g-C_3N_4 samples synthesized using different preparation conditions. The g-C_3N_4 precursors synthesized via hydrothermal treatment at 200 °C are layered rod precursors (Fig. 5-1a), which is also in consistency with those reported in literature papers [30-32]. During the hydrothermal process, self-assembly of melamine and hydrolyzed cyanuric acid occurs. The rod precursor has large inter-lamellar spacing and there exists abundant functional groups (e.g., -NH_2, -OH) present in between the tri-s-triazine layers [22]. The addition of limited amount of cyanuric acid is crucial for increasing inter-lamellar spacing and to increase the amount of functional groups present in the g-C_3N_4 network. By grinding and dispersing the layered g-C_3N_4 powder into a diluted H_2SO_4 solution, H^+ ions can be easily intercalated into the layered structure of the precursors via formation of hydrogen bondings with the functional groups (e.g., -OH) present in between the tri-s-triazine layers. The assembled precursors were then thermally polymerized at 650 °C to obtain the g-C_3N_4 nanostructures with various morphologies. In addition, g-C_3N_4 nanotube shaped product with relatively smooth surface can be obtained after direct thermal condensation treatment (as shown in Fig. 5-1b).

It is obvious that the amount of precursors and pH level utilized for synthesis have a significant impact on the self-assembly process thus directly affecting the morphology of the final g-C_3N_4 product. Surface energy of the sample decreased due to the formation of hydrogen bonding between H^+ ions and the functional groups in the precursor. The nucleation and growth processes resulted in the formation of a belt-like structure at the beginning of the thermal polymerization stage. Monomers were then further deposited onto the edges of the g-C_3N_4 belt. Layered g-C_3N_4 sheets generally have the tendency of forming a scroll-like shape during high-temperature thermal condensation treatment. In case of addition of limited amount of precursor, the growth of sample occurs only along the edges of the g-C_3N_4 belt, and a bended belt-like sample was formed (sample 1, Fig. 5-1c and 1d). By increasing the amount of precursors used to 20 mg, the bended belt-like sample was able to form a spine-like caged shape due to the rolling-up tendency of the material (sample 2, Fig. 5-1e and 1f). By increasing the amount of precursor used further (sample 3), a nucleation and growth process occurs on the sample accompanied by the rolling-up mechanism. The spine-like cage morphology observed for sample 3 became relatively irregularly-shaped (Fig. 5-1g and 1h).

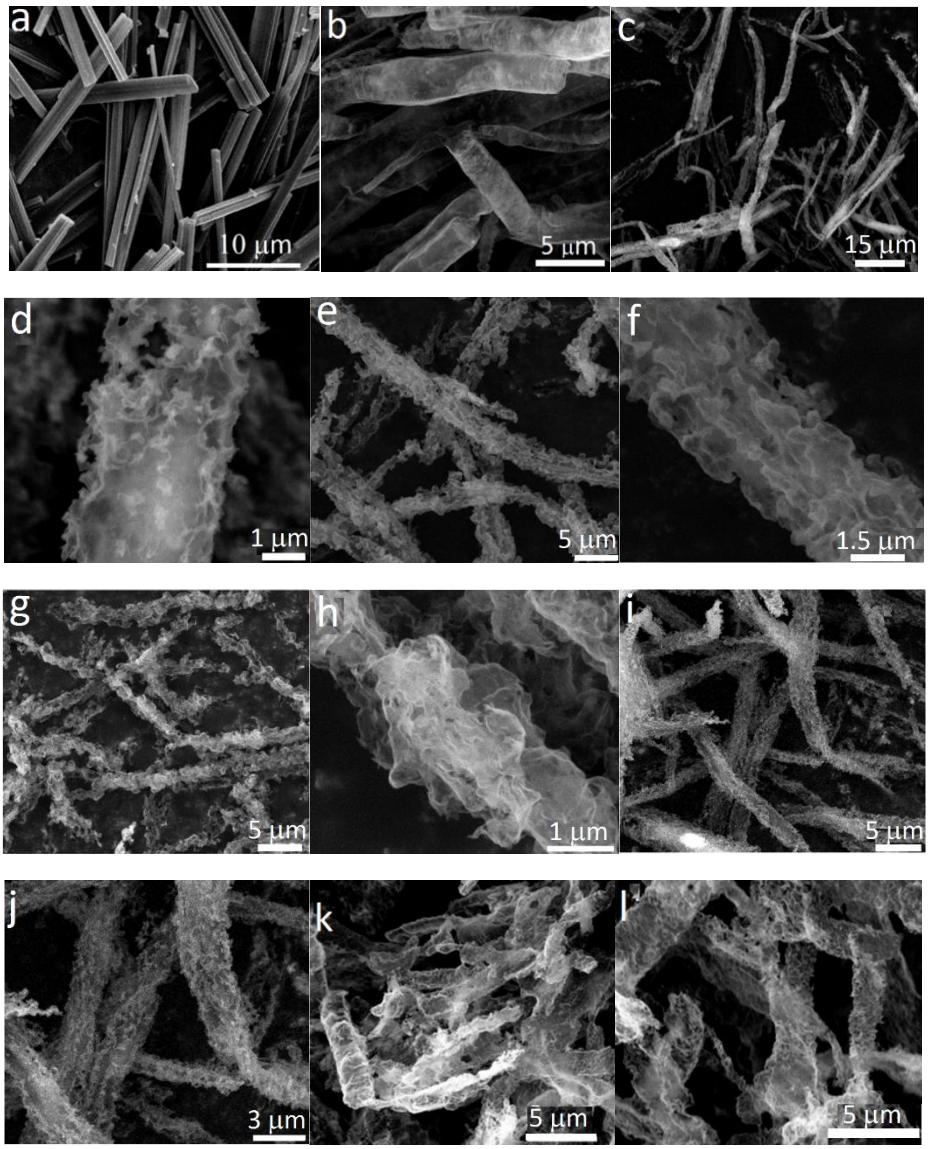

Figure 5-1. SEM images of g-C_3N_4 precursors before (a) and after (b) thermal condensation treatment with no grinding and no H_2SO_4 treatment, and g-C_3N_4 samples prepared with different amount of precursors and different pH level. (c, d) 10 mg of precursor at pH=1; (e, f) 20 mg of precursor at pH=1; (g, h) 40 mg of precursor at pH=1; (i, j) 20 mg of precursor at pH=2; (k, l) 20 mg of precursor at pH=7.

In addition, the pH of H_2SO_4 solutions plays a key role in control of the morphology of g-C_3N_4. When pH level of the solution is around 2, the amount of H^+ ions present in the solution was insufficient to neutralize all the negatively charged ions on the precursors, and only partial assembly of the precursors was achieved. The g-C_3N_4 formed in this case has a broad belt-like morphology (sample 4, Fig. 5-1i and 1j). In case of pH level to be around 7 (in which no assembly occurred), a nanosheets structured g-C_3N_4 was retained (sample 5, Fig. 5-1k and 1l).

These results also indicate that self-assembly process in H_2SO_4 solution plays a key role for

formation of spine-like caged g-C_3N_4. The variation of microstructure from bended belt, spine-like, to belt network is related to the concentration of rod-like g-C_3N_4 precursor and the pH level of the assembly. It is obvious that three-step synthesis method in this study offers the possibility of control and manipulate the microstructure of g-C_3N_4 catalysts.

5.3.2 Phase and composition analysis

Fig. 5-2 shows the X-ray diffraction (XRD) patterns and Fourier transform infrared spectroscopy (FTIR) spectra of g-C_3N_4 samples obtained during different stages of the synthetic process. The XRD peak at 10.8° for hexagonal rods precursor shows a relatively high intensity due to its rod-like morphology nature (Fig. 5-2a). A decrease in intensity of this peak was observed after grinding. For the H_2SO_4 treated precursors, the peak at 10.8° almost disappeared. In addition, huge differences in XRD peak intensities can be observed for the pH adjusted precursors (pH ~ 7) and the pristine hexagonal rods precursor. Moreover, the intensity of peak at around 27º drastically increased after pH adjustment. This demonstrates that a change in precursor microstructure occurred after pH adjustment. For the H_2SO_4 treated precursor with pH level to be around 1, the XRD peak at 18º has the highest intensity (Fig. 5-2a). Although no matched data were found, the appearance of the high intensity peak at 18º is most likely due to the intercalation of H^+ ions into the layered rod-like precursors.

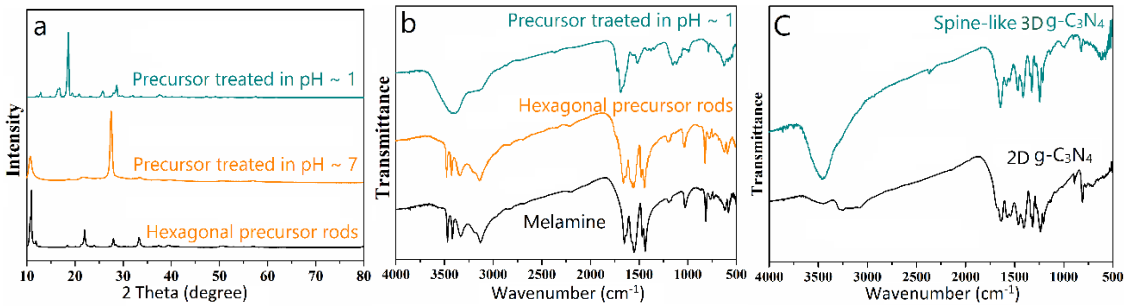

Figure 5-2. XRD patterns and FTIR spectra of the g-C_3N_4 samples. (a) XRD patterns of precursors prepared using different synthetic conditions. (b) FTIR spectra of precursors prepared using different synthetic conditions. (c) FTIR spectra of g-C_3N_4 samples.

The FTIR spectra of the precursors and the g-C_3N_4 samples are shown in Fig. 5-2b and 2c. Fig. 5-2b shows that the hexagonal rods precursor sample has the vibration peaks of both melamine molecule and cyanuric acid molecule [28]. The vibration peaks of the hexagonal rods precursor sample related to the primary amines at 3475 and 3425 cm^{-1} were shifted in comparison with the peak position of melamine (3390.5 cm^{-1}). The N-H deformation vibration

was shifted to 1666 cm^{-1} from 1649 cm^{-1}. Moreover, the C=O vibration peaks from cyanuric acid molecule was shifted from 1670 cm^{-1} to 1749 cm^{-1}. It is obvious that thermal condensation occurring at 200 °C leads to structural change of the hexagonal rods precursor causing the structure of the precursor rods to be different from that of both melamine and cyanuric acid. In case of H_2SO_4 treatment, a clear change in FTIR spectra was observed for the sample prepared via acid treatment (Fig. 5-2b). The vibration bands corresponding to melamine and cyanuric acid molecules almost disappeared. This confirms successful self-assembly of the precursors, meanwhile successful intercalation of the positively charged H^+ ions into the interlayer spaces between the g-C_3N_4 layers [23]. The stretching vibration band is due to the presence of azine unit and carbon-nitrogen heterocyclic ring. The symmetric stretching vibration and antisymmetric stretching vibration of the amino group located at 818, 1167-1804 cm^{-1} and high wavenumber region were observed for all samples. Due to the spine-like morphology nature of the spine-like g-C_3N_4 sample, the intensity of stretching vibration band related with the symmetric vibration of the amino group decreased whereas the antisymmetric amino groups stretching vibration increased (Fig. 5-2c). A drastically enhanced -OH stretch band was observed (~3300 -3400 cm^{-1}) for spine-like g-C_3N_4 sample. The structural and property change occurred on spine-like g-C_3N_4 may also lead to improvement in photocatalytic efficiency of the material [29].

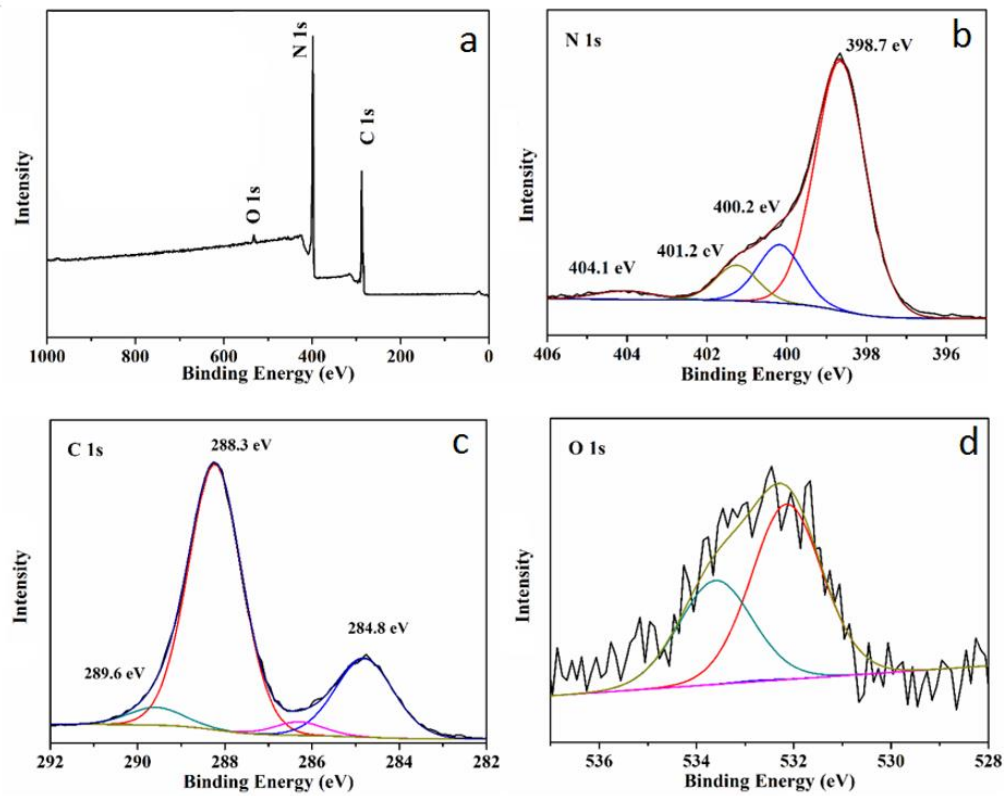

Figure 5-3. XPS spectra of spine-like g-C_3N_4 (Sample 2). (a) Survey spectra. (b) N 1s spectrum. (c) C 1s spectrum. (d) O 1s spectrum. The inset in (a) shows S 2p spectrum.

Fig. 5-3 shows the X-ray photoelectron spectroscopy (XPS) spectra of spine-like g-C_3N_4 (Sample 2). N 1s, C 1s, and O 1s spectra are shown in Fig. 5-3b to 3d. The survey spectrum in Fig. 5-3a confirms the existence of C, N, and trace amount of O in the sample. Fig. 5-3b shows the N 1s spectrum which was fitted into four peaks corresponding to C-N=C (398.7 eV, pyridinic-N), N-$(C)_3$ (400.2 eV, pyrrolic-N), N-H groups (401.2 eV, graphitic-N) and π-excitation (404.1 eV). The C 1s spectrum in Fig. 5-3c has four peaks corresponding to C-C (sp2 hybridized carbon, 284.8 eV), C-O-C and C-OH (epoxy/hydroxyls, 286.24 eV), C-N (288.3 eV), and C=N/C=O (289.6 eV) peaks. The existence of C-O-C peak (286.24 eV) suggests that the surface of the g-C_3N_4 sample was oxidized to certain extent. The O 1s spectrum shown in Fig. 5-3d has two weak peaks which was fitted into two peaks at 532.1 and 533.6 eV corresponding to O-H and C-O bond, respectively. This is due to the trace amount of H_2O and C-OH anchored on the sample surface during the polymerization of cyanuric acid and melamine [28]. The preparation conditions (e.g., starting materials and temperature settings) dependent C/N ratios of the g-C_3N_4 samples can affect the photo-/electro-catalytic properties

of the sample due to the distillation of N at higher temperatures [11]. The C/N molar ratio of sample 2 obtained from XPS analysis is around 0.74 which is close to the stoichiometric ratio of C_3N_4 molecules.

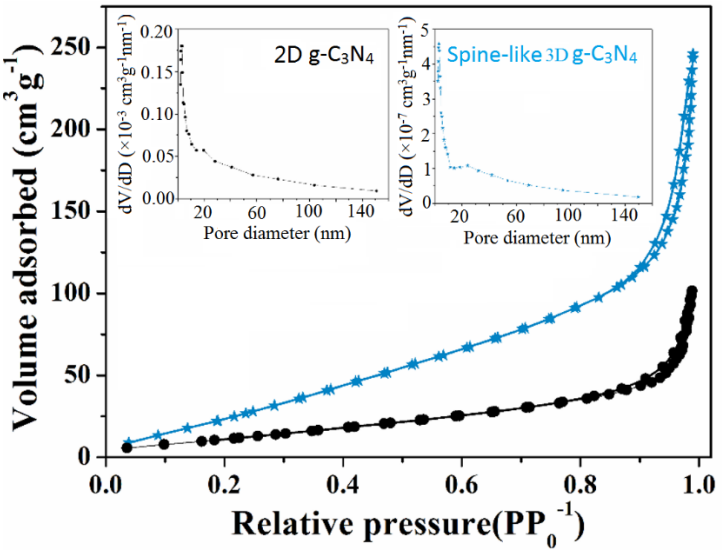

Figure 5-4. Nitrogen adsorption-desorption isotherm curves of bulk g-C_3N_4 and spine-like g-C_3N_4 (sample 2). The insets show the distribution of average pore size of samples.

The specific surface area of sample 2 was characterized using Brunauer-Emmett-Teller (BET) analysis as shown in Fig. 5-4. The adsorption-desorption curves demonstrate the two g-C_3N_4 samples to have type VI mesoporous structure [30]. The specific surface area of bulk and spine-like g-C_3N_4 are 40.6 and 120.1 m^2g^{-1}, respectively. The surface area of spine-like g-C_3N_4 cages is 2 times as high as that of bulk g-C_3N_4. The average pore sizes of bulk g-C_3N_4 and spine-like g-C_3N_4 cages are 20.1 and 25.3 nm, respectively. The spine-like g-C_3N_4 cages with higher specific surface area and larger pore size are able to provide more active sites for forming bondings with other reagents, thus improving photocatalytic performances [31].

Fig. 5-5 shows the $(\alpha h\nu)^{1/2}$ vs photon energy plots and photoluminescence (PL) spectra of 2D g-C_3N_4 and spine-like g-C_3N_4 cages (sample 2). The plots in Fig. 5-5a were obtained from UV-Vis diffuse reflectance spectra using the transformed Kubelkae Munk function $(A(h\nu-E_g)r = \alpha h\nu)$. [32] According to the UV-Vis diffuse reflectance spectra and Mott-Schottky analysis, the bandgap of samples was estimated to be 2.62 eV. The PL spectra in Fig. 5-5b reveals that the PL peaks of spine-like g-C_3N_4 cages (sample 2) with lower intensity were redshifted compared with that of bulk g-C_3N_4 (in which a blue-emission PL peak can be observed at around 477

nm). The reduced PL intensity observed for the spine-like g-C_3N_4 (sample 2) indicates the sample to have more active sites, which favours the separation of photo-generated charge carriers thus causing decrease in radiative recombination rate. Moreover, the redshift occurred for the PL spectrum of spine-like g-C_3N_4 sample is due to the surface functional group change caused by the assembly process in the H_2SO_4 treatment step [33].

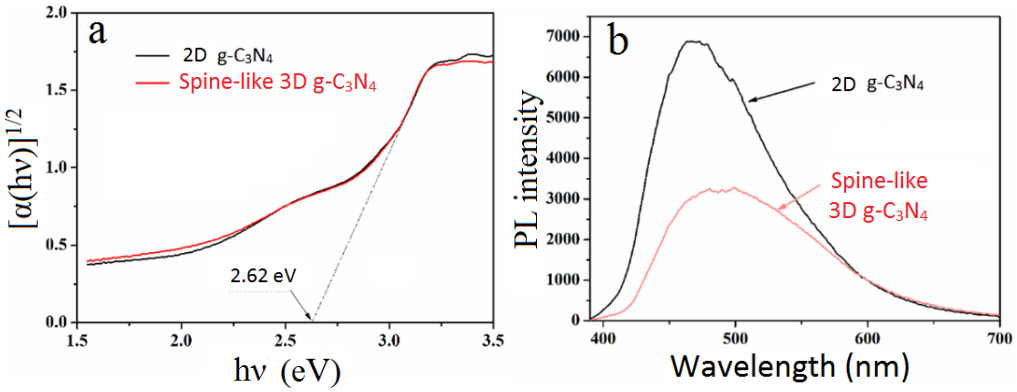

Figure 5-5. (a) UV-Vis diffuse reflectance spectra and (b) PL spectra of bulk g-C_3N_4 and spine-like g-C_3N_4 (sample 2).

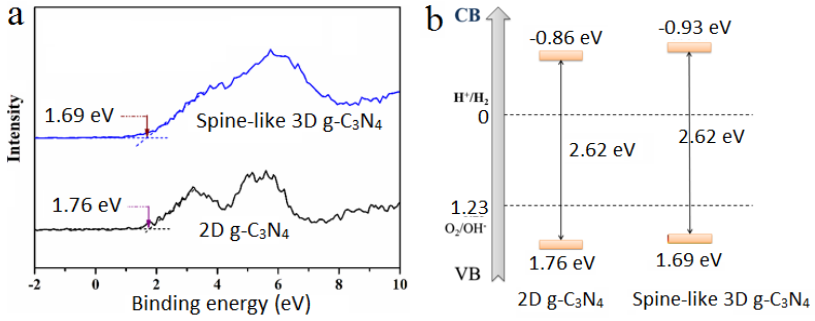

Figure 5-6. (a) XPS band gap spectra and (b) schematic illustration of band gap of bulk g-C_3N_4 and spine-like g-C_3N_4 cages (sample 2).

To further study the band gaps of the samples, XPS valence band spectra were collected. Fig. 5-6 shows the XPS valence band spectra and schematic illustration of bandgaps of bulk g-C_3N_4 and spine-like g-C_3N_4 cage samples (sample 2). The valence band of bulk g-C_3N_4 and spine-like g-C_3N_4 cages were estimated to be 1.76 and 1.69 eV, respectively; while their conduction band were determined to be -0.86 and -0.93 eV, respectively. Change in conduction band and valence band positions confirms the microstructural change occurred on spine-like g-C_3N_4 cages in comparison with the conventional bulk g-C_3N_4. Theoretically, spine-like g-C_3N_4 cages with its relatively more negative conduction band position (compared with that of the bulk g-C_3N_4) might favour photocatalytic reduction reactions.

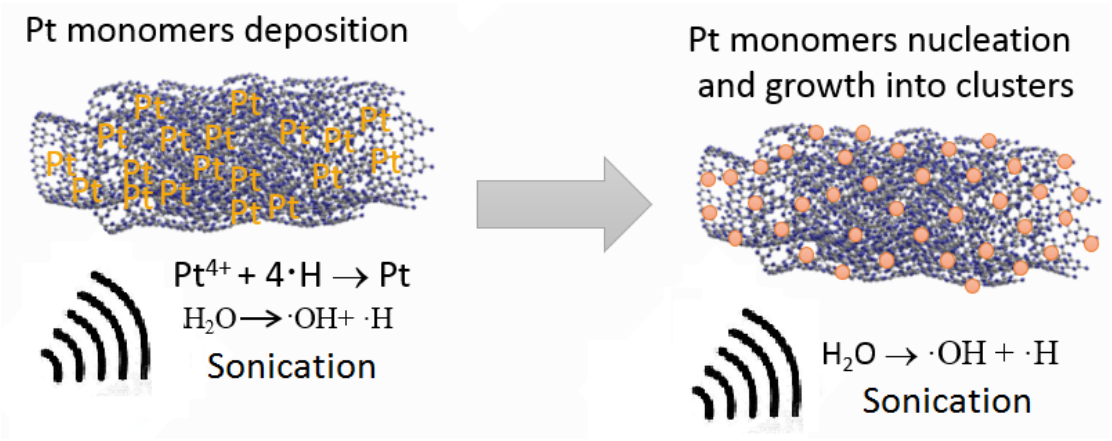

Scheme 5-2. Illustration of construction of Pt clusters embedded spine-like g-C_3N_4 via sonication.

5.3.3 Deposition of Pt clusters

To further expand the applicability of nanostructured spine-like g-C_3N_4 cages, Pt clusters were decorated in g-C_3N_4 via ultrasonic-wave irradiation. Scheme 5-2 illustrates the formation of Pt clusters using the sonochemical method. Ultrasonic irradiation with and without accelerator have been used to synthesize Pt nanoparticles [34-37]. Pt clusters were prepared using ultrasonic irradiation without accelerator [13]. Two types of reducing agents (·H atoms and electrons) were generated during sonication, among which ·H atoms were generated from sonolysis of water (eq. 5-2). The reaction takes place in the inside of the cavitation bubbles or in the aqueous solution, as well as on the interface between the cavitation bubbles and the solution. The ·H atoms created in the collapsing cavitation bubbles react with the Pt^{4+} ions to form Pt^0. The reaction equations are listed as shown below.

$$H_2O \rightarrow \cdot H + \cdot OH \quad (5\text{-}2)$$

$$Pt^{4+} + 4\cdot H \rightarrow Pt^0 + 4\,H^+ \quad (5\text{-}3)$$

$$nPt^0 \rightarrow Pt_n \quad (5\text{-}4)$$

Due to the fact that only very limited amount of ·H can be formed in solution, Pt clusters rather than Pt nanoparticles were formed in the sample. The caged structure of spine-like g-C_3N_4 helps to retain homogeneous distribution of the metal clusters in the samples.

Fig. 5-7 shows the TEM and SEM images of Pt-loaded spine-like g-C_3N_4 before and after sonication treatment. Comparing with the TEM images of the pristine g-C_3N_4 sample (before sonication treatment with Pt) in Fig. 5-7a, the lattice fringes of Pt clusters were clearly observed in Fig. 5-7b, suggesting homogeneous Pt deposition on g-C_3N_4 with no obvious chunky Pt

particles observed in the specimen. The spine-like morphology of the sample remained unchanged after metal deposition as shown in Fig. 5-7c. The inset in Fig. 5-7c shows the Pt 4f spectrum of Pt cluster loaded spine-like g-C_3N_4 cage sample. The peaks at 73.04, 75.01, 76.39, and 78.76 eV confirm the presence of Pt clusters in the spine-like g-C_3N_4 sample. The Pt ratio estimated was 0.1 wt% (obtained via XPS analysis).

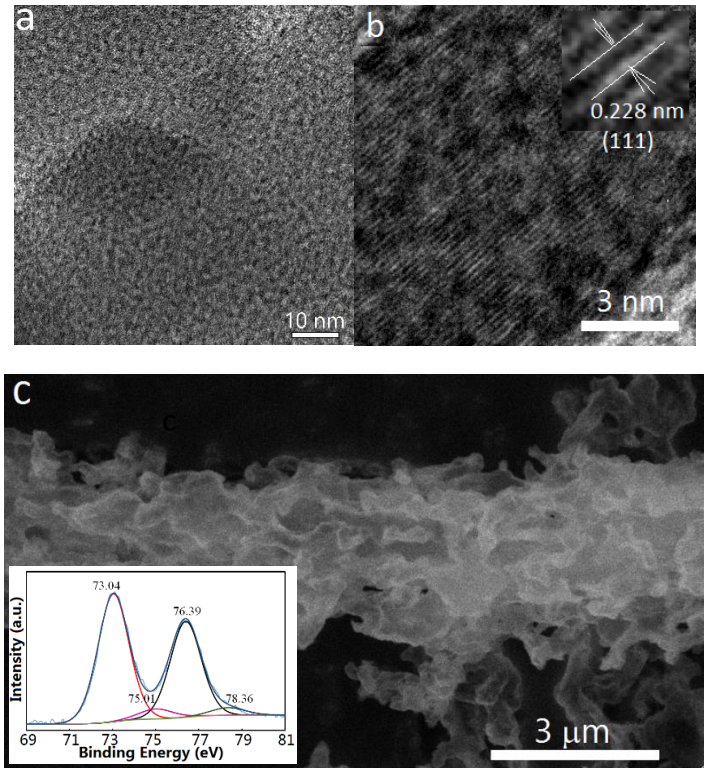

Figure 5-7. (a) TEM image of spine-like 3D g-C_3N_4 cages before Pt clusters embedding. (b) TEM images of Pt deposited spine-like 3D g-C_3N_4 cages. (c) SEM image of Pt deposited spine-like g-C_3N_4 cages. The inset in (b) shows an enlarged TEM image of Pt area with the lattice spacing of 0.228 nm corresponding to the (111) facet of Pt. The inset in (c) shows Pt 4f spectrum of Pt clusters deposited spine-like g-C_3N_4 cages.

5.3.4 Photocatalytic activity

The photocatalytic and photoelectrochemical activities of spine-like g-C_3N_4 and Pt-g-C_3N_4 were assessed through photocatalytic hydrogen evolution and photocatalytic reduction of CO_2 and the results are shown in Fig. 5-8. The H_2 evolution rate of spine-like g-C_3N_4 cages (sample 2) was estimated to be 4500 $\mu molg^{-1}h^{-1}$ which is 8.2 times higher than that of bulk g-C_3N_4 sample (547 $\mu molg^{-1}h^{-1}$) (shown in Fig. 5-8a). Apparent quantum efficiency (AQE) of spine-like 3D g-C_3N_4 nanostructure is relatively high (~ 4.2 % up to 500 nm) due the activation of n-π^* electron transition [30]. Moreover, spine-like g-C_3N_4 revealed relatively high H_2 generation

stability with the H_2 evolution rate remained almost unchanged after 10 cycles. This can be ascribed to the bandgap change (to a relatively negative value for both valence band and conduction band) of the spine-like g-C_3N_4 nanostructure, which is beneficial for photocatalytic reduction reactions. Fig. 5-8b and 8c show the CO and CH_4 evolution performances of the g-C_3N_4 samples during the photocatalytic CO_2 reduction measurement. Fig. 5-8d shows the generation efficiency of CO and CH_4 of samples. Conventional bulk g-C_3N_4 sample exhibited a CO evolution rate of 2.83 $\mu molg^{-1}h^{-1}$, however, negligible activity for CO_2 reduction to CH_4 was observed.

In contrast, spine-like 3D g-C_3N_4 nanostructures show a much higher photocatalytic activity for CO_2 reduction to CO with a CO production rate of 5.7 $\mu molg^{-1}h^{-1}$, and also an enhanced photoreduction activity for the CO_2 conversion to CH_4 (with a CH_4 generation rate of 0.71 $\mu molg^{-1}h^{-1}$). The photocatalytic CO_2 reduction experiment was performed without using any sacrificial agent or co-catalyst. The enhanced photocatalytic activity for CO_2 reduction to CH_4 observed on pristine spine-like 3D g-C_3N_4 nanostructures is due to the shift in valence band and conduction band position, as well as due to the unique 3D caged spine-like nanostructures that results in increased number of defects in the structure. Defects are known to play a dominant role in photocatalytic processes. [38, 39].

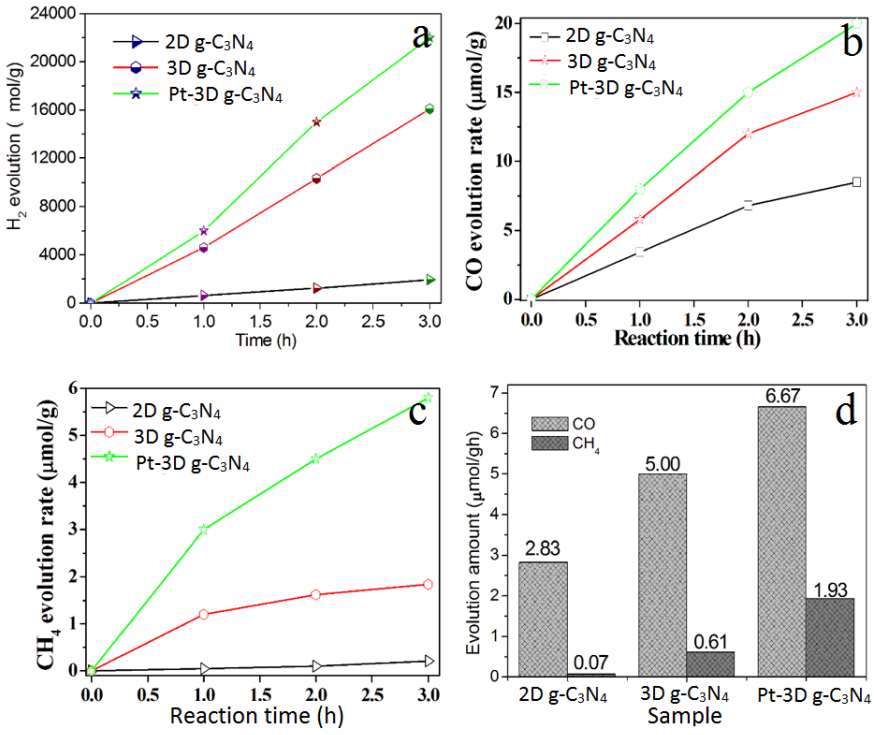

Figure 5-8. (a) Photocatalytic hydrogen evolution plots of different samples under visible light

irradiation (≥ 420 nm). (b) Photocatalytic reduction of CO_2: the CO evolution rate of samples under illumination at 420 nm. (c) Photocatalytic reduction of CO_2: the CH_4 evolution rate of samples under illumination at 420 nm. (d) CO and CH_4 evolution rate plots of samples.

The photochemical performance of Pt deposited spine-like g-C_3N_4 cages was remarkably enhanced. With the loading of Pt clusters, the H_2 evolution rate of 3D Pt-g-C_3N_4 nanostructures increased to ~6000 $\mu molg^{-1}h^{-1}$, a 25 % increase in H_2 evolution rate was observed compared to that of pristine spine-like 3D g-C_3N_4 sample. Addition of Pt cluster has significant effects on the photoreduction activity for the CO_2 reduction to CH_4. The Pt cluster decorated spine-like g-C_3N_4 has a CH_4 evolution rate of 2.7 $\mu molg^{-1}h^{-1}$ that is almost 4 times as much as that of the pristine spine-like g-C_3N_4 nanostructures. For the CO_2 reduction to CO, the CO evolution rate reached 6.67 $\mu molg^{-1}h^{-1}$ on 3D Pt-g-C_3N_4 nanostructures, which is 18 % higher than that on pristine spine-like g-C_3N_4 nanostructures (5.7 $\mu molg^{-1}h^{-1}$). According to the density functional theory analysis, the C–N, C=O, and -OH groups in layered g-C_3N_4 structure cause the shift of d-band center of Pt towards Fermi level, resulting in high stability of adsorbates (Pt in this case) and thus enhancing the catalytic performances of the material [26, 40]. The results indicate that the presence of Pt clusters as co-catalysts substantially enhances the selectivity of 3D Pt-g-C_3N_4 nanostructures for the photoreduction of CO_2 to CH_4, demonstrating a viable route for the development of efficient 3D nanostructured g-C_3N_4 photocatalysts for conversion of CO_2 to useful fuels such as CH_4.

5.4 Conclusions

Nanostructured spine-like 3D g-C_3N_4 nanostructures were synthesized by using a three-step synthetic method involving hydrothermal, self-assembly and H^+ intercalation, as well as thermal condensation processes at high temperatures. The grinding and H_2SO_4 treatment have decisive effects on the microstructure of g-C_3N_4 formed after the thermal condensation step at 650 °C. With the utilization of acid treatment, the microstructure of g-C_3N_4 after thermal condensation treatment at 650 °C was characterized to have bended belt-like shape with solid core surrounded by highly porous and fine fibers to form the spine-like 3D nanostructures, depending on the precursor concentration and pH level of the suspension solution utilized. The formation of unique microstructure of g-C_3N_4 is evidently related to the intercalation of H^+ ions

(derived from H_2SO_4) into the layered structure of g-C_3N_4 precursor via formation of hydrogen bondings with the functional groups (e.g. -OH) present in between the tri-s-triazine layers.

The nanostructured spine-like 3D g-C_3N_4 nanostructures have a relatively high specific surface area, and shift in the conduction band and valence band positions (compared with that of the conventional 2D g-C_3N_4) was observed. The spine-like 3D g-C_3N_4 caged nanostructure possesses significantly increased number of active sites and negatively shifted conduction band position. Moreover, the 3D g-C_3N_4 nanostructures showed a drastically enhanced photocatalytic activity for H_2 generation with a H_2 generation rate of 4500 $\mu molg^{-1}h^{-1}$ that is 8.2 times higher than that on conventional 2D g-C_3N_4. Spine-like 3D g-C_3N_4 nanostructures also showed decent CO_2 photoreduction activity to CH_4 with the CH_4 evolution rate determined to be 0.71 $\mu molg^{-1}h^{-1}$. In addition, the incorporation of Pt cluster on spine-like 3D g-C_3N_4 can substantially enhance the selectivity of the photoreduction performance of 3D Pt-g-C_3N_4 nanostructures for CO_2 reduction to CH_4, achieving an excellent CH_4 evolution efficiency of 2.7 $\mu molg^{-1}h^{-1}$.

5.5 References

[1] G. Zhao, Y. L. Cheng, Y. Z. Wu, X. J. Xu, X. P. Hao, Small, 2018, 14, 1704138.

[2] C. Jia, X. Zhang, K. Matras-Postolek, B. Huang, P. Yang, Carbon, 2018, 139, 415-426.

[3] T. Dong, X. Zhang, P. Wang, H. S. Chen, P. Yang, Electrochimica Acta, 2020, 338, 135885.

[4] S. Cao, J. Low, J. Yu, M. Jaroniec, Adv. Mater., 2015, 27, 2150–2176.

[5] X. Zhang, P. Wang, P. Yang, S. P. Jiang, Inter. J. Hydrog. Energy, 2020, 45, 21523-21531.

[6] Y. Wei, X. Zhang, Y. Liu, C. Jia, P. Yang, Electrochimica Acta, 2020, 349, 136366.

[7] X. X. Zou, Y. Zhang, Chem. Soc. Rev., 2015, 44, 5148-5180.

[8] Y. Yan, B.Y. Xia, Z.C. Xu, X. Wang, ACS Catal., 2014, 4, 1693-1705.

[9] X. Li, J. Yu, M. Jaroniec, Chem. Soc. Rev., 2016, 45, 2603–2636.

[10] F. Chen, Z. Y. Ma, L. Q. Ye, T. Y. Ma, T. R. Zhang, Y. H. Zhang, H. W. Huang, Adv. Mater., 2020, 1908350.

[11] X. Zhang, S. He, S. Jiang, Carbon, 2020, 156, 488-498.

[12] X. Wang, K. Maeda, A. Thomas, K. Takanabe, G. Xin, J. Carlsson, K. Domen, M. Antonietti, Nat. Mater., 2009, 8, 76–80.

[13] X. Zhang, J. P. Veder, S. He, S. P. Jiang, Chem. Comm., 2019, 55, 1233-1236.

[14] Y. Wei, X. Zhang, Z. Liu, H.nS. Chen, P. Yang, J. Power Sources, 2019, 425, 17–26.

[15] Z. Chen, X. Yu, Q. Zhu, T. Fan, Q. Wu, L. Zhang, J. Li, W. Fang, X. Yi, Carbon, 2018, 139, 189-194.

[16] X. Yu, T. Fan, W. Chen, Z. Chen, Y. Dong, H. Fan, W. Fang, X. Yi, Carbon, 2019, 144, 649-658.

[17] X. Li, J. Yu, J. Low, Y. Fang, J. Xiao, X. Chen, J. Mater. Chem. A 2015, 3, 2485–2534.

[18] X. Qian, X. Meng, J. Sun, L. Jiang, Y. Wang, J. Zhang, X. Hu, M. Shalom, J. Zhu, ACS Appl. Mater. Interfaces, 2019, 11, 27226−27232.

[19] M. Ai, J-W. Zhang, R. Gao, L. Pana, X. Zhang, J. J. Zou, Appl. Cata. B: Environ., 2019, 265, 117805.

[20] J. Duan, S. Chen, M. Jaroniec, S. Z. Qiao, ACS Nano, 2015, 9, 931−940.

[21] M. Zhang, J. Xu, R. Zong, Y. Zhu, Appl. Catal. B: Environ., 2014, 147, 229−235.

[22] Y. Xiao, G. Tian, W. Li, Y. Xie, B. Jiang, C. Tian, D. Zhao, H. Fu, J. Am. Chem. Soc., 2019, 141, 2508−2515.

[23] P. Xia, M. Antonietti, B. Zhu, T. Heil, J. Yu, S. Cao, Adv. Funct. Mater., 2019, 1900093.

[24] J. Xu, H. Wang, C. Zhang, X. Yang, S. Cao, J. Yu, M. Shalom, Angew. Chem. Int. Ed., 2017, 56, 8426 –8430.

[25] T. Dong, X. Zhang, P. Wang, H. S. Chen, P. Yang, Carbon, 2019, 149, 222-233.

[26] Y. Zeng, H. Li, J. Luo, J. Yuan, L. Wang, C. Liu, Y. Xia, M. Liu, S. Luo, T. Cai, S. Liu, J. C. Crittenden, Appl. Cata. B: Environ., 2019, 249, 275–281.

[27] Q. Han, B. Wang, Y. Zhao, C. Hu, L. Qu, Angew. Chem. Int. Ed., 2015, 54, 11433 –11437.

[28] S. Guo, Z. Deng, M. Li, B. Jiang, C. Tian, Q. Pan, H. Fu. Angew. Chem. Int. Ed., 2016, 55, 1830 –1834.

[29] Y. Zheng, L. Lin, X. Ye, F. Guo, X. Wang, Angew. Chem. Int. Ed., 2014, 53, 11926 –11930.

[30] Z. G. Liu, G. Wang, P. Yang, J. Ind. Eng. Chem., 2018, 66, 262-268.

[31] Z. G. Liu, G. Wang, H. S, Chen, P. Yang, Chem. Commun., 2018, 54, 4720.

[32] Z. X. Jiang, X. Zhang, H. S. Chen, X. Hu, P. Yang, ChemCatChem, 2019, 11, 4558.

[33] J. Barrio, L. H. Lin, P. Amo-Ochoa, J. Tzadikov, G. M. Peng, J. W. Sun, F. Zamora, X. C. Wang, M. Shalom, Small, 2018, 13, 1800633.

[34] Y. Wei, X. Zhang, Z. Zhao, H. S. Chen, K. Matras-Postolek, B. Wang, P. Yang, Electrochimica Acta, 2019, 297, 553-563.

[35] Z. X. Jiang, X. Zhang, J. P. Wang, L. Chen, H. S. Chen, P. Yang, Chem. Commun., 2018, 54, 13519.

[36] L. Hao, L. Kang, H. W. Huang, L. Q. Ye, K. L. Han, S. Q. Yang, H. J. Yu, M. Batmunkh, Y. H. Zhang, T. Y. Ma, Adv. Mater., 2019, 31, 1900546.

[37] Xueling Song, Xiao Zhang, Ping Yang, RSC Adv., 2016, **6**, 107433 – 107441.

[38] Y. Zheng, Y. Lyu, C. Xie, R. Wang, L. Tao, H. Wu, H. Zhou, S. Jiang, S. Wang, 2018 Adv. Mater., 30, 1801773.

[39] J. Zheng, Y. Lyu, R. Wang, C. Xie, H. Zhou, S. Jiang, S. Wang, 2018, Nat. Commun., 9, 3572.

[40] J. W. Fu, B. C. Zhu, C. J. Jiang, B. Cheng, W. You, J. G. Yu, Small, 2017, 13, 1603938.

Chapter 6: $WO_x(WS_2)/g\text{-}C_3N_4$ layered heterostructures with controlled crystallinity towards superior photocatalytic degradation and H_2 generation*

Abstract

WO_x nanobelts are grown in-situ on ultrathin g-C_3N_4 nanosheets to create WO_x/ g-C_3N_4 layered heterostructures. Amorphous and crystalline thin g-C_3N_4 nanosheets are produced by adjusting thermal polycondensation process of the precursors. Horizontal growth of WO_x nanobelts occurs on ultrathin g-C_3N_4 nanosheets, resulting in formation of WO_x/g-C_3N_4 layered heterostructures. The composition of WO_x (WO_3, WO_2, $W_{18}O_{49}$) is dependent on the preparation conditions (e.g., the amount of ascorbic acid). The compositions of WO_x and crystallinity of g-C_3N_4 affect the performances of the heterostructures with the highest activities to be obtained on $W_{18}O_{49}$/g-C_3N_4 layered heterostructures. Amorphous $W_{18}O_{49}$/g-C_3N_4 layered heterostructures reveal enhanced visible-light-driven photocatalytic performance (4 times higher that of g-C_3N_4), while crystalline $W_{18}O_{49}$/g-C_3N_4 layered heterostructure exhibits superior hydrogen generation (nearly 7 times higher compared with that of g-C_3N_4). In addition, WS_2/WO_x composites are grown onto crystalline graphitic carbon nitride (g-C_3N_4) nanosheets to form heterostructures using a hydrothermal treatment method. WS_2/g-C_3N_4 heterostructures prepared with addition of ascorbic acid reveal enhanced photocatalytic activity due to efficient separation of photogenerated charge carriers. In contrast, sample with relatively lower WS_2 proportion reveals high H_2 generation performance under visible light irradiation. Under full solar spectrum irradiation, the average H_2 evolution rate of sample has increased by 5.7 times comparing with that under visible light test condition.

Reprinted (adapted) with permission from Xiao Zhang, Shuai He, San Ping Jiang, WOx/g-C_3N_4 layered heterostructures with controlled crystallinity towards superior photocatalytic degradation and H_2 generation, Carbon, 2020, 156, 488-498; and Xiao Zhang, Ping Yang, San Ping Jiang, Horizontally-growth of WS_2/WO_3 heterostructures on crystalline g-C_3N_4 nanosheets towards enhanced photo/electro-chemical performance, Journal of

Nanostructure in Chemistry, 2021, https://doi.org/10.1007/s40097-020-00373-7.

6.1 Introduction

Graphitic carbon nitride (*g*-C_3N_4) as a photocatalyst for photocatalytic degradation of organic dyes and hydrogen generation via water splitting under visible light irradiation has stimulated tremendous interest due to its non-metallic composition, desirable bandgap (2.7 eV), and high stability in acidic/basic environment [1-4]. Bulk g-C_3N_4 prepared via conventional methodologies with low specific surface area and irregular morphology shows quick recombination of photogenerated charge carriers which limits its applications [5-9]. Efforts have been made on improving the photocatalytic activities of g-C_3N_4 through elemental doping, morphology control, and heterojunction formation. For instance, enhanced photocatalytic performance has been reported for one dimensional (1D) g-C_3N_4 with different morphologies [10-14]. 2D g-C_3N_4 materials also have been attracting considerable attention due to its high surface area, increased number of active sites on the surface, and excellent electron mobility. Especially, 2D g-C_3N_4 can be used as a base (with decent charge carrier separation ability) for surface material dispersion processes [15].

In order to overcome the disadvantage of quick recombination of photogenerated charge carriers, coupling g-C_3N_4 nanosheets with other compounds have been considered as a prevalent method [16]. For instance, Yu's group reported on a silver chromate (Ag_2CrO_4) as a photosensitizer with narrowed band gap (~1.8 eV) that favours extending light absorption of g-C_3N_4 [16-18]. The g-C_3N_4-based composites can restrain the recombination of photogenerated charge carriers and improve the photocatalytic performance of the composite material [19-21]. The construction of layered-heterostructures provides the possibility of dealing with the poor quantum efficiency of pristine g-C_3N_4 for H_2 generation. Belt and layered second semiconducting materials are excellent candidates for creating g-C_3N_4 based layered heterostructures.

Tungsten oxides (WO_x) as a chemically stable photoanode material reveals tuneable bandgaps (2-3 eV) and high electron mobility [22-25]. WO_x has been used to prepare composite materials with improved photocatalytic activities under visible light

condition [25]. WO_x with different compositions and microstructures has been studied for a variety of applications, e.g., electrocatalysts for water oxidation and Li-ion batteries [26, 27]. Since tungsten possess variable oxidation states (e.g. IV, V, and VI), sub-stoichiometric tungsten oxides exhibit broad absorption in visible and infrared regions due to the presence of oxygen vacancies [28, 29]. For instance, Paik et. al. reported on direct photocatalytic H_2 evolution from sub-stoichiometric tungsten oxide (WO_x) nanowires with the use of sacrificial alcohols [30]. Single layered g-C_3N_4 coupled with Cs_xWO_3 nanorods was also reported to have high photocatalytic H_2 evolution activity and decent rhodamine B (RhB)/phenol degradation activity in full solar spectrum condition [31].

Herein, synthesis of horizontally grown WO_x nanobelts on ultrathin g-C_3N_4 nanosheets with controlled crystallinity and superior photocatalytic activity is introduced in this chapter. In situ grown of WO_x nanobelts on the g-C_3N_4 nanosheets was achieved. Amorphous and crystalline g-C_3N_4 nanosheets were created by control thermal polycondensation reactions of precursors. It was determined that the layered heterostructures consisted of $W_{18}O_{49}$ and amorphous g-C_3N_4 revealed enhanced photocatalytic activities under visible light irradiation; while the crystalline g-C_3N_4/$W_{18}O_{49}$ layered heterostructures show superior H_2 generation performance compared with that of WO_3/g-C_3N_4 and WO_2/WO_3/g-C_3N_4 heterostructures.

6.2 Experimental section

6.2.1 Preparation of g-C_3N_4 and WOx/g-C_3N_4 layer-heterostrucures

Melamine, WCl_6, ascorbic acid (AA), rhodamine B (RhB), and triethanolamine (≥ 78 %), tert-butanol, Nafion solution, ethanol, Na_2SO_4, and H_2SO_4 were purchased from Sigma Aldrich and Sinopharm Chemical Reagent Co. Ltd. Chemicals were of analytical-grade and were used without further purification. Amorphous and crystalline *g*-C_3N_4 nanosheets were prepared using a procedure introduced in chapter 3 [32]. Crystalline g-C_3N_4 was prepared using a slow heat-treatment procedure at 750 ºC and amorphous g-C_3N_4 was prepared via a relatively faster heat-treatment procedure at 650 ºC. The as-prepared g-C_3N_4 sample was dispersed and

sonicated in deionized water. Finally, the suspension was precipitated, and washed with water and ethanol for several times.

The growth of WO_x nanobelts on g-C_3N_4 nanosheets was carried out using hydrothermal synthesis method. 0.06 g of WCl_6 was dissolved in ethanol with 0.6 g of g-C_3N_4 followed by sonication for 5 min. The molar ratio of WCl_6 and AA was adjusted to study the effects of AA on the composition of WO_x formed on g-C_3N_4 nanosheets. After stirring for 20 min, a uniform suspension was obtained. The suspension was then heat-treated at 220 ºC for 12 hours. The resulting sample was washed several times using ethanol. The amount of WCl_6 was adjusted to control the ratio of W/g-C_3N_4. Table 6-1 gives the preparation conditions and properties of samples used in this study.

Table 6-1. Preparation conditions and properties of WO_x/g-C_3N_4 composite samples.

Sample*	g-C_3N_4	W/AA molar ratio	WO_x	Preparation temperature for g-C_3N_4 (°C)
ACN-1	Amorphous	1/1	$W_{18}O_{49}$	650
ACN-2	Amorphous	1/2	$W_{18}O_{49}$	650
ACN-3	Amorphous	1/10	$W_{18}O_{49}$	650
ACN-4	Amorphous	2/1	$W_{18}O_{49}$	650
ACN-5	Amorphous	10/1	WO_2/WO_3	650
CCN-1	Crystalline	1/1	$W_{18}O_{49}$	750
CCN-2	Crystalline	1/2	$W_{18}O_{49}$	750

*ACN denotes amorphous g-C_3N_4 and CCN denotes crystalline g-C_3N_4.

6.2.2 Preparation of WS_2 and g-C_3N_4 composites

WS_2/WO_3/g-C_3N_4 composites were also prepared using a hydrothermal treatment method. Thioacetamide (3 mg, TAA, CH_3CSNH_2, Sigma Aldrich) was dissolved in 25 mL of ethanol solution with 10 mg of g-C_3N_4 first, followed by sonication to achieve better dispersion. The obtained solution was then mixed in a hydrothermal reactor with certain amount of 0.4 M Na_2WO_4 (analytical grade, Sigma Aldrich) solution in deionized water (DI water). The amount of Na_2WO_4 solution added was calculated according to the ratio of W precursor (Na_2WO_4) and g-C_3N_4 in each sample. Table 6-2 shows the preparation conditions of each sample using

crystalline g-C_3N_4 (750) as base. In case of W/C-1 sample, 10 µL of Na_2WO_4 solution was used to reach a Na_2WO_4 to g-C_3N_4 weight ratio of 10 % (Na_2WO_4/g-C_3N_4). The obtained solution was then heat-treated in an oven at 220 ºC for 12 hours followed by washing with ethanol for several times. Similar procedures were done for W/C-0.5 with 5 µL of Na_2WO_4 solution and for W/C-2 with 20 µL of Na_2WO_4 solution. To synthesize WS_2/WO_3/g-C_3N_4 heterostructures, ascorbic acid (AA, $C_6H_8O_6$, Sigma Aldrich) was added. For sample W/C-1A, 10 µL of 0.4 M ascorbic acid (AA) was added to the Na_2WO_4 solution before hydrothermal treatment. The TAA to AA molar ratio for sample W/C-1A and W/C-2A are 1:1 and 10:1, respectively.

Table 6-2. Preparation conditions of samples prepared using crystalline g-C_3N_4 (750) as base.

Sample	Na_2WO_4/g-C_3N_4(750) (wt%)	AA	Treatment at 300 ºC in Ar
Pristine WS_xO_y	N/A (WS_xO_y only)	N/A	no
W/C-0.5	1 : 20	N/A	no
W/C-1	1 : 10	N/A	no
W/C-2	1 : 5	N/A	no
W/C-1A	1 : 10	added	no
W/C-2A	1 : 5	added	no
W/C-1R	1 : 10	N/A	yes

Table 6-3. Preparation conditions of samples W/C-1(650), W/C-1(700), and W/C-1(750).

Sample	Na_2WO_4/g-C_3N_4 (wt%)	Preparation temperature for g-C_3N_4 (ºC)
W/C-1(650)	1:10	650
W/C-1(700)	1:10	700
W/C-1(750)	1:10	750

Sample W/C-1R was obtained by using the same preparation method as for sample W/C-1 except for the addition of Ar gas treatment at 300 ºC for 2 hours as the final step. To test the effects of varying temperature settings on the sample, different temperature conditions were used. Table 6-2 illustrates the preparation conditions used for samples W/C-1(650), W/C-

1(700), W/C-1(750). For comparison, a pure WS_xO_y sample was prepared with no g-C_3N_4 addition utilizing the same preparation procedure as for WS_2/g-C_3N_4 composite samples.

6.2.3 Material characterization

The TEM images, high-angle annular dark-field scanning TEM (HAADF-STEM) images, and the corresponding elemental mapping of samples were recorded using a transmission electron microscope (FEI Titan G2 80-200 TEM/STEM with Chemi STEM Technology, FEI company, US). The UV-Vis diffuse reflectance and absorption spectra of samples were obtained using a UV-Vis spectrophotometer (U-4100, Hitachi). The XRD patterns of samples were taken on an X-ray diffractometer (Bruker D8, Germany) with Cu Kα radiation source. The XPS spectra of samples were recorded on Kratos Axis Ultra DLD spectrometer with a monochromatic AlKα (1486.6 eV) X-rays operating at 150 W.

6.2.4 Photocatalytic and electrochemical characterization

Photocatalytic H_2 generation was measured using a connected system of Pyrex top-irradiation reaction vessel and a glass-closed gas circulation. 10 mg of sample and 100 ml of triethanolamine aqueous solution (triethanolamine : deionized water = 1:9) were mixed followed by sonication (25 min) before light exposure. The system was evacuated to remove air before testing. With constant stirring of the sample solutions, the measurement was then done using a 300 W Xe lamp with a cutoff filter allowing $\lambda >$ 420 nm. Shimadzu GC-7920 gas chromatography (Argon as carrier gas) was used to measure the amount of H_2 evolved.

RhB photocatalytic degradation was carried out under visible light condition. RhB solution (50 ml of 10 mgL^{-1}) was used to mix with 30 mg of the samples followed by stirring in dark for 1 hour in order to achieve equilibrium absorption state. Absorbance of RhB was then measured on a UV-Vis spectrophotometer with 300 W Xe arc lamp and a UV-cut off filter allowing $\lambda \geq 420$ nm.

Electrochemical performance was measured using CHI 660E electrochemical analyzer with a three-electrode system. Graphite rod and Ag/AgCl electrode were used as the counter and reference electrodes, respectively. Catalyst ink (2 $mgmL^{-1}$) was prepared by mixing the as synthesized catalysts with a Nafion (5 wt%) mixture solution

(Nafion:water:alcohol = 0.025:4:1 in V/V), followed by pipetting 6 μL of the prepared catalysts ink onto a glassy carbon electrode with a diameter of 3.0 mm. The catalyst loading was 0.17 $mgcm^{-2}$. Linear sweep voltammetry (LSV) curve was then measured in a 0.5 M H_2SO_4 solution at a scan rate of 5 mVs^{-1}. For the three-electrode system, with 0.1 $molL^{-1}$ of Na_2SO_4 aqueous solution acted as the electrolyte, a Pt plate was used as the counter electrode, Ag/AgCl electrode was used as the reference electrode, a thin film of the catalyst sample casted on the surface of indium tin oxide (ITO) glass was used as the working electrode. Electrochemical impedance spectroscopy (EIS) measurements were done using a 10 mV alternating current amplitude in the frequency ranges of 10 mHz to 100 kHz at open circuit potential. For the photocurrent response measurement, 300 W Xe lamps equipped with different wavelengths of filters was used as the light sources.

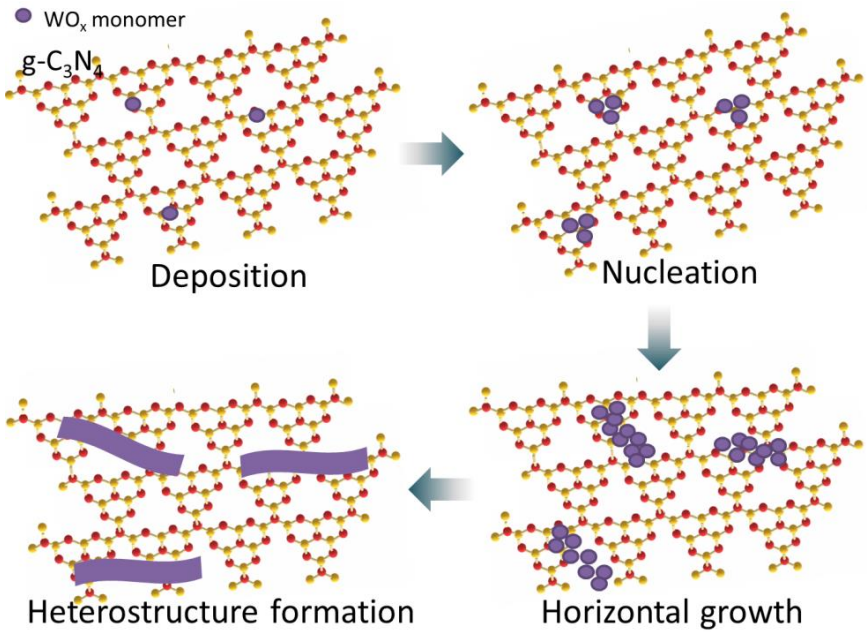

Figure 6-1. Formation of g-C_3N_4/WO_x layered heterostructures.

6.3 Results and discussion

6.3.1 Phase and microstructure of WO_x/g-C_3N_4 layered heterostructures

g-C_3N_4 nanosheets were obtained by thermal polycondensation of melamine at high temperature. The crystallinity of g-C_3N_4 depends on the distribution of heptazine units in the layered networks. Crystalline g-C_3N_4 was synthesized by further thermal polymerization of bulk g-C_3N_4 prepared at a lower temperature using melamine as the

raw material. Slow thermal polymerization process is crucial. The crystallinity of thin g-C_3N_4 nanosheets affects the band gaps which determines the optic adsorption as discussed in literature [32]. Fig. 6-1 shows the formation procedure of WO_x/g-C_3N_4 layered-heterostructures. The WO_x monomer was first deposited onto the surface of g-C_3N_4 nanosheets followed by nucleation process. The nuclei were grown in situ along horizontal directions to form thin WO_x nanobelts as shown below.

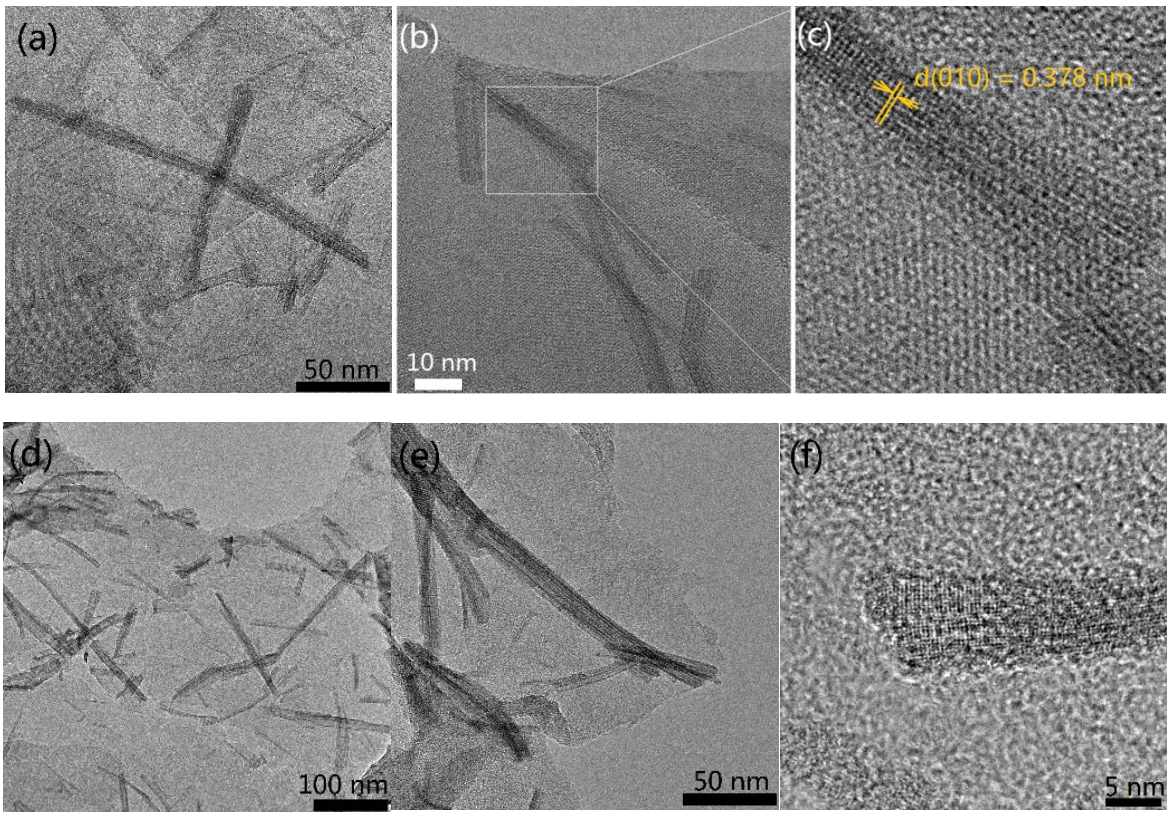

Figure 6-2. TEM images of WO_x/g-C_3N_4 samples with different magnifications. (a, b, c) CCN-1 prepared using crystalline g-C_3N_4 as base with a W/AA ratio of 1:1 and (d, e, f) ACN-1 prepared using amorphous g-C_3N_4 with a W/AA ratio of 1:1.

Fig. 6-2 shows the TEM images of CCN-1 and ACN-1 samples. The results indicate that WO_x nanobelts were grown on few layered g-C_3N_4 to form layered heterostructures. The WO_x nanobelts with high degree of crystallinity (shown in Fig. 6-2c) were homogeneously distributed on crystalline g-C_3N_4 nanosheets (shown in Fig. 6-2a and 2b). In contrast, the degree of crystallinity of WO_x nanobelts decreases when amorphous g-C_3N_4 was used (shown in Fig. 6-2f). The distribution of the nanobelts on g-C_3N_4 nanosheets is not homogeneous but aggregated. This confirms that the crystallinity of g-C_3N_4 affected the growth of the nanobelt [32]. Compared with the amorphous surface,

crystalline surface has a lower energy which causes decrease of nucleation and limits the growth of WO_x nanobelts [33-35]. The slow growth process resulted in formation of WO_x nanobelts with well-developed lattice fringes and homogeneous distribution as shown in Fig. 6-2c. The TEM image in Fig. 6-2c shows that the interplanar distance between adjacent lattice planes (0.378 nm) coincides with the (010) lattice of $W_{18}O_{49}$, and that regular lattice fringes are observed in crystalline g-C_3N_4 [36, 37]. In contrast, no regular lattice fringes were observed in Fig. 6-2f, which is consistent with the amorphous nature of the base material. The growth of the nanobelts occurred within the surface of the nanosheets rather than outside of the nanosheets. TEM images of the heterostructure samples are shown in Fig. 6-3. The bended nanobelts can be observed on the edges of the nanosheets (Fig. 6-3a and 3c). The nanobelts and nanosheets may be consisted of few layers based on the TEM observations.

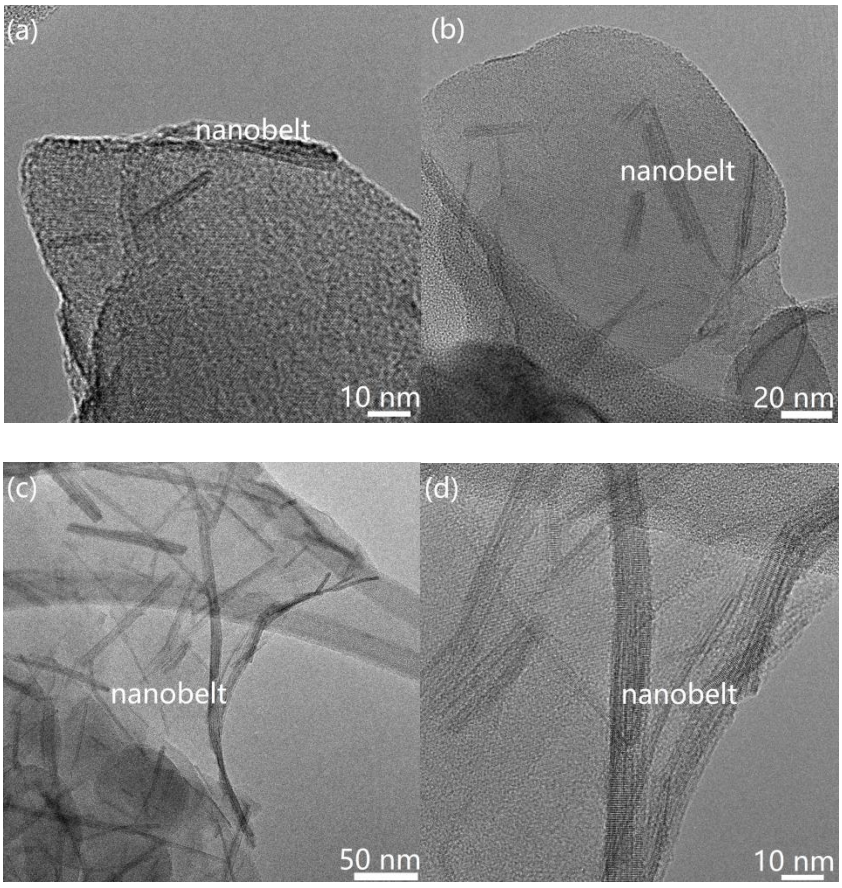

Figure 6-3. TEM images of samples: (a, b) CCN-1; (c, d) CAN-1. The growth of nanobelts occurred on the edge and inside of g-C_3N_4 nanosheets.

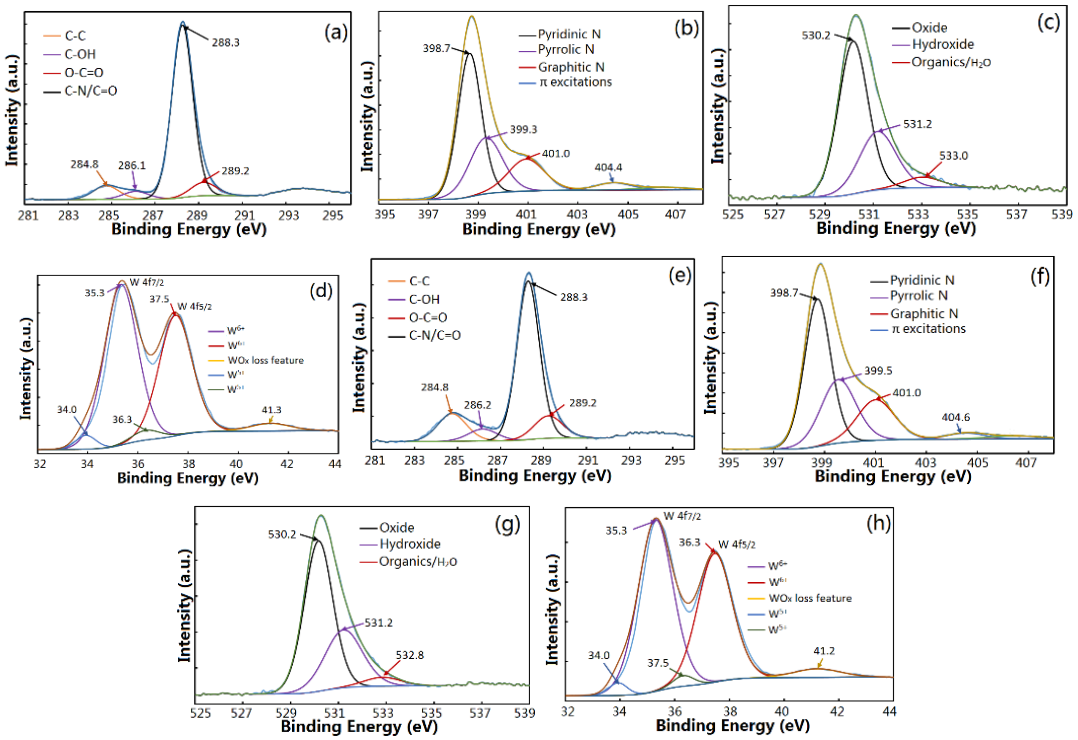

Figure 6-4. C 1s, N 1s, O 1s, W 4f XPS spectra of (a, b, c, d) sample CCN-1 and (e, f, g, h) sample ACN-1.

Fig. 6-4 shows the XPS spectra (e.g. C 1s, N 1s, O 1s, and W 4f) of CCN-1 and ACN-1 samples. The peaks corresponding to C-C (sp^2 hybridized carbon), C-OH (epoxy/hydroxyls), O-C=O, C-N/C=O (carbonyls), and satellite C1s peak of the C1s spectra of samples are shown in Fig. 6-4a and 4e. The N 1s spectra of samples in Fig. 6-4b and 4f shows the four peak positions corresponding to N-H (graphitic N), C-N=C Pyridinic-N), $N-(C)_3$ (Pyrrolic-N), and π excitations. Due to the differences in C 1s spectra of the samples and the similarities observed for N 1s spectra, the C/N ratios of the samples are different. This can be ascribed to the distillation of N elements occurred at higher temperatures [30]. The samples show very similar O 1s, and W 4f spectra in Fig. 6-4c, 4d, 4g, and 4h, suggesting that the distribution states of W and O elements are similar. Fig. 6-4d (sample ACN-1) shows that peaks at 35.3 and 36.3 eV are attributed to $W4f_{7/2}$ and $W4f_{5/2}$ of W^{6+} state, while peaks at 34.0 and 37.5 eV correspond to the W^{5+} state [34]. This indicates that the defects may endow $W_{18}O_{49}$ with specific performances. For the layered-heterostructures of $W_{18}O_{49}$ and crystalline g-C_3N_4 (sample CCN-1), the peak position corresponding to W^{6+} and W^{5+} state changed,

suggesting the difference of bonding state of $W_{18}O_{49}$ on amorphous and crystalline g-C_3N_4.

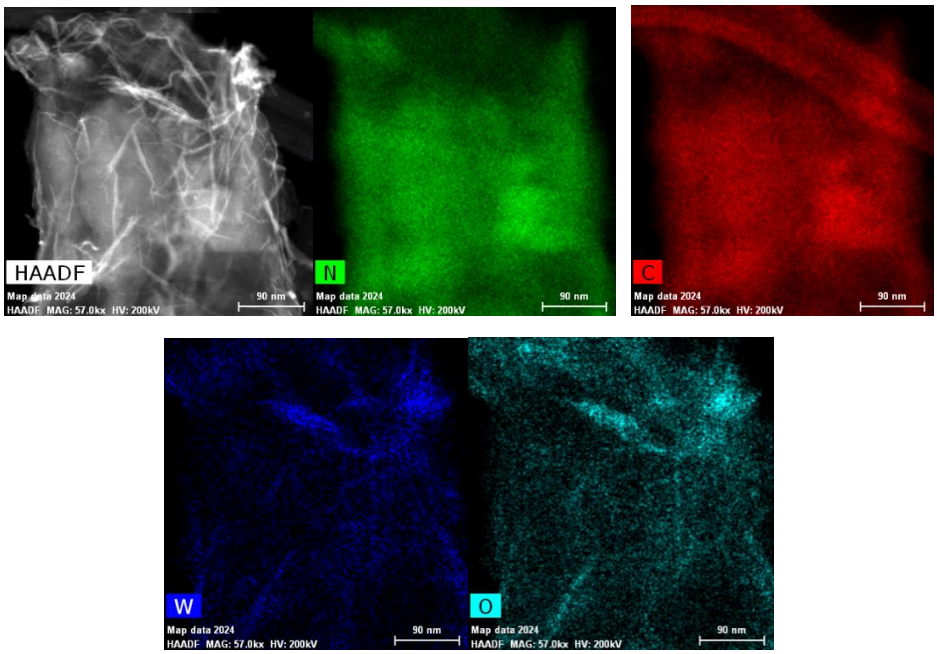

Figure 6-5. HAADF-STEM image and N, C, W, and O mapping of sample CCN-1.

To confirm the formation of WO_x, the HAADF-STEM images and corresponding elemental mapping of CCN-1 were obtained, and the results are shown in Fig. 6-5. Similar result was also obtained for sample ACN-1 in Fig. 6-6. The distribution of N and C is homogeneous, and the distribution of W and O is in the area of $W_{18}O_{49}$ nanobelts. To investigate the formation process of nanobelts, pure WO_x samples were prepared without adding g-C_3N_4 utilizing the same preparation conditions. For the nanobelt shape formation and composite change of WO_x, ascorbic acid (AA) plays an important role. It was found that WO_3 nano-flowers can be obtained in case of no AA addition, whereas in case of AA addition, WO_3 nanofibers can be synthesized.

Since AA works as a reductant during preparation, the composition of WO_x is dependent on on the amount of AA added. Fig. 6-7 shows the XRD patterns of heterostructure samples prepared using amorphous g-C_3N_4 and different amounts of AA. Two XRD peaks corresponding to the (100) and (002) facets of g-C_3N_4 were observed for all samples. The weak peak at 12.8° is caused by the periodic arrangement of the triazine units in g-C_3N_4 and the higher intensity peak at 27.9° is related to the stacking of the conjugated aromatic system of carbon nitride [32]. By using a W/AA molar ratio of 10/1, a mixed phase of WO_2 and WO_3 can

be obtained (sample ACN-5). In this case, due to the trace amount of WOx formed in the composite, the XRD signals can be hard to detect. However, both WO_2 and WO_3 phases were obtained with AA addition. In cases of WO_x/g-C_3N_4 prepared using other W/AA ratios, $W_{18}O_{49}$ phase was observed (dotted line in Fig. 6-7).

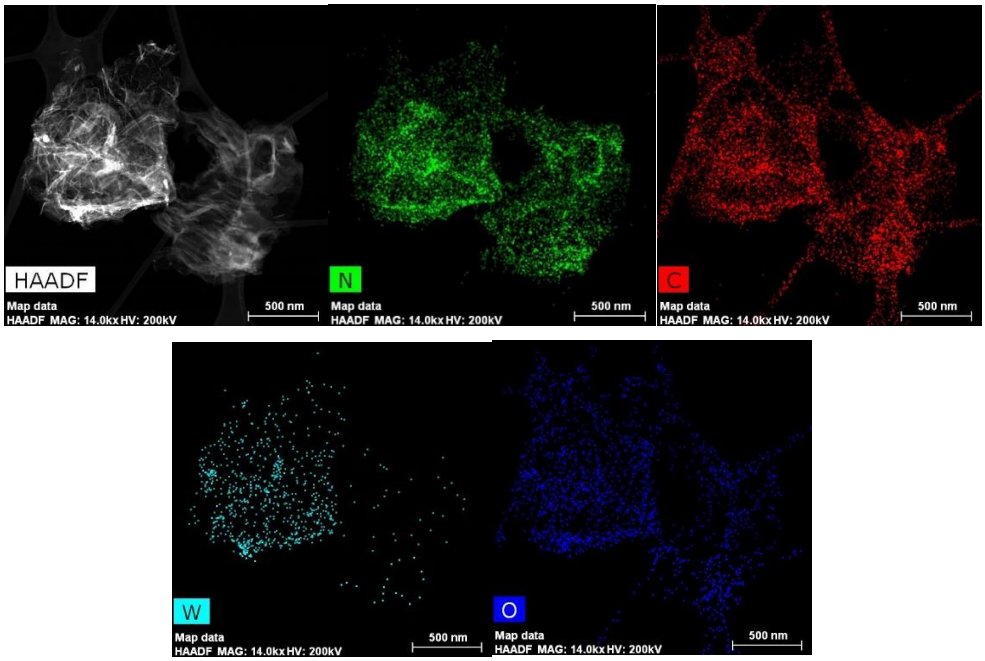

Figure 6-6. HAADF-STEM image and N, C, W, and O mapping of sample ACN-1. The distribution of N and C is homogeneous and the distribution of W and O is in the area of WO_x nanobelts.

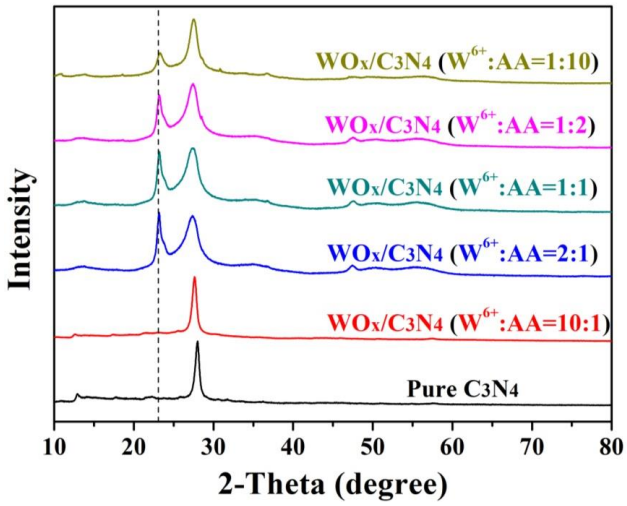

Figure 6-7. XRD patterns of WO_x/g-C_3N_4 heterostructure samples using different amount of AA and amorphous g-C_3N_4.

6.3.2 Photocatalytic activity of WO_x/g-C_3N_4 layered heterostructures

Fig. 6-8 shows the UV-Vis diffuse reflectance spectra and $(\alpha_{hv})^{1/2}$ vs photon energy plots of WO_x heterostructure samples prepared using amorphous g-C_3N_4. The band gap of the samples was estimated by using the transformed Kubelka–Munk function (A(hν-Eg)r = αhν) based on infomations obtained on UV-Vis diffuse reflectance spectra [33-36]. The band gaps of sample ACN-1, ACN-2, ACN-4, and ACN-5 were estimated to be 2.84, 2.82, 2.85, and 2.87 eV, respectively (Fig. 6-8c to 8f). The band gap of amorphous g-C_3N_4 is 2.86 eV (Fig. 6-8b). The change of band gap confirms the formation of $W_{18}O_{49}$/g-C_3N_4 layered-heterostructure. Addition of larger amont of $W_{18}O_{49}$ can result in narrowing of band gap. The absorbance of WO_x/g-C_3N_4 composites in visible light region increased drastically in comparison with that of amorphous g-C_3N_4 (Fig. 6-8a). Especially, the increase of absorbance of sample ACN-1 ($W_{18}O_{49}$/g-C_3N_4) is the highest, which also proves the improved photocatalytic activities of the sample in visible light condition.

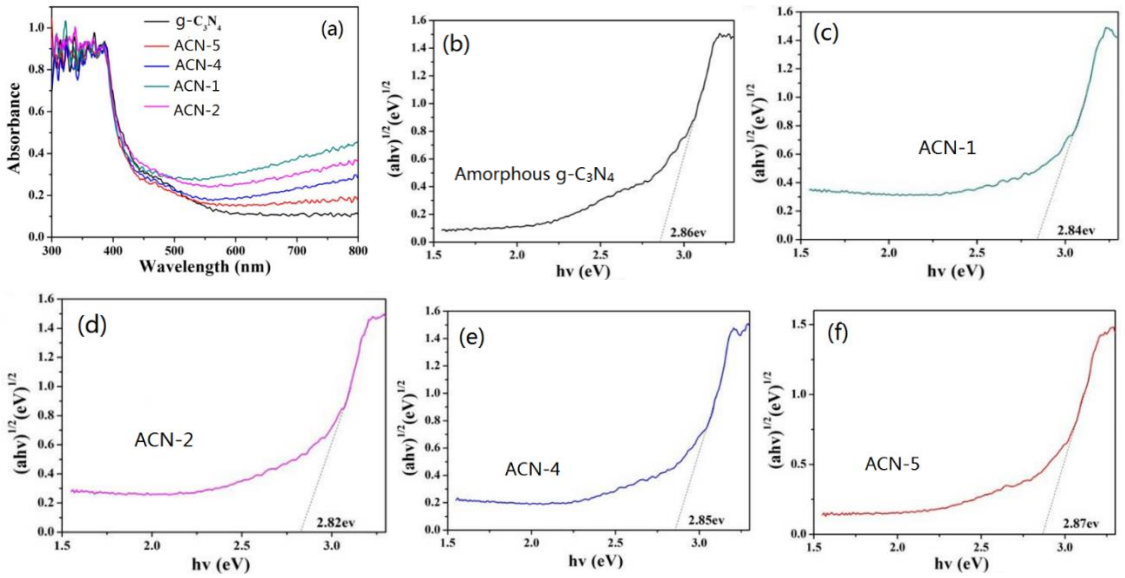

Figure 6-8. (a) UV-Vis diffuse reflectance spectra and $(\alpha h\nu)^{1/2}$ *vs*. photon energy plots for WO_x heterostructure samples using amorphous g-C_3N_4. (b) $(\alpha h\nu)^{1/2}$ vs photon energy plots for g-C_3N_4. (c) $(\alpha h\nu)^{1/2}$ vs photon energy plots for sample ACN-1. (d) $(\alpha h\nu)^{1/2}$ vs photon energy plots for sample ACN-2. (e) $(\alpha h\nu)^{1/2}$ vs photon energy plots for sample ACN-4. (f) $(\alpha h\nu)^{1/2}$ vs photon energy plots for sample ACN-5.

The transient photocurrent response of samples can be related to electron transport. The photocurrent responses of samples under visible light irradiation were measured and the results are shown in Fig. 6-9a. The photocurrent response value of amorphous g-C_3N_4 estimated is

very low. The formation of layered-heterostructures drastically enhances photocurrent response. Especially, the photocurrent response of sample ACN-1 exhibited the highest intensity among all measured samples. Since the transient photocurrent is related to the conductivity of the materials, a higher photocurrent value indicates better conductivity of the material. Electrochemical impedance spectroscopy measurement is another effective way to investigate the charge separation and transfer efficiencies of the composite material.

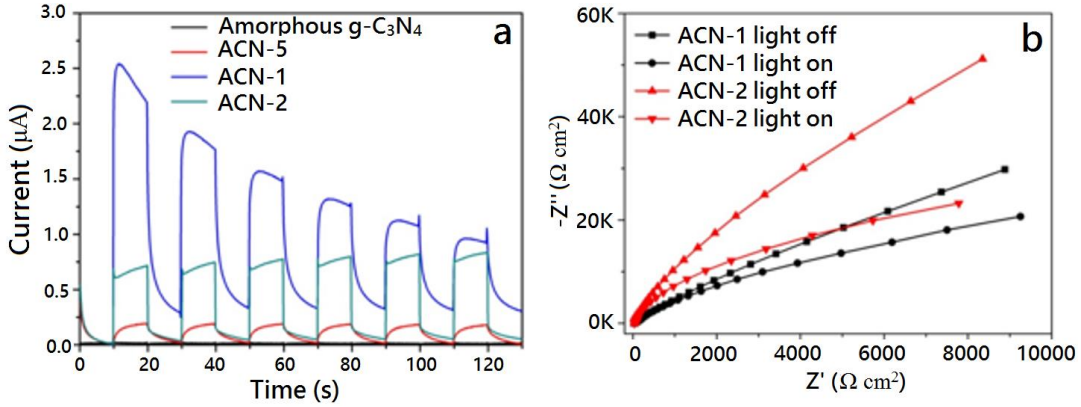

Figure 6-9. (a) Photocurrent of $W_{18}O_{49}$/*g*-C_3N_4 layered heterostructures under visible light irradiation. (b) Nyquist plots of samples with different test conditions.

Nyquist plots of ACN-1 and ACN-2 with or without light irradiation were investigated (see Fig. 6-9b). In case of no light irradiation, sample ACN-1 shows a smaller impedance arc radius than that of sample ACN-2, indicating that sample ACN-1 has higher charge transfer efficiency and that the decoration of $W_{18}O_{49}$ improves the electrical conductivity of the layered heterostructures. In addition, the photogenerated charge carrier separation and transport efficiency of ACN-1 and ACN-2 has increased in case of using light irradiation due to the strong absorption of $W_{18}O_{49}$ in visible light region.

The photocatalytic activity of amorphous WO_x/g-C_3N_4 layered heterostructure samples was examined by RhB photodegradation measurement in aqueous solution under visible light irradiation and the results are shown in Fig. 6-10. The degradation plots of WO_3/g-C_3N_4 prepared with no AA addition is shown for comparison. Both g-C_3N_4 and $W_{18}O_{49}$ are typical visible-light-responsive photocatalysts, however, the quick recombination of photogenerated charge carriers can cause lowering of photocatalytic efficiency of the material [37-39]. $W_{18}O_{49}$ and WO_2/WO_3 revealed higher RhB degradation efficiency than that of WO_3. ~57 % of RhB was degraded by WO_3/g-C_3N_4 sample prepared with no AA addition after 30 min of

degradation (Fig. 6-10a), and this can be associated with the enhanced visible light absorption of the composite material. These results confirm that the composition of WO_x plays the key role for enhancing the photocatalytic performances of amorphous g-C_3N_4. $W_{18}O_{49}$/g-C_3N_4 layered-heterostructures prepared using a W/AA weight ratio of 1:1 shows the best photocatalytic activity (Fig. 6-10a). This demonstrates that the amorphous $W_{18}O_{49}$/g-C_3N_4 layered-heterostructures enhances the separation and transport efficiency of photogenerated electron and hole pairs, thus improving the photocatalytic activities. In addition, the RhB degradation in aqueous solution using crystalline g-C_3N_4 samples was also tested under visible light irradiation. However, the result was not satisfactory, and this is due to the decreasing in numbers of active sites on crystalline g-C_3N_4.

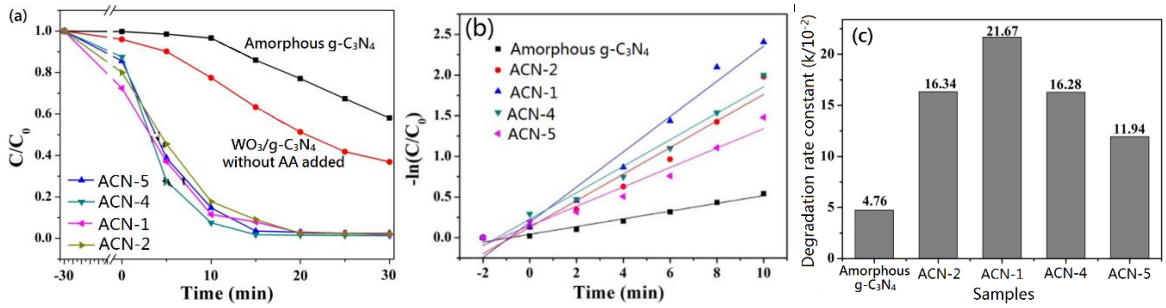

Figure 6-10. (a) Photocatalytic RhB degradation plots for WO_x layered heterostructure samples prepared using amorphous g-C_3N_4 as base under visible light irradiation, (b) degradation kinetics plots of the samples, and (c) comparison of RhB degradation rates for the samples.

To further investigate photocatalytic reaction kinetics of the samples, the photo-degradation plots can be fitted using pseudo first order reaction shown below [39].

$$\ln (C_0/C_t) = kt, \qquad (6\text{-}1)$$

where C_0 and C_t are initial and reaction concentrations at different time point and t is the irradiation time. The degradation rates (i.e., k value) were calculated using the slope of the plots (Fig. 6-10b). As shown in Fig. 6-10c, the degradation rate of ACN-1 sample under visible light irradiation is the highest (21.67×10^{-2} s^{-1}), which is about 3 times higher than that of amorphous g-C_3N_4 sample (4.76×10^{-2} s^{-1}).

The photocatalytic hydrogen generation activity of WO_x/g-C_3N_4 layered heterostructures under visible light irradiation was also investigated and the results are shown in Fig. 6-11. The amount of H_2 evolved (as a function of irradiation time) by the crystalline $W_{18}O_{49}$/g-C_3N_4 layered heterostructure (sample CCN-1) was significantly higher than that of the crystalline g-

C_3N_4 nanosheets (Fig.6-11a). In contrast, samples prepared using amorphous g-C_3N_4 (ACN) as base revealed poor hydrogen generation efficeincy (data not shown in the figure). After ten cycles, the hydrogen generation efficiency of sample CCN-1 remained almost unchanged, suggesting sample CCN-1 with high stability. To further understand the photocatalytic reaction mechanism, tertiary butanol, $AgNO_3$, triethanol amine and para-benzoquinone were used as trapping agents for ·OH, e^-, h^+, and O_2^-, respectively [8, 37]. $AgNO_3$ and para-benzoquinone show no significant effects on photocatalysis. However, decrease in photocatalytic activity occurred when triethanolamine and tert-butanol were added to the solution. For photocatalytic measurement, triethanol amine showed significant effect and tertiary butanol exhibited minor effect in the measurement, indicating that the main active substance in CCN-1 catalysis system is h^+ and the secondary active substance is ·OH. The charge carrier separation and transport occur in the heterojunction interface between $W_{18}O_{49}$ nanobelts and crystalline g-C_3N_4.

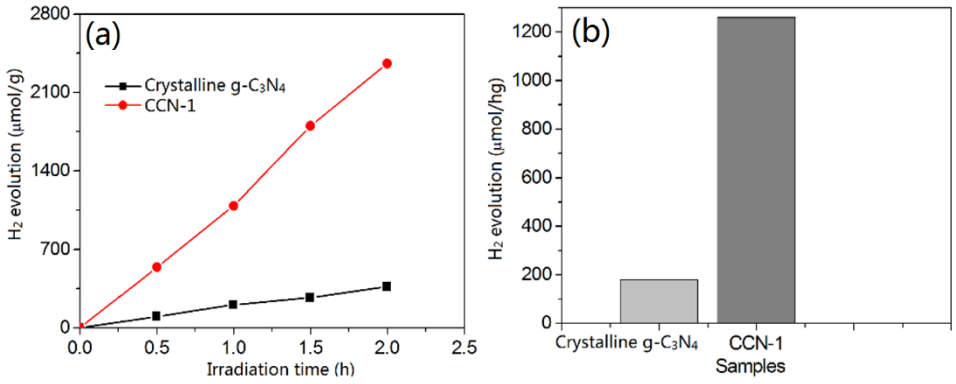

Figure 6-11. (a) H_2 evolution curves and (b) apparent rate constants of H_2 evolution for crystalline g-C_3N_4 and sample CCN-1 under visible light irradiation ($\lambda > 420$ nm).

The amount of H_2 evolved increased linearly with time. Based on the H_2 generation plots, the apparent rate constants of H_2 evolution for crystalline g-C_3N_4 and sample CCN-1 under visible light irradiation ($\lambda > 420$ nm) were obtained. As shown in Fig. 6-11b, the H_2 evolution rate of CCN-1 is about 7 times as high as that of g-C_3N_4. In case of sample CCN-1, the $W_{18}O_{49}$ nanobelts show clearer lattice fringes compared with that of sample ACN-1 (Fig. 6-12). The control of polymerization reaction causes g-C_3N_4 to have different degrees of crystallinity and different C/N ratios [32]. These properties of g-C_3N_4 affect the growth of WO_x on g-C_3N_4. Layered $W_{18}O_{49}$/crystalline g-C_3N_4 heterostructures was obtained via Ohm connection due to slow growth and limited

nucleation. In addition, high crystallinity and less internal defects promote electron migration at the interface for enhancing H_2 generation efficiency.

Fig. 6-12 illustrates the charge transfer process of $W_{18}O_{49}$/g-C_3N_4 heterostructures during H_2 evolution reaction. According to the experiment data, no hydrogen was produced when pure WO_x was used as a photocatalyst due to the band gap of WO_x nanobelts and the fact that its conduction band is more positive than the H^+/H_2 redox potential. After incorporation with crystalline g-C_3N_4, the photocatalytic hydrogen production performance was significantly enhanced. Under visible light irradiation, $W_{18}O_{49}$ and g-C_3N_4 components are simultaneously excited. CCN-1 revealed excellent hydrogen production activity, which is due to the fact that crystalline g-C_3N_4 with less structural defects can lead to slower growth of WO_x nanobelts on g-C_3N_4 and thus resulting in formation of high quality heterostructure with high charge carrier transport efficiency.

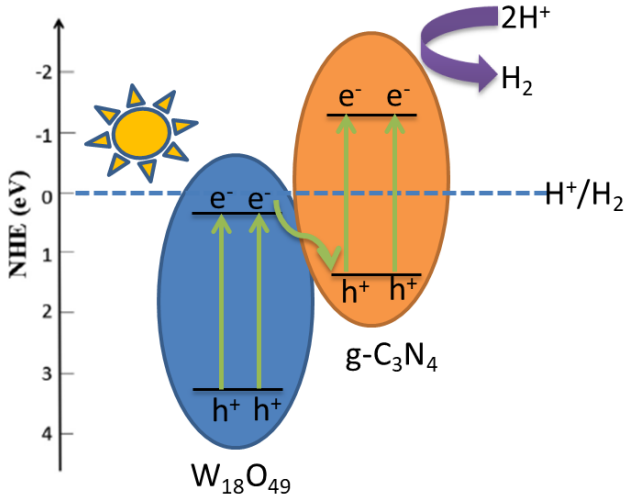

Figure 6-12. Illustration of charge transfer in $W_{18}O_{49}$/*g*-C_3N_4 heterostructures for H_2 evolution reaction.

6.3.3 WS_2/WO_x/g-C_3N_4 composites

To explore the microstructure of WS_2/WO_x/g-C_3N_4 composites, TEM images and elemental mapping images of sample W/C-1A were collected (Fig. 6-13). By combining the results of both XRD and high-resolution TEM (HR-TEM) analysis, it is obvious that WS_2 nanosheets were homogeneously distributed on g-C_3N_4 nanosheets. These WS_2 nanosheets were tightly combined on g-C_3N_4 with the growth of WS_2 occurring along the horizontal direction. No WS_2

nanobelts or bulky WS_2 particle aggregates were observed in sample W/C-1A (WS_2 to g-C_3N_4 ratio to be 1: 10 with AA addition). In the WS_2 nanosheets area shown in the TEM images, lattice fringes were clearly observed. Fig. 6-13e and 13f show the elemental mapping of S and W. It is evident that the distribution of S is not homogeneous, which confirms the presence of WS_2 in the WS_2/g-C_3N_4 composite. In contrast, the distribution of O is homogeneous as shown in Fig. 6-13i, which indicates homogeneous distribution of WO_2 and WO_3 in the sample. This result also supports the idea that only lattice fringes of WS_2 was observed. In addition, homogeneous distribution of elements C and N (shown in Fig. 6-13g and 13h) confirms the g-C_3N_4 to be in nanosheets form.

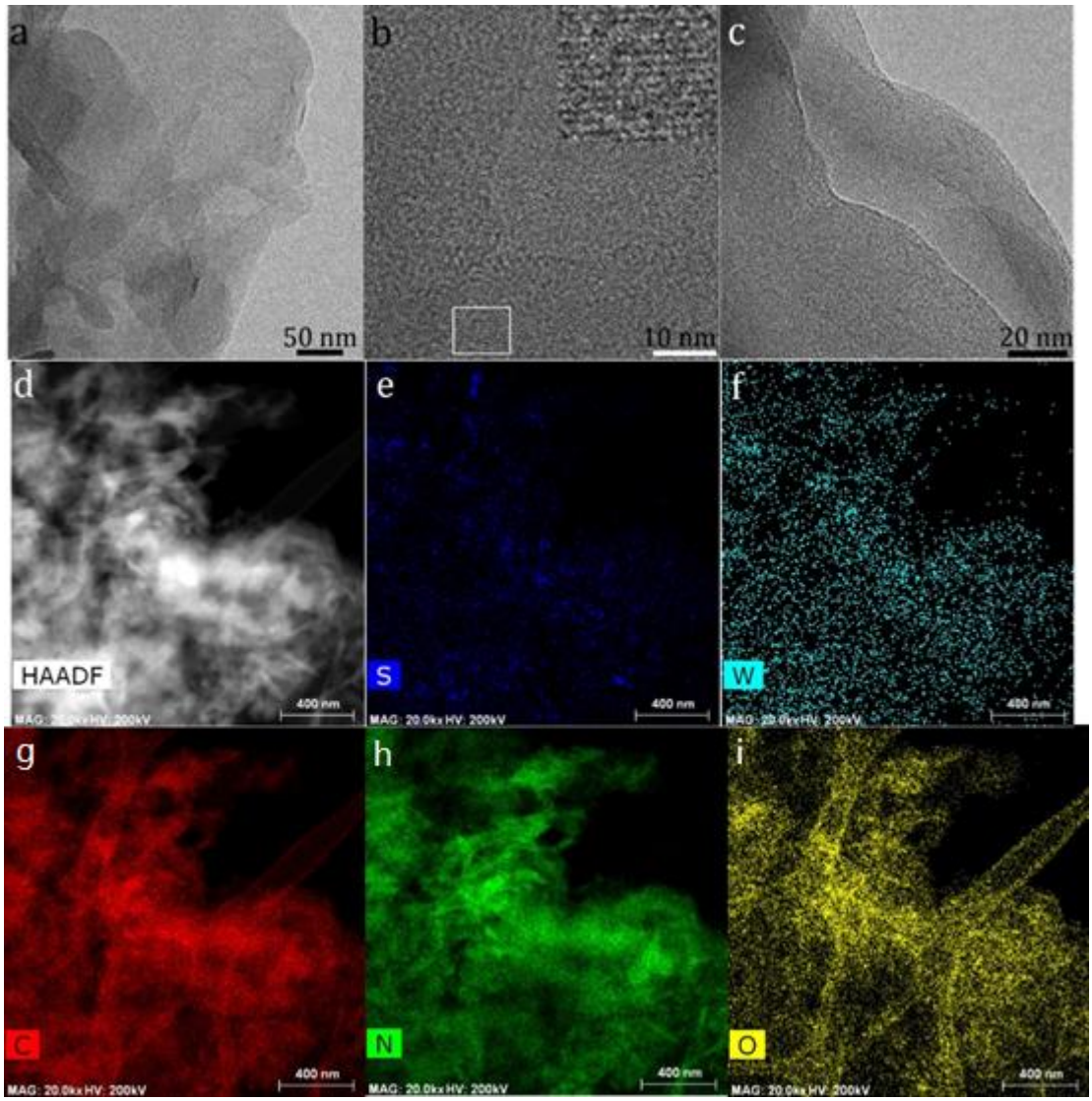

Figure 6-13. TEM images and elemental mapping of sample W/C-1A with AA addition. (a, b, c) TEM images with different magnifications. (d) HAADF-STEM image. (e, f, g, h, i) Mapping of elements S, W, C, N, and O. The inset in (b) shows an enlarged image of the white square area at the bottom, in which the lattice fringes of WS_2 particles were clearly observed.

Fig. 6-14 shows the UV-Vis diffuse reflectance spectra and band gap of sample g-C_3N_4(750), W/C-1, W/C-1R and W/C-1A, with the band gap of the samples calculated using the transformed Kubelka-Munk function below [35, 37].

$$A(h\nu - Eg)^{\frac{2}{n}} = \alpha h\nu \quad (6\text{-}2)$$

The band gap of sample g-C_3N_4(750), W/C-1, W/C-1R and W/C-1A were calculated to be 1.56, 1.27, 0.69 and 1.01 eV, respectively. Reduced band gap can be observed after WS_2 deposition. Both pristine crystalline g-C_3N_4(750) and the WS_2 deposited composite samples show excellent optical absorption from visible to infrared (IR) light range. Increasing in absorbance was observed for the WS_2 decorated samples. The AA treated sample (W/C-1A) shows the highest absorbance. As confirmed from the XRD analysis, addition of AA caused an increasing in WS_2 proportion in the composite sample. Since WS_2 exhibits high absorption in IR region, the WS_2/g-C_3N_4 composite shows enhanced light absorption in visible to IR region, thus promoting the generation of electron and hole pairs, which also improves the photocatalytic performances of the composite material [40, 41].

To study the effect of g-C_3N_4 on electrochemical properties of the composite material, composite samples were prepared using g-C_3N_4 with different degrees of crystallinity. As shown in Fig. 6-14e and 14f, the transient photocurrent response (under visible light irradiation condition) of samples with the same W precursor to g-C_3N_4 ratio (1:10) (as W/C-1) but using g-C_3N_4 synthesized at different temperature settings was measured. Fig. 6-14e shows the photocurrent-time (i-t) curves of WS_2 deposited sample W/C-1(650), W/C-1(700) and W/C-1(750) under visible light irradiation. Fig. 6-14f shows the comparison of photocurrent intensity between pristine g-C_3N_4 (with the numbers shown to be the synthetic temperature of each g-C_3N_4 sample) and WS_2 deposited g-C_3N_4 samples. Crystallinity of pristine g-C_3N_4 samples increases as synthetic temperature increases, among which the g-C_3N_4 synthesized at 750 ºC is crystalline and the one synthesized at 650 ºC is amorphous, while the 700 ºC one has both amorphous and crystalline feature [32]. The photocurrent response value of W/C-1(750) sample is the highest among the three W/C-1 samples due to the high crystallinity of g-C_3N_4(750) substrate. Comparing with sample W/C-1(650) (prepared using amorphous g-C_3N_4), increasing in crystallinity and less defects in sample W/C-1(750) leads to more efficient

separation of photogenerated charge carriers, which causes increasing in conductivity and promotes photocurrent generation. Moreover, according to Fig. 6-14f, higher photocurrent intensity was observed for WS_2 deposited samples comparing with that of pristine crystalline g-C_3N_4(700 & 750) sample, which implies successful formation of WS_2/g-C_3N_4 heterostructure. The phenomenon of improved photocurrent intensity observed for WS_2 deposited samples can be ascribed to the fact that efficient charge transfer between WS_2 and g-C_3N_4 substrate in the heterostructures results in more efficient separation of photogenerated charge carriers. The reduced photocurrent intensity observed for W/C-1(650) compared with that of pristine amorphous g-C_3N_4(650) sample is due to the presence of defects in the composite system which hinders the separation of photogenerated charge carriers.

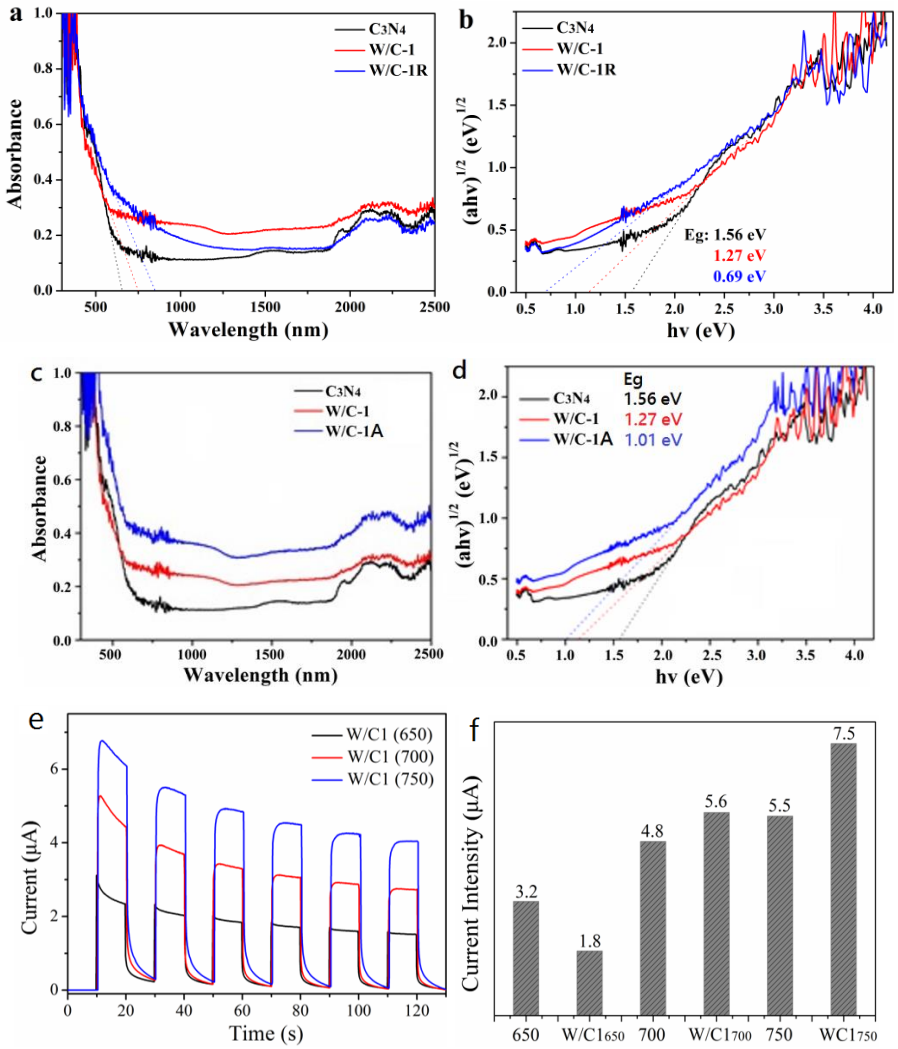

Figure 6-14. (a) UV-Vis diffuse reflectance spectra of g-C_3N_4(750), W/C-1, and W/C-1R. (b) Band gaps (Eg) of g-C_3N_4(750), W/C-1, and W/C-1R. (c) UV-Vis diffuse reflectance spectra of samples g-C_3N_4(750), W/C-1, and W/C-1A. (d) Band gaps of sample g-C_3N_4(750), W/C-1,

and W/C-1A. (e) Photocurrent-time (i-t) curves of W/C-1(650), W/C-1(700) and W/C-1(750) under visible light irradiation. (f) Photocurrent intensity comparison between pristine g-C_3N_4 sample (with the numbers on x-axis shown to be the synthetic temperature of each prisitne g-C_3N_4 sample) and WS_2 decorated W/C-1(650), W/C-1(700), W/C-1(750).

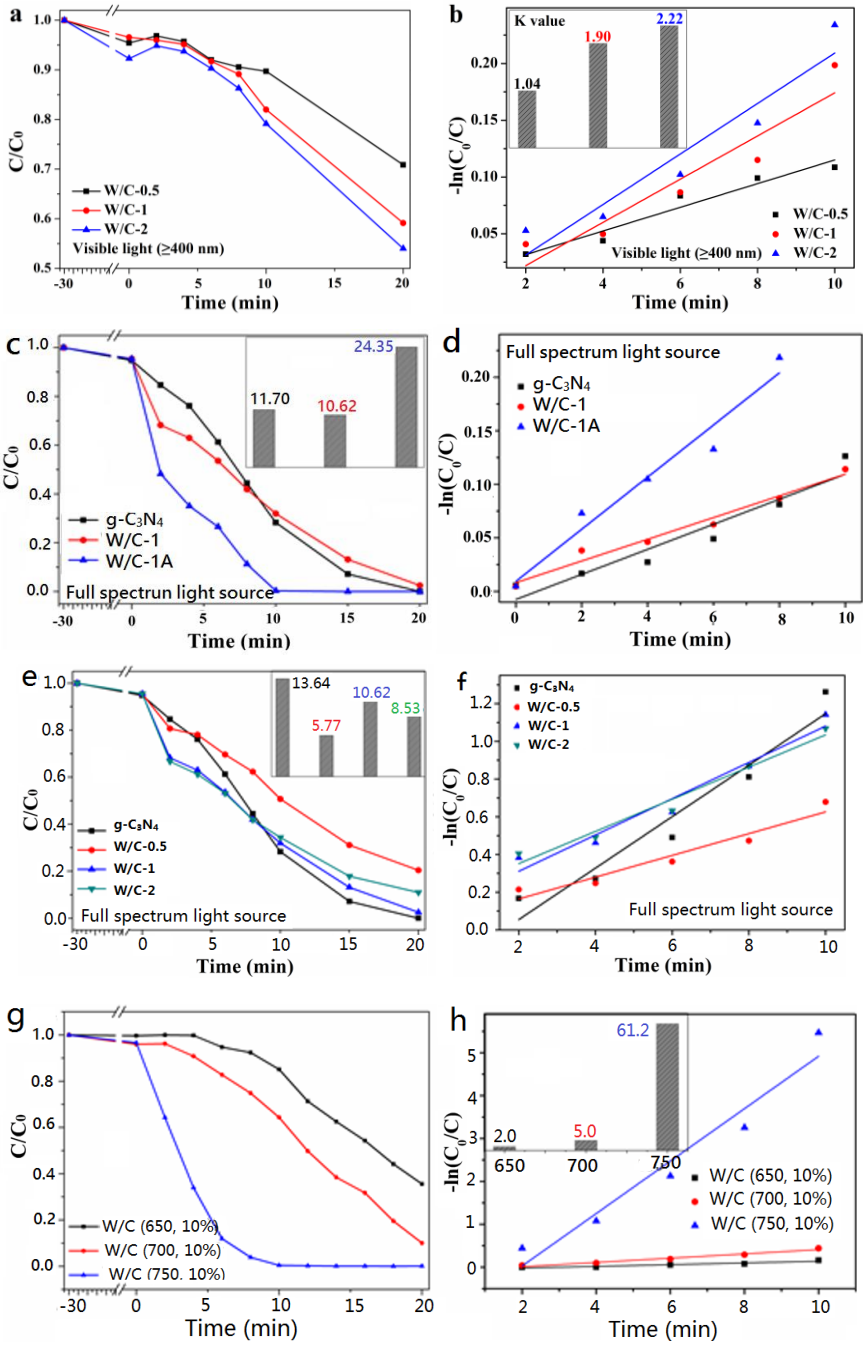

Figure 6-15. (a, c, e, g) RhB photocatalytic degradation plots and (b, d, f, h) Degradation kinetics plots of samples: (a, b) plots for sample W/C-0.5, W/C-1 and W/C-2; (c, d) plots for sample g-C_3N_4(750), W/C-1 and W/C-1A; (e, f) plots for sample g-C_3N_4(750), W/C-1 and W/C-1A; (g, h) plots for sample W/C-1(650), W/C-1(700) and W/C-1(750). The insets in (b, c, e, h) show the histogram of degradation rate K (*$10^{-2}$$min^{-1}$) of the samples.

To further examine the photocatalytic properties of WS_2/g-C_3N_4 composites, organic dye (RhB) photocatalytic degradation under visible light irradiation in aqueous solution was performed and the results are shown in Fig. 6-15. To investigate the photocatalytic reaction kinetics of samples, pseudo first order reaction (eq. 6-1) was used to fit the photodegradation plots. Fig. 6-15a and 6b show the RhB photocatalytic degradation plots and degradation kinetics plots for sample W/C-0.5, W/C-1 and W/C-2 under visible light irradiation. Sample W/C-0.5 with least amount of WS_2/WO_3 exhibits the highest photodegradation efficiency. This is due to the homogeneous distribution of WS_2/WO_3 in W/C-0.5 heterostructure which leads to higher photogenerated charge carrier separation efficiency, whereas less homogeneous WS_2/WO_3 nanosheets in samples W/C-1 and W/C-2 (shown in Fig. 6-15a and 15b) do not favour photogenerated charge carrier separation. Fig. 6-15c and 15d shows the RhB photodegradation plots and degradation kinetics plots for sample g-C_3N_4(750), W/C-1 and W/C-1A under full solar spectrum irradiation. Sample W/C-1A shows the highest degradation activity. The result coincides with the XRD results in which W/C-1A has higher proportions of WS_2 in the sample due to the addition of reducing agents in the sample preparation stage. The addition of AA therefore is determined to be beneficial for enhancing the photocatalytic performances of samples due to the presence of higher proportions of WS_2 in the heterostructure. To examine the role of WS_2 in photodegradation performances, RhB photocatalytic degradation of sample W/C-0.5, W/C-1, and W/C-2 (prepared with no AA addition) was measured. The degradation plots and degradation kinetics plots are shown in Figs. 6-15e and 15f. It is obvious that slow RhB degradation occurred for sample W/C-0.5, W/C-1, and W/C-2 (sample with lower proportions of WS_2), which also coincides with the XRD results. Figs. 6-15g and 15h show the photodegradation curves for sample W/C-1(650), W/C-1(700) and W/C-1(750), among which same amount of W precursor and different types of g-C_3N_4 substrates (with different crystallinities) were used. W/C-1(750) was examined to have the highest degradation activity due to the fact that high crystallinity and less defects in W/C-1(750) helps promoting the separation of photgenerated charge carriers and improving photodegradation efficiency.

To further exploit photocatalytic performances of the composite samples, electrochemical impedance spectroscopy (EIS) measurement was performed. Fig. 6-16a shows the Nyquist

plots (EIS) of g-C_3N_4(650) and W/C-1(650) with or with no visible light irradiation. W/C-1(650) and g-C_3N_4(650) showed identical impedance trend in no irradiation condition. In case of light-on, the slope of the EIS curve of W/C-1(650) is larger than that of pristine sample g-C_3N_4 (650), indicating W/C-1(650) to have lower ion transport rate and lower charge separation and transfer efficiency, which causes decreasing in electrical conductivity. This was also confirmed by the photocurrent measurement, in which W/C-1(650) showed lower photocurrent intensity than that of sample g-C_3N_4(650).

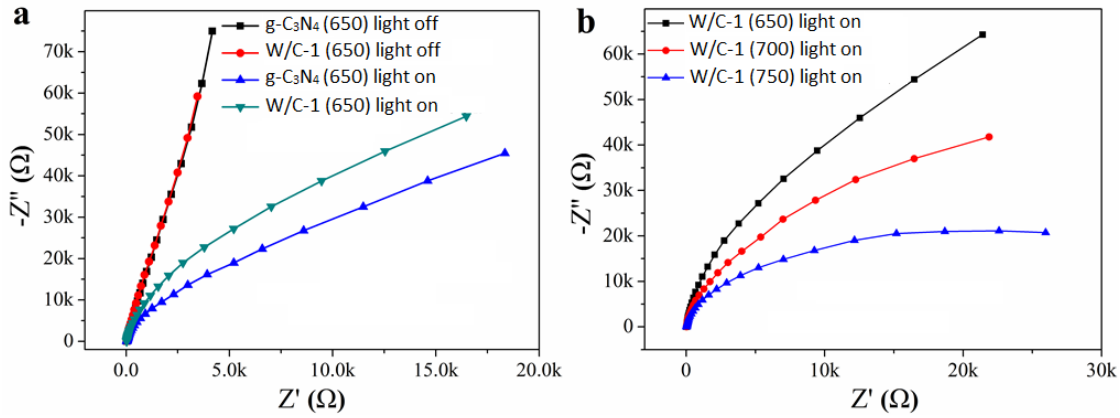

Figure 6-16. (a) EIS curves of g-C_3N_4(650) and W/C1(650) with or without irradiation. (b) EIS curves (light-on) of W/C1(650), W/C1(700) and W/C1(750).

Fig. 6-16b shows the EIS curves of W/C1(650), W/C1(700) and W/C1(750) in case of light-on. Smallest impedance arc radius was observed for sample W/C1(750) heterostructure, proving within the same light absorption range, the crystalline g-C_3N_4 composite possesses the highest charge transfer and separation efficiency thus the highest photocatalytic activities.

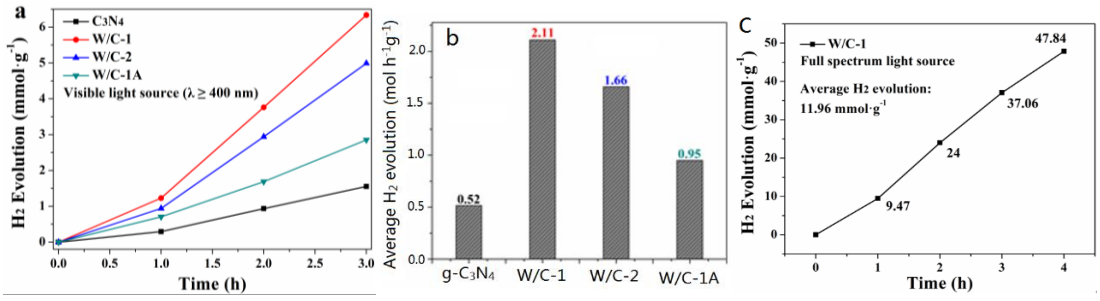

Figure 6-17. (a) Photocatalytic H_2 production measurement under visible light irradiation for sample g-C_3N_4(750), W/C-1, W/C-2 and W/C-1A. (b) Average H_2 evolution rate of each sample. (c) Photocatalytic H_2 generation measurement under full spectrum light irradiation for sample W/C-1.

Photocatalytic H_2 generation measurement under visible light (≥ 420 nm) was done on

sample g-C_3N_4(750), W/C-1, W/C-2 and W/C-1A (shown Fig. 6-17). An increasing trend in hydrogen generation was observed for each sample with increasing irradiation time, with all WS_2 deposited heterostructure samples measured to have higher hydrogen generation activity than that of pristine g-C_3N_4 (750) sample. Among the four samples, W/C-1 shows the highest hydrogen generation activity followed by W/C-2, W/C-1A and g-C_3N_4 (750). The average H_2 generation rate constant for each sample is shown in Fig. 6-17b. The H_2 generation rate of W/C-1 is twice as that of AA treated W/C-1A sample. Pristine WO_3 exhibits relatively low H_2 evolution activity. The reduced band gap of WS_2/WO_3/g-C_3N_4 composite observed after WS_2 deposition is much suitable for H_2 generation.

H_2 evolution measurement on sample W/C-1 (with the highest photocatalytic H_2 generation activity under visible light) in full solar spectrum light condition was also performed (Fig. 6-17c). The result shows that a higher H_2 generation activity was observed for measurement using the full solar spectrum condition. This can be explained by the absorption of both IR and visible light of WS_2/WO_3/g-C_3N_4 composite which helps promoting H_2 generation. The H_2 evolution efficiency in full solar spectrum condition is 5.7 times higher than that in visible light irradiation condition.

6.4 Conclusions

WO_x nanobelts horizontally grown on ultrathin g-C_3N_4 nanosheets for the construction of layered-heterojunctions with enhanced photocatalytic performances have been synthesized for the first time. In situ growth of WO_x nanobelts on amorphous and crystalline g-C_3N_4 nanosheets was achieved via a hydrothermal synthesis method using AA to control the morphology and composition of WO_x. The compositions of WO_x (WO_3, WO_2, $W_{18}O_{49}$) are dependent on the preparation conditions utilized including the weight ratio of W/AA. The distribution of $W_{18}O_{49}$ nanobelts on crystalline g-C_3N_4 nanosheets was much more homogeneous than those on amorphous g-C_3N_4 nanosheets. The layered heterojunction of $W_{18}O_{49}$/g-C_3N_4 revealed enhanced electrochemical performance compared with that of WO_3/g-C_3N_4 and WO_2/WO_3/g-C_3N_4 heterostructures. In addition, the layered heterostructures consisted of $W_{18}O_{49}$ and amorphous g-C_3N_4 revealed outstanding photodegradation performances under visible light

irradiation (about 4 times higher than that of the pristine g-C_3N_4), while the $W_{18}O_{49}$/crystalline g-C_3N_4 layered heterostructure exhibited superior H_2 evolution activity. Moreover, WS_2/g-C_3N_4 composites showed enhanced photocatalytic activities in comparison with the pristine g-C_3N_4 due to efficient separation of photogenerated charge carriers. Under full solar spectrum irradiation, the photocatalytic performance of WS_2/crystalline g-C_3N_4 composite is about 5.7 times higher than that of pristine g-C_3N_4. In comparison with the g-C_3N_4(650&700)/WS_2 composite samples with lower g-C_3N_4 crystallinity, WS_2/g-C_3N_4(750) composite was examined to have the highest activity towards photodegradation and photocurrent response measurement.

6.5 References

[1] Y. Liu, J. Wang, P. Yang, RSC Adv., 2016, 6, 34334-34341.

[2] K. S. Lakhi, D. H. Park, K. Al-Bahily, W. Cha, B. Viswanathan, J. H. Choy, A. Vinu, Chem. Soc. Rev., 2017, 46, 72-101.

[3] Z. Chen, X. Yu, Q. Zhu, T. Fan, Q. Wu, L. Zhang, J. Li, W. Fang, X. Yi, Carbon, 2018, 139, 189-194.

[4] X. Yu, T. Fan, W. Chen, Z. Chen, Y. Dong, H. Fan, W. Fang, X. Yi, Carbon, 2019, 144, 649-658.

[5] Y. Zhang, T. Mori, L. Niu, J. Ye, Energy Environ. Sci., 2011, 4, 4517-4521.

[6] X. Ma, Y. Lv, J. Xu, Y. Liu, R. Zhang, Y. Zhu, J. Phys. Chem. C, 2012, 116, 23485-23493.

[7] Y. Hong, C. Li, D. Li, Z. Fang, B. Luo, X. Yan, H. Shen, B. Mao, W. Shi, Nanoscale, 2017, 9, 14103-14110.

[8] Z. Liu, G. Wang, H.nS. Chen, P. Yang, Chem. Comm., 2018, 54, 4720-4723.

[9] L. Shi, Z. Li, K. Marcus, G. Wang, K. Liang, W. Niu, Y. Yang, Chem. Comm., 2018, 54, 3747-3750.

[10] X. Bai, L. Wang, R. Zong, Y. Zhu, J. Phys. Chem. C, 2013, 117, 9952-9961.

[11] M. Tahir, C. Cao, N. Mahmood, F.K. Butt, A. Mahmood, F. Idrees, S. Hussain, M. Tanveer, Z. Ali, I. Aslam, ACS Appl. Mater. Interfaces, 2014, 6, 1258-1265.

[12] Y. Liu, X. Zhang, J. Wang, P. Yang, Phys. Chem. Chem. Phys., 2016, 18, 31513-31520.

[13] Y. Liu, X. Zhang, J. Wang, P. Yang, RSC Adv., 2016, 6, 112581-112588.

[14] B. Zhu, J. Zhang, C. Jiang, B. Cheng, J. Yu, Appl. Catal. B: Environ., 2017, 207, 27-34.

[15] D. Huang, Z. Li, G. Zeng, C. Zhou, W. Xue, X. Gong, X. Yan, S. Chen, W. Wang, M. Cheng, Appl. Catal. B: Environ., 2019, 240, 153-173.

[16] D. Xu, B. Cheng, W. Wang, C. Jiang, J. Yu, Appl. Catal. B: Environ., 2018, 231, 368-380.

[17] D. Xu, B. Cheng, S. Cao, J. Yu, Appl. Catal. B: Environ., 2015, 164, 380-388.

[18] D. Xu, B. Cheng, J. Zhang, W. Wang, J. Yu, W. Ho, J. Mater. Chem. A, 2015, 3, 20153-20166.

[19] Y. He, L. Zhang, B. Teng, M. Fan, Environ. Sci. Tech., 2015, 49, 649-656.

[20] W. Yu, D. Xu, T. Peng, J. Mater. Chem. A, 2015, 3, 19936-19947.

[21] B. Zhu, P. Xia, Y. Li, W. Ho, J. Yu, Appl. Surf. Sci., 2017, 391, 175-183.

[22] M. A. Cortes-Jácome, M. Morales, C. Angeles Chavez, L. F. Ramírez-Verduzco, E. López-Salinas, J. A. Toledo-Antonio, Chem. Mater., 2007, 19, 6605-6614.

[23] F. Wang, C. Di Valentin, G. Pacchioni, ChemCatChem, 2012, 4, 476-478.

[24] K. Wang, Y. Shi, Q. Dong, Y. Li, S. Wang, X. Yu, M. Wu, T. Ma, J. Phys. Chem. Lett., 2015, 6, 755-759.

[25] X. H. Jiang, Q. J. Xing, X. B. Luo, F. Li, J. P. Zou, S. S. Liu, X. Li, X. K. Wang, Appl. Catal. B: Environ., 2018, 228, 29-38.

[26] X. Shi, L. Cai, I.Y. Choi, M. Ma, K. Zhang, J. Zhao, J. K. Kim, J. K. Kim, X. Zheng, J.H. Park, J. Mater. Chem. A, 2018, 6, 19542-19546.

[27] C. Wang, Y. Zhao, L. Zhou, Y. Liu, W. Zhang, Z. Zhao, W. N. Hozzein, H. M. S. Alharbi, W. Li, D. Zhao, J. Mater. Chem. A, 2018, 6, 21550-21557.

[28] Q. Mi, A. Zhanaidarova, B. S. Brunschwig, H. B. Gray, N. S. Lewis, Energy Environ. Sci., 2012, 5, 5694-5700.

[29] X. Feng, Y. Chen, Z. Qin, M. Wang, L. Guo, ACS Appl. Mater. Interfaces, 2016, 8, 18089-18096.

[30] T. Paik, M. Cargnello, T. R. Gordon, S. Zhang, H. Yun, J. D. Lee, H.Y. Woo, S. J. Oh, C. R. Kagan, P. Fornasiero, C. B. Murray, ACS Energy Lett., 2018, 3, 1904-1910.

[31] A. Shi, H. Li, S. Yin, J. Zhang, Y. Wang, Appl. Catal. B: Environ., 2018, 228, 75-86.

[32] X. Zhang, J. P. Veder, S. He, S. P. Jiang, Chem. Comm., 2019, 55, 1233-1236.

[33] Q. Han, C. Hu, F. Zhao, Z. Zhang, N. Chen, L. Qu, J. Mater. Chem. A, 2015, 3, 4612-4619.

[34] R. Ye, H. Fang, Y. Z. Zheng, N. Li, Y. Wang, X. Tao, ACS Appl. Mater. Interfaces, 2016, 8, 13879-13889.

[35] G. Zhang, A. Savateev, Y. Zhao, L. Li, M. Antonietti, J. Mater. Chem. A, 2017, 5, 12723-12728.

[36] K. Deng, Z. Hou, X. Deng, P. Yang, C. Li, J. Lin, Adv. Func. Mater., 2015, 25, 7280-7290.

[37] C. Jia, X. Zhang, K. Matras-Postolek, B. Huang, P. Yang, Carbon, 2018, 139, 415-426.

[38] X. Zhang, C. Jia, Y. Xue, P. Yang, RSC Adv., 2017, 7, 43888-43893.

[39] Z. Jiang, X. Zhang, J. Wang, L. Chen, H. S. Chen, P. Yang, Chem. Comm., 2018, 54, 13519-13522.

[40] X. Wu, H. Li, J. Su, J. Zhang, Y. Feng, Y. Jia, L. Sun, W. Zhang, M. Zhang, C. Zhang, Appl. Surf. Sci., 2019, 473, 992–1001.

[41] J. Chen, X. Xiao, Yi, Wang, Z. Ye, J. Alloys Compd., 2019, 777, 325-334.

Chapter 7: NiCo-layered double hydroxide/g-C_3N_4 heterostructures with enhanced adsorption capacity and photoreduction of Cr(VI)*

Abstract

Photocatalytic reduction of highly toxic Cr(VI) to Cr(III) using graphitic carbon nitride (g-C_3N_4) based photocatalyst under visible light irradiation condition has been attracting considerable attention recent years. In this chapter, horizontal growth of completely homogeneous NiCo-layered double hydroxides (LDHs) nanoparticles on g-C_3N_4 nanosheets with different degrees of crystallinity (amorphous to crystalline) is introduced. The adsorption performance of g-C_3N_4/NiCoLDH composites were tested under visible light irradiation for congo red (CR) photodegradation and hexavalent chromium ion (Cr(VI)) photoreduction. The presence of NiCoLDH nanoparticles promotes the adsorption of the anionic pollutants while g-C_3N_4 in the composite system promotes fast photodegradation of CR and reduction of Cr(VI). The g-C_3N_4/NiCoLDH composite prepared using amorphous-crystalline g-C_3N_4 homojunctions as the base material shows the best adsorption performance. The kinetic data reveal improved correlation coefficient for the pseudo-second-order (R_2>0.99) and Freundlich isotherm model. A drastically improved photogenerated charge carrier separation efficiency is observed for the g-C_3N_4/NiCoLDH composite sample, thus improving the Cr(VI) adsorption and photo-reduction performance of the sample. The maximum monolayer adsorption capacities of CR and Cr(VI) ions for sample LDH-700 are 1100 and 46 mgg^{-1} (at 30 °C), respectively. These may provide novel perspectives for the study of highly efficient g-C_3N_4-based composites photocatalysts for wastewater treatment related applications.

Reprinted (adapted) with permission from Xiao Zhang, Ping Yang, and San Ping Jiang, Horizontally-grown NiCo-LDHs on g-C_3N_4 nanosheets with enhanced adsorption capacity and photoreduction efficiency of Congo red and Cr(VI), Appl. Sur. Sci., 2021, https://doi.org/10.1016/j.apsusc.2021.149772.

7.1 Introduction

Development of composite materials for wastewater treatment and other pollution related fields have been drawing tremendous attention due to crisis facing the globe including water shortage. Various organic and inorganic pollutants in the wastewater system have been generated by various sources e.g. battery manufacturing industry, printing and cosmetic industry etc. [1-7]. Among them, organic dye pollutants with high intrinsic toxicity and mutagenicity are extremely stable and are hard to be degraded completely [2-3]. Inorganic pollutants including toxic metal ions are another group of extremely toxic contaminants in water. For instance, high valence chromium ions (including Cr(VI)) are strong oxidizers that can induce cancer and other diseases, as well as harm living organisms [8-12].

The removal of pollutants in wastewater by using semiconducting photocatalyst (e.g. layered double hydroxides (LDHs)), has been considered to be one promising approach for wastewater treatment due to the relatively efficient utilization of solar energy [4]. Cr(VI) is a commonly encountered longstanding pollutant in wastewater. Various methods and materials have been developed to remove anionic pollutants for wastewater treatment applications including adsorption, ion exchange, biosorption and photodegradation [13, 14]. Adsorption and photocatalytic degradation under visible light irradiation are two of the most commonly used methods for Cr(VI) reduction and removal of organic dye pollutants due to their ease of operation and low-cost nature. Among the various materials developed, LDHs and their composites are the most popular and commonly used adsorbents for organic pollutants and heavy metal ions [15]. LDHs are hydrotalcite-like anionic compounds with high specific surface area and high pore volume, and are made up of positively charged layered metal hydroxide and intercalated anion/water with excellent anion exchange capability [16, 17]. In case of adsorption removal of heavy metal ions (e.g. Cr(VI) ion, and other toxic heavy metal cations) and organic dyes (e. g. congo red (CR)), the hydroxide ions attracted by the positive charges on the LDH surface and the charge compensating anions, tend to form metal hydroxide with heavy metal ions and other ionic bonding species [17]. Ni, Co, Fe, Mn, Mg and Al are popular choices of doping elements for promoting water treatment performance [18-23]. Carbon-based LDHs composite materials have been widely used in environmental, energy conversion and storage related area including supercapacitor, inorganic and organic pollutants

treatment and water splitting etc. [24-28].

To achieve efficient removal of organic pollutants and heavy metal ions in wastewater, combinations of different methods can be used, for instance, the combination of adsorption and photocatalytic degradation methods. g-C_3N_4, as a key member of the carbon nitride allotrope family, is one of the most promising carbon-based material for promoting photocatalytic degradation activities under visible light irradiation, especially g-C_3N_4 with relatively high crystallinity [29]. The adsorption capacity of g-C_3N_4 is relatively low due to its limited number of polar functional groups and lower specific surface area [5]. LDHs/g-C_3N_4 composite materials are expected to be effective photoelectro-catalysts for removal of organic and metal pollutants by taking the advantage of adsorption capacity of LDHs and high photocatalytic activities of g-C_3N_4. Ou et. al. reported a CoFe-LDH/g-C_3N_4 composite prepared using co-precipitation and calcination method for the removal of Cr(VI) via adsorption and photocatalytic reduction under visible light irradiation condition. The CoFe-LDH component of the composite material possesses high Cr (VI) adsorption efficiency while the g-C_3N_4 nanosheets component possesses excellent photocatalytic activity that can promote reduction of Cr (VI) to Cr (III). 100 % Cr(VI) removal was achieved after 90 min [5]. Hu et. al. developed a hollow NiCo-alloy@g-C_3N_4 microtubule composite using a multi-step calcination method with excellent microwave adsorption capacity in 2–18 GHz frequency range [21]. The activity and performance of LDH/g-C_3N_4 composite materials are related to the intrinsic properties of both LDH and g-C_3N_4 as well as the microstructure of the combined composites.

In this chapter, NiCo-LDH nanoparticles were grown on highly crystalline g-C_3N_4 nanosheets to form a heterostructure. The control of interface reactions leads to completely homogeneous distribution of NiCo-LDH nanoparticles on the g-C_3N_4 substrate and resulted in intimate interfacial contact between NiCo-LDHs and g-C_3N_4 nanosheets. The highly crystalline g-C_3N_4 substrate used as the base material in the composites is also a key for enhancing the photocatalytic activities of the material [30]. Under visible light irradiation, the as-synthesized composite material showed excellent activity and stability for achieving pollutants adsorption and photodegradation. The NiCo-LDHs plays the key role in alleviating CR and Cr(VI) while highly crystalline g-C_3N_4 substrate promotes photodegradation of organic dyes.

7.2 Experimental

7.2.1 Chemicals and fabrication of g-C_3N_4

Chemicals including $Ni(NO_3)\cdot 6H_2O$, $Co(NO_3)\cdot 6H_2O$, urea, CR and $K_2Cr_2O_7$ were purchased from Sigma Aldrich. 1,5-diphenylcarbohydrazide was purchased from Aladdin Bio-Chem Technology Co. LTD. All chemicals used for sample fabrication and characterization were used without further purification. g-C_3N_4 substrate materials were prepared using the similar method as introduced in chapter 3 [29]. The g-C_3N_4 nanosheets substrate was fabricated via a two-step calcination method. Bulk g-C_3N_4 sample (g-C_3N_4(600)) was prepared via calcination at 600 ºC by using melamine as the precursor. The g-C_3N_4 nanosheets samples (g-C_3N_4(600), g-C_3N_4(700), g-C_3N_4(750)) were obtained by polymerization of bulk g-C_3N_4 at 650, 700 and 750 °C respectively.

Table 7-1. Preparation conditions and composition.

Sample	Synthesis method	Composition
g-C_3N_4(600)	One-step calcined	g-C_3N_4
g-C_3N_4(650)	Two-step calcined	g-C_3N_4
g-C_3N_4(700)	Two-step calcined	g-C_3N_4
g-C_3N_4(750)	Two-step calcined	g-C_3N_4
NiCoLDH	Hydrothermal	NiCo-LDH
LDH-600,	Hydrothermal	NiCo-LDH/g-C_3N_4(600ºC)
LDH-650,	Hydrothermal	NiCo-LDH/g-C_3N_4(650ºC)
LDH-700	Hydrothermal	NiCo-LDH/g-C_3N_4(700ºC)
LDH-750	Hydrothermal	NiCo-LDH/g-C_3N_4(750ºC)

7.2.2 Fabrication of NiCo-LDHs and NiCo-LDHs/g-C_3N_4 composite

A one-step hydrothermal treatment method was used for the fabrication of NiCo-LDHs and NiCo-LDHs immobilized g-C_3N_4 nanocomposites. $Ni(NO_3)\cdot 6H_2O$ (1 mmol) and $Co(NO_3)\cdot 6H_2O$ (1 mmol) were mixed in 100 mL of ethanol to form a NiCo precursor solution. A solution consisted of 30 mg of g-C_3N_4 powder and a mixture of 25 mL of ethanol and 0.05 mmol of urea was stirred for 5 min, followed by addition of 5 mL of NiCo precursor solution and stirring for 10 min. The mixture solution was then poured into a hydrothermal reactor and kept in an oven at 120 °C for 12 hours. The obtained powder sample was centrifuged and washed with ethanol for several times. The precipitates were then dried at 80 °C for 12 hours. By using different g-C_3N_4 base polymerized at different temperature settings (600, 650, 700

and 750 °C), four NiCoLDHs immobilized g-C_3N_4 samples were synthesized and were denoted as LDH-600, LDH-650, LDH-700, and LDH-750, respectively. The pristine NiCoLDHs were also synthesized following the same process as for the NiCo-LDHs/g-C_3N_4 composites but with no g-C_3N_4 addition. Table 7-1 illustrates the preparation conditions and compositions.

7.2.3 Characterization

The XRD patterns of the synthesized samples were obtained on Bruker D8 X-ray diffractometer (Germany) using a Cu Kα radiation source. SEM and TEM images were taken to characterise the morphology of the composite samples (QUANTA 250 FEG for SEM, Titan G2 80-200 TEM/STEM with Chemi STEM Technology for TEM, FEI company, US). XPS measurements were carried out on Kratos Axis Ultra DLD spectrometer with the monochromatic Al Kα (1486.6 eV) X-rays source operating at 150 W, the data were collected using a passing energy of 40 eV for the high-resolution spectra and were processed using Casa XPS software. FTIR spectra data were obtained using Nicolet 380 FTIR spectrometer (within 4000-400 cm^{-1} frequency range). The specific surface area of samples was recorded via N_2 adsorption-desorption test by using a multi-functional adsorption instrument (MFA-140, Builder Company, China) to obtain the pore size distribution of samples via Brunauer-Emmett-Teller (BET) analysis.

7.2.4 CR adsorption and photodegradation

CR adsorption efficiency of the composite samples were studied. 10 mg of each samples was mixed with 25 mL of CR solution (10-200 mgL^{-1}), and the pH level was maintained at around 7. The mixture solution was then agitated for 12 hours at 30 °C. To study the kinetics of CR adsorption, a small amount of the mixture solution was taken out from the container from time to time, and the concentration of CR in the supernatant solutions was measured using UV-Vis spectrophotometer (Hitachi U-4100) at 500 nm. CR adsorption capacity q (mg/g) can be estimated using the following equations,

$$q_e = \frac{(C_0 - C_e)V}{W} \quad (7\text{-}1)$$

$$q_t = \frac{(C_0 - C_t)V}{W} \quad (7\text{-}2)$$

where q_e is the amount of CR absorbed at equilibrium, q_t is the amount of CR absorbed at time t (min); C_0 is the initial concentration of CR (mgL^{-1}); C_t and C_e are the concentration of

CR at time t and at equilibrium, respectively; W and V correspond to the mass of adsorbent (g) and the initial volume of CR solution (L).

The kinetics of the CR adsorption can be obtained by data fitting using different kinetics models,

$$\ln(q_e - q_t) = \ln(q_e) - \frac{k1}{2.303}t \quad (7\text{-}3)$$

$$\frac{t}{q_t} = \frac{1}{q_e}t + \frac{1}{k_2 q_e^2} \quad (7\text{-}4)$$

$$q_t = k_i\sqrt{t} + C \quad (7\text{-}5)$$

For the equations shown above, eq. 7-3 is the equation for Pseudo first order model, eq. 9-4 is the one for the Pseudo second order model and eq. 9-5 is the equation for Intraparticle diffusion model. C is the intercept; k_1 and k_2 are the Pseudo first order rate constant (min^{-1}) and Pseudo-second-order rate constant (g mg^{-1} min^{-1}), respectively; k_i is the Intraparticular diffusion rate constant (mg g^{-1} $min^{-0.5}$).

CR adsorption isotherm measurements were also performed on the NiCo-LDHs/g-C_3N_4 samples. 10 mg of sample and 25 mL of 50 mgL^{-1} CR solution were mixed in a sealed Erlenmeyer flask followed by shaking at 30 °C (150 rpm). Certain amount of the NiCo-LDHs/g-C_3N_4 composites solution was then taken at different predetermined time points followed by centrifugation to remove precipitates from the supernatant solution. To measure the concentration of CR in the obtained supernatant solution, a UV-Vis spectrophotometer (Hitachi U-4100) was used at 500 nm. To analyze the adsorption isotherm data of the samples, Freundlich isotherm model (eq. 7-6) and Langmuir equation (eq. 7-7) can be used for adsorption isotherm data fitting,

$$\ln(q_e) = \frac{1}{n}\ln(C_e) + \ln(K_F) \quad (7\text{-}6)$$

$$\frac{C_e}{q_e} = \frac{C_e}{q_m} + \frac{1}{K_L q_m} \quad (7\text{-}7)$$

where K_F and 1/n are the Freundlich adsorption equilibrium constant ((mgg^{-1}) $(mgL^{-1})^n$) and linearity index, respectively; K_L and q_m are the Langmuir adsorption equilibrium constant (Lmg^{-1}) and monolayer adsorption capacity of adsorbents (mgg^{-1}), respectively.

7.2.5 Cr(VI) adsorption and photodegradation

Cr(VI) solutions with concentrations ranged from 5 to 50 mgL^{-1} were prepared by mixing

$K_2Cr_2O_7$ with deionized water. The composites sample (10 mg) was mixed with 25 mL of Cr(VI) solution (10 mgL^{-1}) followed by agitation in a 150 rpm shaker at 30 °C. 2 mL of the mixture solution were then taken out from the container at certain time intervals followed by immediate filtration using 0.45 μm microfiltration membranes. The concentration of Cr(VI) in the remaining filtrate were studied using a UV-Vis spectrophotometer (Hitachi U-4100) at 540 nm. Cr(VI) adsorption isotherm measurements were done by varying the initial concentration of Cr(VI) solution in the range of 5 to 50 mgL^{-1}.

7.3 Results and discussion

7.3.1 Microstructure

Fig. 7-1a shows the XRD patterns of pristine NiCoLDH sample and selected LDH-700 composites. The XRD peaks at 11.6, 23.5, 33.9, and 59.0 degree correspond to the (003), (006), (012), (018) facets of LDH, respectively. For sample LDH -700, the peaks of LDH phase were observed but their positions were shifted towards a smaller angle. The XRD peak of g-C_3N_4 with relatively high intensity was observed. This confirms the formation of the crystalline/amorphous homojunctions of g-C_3N_4 nanosheets during the thermal condensation process at 700 °C [29]. The result of XRD analysis confirms successful deposition of NiCoLDH on g-C_3N_4 nanosheets. Fig. 7-1b shows the EDS spectrum of sample 700-LDH. Sharp peaks of Ni, Co, and O components were observed, confirming the one-step formation of NiCoLDH on g-C_3N_4.

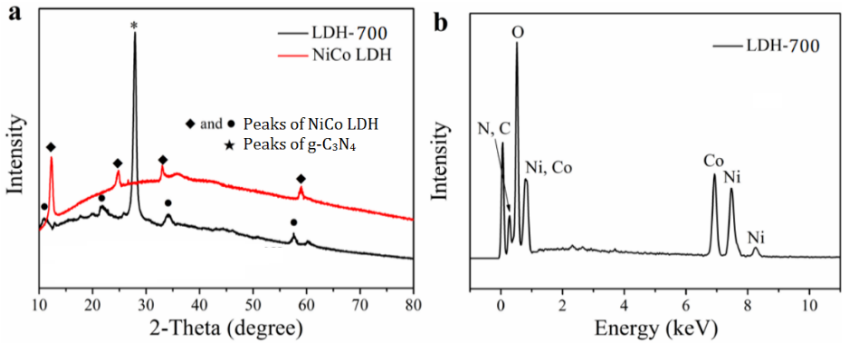

Figure 7-1. (a) XRD patterns of LDH-700 composites and pristine NiCoLDHs sample. (b) EDS spectrum of LDH -700 composites.

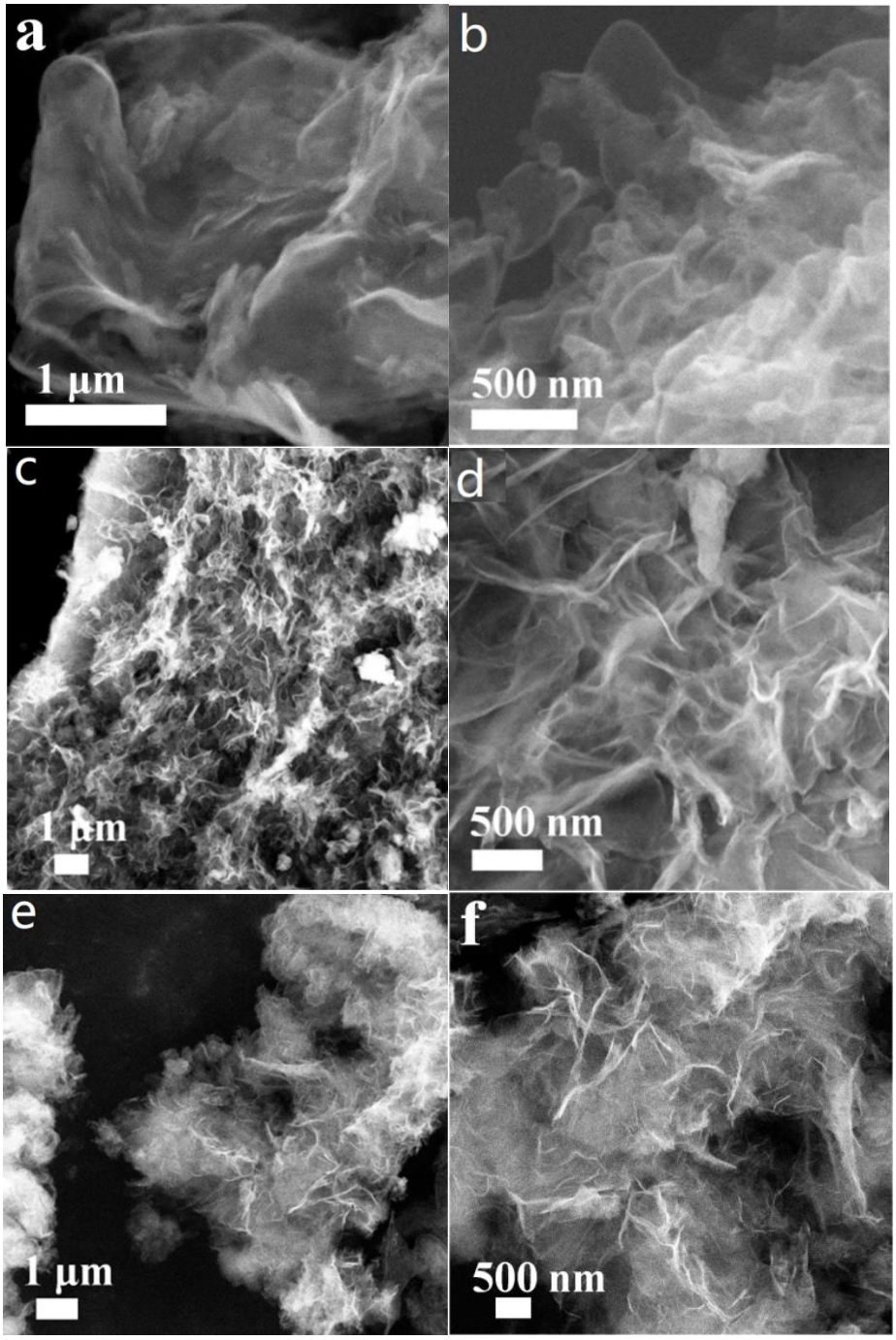

Figure 7-2. SEM images of (a, b) g-C_3N_4(700), (c, d) NiCoLDH, and (e, f) LDH-700.

Fig. 7-2 shows the SEM images of pristine g-C_3N_4, NiCoLDHs and selected NiCoLDH/g-C_3N_4 composite samples. The pristine g-C_3N_4 sample shows a typical nanosheets morphology (Fig. 7-2a and 2b), indicating the formation of ultrathin g-C_3N_4 nanosheets via thermal condensation of bulk g-C_3N_4 at high temperature. In case of pristine NiCoLDH sample, aggregated nanosheets morphology was observed (Fig. 7-2c and 2d). However, the size of the NiCoLDH nanosheets appears to be much smaller in comparison with that of the g-C_3N_4

nanosheets. In situ deposition of NiCoLDH leading to change in surface morphology of g-C_3N_4 nanosheets occurred for the composite sample (Fig. 7-2e and 2f). Homogeneous distribution of NiCoLDHs on the g-C_3N_4 substrate was achieved as shown in Fig. 7-2f. The nanosheets with different morphologies observed for the samples in Fig. 7-2 confirms the formation of NiCoLDHs nanoparticles on surface of g-C_3N_4 substrate. Similar microstructure was also observed for other NiCoLDH/g-C_3N_4 composite samples.

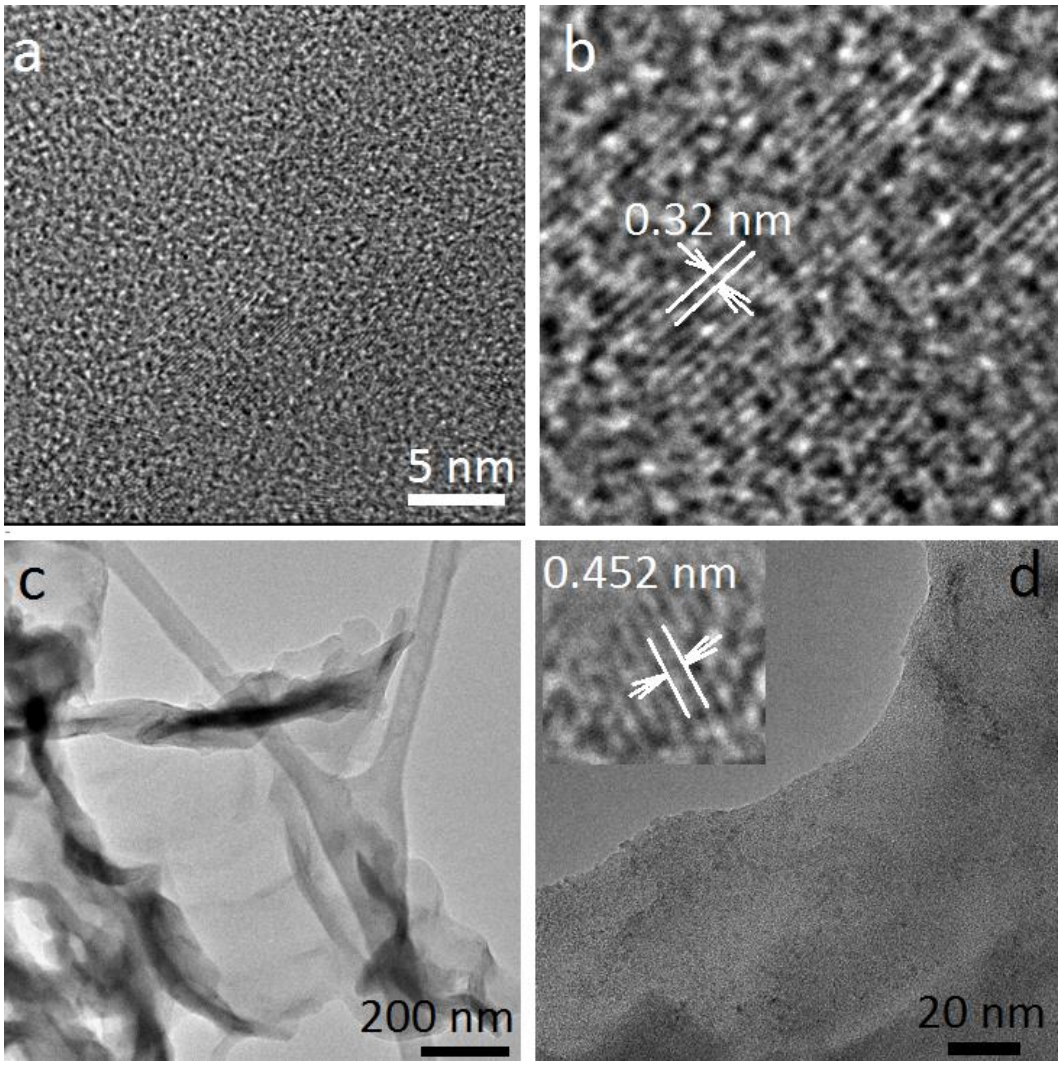

Figure 7-3. TEM images of (a, b) g-C_3N_4 polymerized at 700 °C and (c, d) LDH-700. The inset in (d) shows an enlarged image of TEM observation for LDH-700 with lattice fringes of NiCoLDH phase.

The phase formation of g-C_3N_4 and LDH-700 was further examined by using high resolution TEM and the results are shown in Fig. 7-3. The g-C_3N_4 sample polymerized at 700 ºC shows semi-crystalline feature with lattice fringes of 0.32 nm corresponding to the g-C_3N_4 (002) facet (Fig. 7-3b). Since highly crystalline g-C_3N_4 can be obtained at relatively high calcination

temperature (750 °C), clear lattice fringes of ~ 0.452 nm for (006) facet (associated with NiCoLDHs component) were observed on the surface of g-C_3N_4 (Fig. 7-3d), indicating the existence of layered NiCoLDHs nanoparticles on surface of g-C_3N_4 substrate [31]. However, only limited amount of NiCoLDHs was deposited onto the g-C_3N_4 substrate as observed in the TEM images.

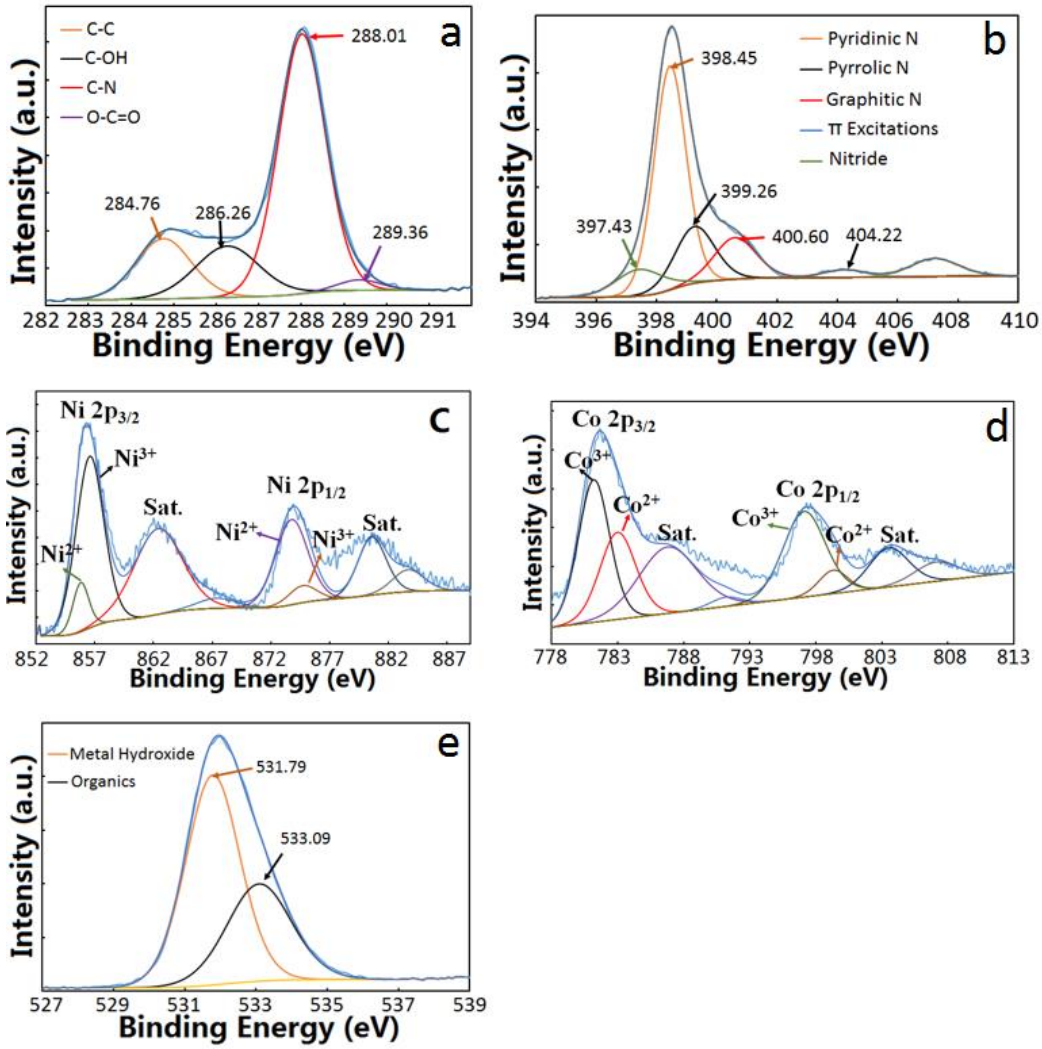

Figure 7-4. XPS spectra of sample LDH-700: (a) C 1s, (b) N 1s, (c) Ni 2p, (d) Co 2p, and (e) O 1s.

The XPS spectra of NiCoLDHs immobilized g-C_3N_4 sample were analyzed and Fig. 7-4 shows the results for sample LDH-700. The C 1s high resolution spectrum shows four typical C 1s peaks at 284.76 (C-C), 286.26 (C-OH), 288.01 (C-N) and 289.36 eV (O-C=O) (Fig. 7-4a). In case of N 1s spectra, four peaks at 398.45, 399.26, 400.60, and 397.43 eV were observed (Fig. 7-4b), corresponding to C-N=C (Pyridinic-N), N-$(C)_3$ (Pyrrolic-N), N-H (graphitic N)

and nitride peak, respectively [29, 32]. Ni 2p spectra in Fig. 7-4c were fitted into two main peaks at 856.29 and 874.10 eV (corresponding to Ni $2p_{3/2}$ and Ni $2p_{1/2}$ peak respectively) and two main shake-up satellite peaks (denoted as "Sat." in Fig. 7-4c and 4d) at 862.38 and 880.60 eV. The Ni $2p_{3/2}$ and Ni $2p_{1/2}$ peaks were fitted into two spin-orbit doublets of Ni^{2+} and Ni^{3+}, indicating Ni species to have two oxidation states in the composites. Peaks centered at 855.80 and 873.76 eV are attributed from Ni^{2+} species whereas the other two peaks are from Ni^{3+} species [33-37]. Fig. 7-4d shows the Co 2p spectra with two main peaks located at 781.64 and 797.38 eV to be the Co $2p_{3/2}$ and Co $2p_{1/2}$ peak. Two main shake-up satellite peaks at 786.79 and 791.19 eV were also observed. Two peaks at 783 and 799.31 eV referring to Co^{2+} peaks were obtained by fitting the doublets. The peaks centered at 781.20 and 797.12 eV can be assigned to the Co^{3+} peak which is also the main valence state due to their relatively strong signal comparing to that of Co^{2+} species in literature [36]. The O 1s spectra with two peaks at 531.79 and 533.09 eV are shown in Fig. 7-4e. The peaks observed correspond to the O species of Ni(Co)OH and the -OH groups of the adsorbed H_2O on the surface of the composites, respectively.

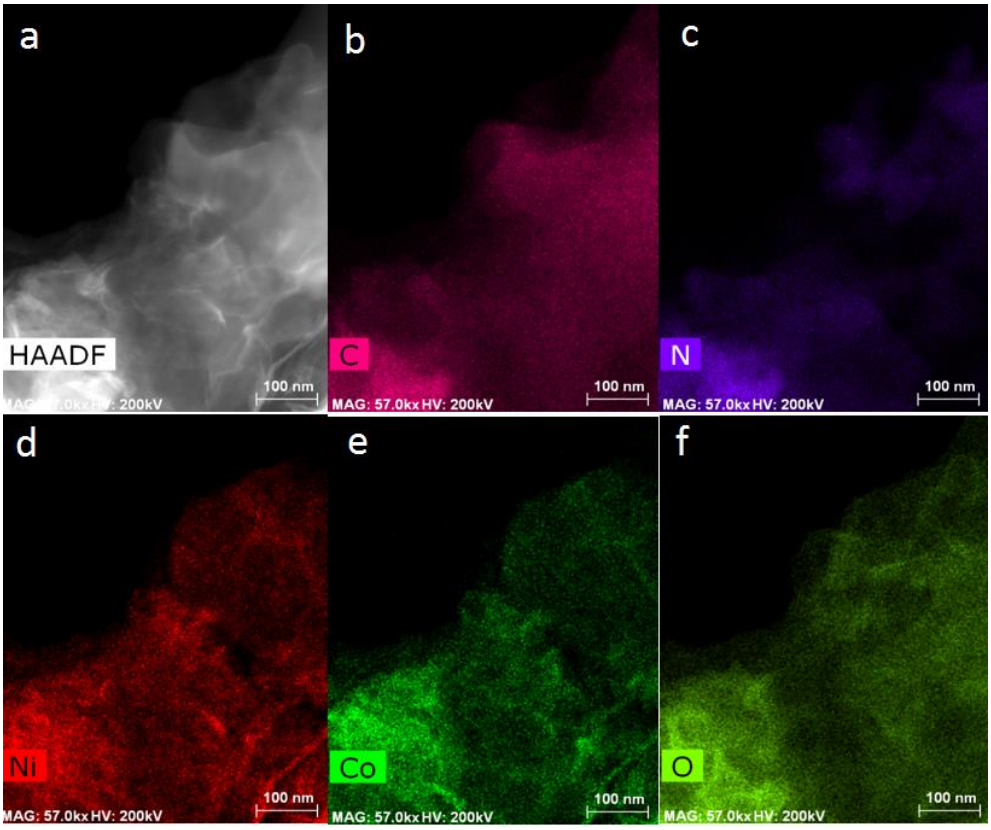

Figure 7-5. HAADF-STEM image (a) and elemental mapping of C (b), N (c), Ni (d), Co (e), and O (f) for sample LDH-700.

The composition of LDH-700 composite (e.g., Ni, Co, and O components of the sample) was studied using HAADF-STEM images and the corresponding elemental mapping (Fig. 7-5). Homogeneous distribution of C and N components was observed. Ni, Co, and O elements were observed on the entire region of g-C_3N_4 nanosheets as shown in Fig. 7-5d to 5f. These confirms the homogeneous distributions of Ni, Co, and O on g-C_3N_4 substrate with no aggregation of NiCoLDHs particles been observed. The proportion of Ni and Co observed in the mapping appears to be quite high (Fig. 7-5d and 5e), indicating the formation of nanosheets type NiCoLDHs in the composite sample.

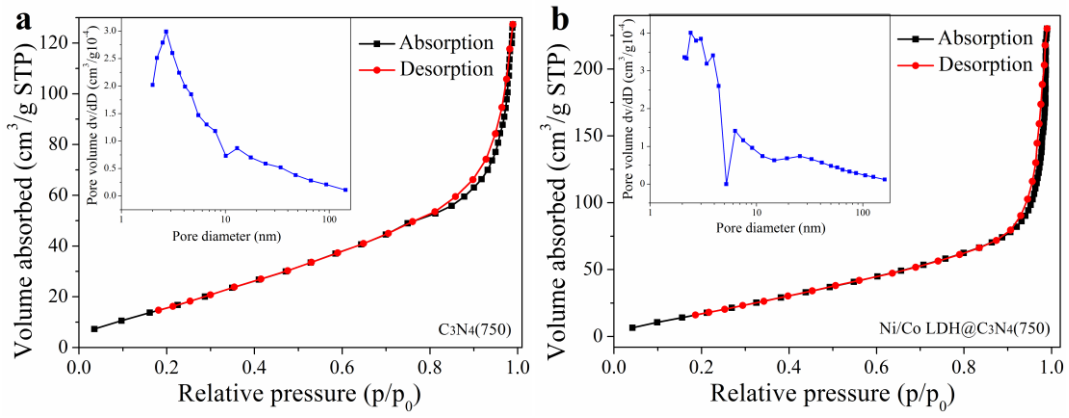

Figure 7-6. Nitrogen adsorption-desorption isotherm curves of bulk g-C_3N_4(700) and LDH-700. The insets show the distribution plots of the average pore size of these samples.

The specific surface area of pristine g-C_3N_4 and LDH-700 composites sample was measured using BET analysis (shown in Fig. 7-6). The mesoporous structure of g-C_3N_4 and LDH-700 composites reveals type VI adsorption isotherm based on the nitrogen adsorption-desorption data collected. The specific surface area of g-C_3N_4 and LDH-700 composites sample are 85.1 and 130.1 m^2g^{-1}, respectively. And the corresponding pore sizes of the samples are 2.0 and 2.5 nm, respectively.

Table 7-2. BET data of the samples.

Sample	BET surface area (m^2/g)	Pore volume (cm^3/g)	Average pore diameter (nm)
g-C_3N_4(750)	75.0	0.16	2.0
g-C_3N_4(700)	85.1	0.19	2.1
g-C_3N_4(650)	96.2	0.23	2.2
LDH-750	130.0	0.36	2.5
LDH-700	130.1	0.38	2.5
LDH-650	140.3	0.43	2.6

LDH-700 composite sample shows a much higher specific surface area due to the formation of nanosheets type NiCoLDHs on g-C_3N_4. No huge differences in the pore size of the samples were observed. However, an obvious change in pore distribution was observed as shown in the insets of the pore distribution plots in Fig. 7-6. Table 7-2 lists the BET specific surface area, pore volume and average pore diameter of the samples.

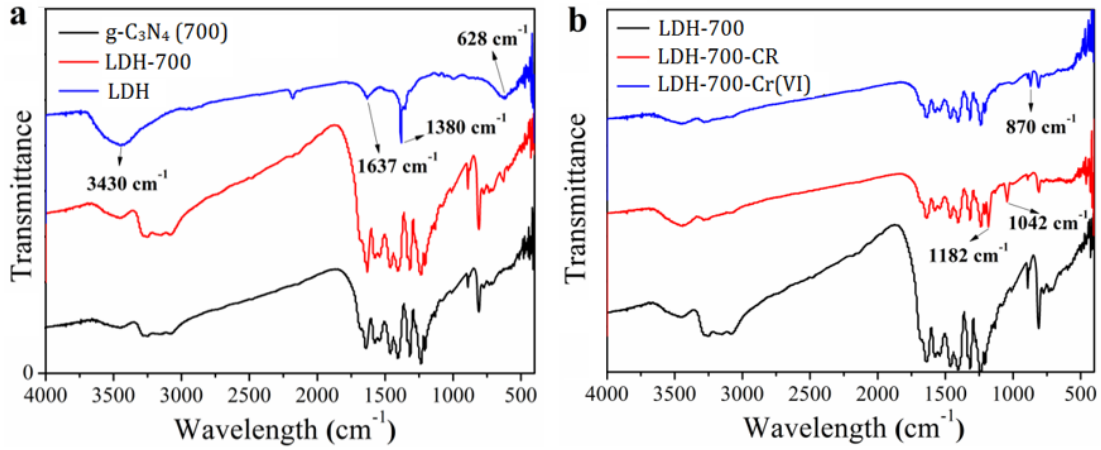

Figure 7-7. FTIR spectra of sample: (a) sample g-C_3N_4, LDH-700, and pristine NiCoLDH; (b) sample LDH-700 after CR and Cr(VI) adsorption comparing with that of the pristine LDH-700 sample.

7.3.2 Adsorption and photocatalytic activities

The FTIR spectra of samples g-C_3N_4(700), LDH -700, and pristine NiCoLDH are shown in Fig. 7-7a. Fig. 7-7b shows the FTIR spectra of sample LDH-700 after CR and Cr(VI) adsorption. The vibration peak associated with primary -OH groups at 3430 cm^{-1} was observed. Shift of position of this vibration peak can be observed for different samples. The stretching vibration of the structural unit of triazine ring in g-C_3N_4 nanosheets is related to the peak at 804 cm^{-1} while the vibration peaks of the structural skeleton of triazine ring is associated with the peaks located in 1650 to 1200 cm^{-1} region [38]. The absorption band from 3400 to 3010 cm^{-1} is attributed to the stretching vibration of terminal -NH_2 and -NH groups derived from incomplete polycondensation of g-C_3N_4 [39]. Typical stretching vibration peaks of NiCo-LDH are located at 1637, 1380, and 382 cm^{-1}. The FTIR spectrum of sample LDH-700 shows stretching vibration peaks of both g-C_3N_4 and NiCo-LDH. After CR adsorption, two additional stretching vibration peaks at 1182 and 1042 cm^{-1} were observed, suggesting successful adsorption of CR. In addition, a stretching vibration peak at 870 cm^{-1} associated with Cr(VI) ions was observed as shown in Fig. 9-7b.

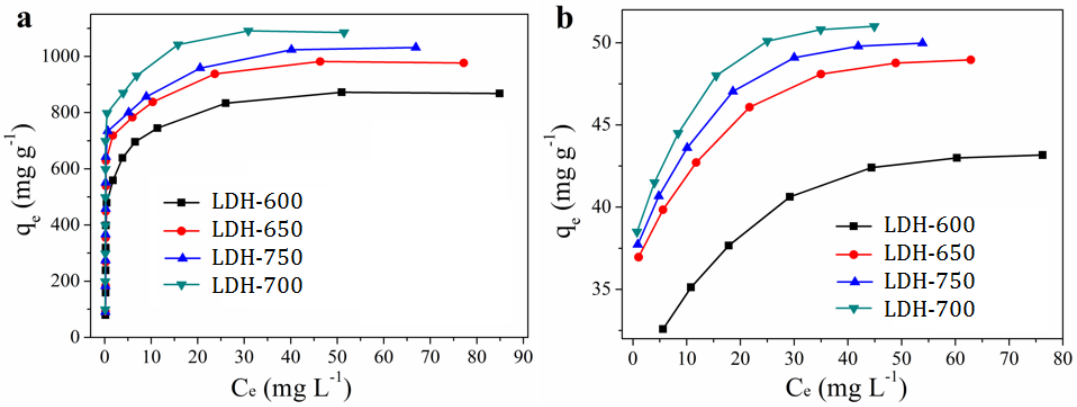

Figure 7-8. Adsorption isotherms of (a) CR and (b) Cr(VI) for LDH-600, LDH-650, LDH-700 and LDH-750 composite samples.

Adsorption isotherms of CR and Cr(VI) species for NiCoLDHs/g-C_3N_4 composite samples were studied to investigate the adsorption capacity of the sample at various equilibrium adsorbate concentrations and the results are shown in Fig. 7-8. Among the samples tested, it is evident that LDH-700 revealed the best CR and Cr (VI) removal efficiency. The high adsorption efficiency of LDH-700 is most likely due to the amorphous and crystalline structural features of g-C_3N_4 substrate polymerized at 700 ^oC [29]. Due to the presence of amorphous/crystalline homojunctions, the separation efficiency of photogenerated electron and hole pairs was enhanced, leading to improved Cr(VI) ions photoreduction efficiency. In addition, the g-C_3N_4 homojunction also possesses more accessible active sites thus resulting in enhanced CR adsorption efficiency.

Fig. 7-9a shows the CR adsorption kinetics curves of g-C_3N_4 and LDH-700 composites using different reaction models. It is clear that both samples exhibited fast CR adsorption kinetics, however, a much higher adsorption capacity was observed for LDH-700 composites comparing with that of pristine g-C_3N_4 sample. The experimental data were fitted by pseudo-first-order and pseudo-second-order model. According to R_2 values and the lowest value of residual root mean square error, the adsorption kinetics of CR can be explained by the pseudo-second-order model for g-C_3N_4 and LDH-700 ($R_2 > 0.99$), suggesting that chemical bondings were formed between CR and adsorbents [19]. The results are shown in Fig. 7-9c and 9d. The pseudo-second-order model demonstrates that CR adsorption was dominated by chemical adsorption rather than physical interaction in case of LDH-700 composite sample.

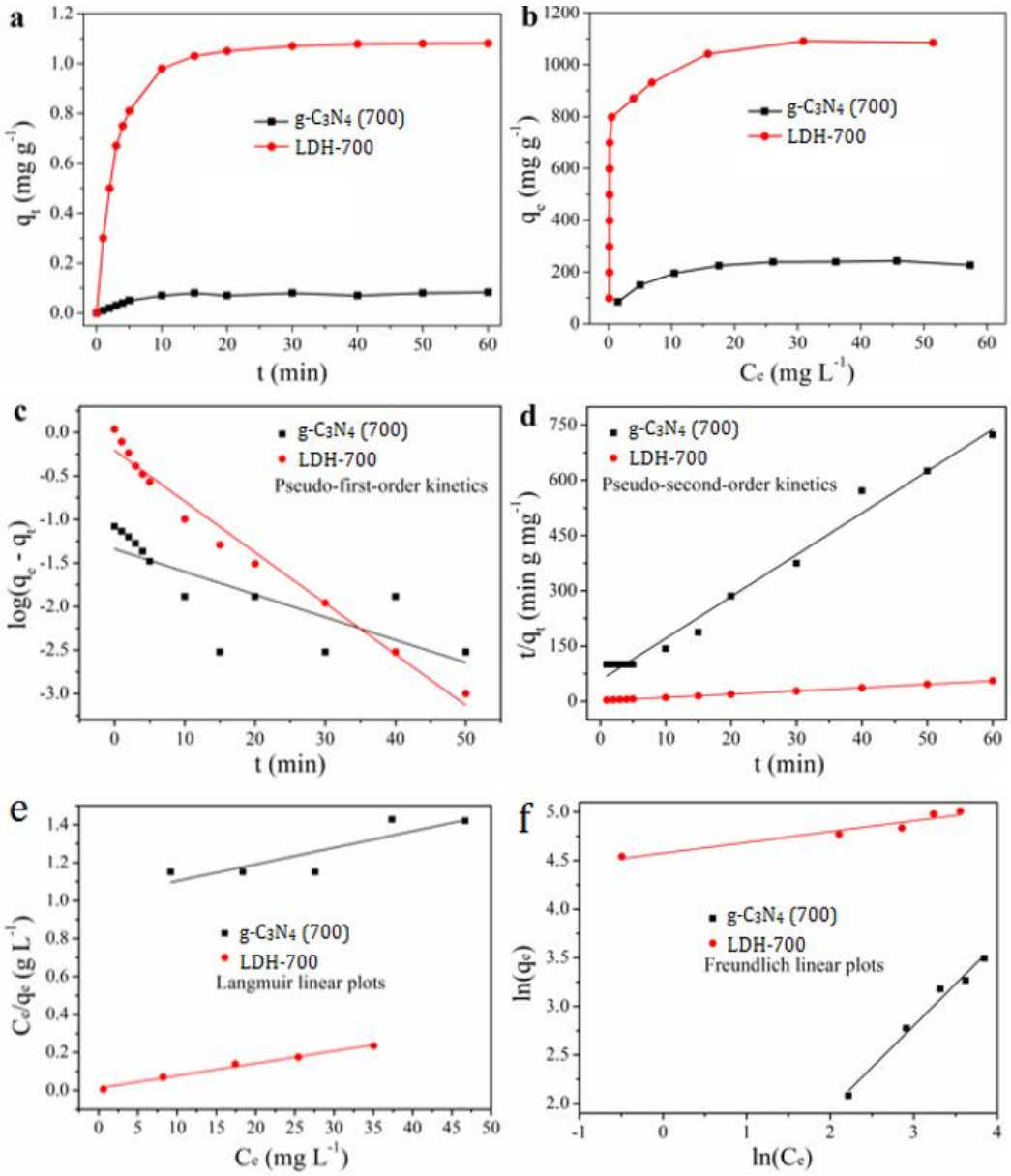

Figure 7-9. (a) CR adsorption kinetics plots of sample g-C_3N_4(700) and LDH-700 at different time intervals. (b) CR adsorption isotherms of g-C_3N_4(700) and LDH-700 sample at 30 °C. (c) Pseudo-first-order plots. (d) Pseudo-second-order plots. (e) Langmuir linear plots. (f) Freundlich linear plots.

To investigate the CR equilibrium adsorption capacity of g-C_3N_4/NiCoLDH composites, the adsorption isotherm experiments were performed to examine the interaction between the adsorbent and adsorbate at equilibrium. Fig. 7-9b shows the adsorption isotherms of CR on g-C_3N_4 and LDH-700 at 30 °C. The maximum CR monolayer adsorption capacities of LDH-700 were 1100 mgg^{-1} at 30 °C. The data for adsorption isotherms were fitted using Langmuir and Freundlich models as shown in Fig. 7-9e and 9f. In general, Langmuir model demonstrates that

adsorbed molecules or ions are attached to the adsorbent surface in a single layer form while Freundlich model suggests that the adsorbent surface has heterogeneous adsorption sites and that the adsorbed molecules or ions have mutual effects on each other [4]. The results indicate that Freundlich model fits better for LDH-700 composite sample.

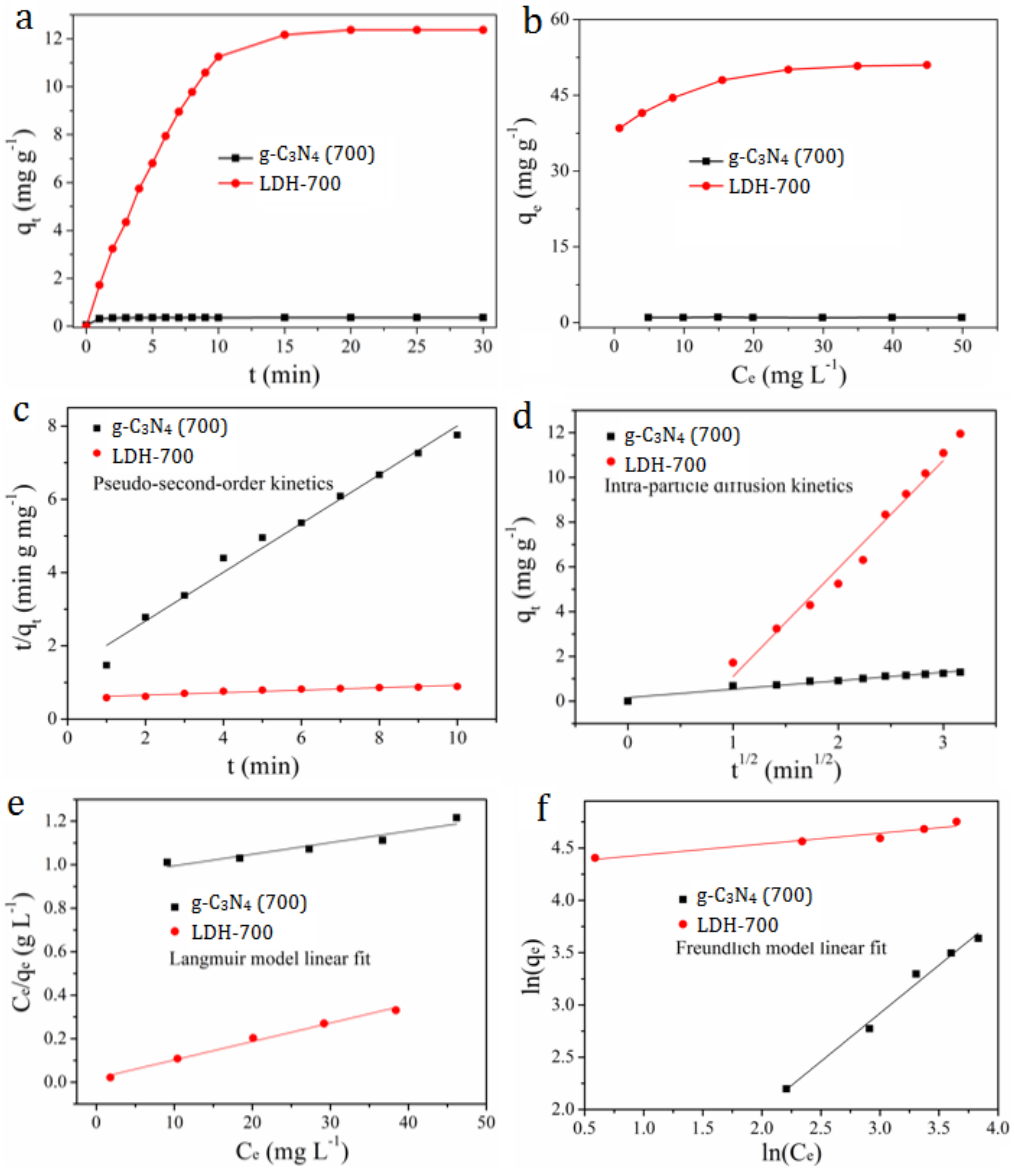

Figure 7-10. (a) Cr(VI) adsorption capacity at different time intervals for sample g-C_3N_4(700) and LDH-700; (b) Cr(VI) adsorption isotherms of sample g-C_3N_4(700) and LDH-700 at 30 °C; (c) pseudo-second-order, (d) intra-particle diffusion kinetics, (e) Langmuir linear plots and (f) Freundlich linear plots for Cr(VI) adsorption.

Fig. 7-10a shows the Cr(VI) adsorption kinetic plots for sample g-C_3N_4(700) and LDH-700. Sample LDH-700 revealed higher Cr(VI) adsorption capacity compared with that of g-C_3N_4. The adsorption dynamics data were simulated by pseudo-second-order and intra-particle

diffusion kinetic models as shown in Fig. 7-10. The equilibrium adsorption calculated using the pseudo-second-order model is more consistent with the experimental data. The Cr(VI) adsorption process involves 3 steps: rapid transport of Cr(VI) ions occurs from the liquid phase to the surface of adsorbents; adsorbates ions then enter the internal pores of the adsorbent from the surface via diffusion; and dynamic equilibrium of adsorption achieved as the final stage. Fig. 7-10b shows the Cr(VI) adsorption isotherms of g-C_3N_4(700) and LDH-700 at 30 °C. The maximum Cr(VI) monolayer adsorption capacity for LDH-700 composites was 46 mgg^{-1} at 30 °C (Fig. 7-10b). Langmuir and Freundlich models were used to fit the experimental data (shown in Fig. 7-10e and 10f). It was determined that Langmuir model fits better for sample LDH-700 compared with using Freundlich model. LDH-700 composites revealed decent adsorption performance compared with that of pristine g-C_3N_4.

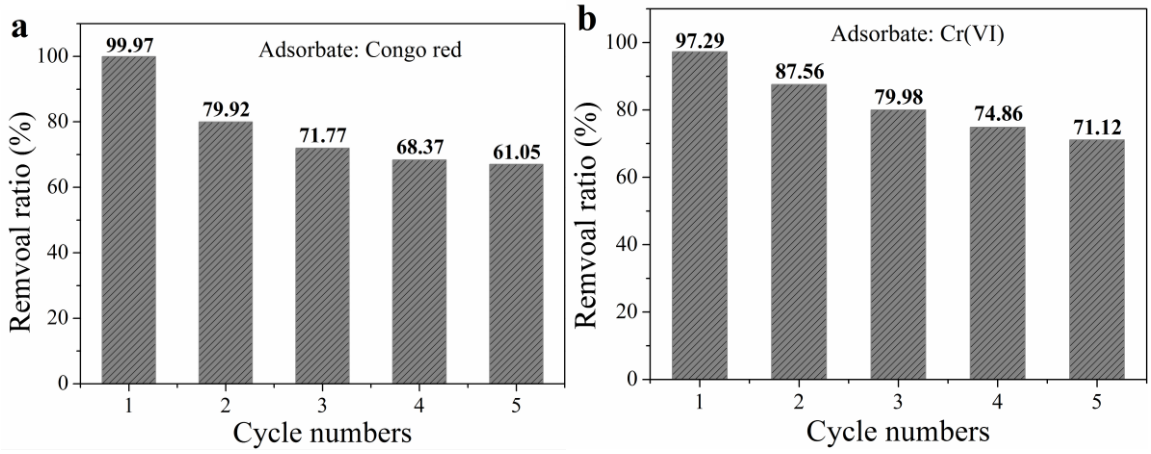

Figure 7-11. Cyclic stability of LDH-700 composite sample for CR (a) and Cr(VI) (b) removal.

The cyclic stability of the adsorbents is vital for achieving practical applications. The solution of the adsorbents after adsorption test was collected by centrifugation to desorb using 15 % diluted ammonia. The obtained powder sample was used for further adsorption test after washing. Fig. 7-11 shows the CR and Cr(VI) removal ratio for sample LDH-700 as a function of cyclic test numbers. After 5 cycles, the CR and Cr(VI) removal ratios of LDH-700 composite remained at 61.05 and 71.2 %, respectively, indicating that the cyclic stability of LDH-700 was not good enough. The decreased removal ratio can be ascribed to the incomplete desorption.

Scheme 7-1 shows the schematic diagram of photocatalytic reduction mechanism for g-C_3N_4/NiCoLDHs composites. The photoreduction process of Cr(VI) to Cr(III) is related to the reduction and oxidation process of Cr ions with the support from various photogenerated

radicals [40]. Under visible light irradiation, photogenerated electron-hole pairs were separated at the presence of g-C_3N_4 nanosheets. The electrons were excited to conduction band (e_{CB}^-) to generate $^{\cdot}O_2^-$ which reacts with Cr(VI) to form Cr(V) and finally forming Cr(III). Due to the presence of positively charged surface of the NiCoLDHs, the CR adsorption occurred through ion exchange with anionic ions exist in the interlayers of NiCoLDHs. In addition, π–π stacking interaction occurs between the benzene rings of CR molecules and g-C_3N_4 nanosheets to achieve anionic dye adsorption. Moreover, -NH_2 groups in CR molecules interact with the -OH groups in g-C_3N_4/NiCoLDHs composites to form hydrogen bondings. The FTIR spectra of g-C_3N_4/NiCoLDHs composites before and after Cr(VI) and CR adsorption (Fig. 7-7) confirms the existence of these functional groups, one of them is the -OH peak of water molecules at ~3430 cm^{-1}, two functional groups peaks from CR at ~1182 and 1042 cm^{-1}, as well as one peak associated with the Cr(VI) ions at ~870 cm^{-1}.

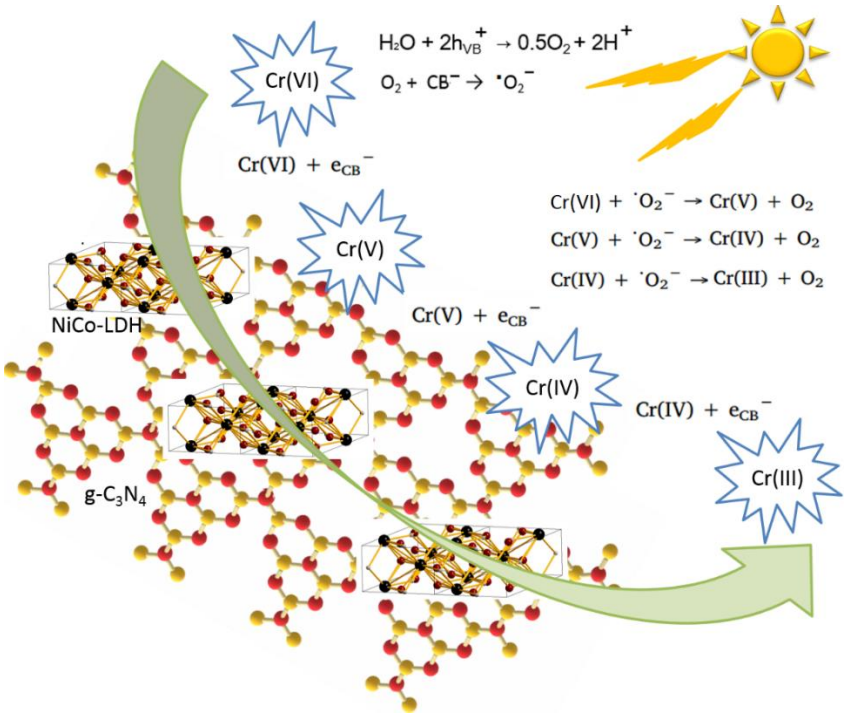

Scheme 7-1. Schematic diagram of photocatalytic reduction mechanism for g-C_3N_4/NiCoLDHs composites.

7.4 Conclusions

Small NiCoLDHs nanoparticles were horizontally-grown on crystalline/amorphous g-C_3N_4 nanosheets to form a novel heterojunction for high-efficient Cr(VI) photoreduction. A series of characterizations confirmed the formation of the ternary heterojunctions. Under optimized

preparation conditions, the obtained g-C_3N_4/NiCoLDHs composites (sample LDH-700) exhibited high CR removal efficiency with high adsorption capacity and excellent reusability for Cr(VI) reduction. The positively charged surface of the g-C_3N_4/NiCoLDHs composites can promote the separation of photogenerated charge carriers and extend the contact time between the Cr ions and absorbent molecules. According to the adsorption data, the adsorption kinetics can be explained by pseudo-second-order model; the adsorption isotherms follow the Freundlich model for CR removal; and Langmuir model fits for photo-reduction and oxidation of Cr(VI). The maximum monolayer adsorption capacities of CR and Cr(VI) ions for sample LDH-700 are 1100 and 46 mgg^{-1} (at 30 °C), respectively. These may provide novel perspectives for the study of highly efficient g-C_3N_4-based composite photocatalysts for water treatment related applications, and offer novel insights for construction of potential adsorbents for Cr(VI)-containing wastewater treatment.

7.5 References

[1] L. A. Kafshgari M. Ghorbani A. Azizi, Appl. Surf. Sci., 2017, 419, 70–83.

[2] P. Jha R. Jobby N. S. Desai, J. Hazard. Mater., 2016, 311, 158–167.

[3] C. Lei, M. Pi, B. Cheng, C. Jiang, J. Qin, Appl. Surf. Sci., 2018, 435, 1002–1010.

[4] Y. Zheng, B. Cheng, W. You, J. Yu, W. Ho, J. Hazard. Mater., 2019, 369, 214–225.

[5] B. Ou, J. Wang, Y. Wu, S. Zhao, Z. Wang, Chem. Eng. J., 2020, 380, 122600.

[6] M. P. Nascimentoa, R. C. Souzab, I. M. Miguela, H. J. C. Voorwalda, Surf. Coat. Tech., 2001, 138, 113–124.

[7] M. Daud, A. Hai, F. Banat, M. B. Wazir, M. Habib, C. Bharath, A. Harthi, J. Mol. Liq., 2019, 288, 110989.

[8] D. J. Paustenbach, B. L. Finley, F. S. Mowat, B. D. Kerger, J. Toxicol. Environ. Heal. A, 2003, 66, 1295–1339.

[9] K. P. Nickens, S. R. Patierno, S. Ceryak, Chem. Biol. Interact., 2010, 188, 276–288.

[10] C. M. Thompson, A. Bichteler, J. E. Rager, M. Suh, D. M. Proctor, L. C. Haws, M. A. Harris, Mutat. Res. Genet. Toxicol. Environ. Mutagen., 2016, 800–801, 28–34.

[11] C. Liu, R. N. Jin, X. k. Ouyang, Y. G. Wang, Appl. Surf. Sci., 2017, 408, 77–87.

[12] M. Liu, T. Wen, X. Wu, C. Chen, J. Hu, J. Li, X. Wang, Dalton Trans., 2013, 42, 14710–

14717.

[13] Z. Yang, J. Wei, G. Zeng, H. Zhang, X. Tan, C. Ma, X. Li, Z. Li, C. Zhang, Coord. Chem. Rev., 2019, 386, 154–182.

[14] Y. Xing, X. Chen, D. Wang, Environ. Sci. Technol., 2007, 41, 1439–1443.

[15] Q. Takashi, K. Tamaoki, NSaitoh, A. Higashi, Y. Konishi, Biochem. Eng. J., 2012, 63, 129–133.

[16] T. Kwon, G. A. Tsigdinos, T. J. Pinnavaia, J. Am. Chem. Soc., 1988, 110, 3653–3654.

[17] M. J. Barnabas, S. Parambadath, A. Mathew, S. S. Park, A. Vinu, C. Ha, J. Solid State Chem., 2016, 233, 133–142.

[18] C. Lei, X. Zhu, B. Zhu, C. Jiang, Y. Le, J. Yu, J. hazard. Mater., 2017, 321, 801–811.

[19] S. Chen, Y. Huang, X. Han, Z. Wu, C. Lai, J. Wang, Q. Deng, Z. Zeng, S. Deng, Chem. Eng. J., 2018, 352, 306–315.

[20] Q. Wang, X. Feng, C. Shi, Ind. Eng. Chem. Res., 2018, 57, 12478−12484.

[21] S. Hu, Y. Zhou, M. He, Q. Liao, H. Yang, H. Li, R. Xu, Q. Ding, Mater. Lett., 2018, 231, 171–174.

[22] F. Mohamed, M. R. Abukhadra, M. Shaban, Sci. Total Environ., 2018, 640/641 () 352–363.

[23] Y. Xie, X. Yuan, Z. Wu, G. Zeng, L. Jiang, X. Peng, H. Li, J. Colloid. Inter. Sci., 2019, 536, 440–455.

[24] B. Bayatsarmadi, Y. Zheng, A. Vasileff, S. Z. Qiao, Small, 2017,13, 1700191.

[25] X. Wang, K. Maeda, A. Thomas, K. Takanabe, G. Xin, J. M. Carlsson, K. Domen, M. Antonietti, Nat. Mater., 2009, 8, 76-80.

[26] G. Zhang, S. Zang, X. Wang, ACS Catal., 2015, 5, 941−947.

[27] J. Yang, C. Yu, X. Fan, J. Qiu, Adv. Energy Mater., 2014, 4, 1400761.

[28] X. Li, J. Shen, W. Sun, X. Hong, R. Wang, X. Zhao, J. Mater. Chem. A, 2015, 3, 13244–13253.

[29] X. Zhang, J. P. Veder, S. He, S. P. Jiang, Chem. Comm., 2019, 55, 1233-1236.

[30] X. Zhang, S. He, S. P. Jiang, Carbon, 2020, 156, 488-498.

[31] X. Zhang, P. Wang, P. Yang, S. P. Jiang, Inter. J. hydrog. Energy, 2020, 45, 21523-21531.

[32] C. Jia, X. Zhang, K. Matras-Postolek, B. Huang, P. Yang. Carbon, 2018, 139, 415-426.

[33] T. Dong, X. Zhang, M. Li, P. Wang, P. Yang, Inorg. Chem. Front., 2018, 5, 3033-3039.

[34] K. Bu, S. Kuboon, J. Deng, H. Li, T. Yan, G. Chen, L. Shi, D. Zhang, Appl. Cata. B: Environ., 2019, 252, 86–97.

[35] D. B. Jiang, C. Jiang, Y. Yuan, L. Feng, X. Liu, F. Dong, B. Dong, Y. X. Zhang, J. Colloid. Inter. Sci., 2019, 540, 398–409.

[36] L. Yue, D. Jia, J. Tang, A. Zhang, F. Liu, T. Chen, C. Barrow, W. Yang, J. Liu, J. Colloid Inter. Sci., 2020, 560, 237–246.

[37] H. Hua, J. Liu, Z. Xu, L. Zhang, B. Cheng, Appl. Sur. Sci., 2019, 478, 981–990.

[38] J. Abdi, M. Vossoughi, N. M. Mahmoodi, I. Alemzadeh, Chem. Eng. J., 2017, 326, 1145–1158.

[39] J. Xu, Q. Z. Gao, X. J. Bai, Z. P. Wang, Y. F. Zhu, Catal. Today, 2019, 332, 227–235.

[40] J. M. Meichtry, M. Brusa, G. Mailhot, M. A. Grela, M. I. Litter, Appl. Catal. B: Environ., 2007, 71, 101–107.

Chapter 8: Summary and Future Work

8.1 Summary

The objective of this PhD project is the development of new synthesis methods to fabricate layered g-C_3N_4 and g-C_3N_4-based composites (with controllable crystallinity, nano-scale morphology and hetero/homostructure) as effective photo-/electro-catalytic materials for H_2 generation, pollutants photodegradation, tunable and stable photoluminescence (PL) materials. Effects of metallic atom doping on photo-/electro-catalytic activities of g-C_3N_4 nano-structured catalysts has also been investigated. In addition, doped CNTs have also been synthesized from rolling-up of layered g-C_3N_4 at high calcination conditions and their electrochemical properties were also investigated. The achievements of the PhD project are summarized as below:

- Superior thin and layered g-C_3N_4 nanocomposites with yellow or red colour and/or crystalline/amorphous lateral-like homostructures were successfully synthesized and their photo-/electro-chemical performances were studied. The highly crystalline g-C_3N_4 and g-C_3N_4 homojunction possess decent photogenerated charge carrier separation efficiencies, resulting in improved photo-/electro-catalytic performances of the material. The g-C_3N_4 homojunction composites show the best RhB degradation efficiency and a photocatalytic H_2 evolution efficiency of 2312 $\mu molh^{-1}g^{-1}$ (in visible light condition) that is much higher than that observed on amorphous and crystalline g-C_3N_4. The red-coloured superior thin g-C_3N_4 nanosheets have a bandgap of 1.9 eV and redshifted absorption spectrum, revealing bright, stable, concentration-dependent photoluminescence (PL) within blue to yellow region as well as outstanding PL stability. Most interestingly, a lateral-like homostructures (red-coloured g-C_3N_4 nanosheets powder) consisted of light-yellow graphitic carbon nitride and red graphitic carbon nitride gave a high PL efficiency of ~ 75 %, and the PL efficiency of the sample remained almost unchanged after 6 months.
- Spine-like g-C_3N_4 cages were synthesized and their photocatalytic H_2 evolution and CO_2 reduction were studied. The H_2 evolution efficiency of the hollow spine-like g-C_3N_4 cages (4000 $\mu molg^{-1}h^{-1}$) is 7.3 times higher than that of the normal bulk g-C_3N_4

nanosheets. The g-C_3N_4 cages showed quite high CH_4 evolution activity (about 8.7 times as much as that of the normal bulk g-C_3N_4). Moreover, the CH_4 generation rate of Pt-loaded g-C_3N_4 cages was about 3 time higher than that of the pristine g-C_3N_4 cages without adding any co-catalyst or sacrificial agent. The relatively negative conduction band position of the hollow spine-like g-C_3N_4 cages (in comparison with that of the bulk g-C_3N_4 nanosheets) favours photocatalytic reduction reactions.

- $W_{18}O_{49}$/g-C_3N_4 and WS_2/WO_x/g-C_3N_4 layered heterostructures were constructed for enhancing charge carrier separation and expanding photo-absorption. The amorphous $W_{18}O_{49}$/g-C_3N_4 layered heterostructures showed enhanced photocatalytic degradation performances under visible light irradiation (4 times higher than that of pristine g-C_3N_4). The crystalline $W_{18}O_{49}$/g-C_3N_4 layered heterostructure exhibited excellent hydrogen generation efficiency (7 times higher than that of pristine g-C_3N_4). The WS_2/WO_x composite layered heterostructures showed a high H_2 evolution rate under full solar spectrum irradiation (5.7 times higher than that under visible light irradiation). In addition, heterostructures formed by using g-C_3N_4 with the highest crystallinity as base possess the highest photodegradation activity and highest photocurrent response rate.
- A composite material consisted of horizontally grown and homogeneously distributed NiCoLDHs nanoparticles on g-C_3N_4 (with different degrees of crystallinity) was studied for CR photodegradation and Cr(VI)) photoreduction in visible light irradiation condition. The presence of NiCoLDHs promotes the adsorption of the anionic pollutants. The g-C_3N_4/NiCoLDH composites (using amorphous-crystalline g-C_3N_4 homojunctions as substrate) showed the best adsorption activity. The kinetic data of the composites revealed improved correlation coefficient for pseudo-second-order (R_2>0.99) and Freundlich isotherm model. Moreover, accelerated separation of photogenerated charge carriers was observed for g-C_3N_4/NiCoLDH composites with enhanced Cr(VI) adsorption efficiency and Cr(VI) photoreduction activity. The maximum monolayer adsorption capacities of CR and Cr(VI) ions for sample LDH-700 were 1100 and 46 mgg^{-1} (at 30 °C), respectively. These may provide novel perspectives for the study of highly efficient g-C_3N_4-based composites photocatalysts in water treatment related fields.

- Construction of Ni and N-doped carbon nanotubes via calcination of g-C_3N_4 at high temperature was investigated. Metal and MoS_2 (2D dichalcogenides material) immobilization on these nanotubes were studied for electrocatalytic applications. For the Pd and Ni bimetallic catalysts, the Pd NPs were self-assembled onto Ni-N-CNTs by using PDDA as the linking molecule while H_2 treatment was utilized as the final step. The use of linking molecules to achieve ionic bonding with Pd NPs and the use of H_2 as the reducing agents were the two key factors for achieving homogeneous distribution and size control of the immobilized metal particles. The size of the Ni metal particles was within single-atom to 2 nm scale, while the Pd particles were within 2-5 nm scale. Among Pd and Ni immobilized N-CNTs samples with different metal ratios, the 20 wt% Pd CNTs sample showed better HER activity than that of the commercial 40 % Pd/C sample under acidic condition. For Ni (with a Ni_3C shell structure) and MoS_2 nanosheets immobilized N-CNTs, secondary diffusion of Ni nanoparticles occurred during the stage of MoS_2 deposition with the assistance of excess of S precursors. A completely homogeneous distribution of Ni NPs (with particle size < 3 nm on average), clusters, and single atoms in the CNTs and MoS_2 nanosheets was achieved. The MoS_2 nanosheets and Ni NPs incorporated MoNiCNTs composites exhibits outstanding HER performance with low onset potential and small Tafel slope value in both acidic and alkaline conditions.

8.2 Future work

- Development of g-C_3N_4 microstructure with different shapes, for instance, combining spine-like g-C_3N_4 cages with other materials (e.g. layered transition metal nanocomposites).
- Size and composition control of g-C_3N_4-based homojunction and heterostructure as well as g-C_3N_4.
- Improvement of photo-and electro-catalytic activities of CNTs-based composite and g-C_3N_4 materials via metal and non-metal immobilization, also expanding light absorption range towards a variety of applications including energy related and wastewater treatment related fields.

- Investigation of applications of luminescent g-C_3N_4-based and g-C_3N_4 materials in light emitting diodes, bioimaging and medical related fields.

Appendix: Permission of Reproduction from the Copyright Owner

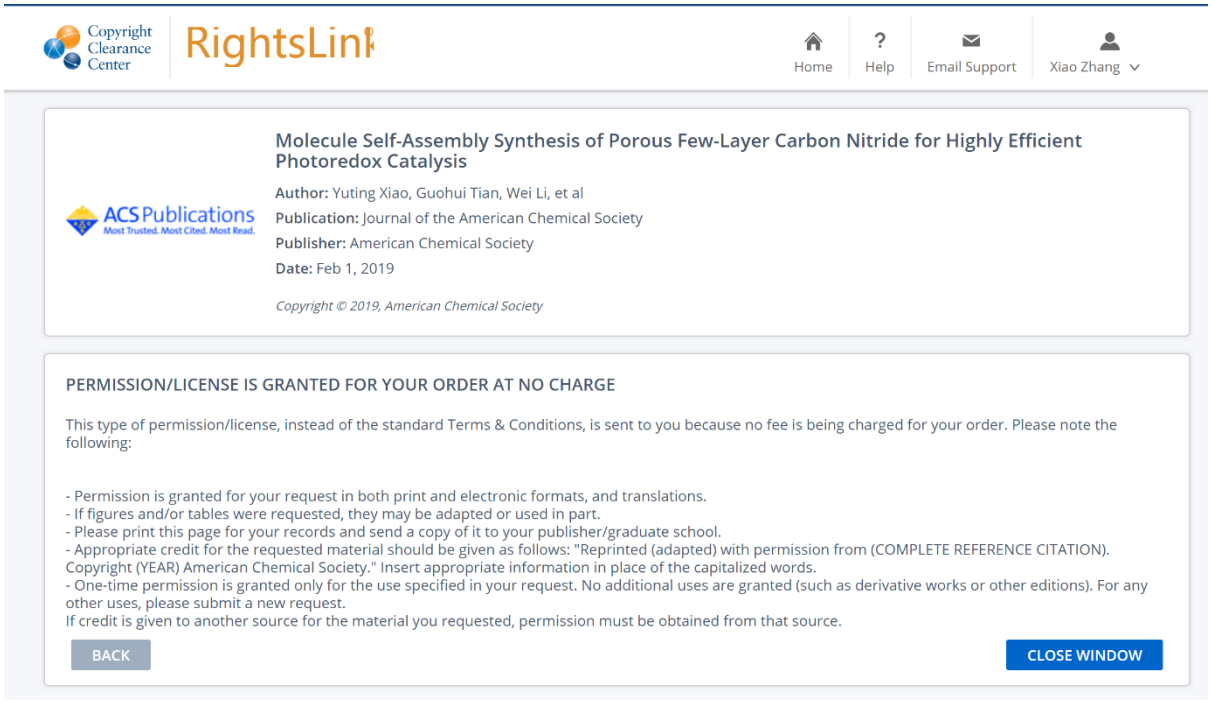

Copyright Clearance Center | RightsLink

Home | Help | Email Support | Xiao Zhang

Molecule Self-Assembly Synthesis of Porous Few-Layer Carbon Nitride for Highly Efficient Photoredox Catalysis

Author: Yuting Xiao, Guohui Tian, Wei Li, et al

Publication: Journal of the American Chemical Society

Publisher: American Chemical Society

Date: Feb 1, 2019

Copyright © 2019, American Chemical Society

PERMISSION/LICENSE IS GRANTED FOR YOUR ORDER AT NO CHARGE

This type of permission/license, instead of the standard Terms & Conditions, is sent to you because no fee is being charged for your order. Please note the following:

- Permission is granted for your request in both print and electronic formats, and translations.
- If figures and/or tables were requested, they may be adapted or used in part.
- Please print this page for your records and send a copy of it to your publisher/graduate school.
- Appropriate credit for the requested material should be given as follows: "Reprinted (adapted) with permission from (COMPLETE REFERENCE CITATION). Copyright (YEAR) American Chemical Society." Insert appropriate information in place of the capitalized words.
- One-time permission is granted only for the use specified in your request. No additional uses are granted (such as derivative works or other editions). For any other uses, please submit a new request.

If credit is given to another source for the material you requested, permission must be obtained from that source.

BACK | CLOSE WINDOW

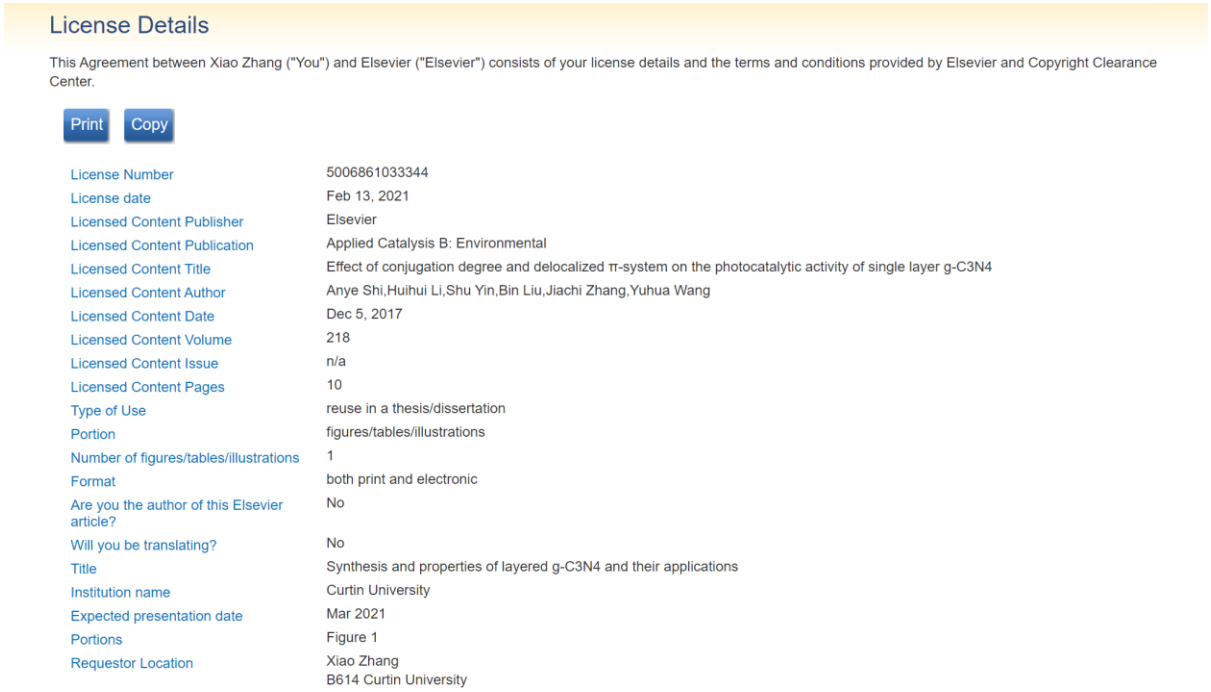

License Details

This Agreement between Xiao Zhang ("You") and Elsevier ("Elsevier") consists of your license details and the terms and conditions provided by Elsevier and Copyright Clearance Center.

Print | Copy

License Number	5006861033344
License date	Feb 13, 2021
Licensed Content Publisher	Elsevier
Licensed Content Publication	Applied Catalysis B: Environmental
Licensed Content Title	Effect of conjugation degree and delocalized π-system on the photocatalytic activity of single layer g-C3N4
Licensed Content Author	Anye Shi,Huihui Li,Shu Yin,Bin Liu,Jiachi Zhang,Yuhua Wang
Licensed Content Date	Dec 5, 2017
Licensed Content Volume	218
Licensed Content Issue	n/a
Licensed Content Pages	10
Type of Use	reuse in a thesis/dissertation
Portion	figures/tables/illustrations
Number of figures/tables/illustrations	1
Format	both print and electronic
Are you the author of this Elsevier article?	No
Will you be translating?	No
Title	Synthesis and properties of layered g-C3N4 and their applications
Institution name	Curtin University
Expected presentation date	Mar 2021
Portions	Figure 1
Requestor Location	Xiao Zhang B614 Curtin University

Salt-Assisted Synthesis of 3D Porous g-C3N4 as a Bifunctional Photo- and Electrocatalyst

Author: Xingyue Qian, Xiaoqian Meng, Jingwen Sun, et al
Publication: Applied Materials
Publisher: American Chemical Society
Date: Jul 1, 2019

PERMISSION/LICENSE IS GRANTED FOR YOUR ORDER AT NO CHARGE

This type of permission/license, instead of the standard Terms & Conditions, is sent to you because no fee is being charged for your order. Please note the following:

- Permission is granted for your request in both print and electronic formats, and translations.
- If figures and/or tables were requested, they may be adapted or used in part.
- Please print this page for your records and send a copy of it to your publisher/graduate school.
- Appropriate credit for the requested material should be given as follows: "Reprinted (adapted) with permission from (COMPLETE REFERENCE CITATION). Copyright (YEAR) American Chemical Society." Insert appropriate information in place of the capitalized words.
- One-time permission is granted only for the use specified in your request. No additional uses are granted (such as derivative works or other editions). For any other uses, please submit a new request.

If credit is given to another source for the material you requested, permission must be obtained from that source.

BACK | CLOSE WINDOW

License Details

This Agreement between Xiao Zhang ("You") and John Wiley and Sons ("John Wiley and Sons") consists of your license details and the terms and conditions provided by John Wiley and Sons and Copyright Clearance Center.

Print | Copy

License Number	5006880903395
License date	Feb 13, 2021
Licensed Content Publisher	John Wiley and Sons
Licensed Content Publication	Advanced Functional Materials
Licensed Content Title	An Unusual Red Carbon Nitride to Boost the Photoelectrochemical Performance of Wide Bandgap Photoanodes
Licensed Content Author	Lianzhou Wang, Jinshu Wang, Yongli Li, et al
Licensed Content Date	Oct 9, 2018
Licensed Content Volume	28
Licensed Content Issue	47
Licensed Content Pages	10
Type of Use	Dissertation/Thesis
Requestor type	University/Academic
Format	Print and electronic
Portion	Figure/table
Number of figures/tables	1
Will you be translating?	No
Title	Synthesis and properties of layered g-C3N4 and their applications
Institution name	Curtin University
Expected presentation date	Mar 2021
Portions	Figure 2
Requestor Location	Xiao Zhang B614 Curtin University Perth, Bentley 6102

License Details

This Agreement between Xiao Zhang ("You") and Elsevier ("Elsevier") consists of your license details and the terms and conditions provided by Elsevier and Copyright Clearance Center.

Print Copy

License Number	5006890440456
License date	Feb 13, 2021
Licensed Content Publisher	Elsevier
Licensed Content Publication	International Journal of Hydrogen Energy
Licensed Content Title	Effect of nonmetal element dopants on photo- and electro-chemistry performance of ultrathin g-C3N4 nanosheets
Licensed Content Author	Yaya Wang,Yongqiang Cao,Yingjie Liu,Ping Yang
Licensed Content Date	Jun 24, 2020
Licensed Content Volume	45
Licensed Content Issue	33
Licensed Content Pages	9
Type of Use	reuse in a thesis/dissertation
Portion	figures/tables/illustrations
Number of figures/tables/illustrations	1
Format	both print and electronic
Are you the author of this Elsevier article?	No
Will you be translating?	No
Title	Synthesis and properties of layered g-C3N4 and their applications
Institution name	Curtin University
Expected presentation date	Mar 2021
Portions	Figure 4
Requestor Location	Xiao Zhang B614 Curtin University Perth, Bentley 6102 Australia Attn: Xiao Zhang
Publisher Tax ID	GB 494 6272 12

License Details

This Agreement between Xiao Zhang ("You") and Elsevier ("Elsevier") consists of your license details and the terms and conditions provided by Elsevier and Copyright Clearance Center.

Print Copy

License Number	5006900367531
License date	Feb 13, 2021
Licensed Content Publisher	Elsevier
Licensed Content Publication	Applied Catalysis B: Environmental
Licensed Content Title	Enhanced photocatalytic hydrogen evolution by partially replaced corner-site C atom with P in g-C3N4
Licensed Content Author	Bin Wang,Hairui Cai,Daming Zhao,Miao Song,Penghui Guo,Shaohua Shen,Dongsheng Li,Shengchun Yang
Licensed Content Date	5 May 2019
Licensed Content Volume	244
Licensed Content Issue	n/a
Licensed Content Pages	8
Type of Use	reuse in a thesis/dissertation
Portion	figures/tables/illustrations
Number of figures/tables/illustrations	1
Format	both print and electronic
Are you the author of this Elsevier article?	No
Will you be translating?	No
Title	Synthesis and properties of layered g-C3N4 and their applications
Institution name	Curtin University
Expected presentation date	Mar 2021
Portions	Figure 1
Requestor Location	Xiao Zhang B614 Curtin University Perth, Bentley 6102 Australia Attn: Xiao Zhang
Publisher Tax ID	GB 494 6272 12
Total	**0.00 AUD**

License Details

This Agreement between Xiao Zhang ("You") and John Wiley and Sons ("John Wiley and Sons") consists of your license details and the terms and conditions provided by John Wiley and Sons and Copyright Clearance Center.

Print Copy

License Number	5006901220401
License date	Feb 13, 2021
Licensed Content Publisher	John Wiley and Sons
Licensed Content Publication	Angewandte Chemie International Edition
Licensed Content Title	Achieving Efficient Incorporation of π-Electrons into Graphitic Carbon Nitride for Markedly Improved Hydrogen Generation
Licensed Content Author	Zhiqun Lin, Zhaoming Xue, Zhen Li, et al
Licensed Content Date	Jan 3, 2019
Licensed Content Volume	58
Licensed Content Issue	7
Licensed Content Pages	5
Type of Use	Dissertation/Thesis
Requestor type	University/Academic
Format	Print and electronic
Portion	Figure/table
Number of figures/tables	1
Will you be translating?	No
Title	Synthesis and properties of layered g-C3N4 and their applications
Institution name	Curtin University
Expected presentation date	Mar 2021
Portions	Figure 1
Requestor Location	Xiao Zhang B614 Curtin University Perth, Bentley 6102 Australia Attn: Xiao Zhang
Publisher Tax ID	EU826007151
Total	**0.00 AUD**

Copyright Clearance Center RightsLink

Home | Help | Email Support | Xiao Zhang

ACS Publications
Most Trusted. Most Cited. Most Read.

Insight into the Crucial Factors for Photochemical Deposition of Cobalt Cocatalysts on g-C3N4 Photocatalysts

Author: Na Zhao, Linggang Kong, Yuming Dong, et al
Publication: Applied Materials
Publisher: American Chemical Society
Date: Mar 1, 2018

PERMISSION/LICENSE IS GRANTED FOR YOUR ORDER AT NO CHARGE

This type of permission/license, instead of the standard Terms & Conditions, is sent to you because no fee is being charged for your order. Please note the following:

- Permission is granted for your request in both print and electronic formats, and translations.
- If figures and/or tables were requested, they may be adapted or used in part.
- Please print this page for your records and send a copy of it to your publisher/graduate school.
- Appropriate credit for the requested material should be given as follows: "Reprinted (adapted) with permission from (COMPLETE REFERENCE CITATION). Copyright (YEAR) American Chemical Society." Insert appropriate information in place of the capitalized words.
- One-time permission is granted only for the use specified in your request. No additional uses are granted (such as derivative works or other editions). For any other uses, please submit a new request.

If credit is given to another source for the material you requested, permission must be obtained from that source.

BACK CLOSE WINDOW

Facile Gel-Based Morphological Control of Ag/g-C3N4 Porous Nanofibers for Photocatalytic Hydrogen Generation

Author: Jiangpeng Wang, Jingkun Cong, Hui Xu, et al
Publication: ACS Sustainable Chemistry & Engineering
Publisher: American Chemical Society
Date: Nov 1, 2017

PERMISSION/LICENSE IS GRANTED FOR YOUR ORDER AT NO CHARGE

This type of permission/license, instead of the standard Terms & Conditions, is sent to you because no fee is being charged for your order. Please note the following:

- Permission is granted for your request in both print and electronic formats, and translations.
- If figures and/or tables were requested, they may be adapted or used in part.
- Please print this page for your records and send a copy of it to your publisher/graduate school.
- Appropriate credit for the requested material should be given as follows: "Reprinted (adapted) with permission from (COMPLETE REFERENCE CITATION). Copyright (YEAR) American Chemical Society." Insert appropriate information in place of the capitalized words.
- One-time permission is granted only for the use specified in your request. No additional uses are granted (such as derivative works or other editions). For any other uses, please submit a new request.

If credit is given to another source for the material you requested, permission must be obtained from that source.

BACK | CLOSE WINDOW

License Details

This Agreement between Xiao Zhang ("You") and John Wiley and Sons ("John Wiley and Sons") consists of your license details and the terms and conditions provided by John Wiley and Sons and Copyright Clearance Center.

Print | Copy

License Number	5006910963234
License date	Feb 13, 2021
Licensed Content Publisher	John Wiley and Sons
Licensed Content Publication	Advanced Materials
Licensed Content Title	Surface Engineering for Extremely Enhanced Charge Separation and Photocatalytic Hydrogen Evolution on g-C3N4
Licensed Content Author	Kejian Ding, Songmei Wu, Haihan Zou, et al
Licensed Content Date	Jan 15, 2018
Licensed Content Volume	30
Licensed Content Issue	9
Licensed Content Pages	8
Type of Use	Dissertation/Thesis
Requestor type	University/Academic
Format	Print and electronic
Portion	Figure/table
Number of figures/tables	1
Will you be translating?	No
Title	Synthesis and properties of layered g-C3N4 and their applications
Institution name	Curtin University
Expected presentation date	Mar 2021
Portions	Figure 2
Requestor Location	Xiao Zhang B614 Curtin University Perth, Bentley 6102 Australia Attn: Xiao Zhang
Publisher Tax ID	EU826007151
Total	**0.00 AUD**

License Details

This Agreement between Xiao Zhang ("You") and John Wiley and Sons ("John Wiley and Sons") consists of your license details and the terms and conditions provided by Joh Wiley and Sons and Copyright Clearance Center.

Print Copy

License Number	5006921304348
License date	Feb 13, 2021
Licensed Content Publisher	John Wiley and Sons
Licensed Content Publication	Advanced Materials Interfaces
Licensed Content Title	2D Nanocomposite of g-C3N4 and TiN Embedded N-Doped Graphene for Photoelectrochemical Reduction of Water Using Sunlight
Licensed Content Author	Angshuman Nag, Satishchandra Ogale, Reshma Bhosale, et al
Licensed Content Date	Nov 14, 2018
Licensed Content Volume	5
Licensed Content Issue	24
Licensed Content Pages	8
Type of Use	Dissertation/Thesis
Requestor type	University/Academic
Format	Print and electronic
Portion	Figure/table
Number of figures/tables	2
Will you be translating?	No
Title	Synthesis and properties of layered g-C3N4 and their applications
Institution name	Curtin University
Expected presentation date	Mar 2021
Portions	Scheme 1, Figure 1
Requestor Location	Xiao Zhang B614 Curtin University Perth, Bentley 6102 Australia Attn: Xiao Zhang
Publisher Tax ID	EU826007151
Total	**0.00 AUD**

License Details

This Agreement between Xiao Zhang ("You") and John Wiley and Sons ("John Wiley and Sons") consists of your license details and the terms and conditions provided by John Wiley and Sons and Copyright Clearance Center.

Print Copy

License Number	5006930595876
License date	Feb 13, 2021
Licensed Content Publisher	John Wiley and Sons
Licensed Content Publication	Angewandte Chemie International Edition
Licensed Content Title	Adjusting the Reduction Potential of Electrons by Quantum Confinement for Selective Photoreduction of CO2 to Methanol
Licensed Content Author	Jinlong Gong, Zhibin Luo, Zhiqi Huang, et al
Licensed Content Date	Feb 6, 2019
Licensed Content Volume	58
Licensed Content Issue	12
Licensed Content Pages	5
Type of Use	Dissertation/Thesis
Requestor type	University/Academic
Format	Print and electronic
Portion	Figure/table
Number of figures/tables	1
Will you be translating?	No
Title	Synthesis and properties of layered g-C3N4 and their applications
Institution name	Curtin University
Expected presentation date	Mar 2021
Portions	Figure 2
Requestor Location	Xiao Zhang B614 Curtin University Perth, Bentley 6102 Australia Attn: Xiao Zhang
Publisher Tax ID	EU826007151
Total	**0.00 AUD**

License Details

This Agreement between Xiao Zhang ("You") and John Wiley and Sons ("John Wiley and Sons") consists of your license details and the terms and conditions provided by John Wiley and Sons and Copyright Clearance Center.

Print Copy

License Number	5006930931170
License date	Feb 13, 2021
Licensed Content Publisher	John Wiley and Sons
Licensed Content Publication	Advanced Functional Materials
Licensed Content Title	Localized Surface Plasmon Resonance Enhanced Photocatalytic Hydrogen Evolution via Pt@Au NRs/C3N4 Nanotubes under Visible-Light Irradiation
Licensed Content Author	Qingbo Meng, Akira Fujishima, Kazuya Nakata, et al
Licensed Content Date	Nov 20, 2018
Licensed Content Volume	29
Licensed Content Issue	3
Licensed Content Pages	10
Type of Use	Dissertation/Thesis
Requestor type	University/Academic
Format	Print and electronic
Portion	Figure/table
Number of figures/tables	1
Will you be translating?	No
Title	Synthesis and properties of layered g-C3N4 and their applications
Institution name	Curtin University
Expected presentation date	Mar 2021
Portions	Figure 1
Requestor Location	Xiao Zhang B614 Curtin University Perth, Bentley 6102 Australia Attn: Xiao Zhang
Publisher Tax ID	EU826007151
Total	**0.00 AUD**

License Details

This Agreement between Xiao Zhang ("You") and Elsevier ("Elsevier") consists of your license details and the terms and conditions provided by Elsevier and Copyright Clearance Center.

Print Copy

License Number	5006931170178
License date	Feb 13, 2021
Licensed Content Publisher	Elsevier
Licensed Content Publication	Applied Catalysis B: Environmental
Licensed Content Title	Ultrathin 2D/2D WO3/g-C3N4 step-scheme H2-production photocatalyst
Licensed Content Author	Junwei Fu,Quanlong Xu,Jingxiang Low,Chuanjia Jiang,Jiaguo Yu
Licensed Content Date	Apr 1, 2019
Licensed Content Volume	243
Licensed Content Issue	n/a
Licensed Content Pages	10
Type of Use	reuse in a thesis/dissertation
Portion	figures/tables/illustrations
Number of figures/tables/illustrations	2
Format	both print and electronic
Are you the author of this Elsevier article?	No
Will you be translating?	No
Title	Synthesis and properties of layered g-C3N4 and their applications
Institution name	Curtin University
Expected presentation date	Mar 2021
Portions	Figure 1, Scheme 2
Requestor Location	Xiao Zhang B614 Curtin University Perth, Bentley 6102 Australia Attn: Xiao Zhang
Publisher Tax ID	GB 494 6272 12
Total	**0.00 AUD**

License Details

This Agreement between Xiao Zhang ("You") and Elsevier ("Elsevier") consists of your license details and the terms and conditions provided by Elsevier and Copyright Clearance Center.

Print Copy

License Number	5006940251053
License date	Feb 13, 2021
Licensed Content Publisher	Elsevier
Licensed Content Publication	Applied Catalysis B: Environmental
Licensed Content Title	A New and stable Mo-Mo2C modified g-C3N4 photocatalyst for efficient visible light photocatalytic H2 production
Licensed Content Author	Jie Dong,Ying Shi,Cunping Huang,Qiang Wu,Tao Zeng,Weifeng Yao
Licensed Content Date	Apr 1, 2019
Licensed Content Volume	243
Licensed Content Issue	n/a
Licensed Content Pages	9
Type of Use	reuse in a thesis/dissertation
Portion	figures/tables/illustrations
Number of figures/tables/illustrations	2
Format	both print and electronic
Are you the author of this Elsevier article?	No
Will you be translating?	No
Title	Synthesis and properties of layered g-C3N4 and their applications
Institution name	Curtin University
Expected presentation date	Mar 2021
Portions	Figure 1, Figure 4
Requestor Location	Xiao Zhang B614 Curtin University Perth, Bentley 6102 Australia Attn: Xiao Zhang
Publisher Tax ID	GB 494 6272 12
Total	**0.00 AUD**

License Details

This Agreement between Xiao Zhang ("You") and Elsevier ("Elsevier") consists of your license details and the terms and conditions provided by Elsevier and Copyright Clearance Center.

Print Copy

License Number	5006940881932
License date	Feb 13, 2021
Licensed Content Publisher	Elsevier
Licensed Content Publication	Journal of Alloys and Compounds
Licensed Content Title	Hexagonal g-C3N4 nanotubes with Pt decorated surface towards enhanced photo- and electro-chemistry performance
Licensed Content Author	Zhixiang Jiang,Changchao Jia,Bo Wang,Ping Yang,Guanggang Gao
Licensed Content Date	Jun 15, 2020
Licensed Content Volume	826
Licensed Content Issue	n/a
Licensed Content Pages	1
Type of Use	reuse in a thesis/dissertation
Portion	figures/tables/illustrations
Number of figures/tables/illustrations	2
Format	both print and electronic
Are you the author of this Elsevier article?	No
Will you be translating?	No
Title	Synthesis and properties of layered g-C3N4 and their applications
Institution name	Curtin University
Expected presentation date	Mar 2021
Portions	Figure 1, Figure 2
Requestor Location	Xiao Zhang B614 Curtin University Perth, Bentley 6102 Australia Attn: Xiao Zhang
Publisher Tax ID	GB 494 6272 12
Total	**0.00 AUD**

License Details

This Agreement between Xiao Zhang ("You") and Elsevier ("Elsevier") consists of your license details and the terms and conditions provided by Elsevier and Copyright Clearance Center.

Print Copy

License Number	5006941273030
License date	Feb 13, 2021
Licensed Content Publisher	Elsevier
Licensed Content Publication	Applied Catalysis B: Environmental
Licensed Content Title	Hydroxyl decorated g-C3N4 nanoparticles with narrowed bandgap for high efficient photocatalyst design
Licensed Content Author	Lijing Wang,Gang Zhou,Yu Tian,Likai Yan,Mingxiao Deng,Bai Yang,Zhenhui Kang,Haizhu Sun
Licensed Content Date	5 May 2019
Licensed Content Volume	244
Licensed Content Issue	n/a
Licensed Content Pages	10
Type of Use	reuse in a thesis/dissertation
Portion	figures/tables/illustrations
Number of figures/tables/illustrations	2
Format	both print and electronic
Are you the author of this Elsevier article?	No
Will you be translating?	No
Title	Synthesis and properties of layered g-C3N4 and their applications
Institution name	Curtin University
Expected presentation date	Mar 2021
Portions	Figure 1, Figure 2
Requestor Location	Xiao Zhang B614 Curtin University Perth, Bentley 6102 Australia Attn: Xiao Zhang
Publisher Tax ID	GB 494 6272 12
Total	**0.00 AUD**

License Details

This Agreement between Xiao Zhang ("You") and Elsevier ("Elsevier") consists of your license details and the terms and conditions provided by Elsevier and Copyright Clearance Center.

Print Copy

License Number	5006950275398
License date	Feb 13, 2021
Licensed Content Publisher	Elsevier
Licensed Content Publication	Applied Catalysis B: Environmental
Licensed Content Title	Sea-urchin-structure g-C3N4 with narrow bandgap (~2.0 eV) for efficient overall water splitting under visible light irradiation
Licensed Content Author	Yunxiong Zeng,Hao Li,Jinming Luo,Jili Yuan,Longlu Wang,Chengbin Liu,Yingchun Xia,Meijun Liu,Shenglian Luo,Tao Cai,Su Liu,John C. Crittenden
Licensed Content Date	Jul 15, 2019
Licensed Content Volume	249
Licensed Content Issue	n/a
Licensed Content Pages	7
Type of Use	reuse in a thesis/dissertation
Portion	figures/tables/illustrations
Number of figures/tables/illustrations	2
Format	both print and electronic
Are you the author of this Elsevier article?	No
Will you be translating?	No
Title	Synthesis and properties of layered g-C3N4 and their applications
Institution name	Curtin University
Expected presentation date	Mar 2021
Portions	Scheme 1, Figure 1
Requestor Location	Xiao Zhang B614 Curtin University Perth, Bentley 6102 Australia Attn: Xiao Zhang
Publisher Tax ID	GB 494 6272 12

License Details

This Agreement between Xiao Zhang ("You") and John Wiley and Sons ("John Wiley and Sons") consists of your license details and the terms and conditions provided by John Wiley and Sons and Copyright Clearance Center.

Print Copy

License Number	5006950918000
License date	Feb 13, 2021
Licensed Content Publisher	John Wiley and Sons
Licensed Content Publication	Small
Licensed Content Title	Impact of Interfacial Electron Transfer on Electrochemical CO2 Reduction on Graphitic Carbon Nitride/Doped Graphene
Licensed Content Author	Shi-Zhang Qiao, Yao Zheng, Yan Jiao, et al
Licensed Content Date	Feb 4, 2019
Licensed Content Volume	15
Licensed Content Issue	10
Licensed Content Pages	7
Type of Use	Dissertation/Thesis
Requestor type	University/Academic
Format	Print and electronic
Portion	Figure/table
Number of figures/tables	1
Will you be translating?	No
Title	Synthesis and properties of layered g-C3N4 and their applications
Institution name	Curtin University
Expected presentation date	Mar 2021
Portions	Figure 1
Requestor Location	Xiao Zhang B614 Curtin University Perth, Bentley 6102 Australia Attn: Xiao Zhang
Publisher Tax ID	EU826007151
Total	**0.00 AUD**

Copyright Clearance Center | Marketplace™

Royal Society of Chemistry - License Terms and Conditions

This is a License Agreement between Xiao Zhang ("You") and Royal Society of Chemistry ("Publisher") provided by Copyright Clearance Center ("CCC"). The license consists of your order details, the terms and conditions provided by Royal Society of Chemistry, and the CCC terms and conditions.

All payments must be made in full to CCC.

Order Date	13-Feb-2021	**Type of Use**	Republish in a thesis/dissertation
Order license ID	1097221-1	**Publisher**	ROYAL SOCIETY OF CHEMISTRY
ISSN	1460-4744	**Portion**	Chart/graph/table/figure

LICENSED CONTENT

Publication Title	Chemical Society reviews	**Country**	United Kingdom of Great Britain and Northern Ireland
Author/Editor	Royal Society of Chemistry (Great Britain)	**Rightsholder**	Royal Society of Chemistry
Date	01/01/1972	**Publication Type**	e-Journal
Language	English	**URL**	http://www.rsc.org/csr

REQUEST DETAILS

Portion Type	Chart/graph/table/figure	**Distribution**	Worldwide
Number of charts / graphs / tables / figures requested	1	**Translation**	Original language of publication
Format (select all that apply)	Print, Electronic	**Copies for the disabled?**	No
Who will republish the content?	Academic institution	**Minor editing privileges?**	No
Duration of Use	Life of current edition	**Incidental promotional use?**	No
Lifetime Unit Quantity	Up to 9,999	**Currency**	AUD
Rights Requested	Main product		

NEW WORK DETAILS

Title	Synthesis and properties of layered g-C3N4 and their applications	**Institution name**	Curtin University
Instructor name	Xiao Zhang	**Expected presentation date**	2021-03-01

ADDITIONAL DETAILS

Order reference number	N/A	**The requesting person / organization to appear on the license**	Xiao Zhang

REUSE CONTENT DETAILS

Title, description or numeric reference of the portion(s)	Figure 1	**Title of the article/chapter the portion is from**	Carbon nitrides and metal nanoparticles: from controlled synthesis to design principles for improved photocatalysis
Editor of portion(s)	N/A	**Author of portion(s)**	Royal Society of Chemistry (Great Britain)
Volume of serial or monograph	47	**Issue, if republishing an article from a serial**	N/A
Page or page range of portion	7783-7817	**Publication date of portion**	2018-09-20

Copyright Clearance Center | Marketplace™

Royal Society of Chemistry - License Terms and Conditions

This is a License Agreement between Xiao Zhang ("You") and Royal Society of Chemistry ("Publisher") provided by Copyright Clearance Center ("CCC"). The license consists of your order details, the terms and conditions provided by Royal Society of Chemistry, and the CCC terms and conditions.

All payments must be made in full to CCC.

Order Date	13-Feb-2021	**Type of Use**	Republish in a thesis/dissertation
Order license ID	1097218-1	**Publisher**	ROYAL SOCIETY OF CHEMISTRY
ISSN	1364-548X	**Portion**	Chart/graph/table/figure

LICENSED CONTENT

Publication Title	Chemical communications	**Country**	United Kingdom of Great Britain and Northern Ireland
Author/Editor	Royal Society of Chemistry (Great Britain)	**Rightsholder**	Royal Society of Chemistry
Date	01/01/1996	**Publication Type**	e-Journal
Language	English		

REQUEST DETAILS

Portion Type	Chart/graph/table/figure	**Distribution**	Worldwide
Number of charts / graphs / tables / figures requested	2	**Translation**	Original language of publication
Format (select all that apply)	Print, Electronic	**Copies for the disabled?**	No
Who will republish the content?	Academic institution	**Minor editing privileges?**	No
Duration of Use	Life of current edition	**Incidental promotional use?**	No
Lifetime Unit Quantity	Up to 9,999	**Currency**	AUD
Rights Requested	Main product		

NEW WORK DETAILS

Title	Synthesis and properties of layered g-C3N4 and their applications	**Institution name**	Curtin University
Instructor name	Xiao Zhang	**Expected presentation date**	2021-03-01

ADDITIONAL DETAILS

Order reference number	N/A	**The requesting person / organization to appear on the license**	Xiao Zhang

REUSE CONTENT DETAILS

Title, description or numeric reference of the portion(s)	Fig.1, Scheme 1	**Title of the article/chapter the portion is from**	An amorphous/crystalline g-C3N4 homojunction for visible light photocatalysis reactions with superior activity
Editor of portion(s)	N/A	**Author of portion(s)**	Royal Society of Chemistry (Great Britain)
Volume of serial or monograph	54	**Issue, if republishing an article from a serial**	N/A
Page or page range of portion	4720-4723	**Publication date of portion**	2018-04-16

Appendix: Co-author Attribution Statement

Chapter 3:

1. *"Construction of 2D g-C_3N_4 lateral-like homostructures and their photo- and electro-catalytic activities, Chem. Commun., 2019, 55, 1233—1236."*

	Conception and design	**Experiments conduction & data acquisition**	**Data processing & analysis**	**interpretation & discussion**	**Manuscript writing, revision and finalisation**	**Final approval**
Xiao Zhang	×	×	×	×	×	×
	I acknowledge that these represent my contribution to the above result output. Signed.					
Dr. Jean-Pierre Veder		×	×	×	×	×
	I acknowledge that these represent my contribution to the above result output. Signed.					
Dr. Shuai He		×				×
	I acknowledge that these represent my contribution to the above result output. Signed.					
Dr. Sanping Jiang	×		×	×	×	×
	I acknowledge that these represent my contribution to the above result output. Signed.					

2. *"Photo-chemical property evolution of superior thin g-C_3N_4 nanosheets with their crystallinity and Pt deposition, International Journal of Hydrogen Energy, 2020, 45, 21523-21531."*

	Conception and design	**Experiments conduction & data acquisition**	**Data processing & analysis**	**interpretation & discussion**	**Manuscript writing, revision and finalisation**	**Final approval**
Xiao Zhang	×	×	×	×	×	×
	I acknowledge that these represent my contribution to the above result output. Signed.					
Peng Wang		×				×
	I acknowledge that these represent my contribution to the above result output. Signed.					
Dr. Ping Yang	×		×	×	×	×
	I acknowledge that these represent my contribution to the above result output. Signed.					
Dr. Sanping Jiang	×		×	×	×	×
	I acknowledge that these represent my contribution to the above result output. Signed.					

Chapter 4:

1."The edge-epitaxial growth of yellow g-C_3N_4 on red g-C_3N_4 nanosheets with superior photocatalytic activities, Chem. Commun. 2021, 57, 3119 – 3122." & 2."Bright and tunable photoluminescence from the assembly of red g-C_3N_4 nanosheets, J. Lumin. 2021, 235, 118055."

	Conception and design	**Experiments conduction & data acquisition**	**Data processing & analysis**	**interpretation & discussion**	**Manuscript writing, revision and finalisation**	**Final approval**
Xiao Zhang	×	×	×	×	×	×
	I acknowledge that these represent my contribution to the above result output. Signed.					
Dr. Ping Yang	×		×	×	×	×
	I acknowledge that these represent my contribution to the above result output. Signed.					
Dr. Sanping Jiang	×		×	×	×	×
	I acknowledge that these represent my contribution to the above result output. Signed.					

Chapter 5:

"Pt nanoparticles embedded spine-like g-C_3N_4 cages with superior photocatalytic activity for H_2 generation and CO_2 reduction, Nanotechnology, 2021, 32, 175401."

	Conception and design	**Experiments conduction & data acquisition**	**Data processing & analysis**	**interpretation & discussion**	**Manuscript writing, revision and finalisation**	**Final approval**
Xiao Zhang	×	×	×	×	×	×
	I acknowledge that these represent my contribution to the above result output. Signed.					
Dr. Ping Yang	×		×	×	×	×
	I acknowledge that these represent my contribution to the above result output. Signed.					
Dr. Sanping Jiang	×		×	×	×	×
	I acknowledge that these represent my contribution to the above result output. Signed.					

Chapter 6:

1. *"WOx/g-C_3N_4 layered heterostructures with controlled crystallinity towards superior photocatalytic degradation and H_2 generation, Carbon, 2020, 156, 488-498"*

	Conception and design	**Experiments conduction & data acquisition**	**Data processing & analysis**	**interpretation & discussion**	**Manuscript writing, revision and finalisation**	**Final approval**
Xiao Zhang	×	×	×	×	×	×
	I acknowledge that these represent my contribution to the above result output. Signed.					
Dr. Shuai He		×				×
	I acknowledge that these represent my contribution to the above result output. Signed.					
Dr. Sanping Jiang	×		×	×	×	×
	I acknowledge that these represent my contribution to the above result output. Signed.					

2. *"Horizontally-growth of WS_2/WO_3 heterostructures on crystalline g-C_3N_4 nanosheets towards enhanced photo/electro-chemical performance, Journal of Nanostructure in Chemistry, 2021, https://doi.org/10.1007/s40097-020-00373-7."*

	Conception and design	**Experiments conduction & data acquisition**	**Data processing & analysis**	**interpretation & discussion**	**Manuscript writing, revision and finalisation**	**Final approval**
Xiao Zhang	×	×	×	×	×	×
	I acknowledge that these represent my contribution to the above result output. Signed.					
Dr. Ping Yang	×		×	×	×	×
	I acknowledge that these represent my contribution to the above result output. Signed.					
Dr. Sanping Jiang	×		×	×	×	×
	I acknowledge that these represent my contribution to the above result output. Signed.					

Chapter 7

"Horizontally-grown NiCo-LDHs on g-C_3N_4 nanosheets with enhanced adsorption capacity and photoreduction efficiency of Congo red and Cr(VI), Appl. Sur. Sci., 2021, https://doi.org/10.1016/j.apsusc.2021.149772."

	Conception and design	**Experiments conduction & data acquisition**	**Data processing & analysis**	**interpretation & discussion**	**Manuscript writing, revision and finalisation**	**Final approval**
Xiao Zhang	×	×	×	×	×	×
	I acknowledge that these represent my contribution to the above result output. Signed.					
Dr. Ping Yang	×		×	×	×	×
	I acknowledge that these represent my contribution to the above result output. Signed.					
Dr. Sanping Jiang	×		×	×	×	×
	I acknowledge that these represent my contribution to the above result output. Signed.					